Dipl.-Ing. Stefan Leitner

Low-Cost Sub-Fractional HP Outer-Rotor BLDC Claw-Pole Motor Designs with Reduced Cogging Torque

DISSERTATION

to obtain the university degree of
Doktor der technischen Wissenschaften (Dr. techn.)

submitted to

Graz University of Technology, Austria

Supervisor and First Assessor:

Prof. Annette Muetze
Electric Drives and Machines Institute, Graz University of Technology, Austria

Second Assessor:

Prof. Yves Perriard
Integrated Actuators Laboratory, Swiss Federal Institute of Technology in Lausanne, Switzerland

Graz, July 2020

AFFIDAVIT

I declare that I have authored this thesis independently, that I have not used other than the declared sources/resources, and that I have explicitly indicated all material which has been quoted either literally or by content from the sources used. The text document uploaded to TUGRAZonline is identical to the present doctoral thesis.

.....	.....
Date	Signature

“Simplicity is the ultimate sophistication.”

-Leonardo da Vinci

Contents

Abstract

The increasing performance requirements on automotive auxiliary drives have led to a paradigm shift in the design of sub-fractional horsepower brushless direct current (BLDC) motors. While minimum cost used to be the primary design criteria, thereby accepting sub-optimal motor behavior, their overall performance is gaining in importance. The large cogging torque and torque ripple of single-phase BLDC motors, which often lead to disturbing structure- and airborne noise, have become unacceptable in many applications. However, the implementation of cogging torque reduction measures typically involves additional fabrication steps, thus increasing the cost, which is a disqualifier for mass-produced low-cost applications.

This thesis presents single-phase BLDC motor designs in which the cogging torque and, in turn, the output torque ripple can be reduced at no increase to the manufacturing cost. On the basis of the claw-pole motor topology, consisting of a ring winding housed between two specially shaped deep-drawn steel sheet parts, various design improvements are proposed and analyzed in detail. Therefore, different analytic and numerical models are developed and used to study phenomena such as cogging torque, back-EMF, magnetic forces, and iron losses. Subsequently, the simulation results are verified by experiments, notably by rheometer-based techniques presented for the first time.

The main findings are presented hereafter. Implementing the claw-pole motor with an asymmetric air-gap can facilitate the starting and, simultaneously, provide maximum design freedom concerning the claw-pole shapes for the implementation of cogging torque reduction measures. In case of static eccentricity or a non-uniform magnetization pattern, the studied four-pole four-slot claw-pole motor shows pulsating unbalanced radial magnetic forces with a dominating fourth order harmonic component. Implementing a single-sided skew of 30° can successfully reduce the cogging torque by about 25 %, while the back-EMF reduction is below 2 %. This cogging torque reduction results in an output torque ripple reduction of about 12%. The proposed auxiliary slots can effectively modulate the cogging torque of the claw-pole

motor. Realizing a single-sided skew of 45° in addition to auxiliary slots can successfully reduce the cogging torque by 70 %. The cogging torque decline is accompanied by a reduction in the back-EMF of 12 %, while the output torque ripple is reduced by 17 %. The application of a single-sided skew generally induces axial magnetic forces which can reduce the bearing system's lifetime as well as cause vibrations and noise. Owing to the proposed design with a V-skew, the axial magnetic forces are balanced while, concurrently, the cogging torque is successfully reduced by about 50 % and the back-EMF is marginally reduced by about 1 %. Using a rheometer, the motor's cogging torque and hysteresis torque waveforms in the sub-milli-Newton meter range can be measured with excellent accuracy. Moreover, the rheometer is used to accurately determine the iron losses of the motors under investigation by studying the observed offset torque. It is advantageous that all manufacturing influences are included in the measured iron losses because, as opposed to the investigation of sheet material properties, the assembled motor is studied.

As identified in this thesis, the single-phase BLDC claw-pole motor topology is suitable for the implementation of cogging torque reduction measures at no increase to the manufacturing cost. However, as motor performance parameters are typically interdependent, a beneficial change in one parameter is often linked to a detrimental change in another parameter. Cogging torque reduction always comes with a reduction in the average output torque or efficiency, but it can successfully reduce the output torque ripple. The developed design improvements are by no means limited to motors as part of automotive auxiliary drive applications; they can generally be used in any cooling system, especially those in electronics, such as personal computers, household appliances, office automation, and even within the aerospace industry.

Zusammenfassung (in German)

Die steigenden Anforderungen an elektrische Hilfsantriebe in Fahrzeuganwendungen haben zu einem Paradigmenwechsel im Hinblick auf den Entwurf der oft verwendeten bürstenlosen Gleichstrommotoren [engl. brushless direct current (BLDC) motors] geführt. Während früher oft suboptimales Motorverhalten in Kauf genommen wurde, um die Herstellungskosten zu reduzieren, gewinnen die verschiedenen Performance Parameter von elektrischen Kleinantrieben zunehmend an Bedeutung – besonders vor dem Hintergrund sinkender Fahrzeuggeräuschpegel. Das relativ große Rastmoment dieser Kleinmotoren, und der unter anderem daraus resultierende Drehmomentrippel, führt oft zu inakzeptablem Körper- und Luftschall. Jedoch ist die Implementierung von rastmomentreduzierenden Maßnahmen in der Motorauslegung typischerweise mit zusätzlichen Kosten verbunden und daher ein Ausschlusskriterium für Massenproduktion.

Diese Arbeit präsentiert einphasige BLDC-Motorbauarten bei denen das Rastmoment (und in weiterer Folge der Drehmomentrippel) reduziert werden kann, ohne dass dadurch die Herstellungskosten steigen. Basierend auf dem Klauenpolkonzept, charakterisiert durch eine Ringwicklung zwischen zwei gestanzten und tiefgezogenen Polkonstruktionen, werden verschiedene Verbesserungsmaßnahmen vorgeschlagen und analysiert. Diverse analytische und numerische Modelle werden entwickelt, um Motor-Leistungsparameter, wie zum Beispiel das Rastmoment, die induzierte Spannung, die magnetischen Kräfte und die Eisenverluste, zu untersuchen. Anschließend werden die Simulationsergebnisse durch verschiedene Experimente verifiziert, im Speziellen mit neuartigen rheometerbasierten Techniken.

Die Hauptaussagen stellen sich wie folgt dar: Die Implementierung eines asymmetrischen Luftspalts erleichtert das Anlaufen des Klauenpolmotors bei gleichzeitiger maximaler Gestaltungsfreiheit der Klauenpolgeometrie, um rastmomentreduzierende Maßnahmen applizieren zu können. Statische Exzentrizität oder ungleiche Magnetisierung können zu einem pulsierenden einseitigen magnetischen Zug mit vierfacher Drehfrequenz führen. Durch eine einseitige 30° Schrägung der Klauen

kann das Rastmoment um 25 % reduziert werden, bei einer Reduktion der induzierten Spannung unter 2 %. Diese Rastmomentreduktion führt zu einer Drehmomentrippelreduktion von ca. 12 %. Durch das gezielte Einfügen von Zusatznuten, kann das Rastmoment des Klauenpolmotors moduliert werden. Werden Zusatznuten mit einer einseitigen Klauenschrägung von 45° kombiniert, kann das Rastmoment um 70 % reduziert werden. Dies hat eine Reduktion der induzierten Spannung von 12 % zur Folge, jedoch auch eine Reduktion des Drehmomentrippels von 17 %. Die Implementierung einer einseitigen Klauenschrägung ruft im Allgemeinen Axialkräfte hervor, welche die Lagerlebensdauer reduzieren, sowie Vibrationen und Geräusche hervorrufen können. Durch die vorgeschlagene V-Schrägung können die magnetischen Axialkräfte kompensiert werden, bei gleichzeitiger Rastmomentreduktion von ca. 50 % und einer Reduktion der induzierten Spannung von nur ca. 1 %. Die Rast- und Hysteresemomente von elektrischen Kleinmotoren, mit Spitzenwerten im sub-milli-Newton Meter Bereich, kann mit Hilfe eines Rheometers mit sehr hoher Genauigkeit gemessen werden. Darüber hinaus können auch die Eisenverluste dieser Motoren bestimmt werden, indem man den Gleichanteil der gemessenen Kurvenform analysiert. Hierbei sind vorteilhafterweise, im Gegensatz zur Vermessung von Blechproben, alle Herstellungseinflüsse, die die Eisenverluste typischerweise signifikant verändern, inhärent berücksichtigt, weil der fertige Motor untersucht werden kann.

Es zeigt sich, dass die einphasige BLDC-Klauenpolmotortopologie geeignet ist, rastmomentreduzierende Maßnahmen zu implementieren, ohne dass dadurch die Herstellungskosten steigen. Jedoch sind die Motor-Leistungsparameter im Allgemeinen interdependent, wobei eine Verbesserung des einen oft zu einer Verschlechterung des anderen führen kann. Rastmomentreduktion geht typischerweise mit einer Reduktion des Wirkungsgrades oder des mittleren Drehmoments einher, jedoch kann der Drehmomentrippel erfolgreich reduziert werden. Die entwickelten Verbesserungsmaßnahmen beschränken sich nicht auf Motoren für Fahrzeuganwendungen, sondern können in jeglichen Kühlsystemen, speziell in solchen von elektronischen Geräten (z.B. Computer, Haushaltsgeräte, Büroautomatisierung, Raumfahrtindustrie) eingesetzt werden.

Acknowledgements

The present dissertation was written within the framework of the Christian Doppler Laboratory for Brushless Drives for Pump and Fan Applications at Graz University of Technology, Graz, Austria, between November 2016 and July 2020. This endeavor would have never been possible without the help and support from the following people:

First and foremost, I would like to thank my doctorate supervisor Prof. Dr.-Ing. Annette Muetze who gave me the opportunity to write this thesis, supported me on the way, and always trusted and encouraged me.

Special thanks go to my beloved girlfriend Johanna, my parents Gabriela and Hans-Peter, as well as my friends and relatives for their endless understanding, support, and encouragement.

Next, I would like to thank my colleagues at the Electric Drives and Machines Institute for their support, the interesting discussions, and, most importantly, all the fun we had in- and outside the university.

I would also like to thank Prof. Dr. Yves Perriard from the Integrated Actuators Laboratory at Swiss Federal Institute of Technology in Lausanne, Switzerland for the valuable discussions and taking on the role as second assessor.

I am also grateful to DI Hans-Joerg Gasser, Dr. Gerhard Schoener, Dr. Markus Mosshammer, and Dr. Philipp Scheiber from Mechatronic Systems GmbH, Wies, Austria, for the fruitful collaboration, and DI Gerhard Murer and Dr. Georg Krenn from Anton Paar GmbH, Graz, Austria, for providing the opportunity to perform experiments with the rheometer.

The financial support from the Christian Doppler Research Association (CDG) is gratefully acknowledged.

Motivation

Beyond all doubt, small electric motors and drives make our lives easier and more pleasant. Often remaining unnoticed, they fulfill many different tasks in many different economic sectors, reducing manual labor and increasing mankind's comfort. Yet, these motors can be considered the forgotten stepchild of the research community. To date, neither has their full potential been unlocked, nor have many of them been thoroughly investigated experimentally. The reasons for this are mani-fold.

For one, small electric motors and drives are typically part of mass-produced and hence primarily cost-driven applications, in which sub-optimal motor behavior or performance (e.g., low efficiency, high cogging torque, high torque ripple, noise and vibrations) has long been deemed acceptable. For another, a large variety of creative small motor principles and designs exists, which work on different functioning principles, each tailored to meet application-specific requirements. Classic examples thereof include hysteresis, shaded-pole, switched reluctance, stepper, claw-pole, and capacitor motors. Other examples include the slotless motor concepts from Maxon Motor AG and Dr. Fritz Faulhaber GmbH & Co. KG. Furthermore, interesting rather new developments include printed circuit board (PCB) axial flux permanent-magnet (PM) motors and slotless radial flux PM motors with flex-PCB air-gap windings. However, the experimental investigation of small electric motors is often challenging due to their small dimensions, the significant influence of friction, and the shortage of appropriate measurement equipment.

While minimum cost used to be the primary design criterion of small electric motors, their performance has been becoming more and more important as of late, partly due to the increase in electrification. Hence, low-cost motor design improvements and proper simulation and measurement techniques are gaining in importance, to which this thesis aims to make a contribution.

Part I

The BLDC Claw-Pole Motor

Chapter 1

Introduction

First, this chapter explains the context of this thesis, focusing on the current developments within the automotive industry as to auxiliary drives and their characteristics. Second, the working principle and characteristics of fractional horsepower brushless direct current motors are discussed, as well as the cogging torque and iron losses of permanent-magnet machines. Then, a historic overview of claw-pole machines is given. Last, the contributions of this thesis are detailed, as are the list of first author publications and the thesis outline.

1.1 Context

Since their invention in the 19th century, electric machines have been making our lives easier. As generators, they convert mechanical energy into electrical energy on which we all so much depend. As motors, they convert electrical energy into mechanical energy, taking the work out of our hands in many ways and making many things possible in the first place. Today, electric motors account for about 50 % of global electricity consumption [1]; in the EU, US, China, India, and Japan this actually reaches approximately 70 % [2]. By far, the largest portion thereof is held by the pumping, compressed air, and fan systems, as well as material handling and processing systems, all at the industrial scale consisting of integral horsepower (IHP) motor drives.[1] However, quantitatively speaking, the majority of motor units (about 90 %) is in the fractional horsepower (FHP)[2] or in the sub-fractional horsepower (SFHP)[3] range, accounting for about 9 % of the total electricity used by electric motors due to

[1] IHP motors are motors with a power of one horsepower or above.
[2] FHP motors are motors with a power below one horsepower.
[3] For very low power systems (e.g., in the 1 W range), the terms sub-FHP (SFHP) or "micro" motors are commonly used.

their low power [1]. These motors are produced in very high volumes, and they are typically highly integrated customized solutions, fulfilling a specific purpose. Given the many different applications, an abundance of FHP and SFHP motor topologies of varying shapes and sizes has been developed. With such a plethora of customized solutions, standards for testing, sizing, or efficiency classification of such motors have not yet been established.

1.1.1 Overview of Automotive Auxiliary Drives

According to a 2017 ZVEI report,[4] 22 % of the electric drives manufactured in Germany were FHP motors, amounting to about two million Euros. Most FHP motors are sold in the automotive sector, followed by the white goods and industrial sectors. The demand for increased comfort, safety, and performance has led simultaneously to more than 100 auxiliary drives being installed in a mid-size or large executive car [3]. Typical applications are depicted in Fig. 1.1.

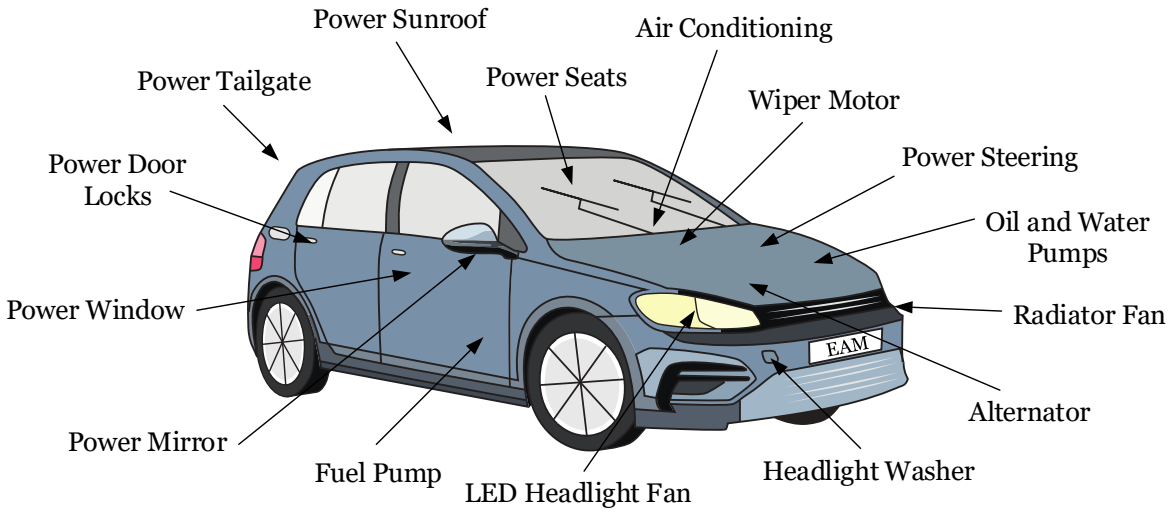

Fig. 1.1: Auxiliary drive examples [4]; picture credit: D. Klein.

Auxiliary drive applications can be classified into three main categories:

- Pumps (e.g., fuel, vacuum [5], oil [6], and water [7] pumps);
- Fans and blowers (e.g., LED headlight [8, 9] and engine cooling fans, air conditioning systems, seat ventilations [10], sensor blowers [11]); and

[4] ZVEI is the German Electrical and Electronic Manufacturers' Association (Zentralverband Elektrotechnik- und Elektronikindustrie e.V.).

- Actuators (e.g., power windows, power door locks, power seats, power mirrors, steering assistant).

Illustratively, Fig. 1.2 exhibits a typical radial fan drive with an integrated brushless direct current (BLDC) motor, used to both cool and defrost LED headlights.

Fig. 1.2: Radial fan drive for the thermal management of LED headlights (© MSG Mechatronic Systems GmbH).

The majority of the auxiliary drives installed in a car are comfort-related. Hence, the exact number strongly depends on the vehicle type and its equipment. New applications are likely to emerge in the future due to the increase in electrification (e.g., electro-mechanical brakes replacing electro-hydraulic brakes). A paradigm shift from brushed to brushless motor concepts has been taking place, especially for long-term auxiliary drive applications such as fan and pumping systems [12, 13].

A standard Volkswagen Golf 7 features about 50 auxiliary drives [14]. Considering some one million units manufactured in 2017 [15] results in 50 million auxiliary drives installed for the Golf 7 alone. In 2017, around 97 million cars were produced worldwide [16]. Assuming 50 auxiliary drives per car[5] yields around 5 billion small electric motors used in the automotive industry each year. This large number illustrates that even tiny reductions in the manufacturing and material costs or energy consumption of these drives may lead to immense savings both cost and energywise. In fact, energy efficiency has also been gaining in importance in light of the limited battery capacity (especially for electric vehicles in which the driving

[5]Since some cars have fewer and other cars have many more auxiliary drives installed, assuming an average of 50 auxiliary drives per car seems reasonable.

range depends on the battery capacity), the ever-increasing number of auxiliary drives, and their still relatively poor efficiency of, e.g., 30 %.

Since the demand for cars with reduced noise levels has been increasing in recent years, the noise of auxiliary drives, which is then masked by the combustion engine and other dominant noise sources, may reappear and become disturbing [17]. As a result, especially in electric vehicles, the application of conventional auxiliary drives is often not possible, unless costly vibration absorbers are utilized.

Hence, low-cost improvements of the auxiliary drive's motor behavior (e.g., increased efficiency, reduced torque ripple, reduced noise and vibrations) are desirable and have been gaining in significance.

1.1.2 Characteristics of Automotive Auxiliary Drives

As mentioned in Section 1.1, automotive auxiliary drives are typically highly integrated solutions. In addition to weight, they are subject to tight size constraints, because space is extremely limited in a car, which generally restricts the achievable torque. Moreover, they have to operate over both a large voltage range (e.g., 8 V to 16 V) and a large temperature range (e.g., −40°C to 135°C). While low temperatures increase the viscous friction of the bearing lubricants and the working fluid (e.g., a circulator pump with a canned motor), high temperatures decrease the strength of the permanent-magnets (PMs), making them prone to demagnetization. In addition, the electromagnetic compatibility requirements, automotive auxiliary drives have to comply with, have been becoming increasingly strict as of late.

Even though they are geometrically small, auxiliary drives can cause disturbing noise as a result of pulsating radial, axial, and tangential magnetic forces, the last of which is related to the motor torque.[6] This can be particularly problematic for drives installed in a noise-sensitive environment such as the car interior (e.g., air conditioning, sensor blowers, and seat ventilations). However, as opposed to IHP electric motors and drives, the maximum sound pressure levels of FHP and SFHP electric motors and drives are either insufficiently or not at all defined in the automotive standards. This is due to the fact that their overall noise, vibration, and harshness (NVH) behavior is significantly determined by the mounting and adjacent construction elements [18, 19].[7] Companies have developed in-house standards for airborne and structure-borne noise measurements (e.g., the Volkswagen standard

[6] Besides electromagnetic noise, distinct aerodynamic noise and mechanical noise can also occur.
[7] Typically, the application as a whole must fulfill specific noise requirements.

VW 82 469 [20]), including different limit curves and total sound pressure levels (SPLs) for airborne noise measurements.[8]

Because automotive auxiliary drives are typically mass-produced, they are primarily cost-driven. Therefore, sub-optimal motor behavior (e.g., low efficiency, high cogging torque, and high output torque ripple) has often been accepted so far, provided the functionality of the product is not compromised. For reasons of cost, many auxiliary drive applications comprise single-phase instead of three-phase BLDC motors, e.g., unidirectional variable-speed automotive fan and pump applications. However, single-phase BLDC motors inherently have much larger output torque fluctuations and ripple than three-phase variants, due to the fluctuating power. These motors typically also suffer from comparatively large cogging torque (resulting from cost-related sub-optimal slot-pole combinations), which can significantly increase the torque ripple and torque fluctuations [21]. The cogging torque induced output torque fluctuations and ripple can cause structure- and airborne noise during operation when system resonances are triggered [17, 22], see Fig. 1.3.[9]

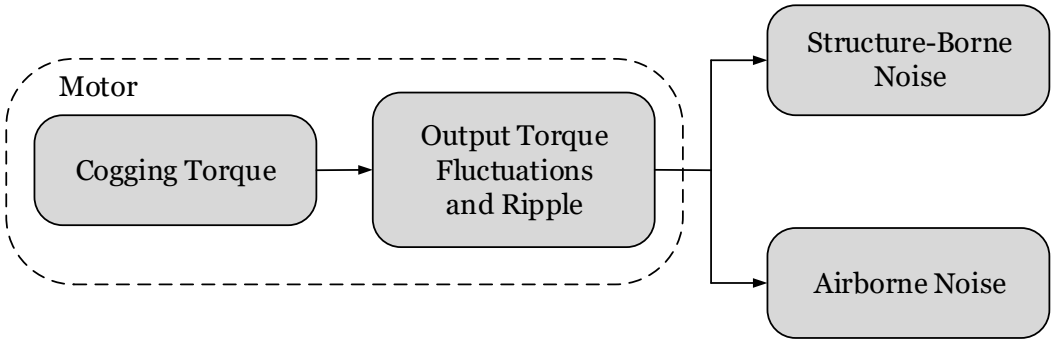

Fig. 1.3: Cause-effect-chain of noise indirectly caused by cogging torque.

Unfortunately, cogging torque reduction measures (e.g., rotor or stator skewing) to smooth down the output torque waveform are hardly applied to low-cost BLDC motors for the following two reasons:

1. It is often not possible due to their small dimensions and short axial length.[10]

[8] Typically, the loudest position has to be considered for the maximum total SPL. In case of a fan, this is often near the inlet or outlet.

[9] Other reasons for output torque ripple and fluctuations include the commutation process, ripples in the current due to PWM, as well as harmonics of the back-EMF and current waveforms [21].

[10] See the short lamination stack with interlocking of the well-known single-phase BLDC salient-pole motor shown in Fig. 2.11(b) used for fan applications, which is studied, e.g., in [23–25]. The

2. It is often not possible due to the greatly increased manufacturing complexity and cost, since the number of fabrication operations is increased [26–28].[11]

Remark: While often desirable in three-phase PM motors, fully eliminating the cogging torque can be detrimental in single-phase variants. Many designs rely on specific cogging (or parking) positions of the rotor (realized, e.g., by means of an asymmetric air-gap) from which the motor can start. Hence, the cogging torque must not be fully eliminated, which is neither possible, nor useful anyway. However, a specific partial reduction of the cogging torque will, in most cases, be desirable.

The main objective of this thesis is to develop single-phase BLDC motor designs with reduced cogging torque at no (or little) increase to the manufacturing cost. In this regard, Fig. 1.4(a) exhibits the key element of this thesis, the single-phase BLDC claw-pole motor with a ring winding. This motor has been identified as

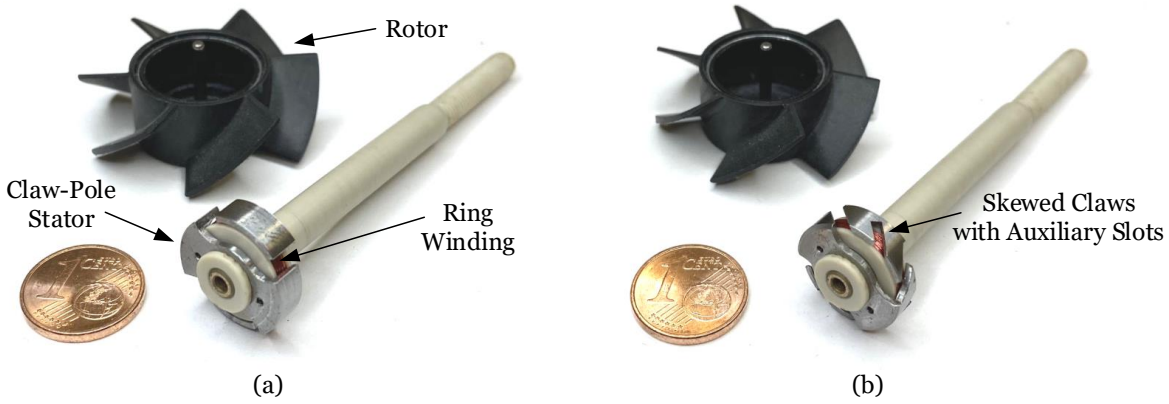

Fig. 1.4: (a) single-phase BLDC claw-pole motor under investigation (*Baseline*) and (b) one of the proposed low cogging torque motor designs (*Design 3*).

having a high potential in terms of the inexpensive implementation of cogging torque reduction measures. Hence, it serves as the *Baseline* for the proposed motor designs. Throughout this thesis, different claw-pole motor design improvements are proposed to reduce the cogging torque and, in turn, decrease the output torque ripple and smooth down the output torque waveform. Illustratively, Fig. 1.4(b) shows one of the proposed low cogging torque designs, *Design 3*, which features skewed claws with auxiliary slots, see the analysis in Chapter 7.

interlocking generally prevents stator skewing. Due to the short axial length of the motor, axial segmentation of the magnets to implement rotor skewing is unpractical.

[11] The realization of a skewed stator stack or skewed magnets is costly. The implementation of a skewed magnetization on a ring magnet requires a rather complicated magnetization fixture.

1.2 State-of-the-Art

This section discusses the working principle of brushless PM motors, focusing on BLDC motors, and gives an overview of the characteristics of SFHP variants, as well as the cogging torque and iron losses of such electric machines. In the last part, a historic review of claw-pole machines is included.

1.2.1 Brushless PM Motors

Brushless PM motors have become omnipresent in various fields of electric machine application and power levels owing to their advantageous traits like high power density, good controllability, low maintenance, and high efficiency [29]. The automotive sector is just one of many industries in which brushless PM motors have been substituting established brushed PM motor concepts in light of size reduction, improved energy efficiency, and reduced maintenance, even for SFHP applications [30].

Fig. 1.5 shows a brushless PM motor classification with respect to the waveforms of the phase quantities, i.e., the back-EMF u_{EMF} and the phase current i_{p}, differentiating between brushless AC (BLAC) and brushless DC (BLDC) motor drives,[12] both of which are electronically commutated using power electronic switches[13]:

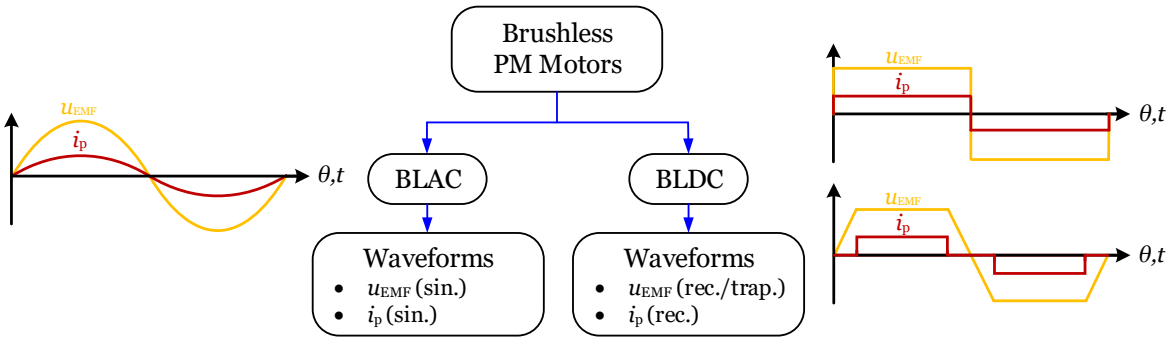

Fig. 1.5: Classification of brushless PM motors with respect to their phase quantities.

[12] BLAC-BLDC hybrids also exist in which the back-EMF is trapezoidal in shape and the phase current is sinusoidally shaped. In this case, the phase current generates useful torque only with the first order harmonic component of the back-EMF.

[13] Strictly speaking, PM stepper motors also belong to the category of brushless PM motors. However, they typically feature a much higher number of poles than BLAC or BLDC motors, perform stepwise motions for position control, and operate at rather low speeds. In case of full-step or half-step commutation, they resemble BLDC motors; in case of micro-step commutation, they are similar to BLAC motors.

- BLAC motors are essentially synchronous machines with PM excitation on the rotor, having sinusoidal back-EMF and phase current waveforms, see Fig. 1.5. (The former results from sinusoidal air-gap flux density and flux linkage waveforms.)
- BLDC motors are essentially inside-out brushed DC (BDC) motors with PM excitation on the rotor, having rectangular or trapezoidal back-EMF[14] and rectangular phase current waveforms, see Fig. 1.5. (The former results from rectangular-like air-gap flux density and triangular-like flux linkage waveforms.)

Three-phase BLAC motors are typically of the inner-rotor type and require costly position sensors (e.g., incremental encoders, resolvers)[15] to enable highly dynamic motion control, essential for robotics, for instance. In less dynamic applications (e.g., fan and pumping systems), three-phase and single-phase BLDC motors of inner-rotor type or outer-rotor type are used which only require simple, and hence comparatively cheap, discrete position sensors (e.g., Hall sensors) for commutation.[16] They are easy to control and have a relatively inexpensive stator, including single-tooth windings. Yet, BLDC motors have higher eddy current losses in the rotor magnets (due to their "jumping" stator magnetic field) and a higher torque ripple when fed from a voltage source.[17] The thermal utilization of BLAC and BLDC motors is generally the same [32]. However, for two equivalent motors, the BLDC variant has a 15 % higher overload capability than the BLAC motor for the same inverter current limit.

Each phase of a brushless PM motor with surface-mounted PMs on the rotor can be modeled by the electrical equivalent circuit illustrated in Fig. 1.6,[18] where

[14] Taking the magnet transition zones into account, the back-EMF is shaped more like a trapezoid than a rectangle, as discussed in the context of Fig. 1.10.

[15] Different sensorless control strategies have been proposed, e.g., using high frequency injection [31]. Yet, their reliability and accuracy is often rather poor.

[16] As opposed to three-phase BLAC motors, in three-phase BLDC motors only two out of the three phases are carrying current at any given time.

[17] Torque ripple can be caused by cogging torque, commutation (when the current slope of the incoming and outgoing phases differs), as well as non-ideal back-EMF and phase current waveforms. When fed from a current source, i.e., when the waveform of the current can be fully controlled and is, e.g., not limited by the voltage source, torque pulsations can be compensated. However, because of their cost-drivenness, FHP BLDC motors are rarely operated from current sources.

[18] Interior PM motors, which feature reluctance torque in addition to alignment torque, are modeled by two separate equivalent circuits, one for the direct axis and one for the quadrature axis.

$u_{\mathrm{inv}}(t)$ is the inverter voltage applied to the phase, $u_{\mathrm{EMF}}(t)$ is the back-EMF, R is the phase resistance, L_σ is the leakage inductance, L_m is the main inductance, and $i_\mathrm{p}(t)$ is the phase current. In addition, Fig. 1.6 shows typical waveforms of $u_{\mathrm{inv}}(t)$, $u_{\mathrm{EMF}}(t)$, and $i_\mathrm{p}(t)$ of a single-phase BLDC motor with a unifilar winding fed from a constant voltage source using an H-bridge converter.[19] (A detailed step-by-step analytic derivation of the phase current waveforms for a bifilar winding is presented in Appendix B.)

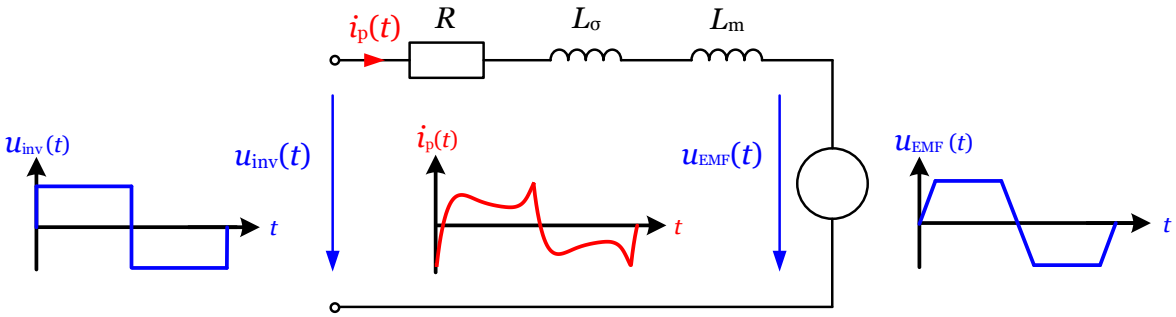

Fig. 1.6: Single-phase electrical equivalent circuit of a brushless PM motor with surface-mounted PMs and typical waveforms of a single-phase BLDC motor.

Since the motors studied in this thesis are exclusively single-phase BLDC motors, their working principle is elaborated upon below. (For reasons of clarity, effects such as saturation, eddy currents, leakage, and fringing are neglected.)

Working Principle of Single-Phase BLDC Motors

As mentioned in the context of Fig. 1.5, compared to the sinusoidal waveforms in a BLAC motor, the flux linkage, back-EMF, and phase current waveforms of a BLDC motor differ. The main reason for this is the typically radial magnetization of the PMs on the rotor ideally yielding a rectangular[20] air-gap flux density distribution $B_{\delta,\mathrm{PM}}$, as illustrated in Fig. 1.7 for a four-pole machine in an unrolled view.[21]

The angle φ_m is the mechanical angle in a coordinate system fixed on the stator and the pole pitch is $\tau_\mathrm{p} = \frac{2r_\delta\pi}{2p}$. ($p$ is the number of pole pairs and r_δ is the air-gap

[19] Other than a unifilar winding, a bifilar winding is obtained by winding two wires (i.e., sub-phase A and sub-phase B) simultaneously and connecting the two wires in opposite directions. Thereby, two oppositely coupled coils are obtained, as discussed in Subsections 2.1.1 and 2.1.2.

[20] Ideally, the magnet pole coverage α_p is 1.

[21] For the illustration, leakage, conductors, and slots are neglected.

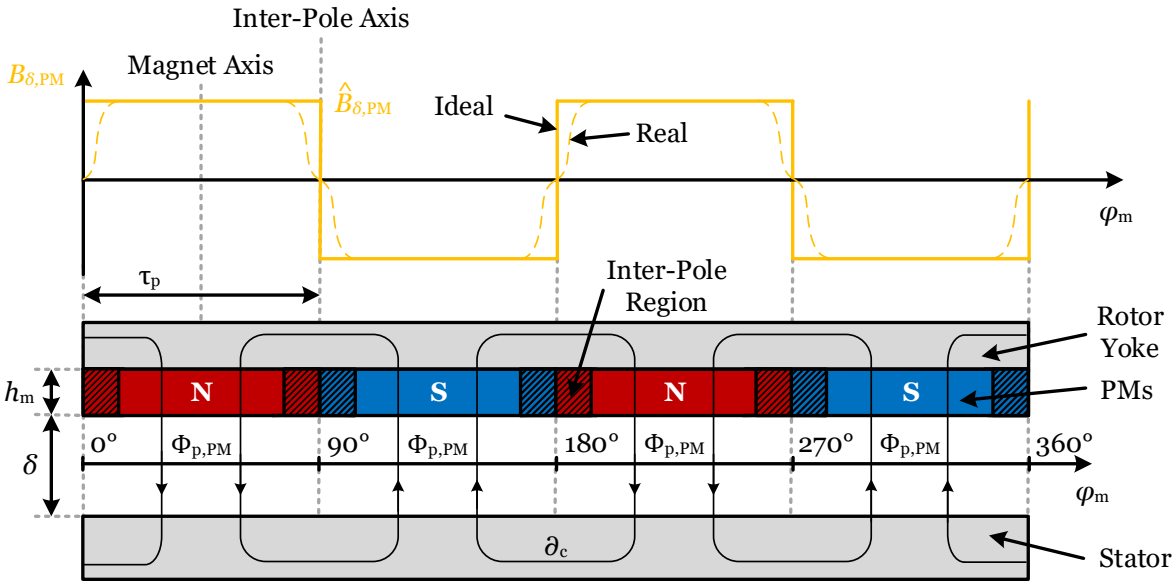

Fig. 1.7: Rotor magnetic field: Air-gap flux density $B_{\delta,\mathrm{PM}}$ and PM flux per pole $\Phi_{\mathrm{p,PM}}$ of a four-pole PM motor in the no-load condition.

radius.) The PM flux per pole is $\Phi_{\mathrm{p,PM}} = \hat{B}_{\delta,\mathrm{PM}} \tau_\mathrm{p} l_\mathrm{ax}$, which separates in the stator and rotor yoke sections. ($\hat{B}_{\delta,\mathrm{PM}}$ is the maximum value of $B_{\delta,\mathrm{PM}}$ and l_ax is the axial length of the machine.) The magnet height h_m and the air-gap length δ are indicated, as are the magnet and inter-pole axes. The hatched PM sections depict the inter-pole region, which is where the direction of the magnetization steadily changes. The resulting real flux density distribution of $B_{\delta,\mathrm{PM}}$ is depicted by the dashed line in Fig. 1.7.[22]

The calculation of $\hat{B}_{\delta,\mathrm{PM}}$ is described in the following: Applying Ampere's law to two consecutive rotor poles, along the contour ∂_c shown in Fig. 1.7, yields the rotor magnetomotive force (MMF) $\Theta_{\delta,\mathrm{PM}}$:

$$\Theta_{\delta,\mathrm{PM}} = 0 = \oint_{\partial_\mathrm{c}} H ds = H_{\mathrm{fe,r}} l_{\mathrm{fe,r}} + H_{\mathrm{fe,s}} l_{\mathrm{fe,s}} + 2H_{\delta,\mathrm{PM}} \delta + 2H_\mathrm{m} h_\mathrm{m}, \tag{1.1}$$

where H is the magnetic field, ds is the differential length element, $l_{\mathrm{fe,r}}$ and $l_{\mathrm{fe,s}}$ are the lengths of the iron paths in the rotor and the stator, $H_{\mathrm{fe,r}}$ and $H_{\mathrm{fe,s}}$ are the magnetic fields in the rotor iron and the stator iron, δ is the air-gap length, $H_{\delta,\mathrm{PM}}$ is the magnetic field in the air-gap caused by the PM, h_m is the magnet height, and H_m is the magnetic field in the PM. Due to the high permeability of the iron material, the MMF drop in

[22] In practice, α_p is below 1 (e.g., between 0.6 and 0.8). Then, the PM flux per pole is $\Phi_{\mathrm{p,PM}} = \hat{B}_{\delta,\mathrm{PM}} \tau_\mathrm{p} l_\mathrm{ax} \alpha_\mathrm{p}$.

the iron parts in (1.1) can typically be neglected, yielding the following:

$$0 = H_{\delta,\mathrm{PM}}\delta + H_{\mathrm{m}}h_{\mathrm{m}}. \tag{1.2}$$

The operating point (OP) of the PM is the intersection of the loadline of the magnetic circuit[23] and the PM's BH-curve in the second quadrant characterized by the remanent flux density B_{rem} and the coercivity H_{co}, as shown in Fig. 1.8.

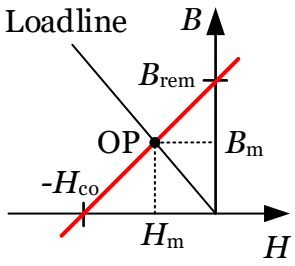

Fig. 1.8: Illustration of the operating point of a PM-excited magnetic circuit with an air-gap.

The operating point and hence the flux density in the PM B_{m} can be calculated as

$$B_{\mathrm{m}} = B_{\mathrm{rem}} + \mu_0\mu_{\mathrm{rec}}H_{\mathrm{m}}, \tag{1.3}$$

where μ_{rec} is the relative recoil permeability of the PM and μ_0 is the permeability of free space.

Neglecting leakage effects, the flux density in the air-gap is approximately equal to that in the PM, i.e., $B_{\delta,\mathrm{PM}} \approx B_{\mathrm{m}}$. Separating H_{m} from (1.3), taking $B_{\delta,\mathrm{PM}} \approx B_{\mathrm{m}}$ into account, and inserting the result into (1.2), the maximum air-gap flux density caused by the PMs can be estimated as follows [33]:

$$\hat{B}_{\delta,\mathrm{PM}} = \frac{B_{\mathrm{rem}}}{1 + \mu_{\mathrm{rec}}\frac{\delta}{h_{\mathrm{m}}}}. \tag{1.4}$$

As per (1.4), a large air-gap flux density is obtained by selecting a PM with a high B_{rem}, designing a small δ, and/or increasing h_{m}.

In the actual BLDC motor, the PM flux per pole $\Phi_{\mathrm{p,PM}}$ links with the coils in the stator as illustrated in Figs. 1.9(a)–(c) for three different rotor positions θ, where N is the number of turns of a coil and $\boldsymbol{A}_{\mathrm{c}}$ is the coil's area vector. (The black dot in the rotor

[23] The slope of the loadline depends on δ and h_{m}. By decreasing the δ/h_{m} ratio, the operating point approaches the remanent flux density B_{rem}.

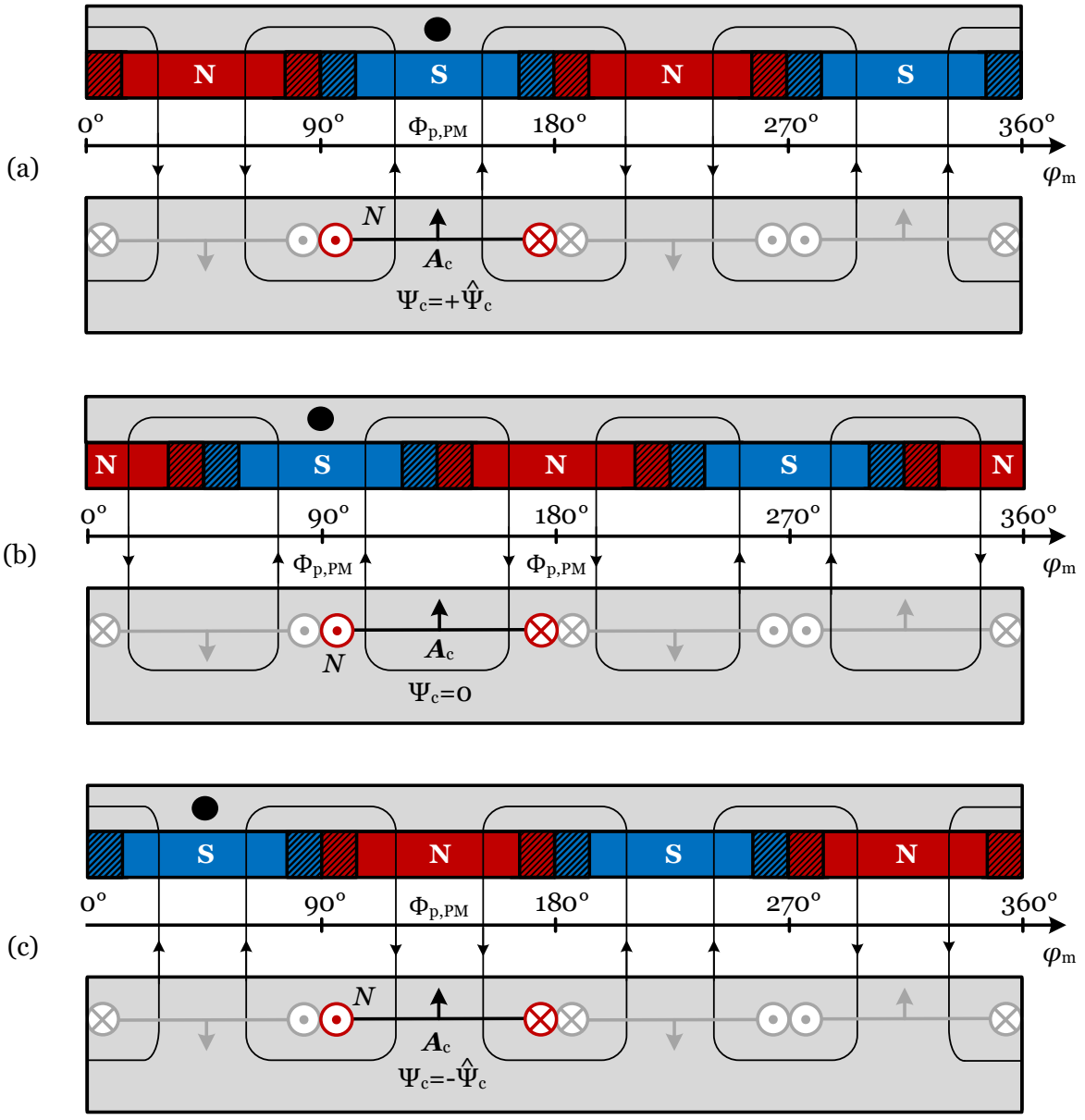

Fig. 1.9: Flux linkage of a four-pole single-phase BLDC motor in the no-load condition for different rotor positions: (a) $\theta = 0°$, (b) $\theta = 45°$, and (c) $\theta = 90°$.

yoke helps keep track of the change in the rotor position.) When $\Phi_{p,PM}$ points in the same direction as $\boldsymbol{A}_c$, the flux is counted positive, otherwise it is deemed negative. The flux linkage of one coil in the stator can then be determined as $\Psi_c(\theta) = N\Phi_{net}(\theta)$, where $\Phi_{net}(\theta)$ is the net flux through that coil at the rotor position θ.

- For $\theta = 0°$, the full-pitch stator coil is fully aligned with the magnet axis of the south pole, linking the maximum positive flux, i.e., $\Psi_c = +N\Phi_{p,PM} = +\hat{\Psi}_c$, see

Fig. 1.9(a).

- For $\theta = 45°$, the full-pitch stator coil is fully aligned with the magnet inter-pole axis and the positive and negative flux parts cancel out, causing zero net flux, i.e., $\Psi_c = 0$, see Fig. 1.9(b).
- For $\theta = 90°$, the full-pitch stator coil is fully aligned with the magnet axis of the north pole, linking with the maximum negative flux, i.e., $\Psi_c = -N\Phi_{p,PM} = -\hat{\Psi}_c$, see Fig. 1.9(c).

The ideal flux linkage waveform of the stator coil is illustrated in Fig. 1.10, including the rotor positions shown in Figs. 1.9(a)–(c). Starting from the maximum

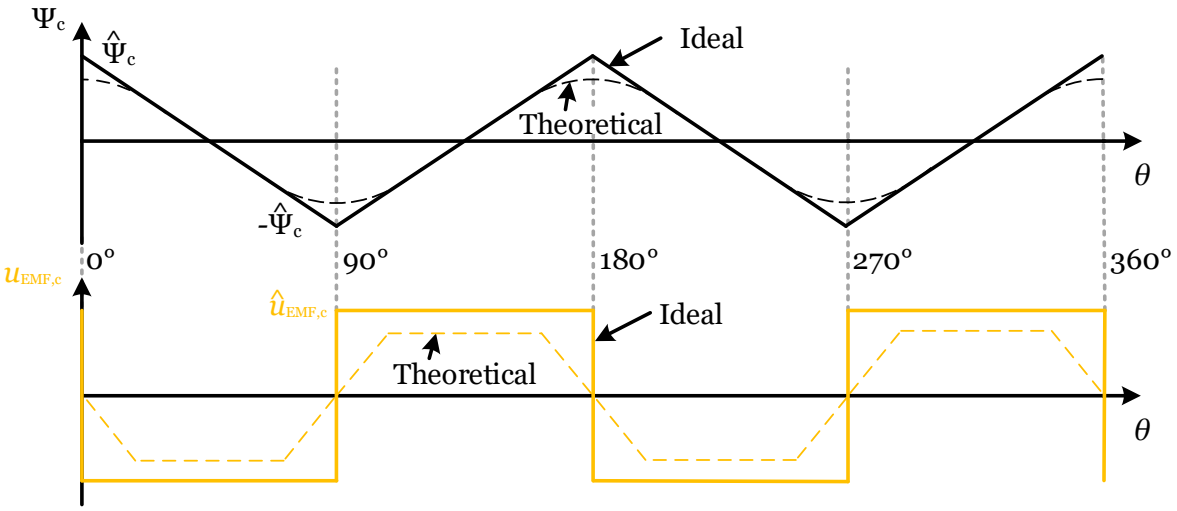

Fig. 1.10: Flux linkage and back-EMF waveforms of the PM motor from Fig. 1.9.

positive flux linkage $+\hat{\Psi}_c$ at $\theta = 0°$, Ψ_c decreases linearly, passes zero at $\theta = 45°$, until it reaches $-\hat{\Psi}_c$ at $\theta = 90°$.

As depicted in Fig. 1.10, the ideal coil flux linkage waveform is triangular. This leads to a rectangular back-EMF waveform because the back-EMF is proportional to the (time or position) derivative of the flux linkage[24] [33]:

$$u_{EMF,c} = \frac{d\Psi_c}{dt} = \frac{\partial \Psi_c}{\partial \theta} \cdot \frac{d\theta}{dt} = \omega \frac{\partial \Psi_c}{\partial \theta}, \tag{1.5}$$

where $u_{EMF,c}$ is the back-EMF induced in one coil and ω is the angular frequency.

Based on (1.5), the maximum value of $u_{EMF,c}$ can be calculated as

$$\hat{u}_{EMF,c} = \omega_{el} \frac{\Delta \Psi_c}{\Delta \theta_{el}} = p\omega \frac{2\hat{\Psi}_c}{\pi} = \frac{2}{\pi} p\omega N \hat{B}_{\delta,PM} \tau_p l_{ax}, \tag{1.6}$$

[24] Remark: $\frac{d}{d\theta}(k_c\theta) = k_c$, where k_c is an arbitrary constant.

where the electrical frequency is $\omega_{\mathrm{el}} = p\omega$ and the electrical angle is $\theta_{\mathrm{el}} = p\theta$. The maximum value of the total back-EMF of the motor shown in Fig. 1.9 can be calculated as $\hat{u}_{\mathrm{EMF}} = N_{\mathrm{cs}}\hat{u}_{\mathrm{EMF,c}}$, where N_{cs} is the number of coils in series per phase. ($N_{\mathrm{cs}} = 4$ in Fig. 1.9.)

Due to the continuous transition of the air-gap flux density in the inter-pole region indicated in Fig. 1.7, the flux linkage waveform exhibits a rather quadratic behavior in the proximity of the maximum and minimum values, respectively. (See the dashed waveform in Fig. 1.10 denoted as Theoretical.) This quadratic behavior, in turn, causes a linear variation in the back-EMF[25] (see the waveform denoted as Theoretical in Fig. 1.10), causing the well-known trapezoidal back-EMF waveform.[26] Consequently, (1.6) must be multiplied by the magnet pole coverage α_{p}.

To generate torque in a single-phase BLDC motor, constant current must be injected during the flat-top portions of the back-EMF, which is initiated by the position signal of the Hall effect sensor. Hence, the ampere-conductor distribution of the stator ideally remains constant and fixed in space for a predetermined commutation interval [33]. When current flows in the stator winding, the air-gap flux density caused by the phase current $B_{\delta,i_{\mathrm{p}}}$ is generated, as shown in Fig. 1.11 and described below.[27]

In the single-phase BLDC motor shown, the coils are placed in slots with the slot opening w_{slot}, wound onto four salient stator poles. The number z_Q is the total number of conductors per slot and δ_{eff} is the effective air-gap length, i.e., $\delta_{\mathrm{eff}} = \delta + h_{\mathrm{m}}$.[28]

The calculation of $\hat{B}_{\delta,i_{\mathrm{p}}}$ is described in the following: Applying Ampere's law to two consecutive stator poles along the contour ∂_{c} shown in Fig. 1.11 yields the stator magnetomotive force (MMF) $\Theta_{\delta,i_{\mathrm{p}}}$:

$$\Theta_{\delta,i_{\mathrm{p}}} = z_Q i_{\mathrm{p}} = 2Ni_{\mathrm{p}} = \oint_{\partial_{\mathrm{c}}} H ds = H_{\mathrm{fe,r}} l_{\mathrm{fe,r}} + H_{\mathrm{fe,s}} l_{\mathrm{fe,s}} + 2H_{\delta,i_{\mathrm{p}}}\delta_{\mathrm{eff}}, \tag{1.7}$$

where $H_{\delta,i_{\mathrm{p}}}$ is the stator magnetic field in the effective air-gap.

Due to the high permeability of the iron material, the MMF drop in the iron parts in (1.7) can be neglected, which results in

$$Ni_{\mathrm{p}} \approx H_{\delta,i_{\mathrm{p}}}\delta_{\mathrm{eff}}. \tag{1.8}$$

[25] Remark: $\frac{d}{d\theta}\left(k_c\theta^2\right) = 2k_c\theta$, where k_c is an arbitrary constant.
[26] The reduction in the maximum flux linkage causes a reduction in the maximum back-EMF.
[27] For illustration, the cross-slot H-field, other stray fields, and the field of the PM are neglected.
[28] A relative recoil permeability of $\mu_{\mathrm{rec}} \approx 1$ is assumed for the PM.

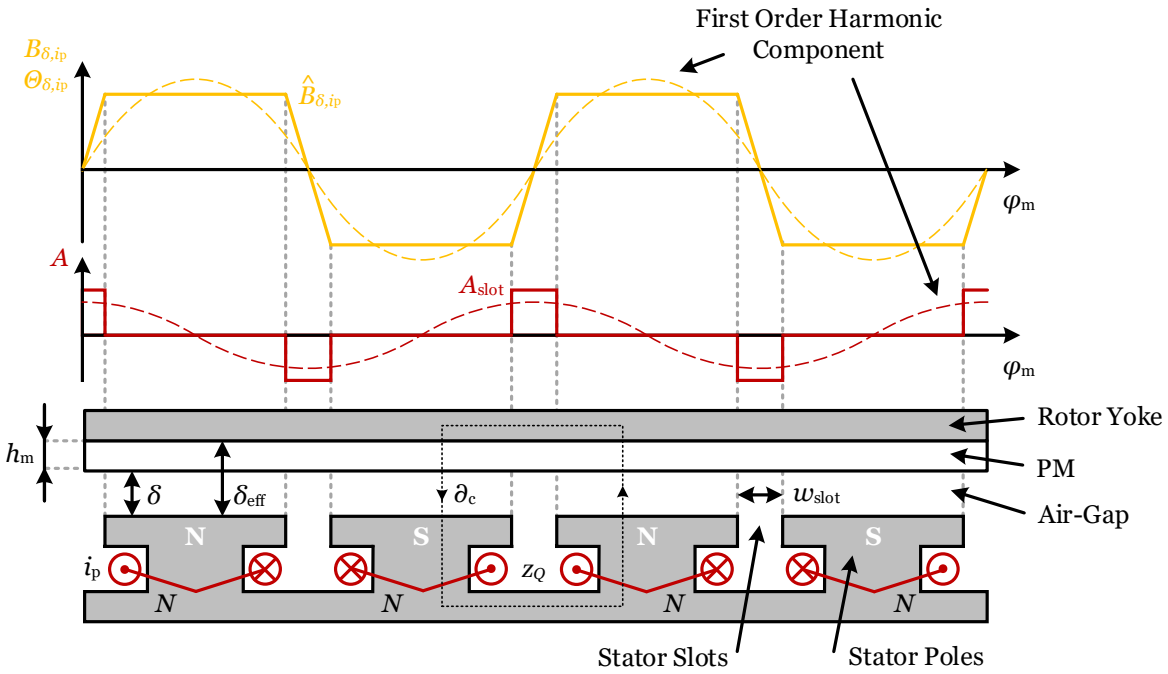

Fig. 1.11: Stator magnetic field: Air-gap flux density B_{δ,i_p} derived from the linear current density A of the excited stator of the four-pole single-phase BLDC motor.

Solving (1.8) for H_{δ,i_p} and considering $B_{\delta,i_p} = \mu_0 H_{\delta,i_p}$, the maximum air-gap flux density caused by the current-carrying conductors in the stator can be calculated as

$$\hat{B}_{\delta,i_p} = \frac{\mu_0 N i_p}{\delta_{eff}} = \frac{\mu_0}{\delta_{eff}} \Theta_{\delta,i_p}. \tag{1.9}$$

While (1.9) is used to calculate the maximum value of B_{δ,i_p}, its actual waveform considering the slot opening w_{slot} can be determined using the concept of linear current density A. The slot's local linear current density can be calculated as [34]

$$A_{slot} = \frac{z_Q i_p}{w_{slot}}. \tag{1.10}$$

Accordingly, Fig. 1.11 shows the waveform of the linear current density A for the current-carrying conductors exhibited.[29] The waveform of the stator MMF Θ_{δ,i_p} [and from it that of the air-gap flux density B_{δ,i_p}, see (1.9)] is then calculated integrating A over the stator surface:

$$\Theta_{\delta,i_p} = \int A(\varphi_m) r_s d\varphi_m, \tag{1.11}$$

[29] Alternatively, the slot-conductor distribution can be modeled by Dirac delta functions.

where r_s is the stator radius. Given the block shape of A in Fig. 1.11, B_{δ,i_p} yields a trapezoidal waveform.[30] For illustration, the first order harmonic components of A and B_{δ,i_p} are indicated.

The average linear current density over a pole pitch $\overline{A}_{\tau_p}$ is defined as the total number of current-carrying conductors around the air-gap circumference. For the four-pole four-slot BLDC motor depicted in Fig. 1.11, it can be obtained as

$$\overline{A}_{\tau_p} = \frac{2pz_Q I_{p,av}}{2\pi r_s}, \tag{1.12}$$

where $I_{p,av}$ is the average phase current over a pole pitch.

The average electromagnetic (or alignment) torque $\overline{T}_{em}$ can then be calculated based on the average Lorentz force $\overline{F}$ using the average linear current density $\overline{A}_{\tau_p}$ and the average air-gap flux density caused by the PMs $\overline{B}_{\delta,PM}$ as follows:

$$\overline{T}_{em} = r_s \overline{F} = r_s l_{ax} 2pz_Q I_{p,av} \overline{B}_{\delta,PM} = 2\pi r_s^2 l_{ax} \overline{A}_{\tau_p} \overline{B}_{\delta,PM}, \tag{1.13}$$

where l_{ax} is the axial length of the motor.

The instantaneous electromagnetic torque T_{em}, however, fluctuates heavily for a single-phase motor. It can be calculated from the inner power P_i using the angular speed ω, the back-EMF, and the phase current,[31] as shown in Fig. 1.12:

$$T_{em} = \frac{P_i}{\omega} = \frac{u_{EMF} i_p}{\omega}. \tag{1.14}$$

In the region where the back-EMF changes its polarity, the torque is theoretically zero because the current is zero. As shown in Fig. 1.12, the torque T_{em} fluctuates heavily, but the average electromagnetic torque $\overline{T}_{em}$ is positive, as denoted by the dashed line. ($\hat{T}$ is the maximum torque, and $\check{T}$ is the minimum torque.)

The definition of torque ripple T_{rip} used in this thesis is [32, 35]

$$T_{rip} = \frac{(\hat{T} - \check{T})}{(\hat{T} + \check{T})} \cdot 100\,\%. \tag{1.15}$$

[30] Conversely, step functions are obtained when Dirac delta functions are used to model A.

[31] As discussed in Subsection 1.2.3, in a PM motor, the cogging torque is superposed upon the electromagnetic (or alignment) torque T_{em}, changing the output torque ripple. Other reasons for output torque ripple include the commutation process, ripples in the current due to PWM, as well as harmonics of the back-EMF and current waveforms [21].

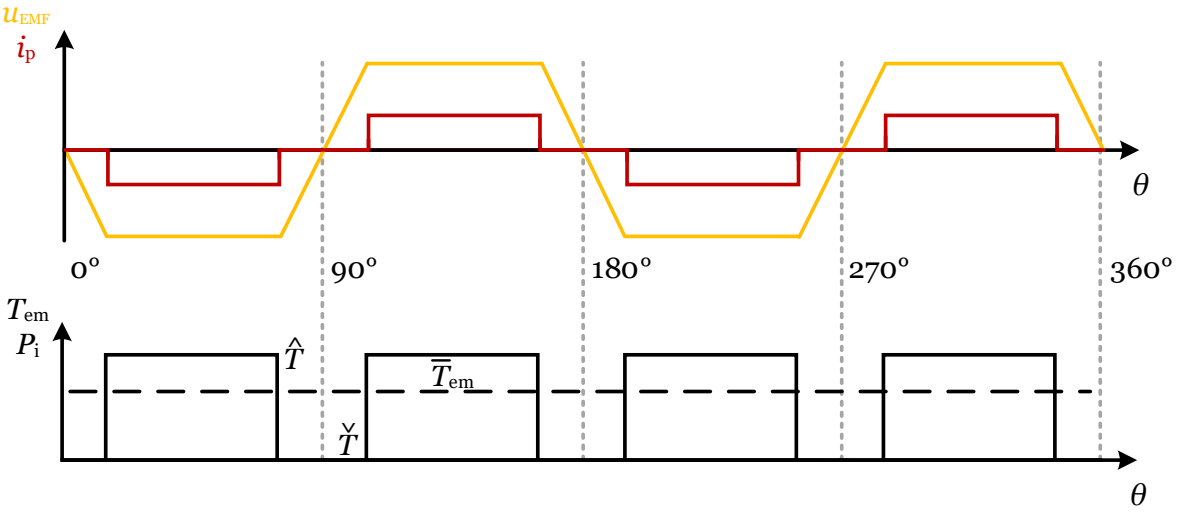

Fig. 1.12: Back-EMF, phase current, electromagnetic torque, and inner power waveforms of a single-phase BLDC motor.

1.2.2 Characteristics of FHP and SFHP Electric Motor Drives

While the design target of very large machines, e.g., hydro or turbo generators, is to determine the main dimensions based on the desired operational parameters, IHP, FHP, and SFHP machines are usually designed to yield the maximum performance (i.e., torque, power) for a given volume [36].[32] As mentioned in Section 1.1, other than IHP drive systems, FHP and SFHP drive systems are typically highly integrated customized solutions, designed for a specific application. Due to the high integration and customization, FHP and SFHP motors and drives have thus far been exempted from standardization. In light of the fact that energy conversion efficiency used to be of secondary importance, a plethora of different "creative" motor concepts, topologies, and designs has been developed.[33] Depending on the application (and permissible cost), a tradeoff is made weighing their advantages and disadvantages. Compared to larger motors, the efficiencies of FHP and SFHP motors are significantly lower (typically between 20 and 50 %) for reasons elaborated upon hereafter.

Based on a given electric machine, it is not possible to simply downscale the

[32] As opposed to FHP and SFHP machines, high power and torque densities are essential for IHP machines. Hence, the design of IHP machines is typically determined thermally.

[33] Classic examples thereof include hysteresis, shaded-pole, switched reluctance, stepper, claw-pole, and capacitor motors. Other examples include the slotless motor concepts from Maxon Motor AG and Dr. Fritz Faulhaber GmbH & Co. KG. Furthermore, interesting rather new developments include printed circuit board (PCB) axial flux PM motors and slotless radial flux PM motors with flex-PCB air-gap windings.

construct geometrically for deviating requirements known as a scaling effect. A non-exhaustive list of the particularities of FHP and SFHP motors is provided below:

- Decreasing the machine diameter generally reduces the room for the winding and hence requires a decrease in the wire diameter. This leads to larger per-unit winding resistance R and hence copper losses ($P_{\mathrm{Cu}} = I^2 R$) for the same current I, reducing the efficiency substantially.
- The phase inductance L decreases nonlinearly with decreasing dimensions, which together with the relatively high R leads to small electrical time constants $\tau_{\mathrm{el}} = L/R$. Also, the leakage in the end-turn region of the machine can be dominant for machines with a very short axial length.
- In light of cost-reduction, rather weak magnets (e.g., ferrite, bonded NdFeB) are utilized, which typically reduce the power density of the motor.
- The relative air-gap length increases with decreasing dimensions due to manufacturability and the manufacturing tolerances, causing a rather low air-gap flux density for a given magnet.
- As to a cost-performance tradeoff, the peak air-gap flux density is often designed according to $\hat{B}_{\delta,\mathrm{PM}} \approx \frac{1}{2} B_{\mathrm{rem}}$. Considering ferrite and bonded NdFeB magnets, this leads to values of $\hat{B}_{\delta,\mathrm{PM}}$ in the range of $0.1 - 0.4\,\mathrm{T}$, instead of about $0.8\,\mathrm{T}$ in IHP machines in which sintered NdFeB magnets are typically used.
- While larger machines typically have current densities between 5 and 7 $\mathrm{A/mm^2}$ (continuous running duty), those of machines below 50 W are typically higher than $10\,\mathrm{A/mm^2}$.[34] However, the permissible current densities significantly vary with the application (e.g., plastic housing or not) and the duration of current flow. (For short-time duty, much larger current densities are permissible.) Furthermore, the limited current source may not allow thermal exploitation of the machine.
- While the electromagnetic noise of IHP motors is typically dominated by the radial magnetic forces deforming the relatively thin stator yoke, the electromagnetic noise of FHP and SFHP motors is often rather due to fluctuations of the tangential and axial magnetic forces.
- Their losses are typically dominated by the copper losses, unless very high rotational speeds cause the iron losses to outweigh the copper losses.

[34] The permissible current densities typically increase with decreasing linear dimensions because the cooling surface scales with the square of the linear dimensions but the losses scale with the cube of the linear dimensions. Hence, smaller volumes are in general easier to cool.

- Given their small dimensions, the iron core components are inherently vulnerable to manufacturing tolerances and influences (e.g., laser cutting, punching, interlocking, press-fitting), especially the narrow teeth sections. Such measures usually reduce the core's permeability and hence increase the iron losses (especially the hysteresis losses, preventing the usage of data sheet loss densities for the estimation of the iron losses), and decrease the air-gap flux density.
- The influence of friction also increases relatively with decreasing motor dimensions, adding to the losses and reducing the efficiency.

Theoretically, symmetric motors which have an even number of stator slots (e.g., the studied single-phase BLDC claw-pole motor) have balanced radial magnetic forces since the acting forces cancel out,[35] owing to the geometric symmetry between the rotor and stator around the air-gap [38]. Yet, due to the rather large manufacturing tolerances of mass-produced SFHP motors, imperfections which can lead to unbalanced radial magnetic forces (URMFs) are inevitably introduced [37, 39, 40]. The main reasons for URMFs in symmetric motors are eccentricity[36] and non-uniform magnetization.[37]

As mentioned in Subsection 1.1.2, sub-optimal motor behavior is often accepted in FHP and SFHP motors when cost can be reduced, provided that the functionality of the product is not compromised. Hence, inexpensive single-phase BLDC motors (with concentrated single-tooth windings) are often chosen over costly three-phase BLAC motors (with distributed windings), despite the much larger output torque ripple of the former. To reduce the number of power electronic switches, single-phase motors are often realized with a bifilar winding instead of a unifilar one. As opposed to the four switches of a H-bridge inverter necessary to drive a unifilar winding, a bifilar winding requires only two switches yet exhibits half the copper utilization, because only one sub-phase is energized at any given time. (See Section 2.1 for more detailed information on the concept of a bifilar winding.)[38]

[35] In unsymmetrical motor designs, which have an uneven number of stator slots [37], the air-gap flux density distribution is non-uniform, causing unbalanced radial magnetic forces.

[36] Especially the bearing clearance, which can increase over time due to wear and tear, increases the eccentricity and, as a result, the noise significantly [17].

[37] The magnetization strongly depends on the accuracy of the magnetization fixture used. It has been observed that the magnetization can vary for the pole pairs, forming non-uniform magnetization.

[38] However, a recent trend has been identified in which integrated driver circuits with logic and driver within one package are used for low-cost applications in light of reliability (e.g., [41–43]), where the number of switches is of secondary importance. Disadvantageously, such integrated solutions typically have a very high on-state resistance, which decreases the overall drive efficiency.

Due to the merely alternating magnetic field of single-phase motors, they are often characterized by starting problems. Hence, air-gap asymmetry or parking magnets are often implemented to realize a preferred rotational direction and thereby facilitate the starting. (See Section 2.3 for more detailed information on the starting capability of single-phase PM motors.) Consequently, single-phase motors are only suitable for unidirectional applications such as fan and pumping systems. In addition, these motors typically have sub-optimal slot-pole combinations [see the discussion within the context of (1.20)], leading to relatively large cogging torque [21]. During operation, the cogging torque is superposed upon the alignment torque. The cogging torque is often in the same order of magnitude as the alignment torque, leading to very large output torque ripple. As mentioned in Subsection 1.1.2, these torque fluctuations can lead to both structure- and airborne noise, see Fig. 1.3.

1.2.3 Cogging Torque

This subsection discusses the cogging torque phenomenon in detail, providing the context of the proposed design improvements elaborated upon in Chapters 4–8. After a short theoretical review, possible cogging torque reduction methods are presented. In the last part, the particularities of the cogging torque of SFHP motors and the difficulties in its experimental investigation are addressed.

Phenomenon

Put simply: *Magnets attract magnetic material*. In a PM motor, the magnets mounted on the rotor always aim to align with the maximum amount of iron material–they are aiming to minimize the reluctance. The positions of minimum reluctance are called cogging positions. When the rotor is deflected from said positions, a torque results–called cogging torque T_c–trying to restore the rotor to the positions of minimum reluctance, as explained in the following in more detail.

Cogging torque is a characteristic of most PM motors.[39] On the one hand, it is a no-load torque [40] which can cause noise [17, 48] as it is superposed upon the alignment

[39] Exceptions are PM motors which lack slots, e.g., inner- or outer-rotor motors with air-gap windings (see, e.g., [44–47]), inner-rotor motors with a segmented stator wound from the outside, or inner- or outer-rotor motors with magnetic slot wedges.

[40] While the cogging torque is a no-load torque caused by the PMs, the reluctance torque is a torque in the load condition proportional to the square of the current and the rate of change of inductance with the rotor position [33]. The reluctance torque results from the saliency of the rotor, e.g., in an interior PM motor.

torque shown in Fig. 1.12, forming a complex instantaneous output torque waveform. (The harmonics of the resulting torque ripple can excite system resonances depending on the rotational speed.) On the other hand, in single-phase motors, the cogging torque altered by an asymmetric air-gap can facilitate the starting and reduce the total output torque ripple to some extent, providing torque at positions of zero alignment torque, as discussed in Section 5.4.[41]

Technically speaking, cogging torque T_c is the interaction between the PM rotor magnetic flux and the variable air-gap reluctance (or permeance) due to the stator slot geometry [22,33]. Formally, it can be calculated from the rate of change of magnetic co-energy W_{co} with respect to the rotor position θ in the zero-current condition [26]:

$$T_c = \left.\frac{dW_{co}}{d\theta}\right|_{i=0}. \tag{1.16}$$

Hence, cogging torque occurs when W_{co} varies as the rotor moves. Neglecting saturation, (1.16) can be simplified to the following relationship [38]:

$$T_c = -\frac{\phi^2}{2}\frac{d\mathcal{R}}{d\theta}, \tag{1.17}$$

where ϕ is the magnet flux crossing the air-gap, $\mathcal{R}$ is the total reluctance through which ϕ passes, and θ is the rotor position.[42] Hence, cogging torque primarily occurs when the reluctance changes with the rotor position.

In finite-element analysis, the cogging torque is typically calculated for each rotor position integrating the Maxwell stress tensor on a surface containing the rotor, in the zero-current condition. For improved accuracy, it is often calculated as the mean value of the Maxwell stress tensor in the whole air-gap volume $l_{ax}\Gamma_\delta$ [28,49][43]:

$$T_c = \frac{l_{ax}}{\mu_0 \delta}\int_{\Gamma_\delta} r_d B_r B_t \, d\Gamma_\delta, \tag{1.18}$$

where l_{ax} is the axial length of the machine, μ_0 is the permeability of free space, δ is the air-gap length, r_d is the dummy radius, and B_r and B_t are the radial and tangential flux density components in the elements of the air-gap annulus Γ_δ.

[41] In PM stepper motors, the cogging (or detent torque) is often useful in preventing the rotor to move in the no-load condition when an external load is applied.

[42] The magnet flux ϕ is typically not constant due to leakage effects. It is often a function of the rotor position θ.

[43] End effects are neglected.

Figs. 1.13(a) and (b) exhibit the cogging torque mechanism of a two-pole inner-rotor PM machine and a two-pole outer-rotor PM machine; both have salient stator poles. The magnet flux ϕ is indicated for the air-gap only. When the rotor is

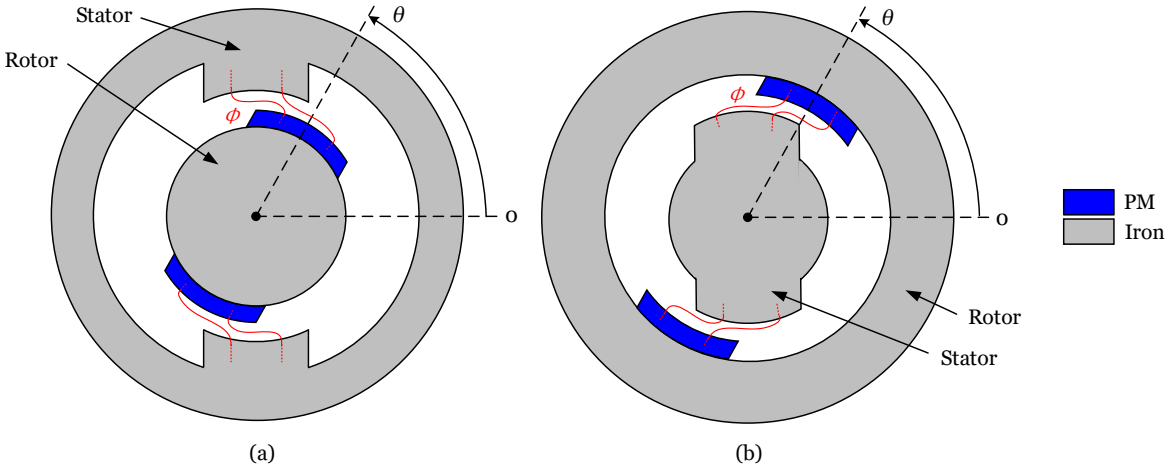

Fig. 1.13: Cogging torque mechanism of a two-pole PM machine with salient stator poles: (a) inner-rotor topology and (b) outer-rotor topology.

released from the position shown, it will experience a torque and start rotating in the counterclockwise (CCW) direction to align with the salient stator poles.[44] As the resulting oscillation will always be damped, the rotor will finally come to rest directly below the stator poles, aligned with the same.

Fig. 1.14 shows the qualitative cogging torque waveform of any of the two-pole PM machines with salient stator poles illustrated in Figs. 1.13(a) and (b), indicating the stable and unstable equilibrium positions.

- For $\theta = 0°$, the rotor is in an unstable equilibrium position: for any deflection, the cogging torque will accelerate the rotor into the direction of the applied deflection.
- For $\theta = 90°$, the rotor is in a stable equilibrium position: when it is deflected, the cogging torque acts to restore the rotor to its initial position.

Principally, every cogging torque waveform T_c (e.g., the one shown in Fig. 1.14) can be described as a Fourier series without zero component [28]:

$$T_c = \sum_{k=1}^{\infty} T_k \sin(kQ\theta + \varphi_k), \tag{1.19}$$

[44] A flux line essentially acts like a spring trying to minimize its length.

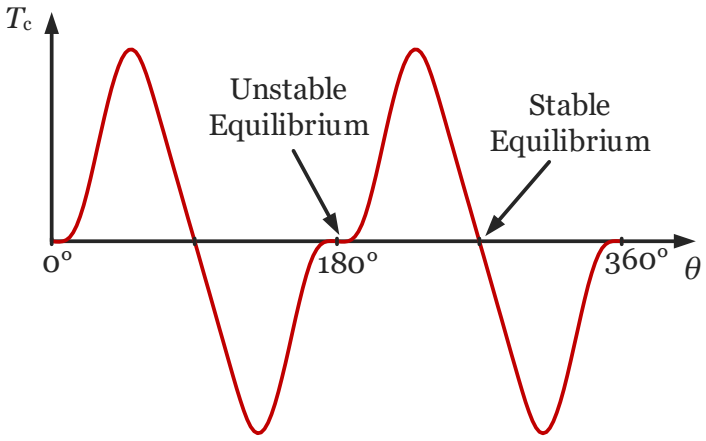

Fig. 1.14: Qualitative cogging torque waveform of the two-pole PM machine with salient stator poles illustrated in Figs. 1.13(a) and (b).

where k is the cogging torque harmonic order, T_k and φ_k are the amplitude and phase of the kth harmonic component, and Q is the number of slots. The cogging torque of a PM motor strongly depends on factors such as the slot geometry (especially the slot opening), slot-pole combination, pole shape, PM magnetization pattern, as well as the shape, width, and strength of the PMs. Depending on these factors, the cogging torque can be rich in harmonic components; yet, it is characterized by a zero average value, as per (1.17) and (1.16).

For the design of PM motors, prediction of the cogging torque waveform is essential. While analytic methods to estimate the cogging torque of electric machines exist (e.g., [50–52]), the accurate calculation of the cogging torque typically requires the finite-element method [33]. However, as the cogging torque is sensitive to parameter variations, it is important to determine the cogging torque experimentally as well.

Parameters Influencing the Cogging Torque

The cogging torque can be influenced already during the early design stage of an electric machine if manufacturing, complexity, cost, and performance permit. As implied in the context of (1.17), abrupt changes in the reluctance seen from the perspective of the rotor magnets cause high cogging torque amplitudes. In other words, the smoother (or the less) the reluctance changes with the rotor position, i.e., low $\frac{d\mathcal{R}}{d\theta}$, the lower is the cogging torque, see (1.17). Motors with an air-gap winding do not have cogging torque, because the air-gap reluctance (and hence the magnetic coenergy) does not change with the rotor position as long as saturation does not

occur. However, because the winding does not lie in slots, these motors have a larger effective air-gap, requiring stronger magnets for the same no-load air-gap flux density and thus performance. Closing the slots completely can also remove the cogging torque but increases the manufacturing complexity (e.g., difficult winding insertion and use of magnetic wedges or a segmented outer-stator wound from the outside) as well as the leakage inductance due to increased stray flux.

One of the first steps during the design process of a PM motor is the selection of the slot-pole combination. The goodness factor C_T indicates if a certain slot-pole combination may cause a rather high or low inherent cogging torque [27]:

$$C_T = \frac{2pQ}{\mathrm{LCM}(2p, Q)}, \tag{1.20}$$

where LCM denotes the *least common multiple* of two integers, p is the number of pole pairs, and Q is the number of slots. A small goodness factor (e.g., $C_T = 1$) indicates a slot-pole combination with low inherent cogging torque, while a large goodness factor (e.g., $C_T = 4$) means a high cogging torque slot-pole combination. In general, fractional slot motors have lower cogging torque than integral slot motors, and the cogging torque typically decreases with an increasing slot number.

Besides the slot-pole combination, the following points must be considered during the design process of an electric machine, which significantly influence the extent and the harmonic components of the cogging torque [22, 33, 38, 53]:

- Magnet strength (especially B_{rem}) and magnet position;
- Magnet width, height, and shape (when surface-mounted segmented magnets, e.g., with rounded edges or loaf-shaped, are used instead of a ring magnet);
- Magnetization pattern (e.g., radial, parallel, or polar anisotropic);
- Slot geometry (especially the slot opening in the stator lamination);
- Proper radial tooth tip length to prevent saturation; and
- Air-gap length and air-gap variation.

The cogging torque may also be sensitive to manufacturing irregularities (e.g., rotor eccentricity, magnet positioning errors), manufacturing impacts (e.g., interlockings, weldseam, keybar slots, notches, and flat surfaces on the outer stator perimeter for alignment [54]), mechanical tolerances, material properties (e.g., stator lamination anisotropies), soft magnetic material in the housing (e.g., screws), and saturation in general.

Cogging Torque Reduction Techniques

Many cogging torque reduction methods have been reported and studied in the literature. A non-exhaustive list is provided below [22, 26, 27, 33, 53, 55, 56]:

- Selecting a proper slot-pole combination, see (1.20)[45];
- Implementing skewed rotor magnets[46];
- Realizing a stepped skew using axially segmented magnets[47];
- Imposing a skewed magnetization pattern in a ring magnet[48];
- Skewing the stator lamination stack;
- Varying the slot width, i.e., irregular slotting;
- Varying the magnet width;
- Decentering selected magnets;
- Implementing dummy slots, i.e., bifurcated teeth or auxiliary slots;
- Realizing dummy teeth, i.e., interpoles; and
- Implementing tooth tips of different width and shape.

(The implementation of a single-sided skew causes axial magnetic forces which increase with increasing skewing angle, see the discussion in Chapter 8.)

Cogging Torque Particularities of SFHP Motors

Although various cogging torque reduction methods have been reported in the literature as mentioned previously, hardly any of them are applied to low-cost SFHP PM motors, mostly for cost reasons [26, 53]. The implementation of skewing for instance usually increases the number of manufacturing steps, the manufacturing complexity, and hence the cost [26]. Also, certain low-cost designs often have inherent restrictions as a result of their aspect ratios and small dimensions. Due to their small dimensions, the number of realizable slot-pole combinations is clearly limited, as is the maximum number of slots. Hence, SFHP motors typically have sub-optimal slot-pole combinations with a low number of slots and a rather large slot width to facilitate the winding process. Both characteristics lead to high cogging torque and hence high output torque ripple, which is especially true for single-phase variants.

[45] The cogging torque is typically lower for uneven values of Q and generally decreases with increasing Q.

[46] The fabrication of such complicated shapes is costly and typically involves the waste of magnet material due to milling.

[47] This involves simpler and inexpensive magnet shapes compared to skewed magnets.

[48] This requires a special magnetization fixture.

As discussed in detail in Section 2.3, single-phase PM motors often feature magnetic circuit imbalances forming asymmetric air-gaps (e.g., tapered, stepped, or notched air-gaps [57]) to create a specific parking position for the PM rotor. This enables the starting of a unidirectional motor (e.g., a fan or pump motor). Such modifications both phase shift the cogging torque and also alter the shape of the cogging torque waveform (see Section 5.4). Due to the phase shift, the zero positions of the cogging torque are shifted from those of the alignment torque. Hence, cogging torque is provided in positions of zero alignment torque, friction-related standstill is prevented, and the total output torque ripple is reduced, as discussed in Section 5.6.

Especially in single-phase SFHP PM motors, knowledge of the exact cogging torque waveform is essential as it is 1) often in the same order of the alignment torque and 2) in fact, superposed onto the alignment torque, forming a complex output torque waveform with a large ripple. However, the correct experimental investigation of cogging torque is a challenging task, especially for SFHP motors, as explained below.

Cogging Torque Measurement

Two main measuring methods can be distinguished between: the static and dynamic cogging torque measurements. The static measurement is essentially lever-based, where either the reaction torque of the stator is measured [54, 58], or force is applied to the rotor observing the change in the rotor position [59–62]. The dynamic measurement is usually performed using torque transducers [33, 63–68] (often with bias torque for a measuring-range extension) which must have sufficient bandwidth and accuracy to capture all cogging harmonics. The driving motors used include hydraulic motors [63], stepper motors [65, 67, 68], and brushed or brushless motors [67], often with a gear box in between to minimize the driving motor's influence on the motor under test (MUT). (However, a gear box usually has the disadvantage of backlash, which can affect the measurement results.)

All of the cogging torque measuring methods described above are influenced by friction which is (if accounted for at all) inaccurately assumed to be constant and simply subtracted from the measured torque waveform. In addition, the hysteresis torque component in the measured torque waveform, which relates to the hysteresis losses (see Subsection 1.2.4), is usually simply neglected. However, especially in FHP and SFHP motors, significant hysteresis torque can occur due to the low-quality steels typically used.

As opposed to IHP and FHP motors, measuring the cogging torque of SFHP motors (e.g., motors in the 1 W range, which have cogging torque peak values in the sub-milli-Newton meter range) is most challenging because the mentioned hysteresis torque and especially the bearing friction of either the MUT or the measuring device itself can significantly influence the results. Furthermore, proper instrumentation, having adequate measurement range and accuracy, is hard to find.

In this thesis, an unconventional rheometer-based cogging torque measurement method is proposed (see Subsection 3.2.2 as well as Chapters 6–9) which does not have the above mentioned disadvantages.[49]

1.2.4 Iron Losses

Iron losses are typically the second largest loss component in a brushless PM motor [33].[50] They strongly depend on the operating speed, materials used, and machine topology. Their share in the total losses can be influenced by design. A quick overview of iron loss models and measurements is given here.

Iron Loss Models

A plethora of different iron loss models is available in the literature. Reference [69] subdivides the iron loss calculation models into three main categories: a) Steinmetz-based models, b) mathematical hysteresis models, and c) loss separation models. For the analyses in this thesis, the standard Steinmetz equation [70] as well as the loss separation according to Jordan [71] are used, which are briefly overviewed below.[51]

The standard Steinmetz equation describes the iron losses P_{fe} as a function of the frequency f and the flux density amplitude $\hat{B}$:

$$P_{\mathrm{fe}} = k_{\mathrm{s}}\, f^{\alpha_{\mathrm{s}}}\, \hat{B}^{\beta_{\mathrm{s}}} \tag{1.21}$$

where k_{s}, α_{s}, and β_{s} are material- and geometry-specific parameters determined experimentally. Yet, the standard Steinmetz equation is only valid for limited frequency

[49] Initially, a static cogging torque measurement approach was used, which is discussed in Appendix K. However, the obtained results lacked accuracy. Hence, the torque measurements presented in this thesis have been performed only with the rheometer.

[50] Conversely, in off-the-shelf induction motors, the iron losses and the copper losses are usually of similar magnitude.

[51] In these rather simple iron loss models, a sinusoidal variation of the flux density is assumed. More sophisticated iron loss models, which also take the flux density harmonic components into account, are summarized in [69].

and flux density ranges, and no distinction between the different loss components is made.

With the loss separation according to Jordan, the iron losses P_{fe} are separated into static (i.e., hysteresis) and dynamic (i.e., eddy current) components, P_{hys} and P_{eddy}, respectively, as follows:

$$P_{\mathrm{fe}} = P_{\mathrm{eddy}} + P_{\mathrm{hys}} = c_{\mathrm{eddy}}\, f^2\, \hat{B}^2 + c_{\mathrm{hys}}\, f\, \hat{B}^2, \tag{1.22}$$

where, in addition to the parameters defined in the context of (1.21), c_{eddy} and c_{hys} are the eddy current and hysteresis coefficients. (The respective hysteresis and eddy current torque components are discussed in Subsection 3.2.4 and Section 9.2.)

The eddy current losses are linearly proportional to the electrical conductivity γ_{el} of the core material[52] and proportional to the square of the steel sheet thickness t_{steel}, the frequency f, and the flux density amplitude $\hat{B}$:

$$P_{\mathrm{eddy}} \propto \gamma_{\mathrm{el}}\, t_{\mathrm{steel}}^2\, \hat{B}^2\, f^2. \tag{1.23}$$

Since $\hat{B}$ and f determine the torque and power of the motor, and are hence more or less fixed, the eddy current losses are most effectively reduced by reducing t_{steel} and/or γ_{el}. The effectiveness of using thin steel sheets in an electrical machine is illustrated in Fig. 1.15(a), where a time-varying flux density B in the z-direction is assumed in the core material shown. Comparing the solid iron material on the left

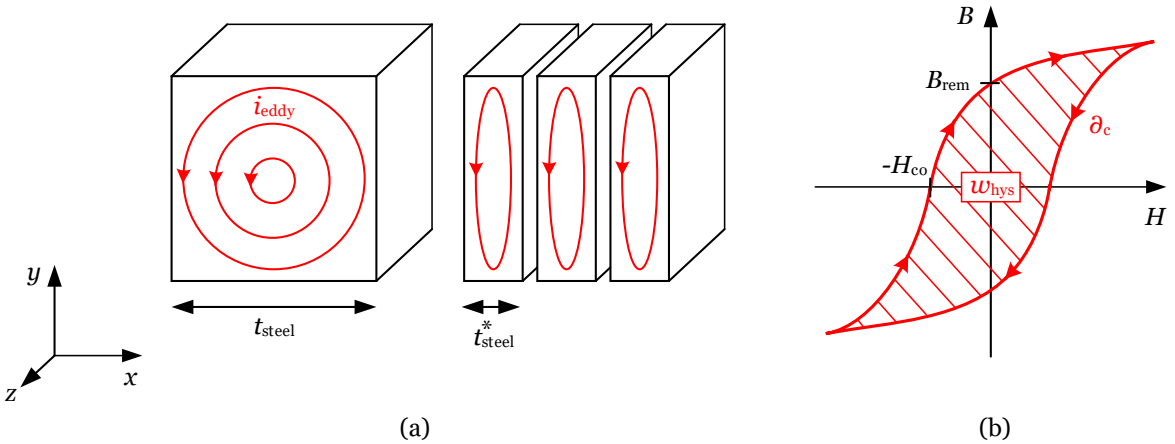

Fig. 1.15: (a) eddy currents in core material and (b) hysteresis curve of core material.

[52] γ_{el} can be reduced by adding silicon to the core material.

(see t_{steel}) with the laminated one on the right (see t^*_{steel}), it is evident that laminations are effective in limiting the formation of eddy currents i_{eddy}.[53]

The hysteresis losses are proportional to the specific magnetic loss energy w_{hys} of the used material and the frequency:

$$P_{\text{hys}} \propto w_{\text{hys}}\, f. \tag{1.24}$$

The specific loss energy equals the area of the BH-curve and can be determined as

$$w_{\text{hys}} = \oint_{\partial_c} H\, dB, \tag{1.25}$$

where ∂_c is the contour of the BH-curve, as shown in Fig. 1.15(b). Hence, using high-quality material with a smaller hysteresis automatically reduces the hysteresis losses for a given operating frequency.

Iron Loss Measurements

The fact that iron losses cannot be measured directly presents a significant challenge for their accurate determination. Most research and standards focus on sheet material properties (for an easy comparison of different materials, neglecting, however, the actual machine geometry [74]) using strip samples in Epstein frames [75–80] or single-sheet testers of conventional [81] or rotational [82–84] types, with typically sinusoidal flux density waveforms. With these methods, the manufacturing influence of, e.g., punching as well as laser and water jet cutting techniques can be investigated comparing steel sheet samples of different widths. Less frequently, investigations utilizing ring samples [85–87] or the actual stator core [74] are performed, which represent the true geometry more accurately (especially in the stator yoke section) and also may include some manufacturing influences such as stack bonding, interlockings, and welding (e.g., plasma, laser, resistance). Yet, the narrow teeth sections are not covered, which is where the manufacturing processes show the greatest effects, especially for the small core geometries of SFHP motors.

However, significant discrepancies may occur between the iron losses of the material samples or the actual stator core and those of the fully-assembled machine due to the non-sinusoidal flux density waveforms and manufacturing influences

[53] Traction motors are typically implemented with a lamination thickness ranging from 0.2 to 0.35 mm [72]. Even thicknesses of, e.g., $t_{\text{steel}} = 0.1$ mm are available on the market [73], but poor mechanical stability and stacking factors often outweigh the reduction in the eddy currents.

such as heat shrinking and form fitting [69]. The determination of the iron losses of fully-assembled PM-less machines is regulated by international IEC and IEEE standards [88, 89], in which the iron losses are separated from the total losses by the subtraction of the copper losses and mechanical losses (such as windage and friction). To this aim, different operating points are investigated experimentally. However, it is disadvantageous that the error propagation of the individual loss determinations affects the obtained iron losses.

Unlike the determination of the overall efficiency, the iron loss determination of PM synchronous machines is not yet regulated within the standards. Simple no-load and deceleration tests cannot be used with PM machines to separate the iron losses from the mechanical losses, due to the permanent presence of the magnetic field causing iron losses [90]. In a rather complex approach, the PMs are replaced by dummy material of the same weight in a second no-load measurement to determine the mechanical losses, while the rotor is driven externally by another motor. However, again, the iron losses are obtained by the subtraction of other losses.

Compared to IHP and FHP PM motors, iron loss measurements of the actual SFHP motor are rarely found in the literature (e.g., [7]). In this thesis, a rheometer-based iron loss measurement is proposed for the analysis of SFHP PM motors. The rheometer is used to measure the no-load torque waveform for different operating speeds, studying the change in the offset torque component (see Subsection 3.2.4 and Section 9.2).

1.2.5 Claw-Pole Machines – Then and Now

Basically, claw-pole machines are synchronous machines characterized by a global ring winding for excitation between a first and a second "disk-like" pole piece forming an electromagnet, see Fig. 1.16. At their outer perimeter, the two pole pieces feature claws extending into the axial direction building claw-poles. The claw-poles of the first pole piece mesh with those of the second pole piece forming gaps in between. Exciting the global ring winding, the claw-poles of one pole piece become south poles while those of the other pole piece become north poles, and a multi-polar magnetic field is obtained in the air-gap. Claw-pole machines have flux components in the axial, radial, and tangential directions. Typically, 3-D finite-element analysis is required due to their high saturation, complicated structure which causes geometry-induced high leakage flux in the inter-claw region, and high eddy current losses due

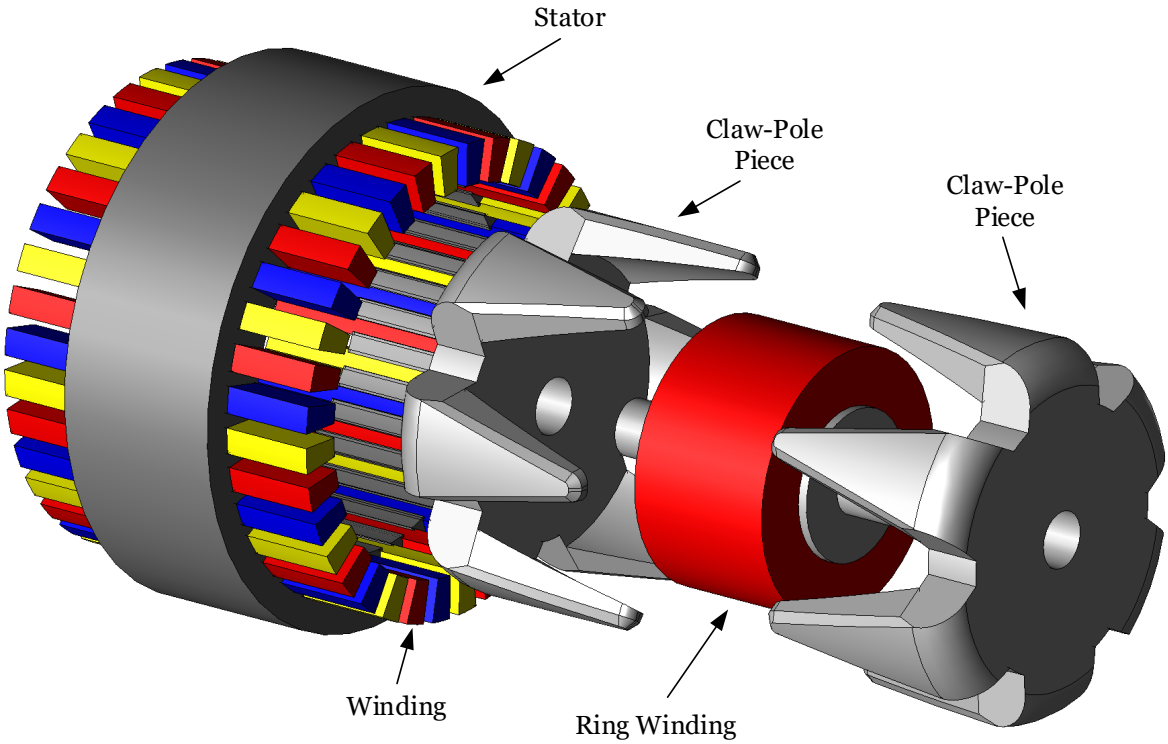

Fig. 1.16: Exploded view of a typical claw-pole alternator; modified geometry data from the JMAG® [91] application catalog: 25 - Analysis of a claw-pole alternator.

to the absence of core laminations. Fortunately, they are very cost-effective, as they have a reduced component count and provide the opportunity to easily realize a high pole number with one winding only [29,32,92], see the discussion in Appendix C.

The claw-pole concept is anything but new. In fact, claw-pole machines have been used for a very long time. The roots of electric machines with claw-poles date back to the 19th century. Patented by J. D. Gibbs und E. Fesquet in 1889 [93], claw-pole machines have been and still are used in many different applications, ranging from tiny fan and stepper motors to car alternators and to small and medium scale wind generators.[54] In 1891, a claw-pole machine as part of a hydropower plant (100 kVA, 13 kV, 40 Hz, 32 pole) was used for the first long-distance three-phase AC transmission (175km), between Lauffen am Neckar and Frankfurt am Main, within the framework of the International Electrotechnical Exhibition [95, 96]. However, in hydropower plants, the claw-pole machine was soon replaced by salient-pole synchronous machines but found application in medium frequency generators (i.e., 0.5 to 10 kHz) used for inductive heating in the first half the 20th century [97].

[54] Claw-pole machines have also been studied for large wind generators in the Mega Watt range [94].

In the 1960s and 1970s, claw-pole generators were used in busses and trains, e.g., to supply the air-conditioning unit. Since then, claw-pole alternators, also known as Lundell generators, have become omnipresent in automotive applications and can be found in almost every motor vehicle as part of the on-board power supply. They have been studied extensively in the literature [97–102]. More recent research in this regard has either focused on alternator optimization with respect to noise emissions [103–106] or hybrid (PM assisted) excitation to compensate for leakage flux in the inter-claw region and thereby increase the power density [107–110].

In the 1980s, the claw-pole concept experienced a renaissance for brushless SFHP motor applications due to the low manufacturing costs, many applications of which are used to this day. Examples worth mentioning include single-phase fan motors with a rather low pole count [35, 111, 112] (notably pushed by a company known today as ebm-papst GmbH) and two-phase stepper motors with a rather high pole count [19, 113–115].

At the beginning of the 21st century, the Robert Bosch GmbH developed an inner-rotor BLDC claw-pole motor for an automotive water pump application [7, 116–118], as did the Bühler Motor GmbH [119]. The same motor topology was also used in a gear box lubrication pump application by FTE automotive in 2014 [6]. The input power of these applications is between 10 and 20 W. (Applications with higher power usually use three-phase BLDC or BLAC motors with a lamination stack having salient stator poles.)

With the substantial improvement of soft magnetic composites (SMC) in recent decades, claw-pole motors, among many different other transverse flux machines, regained attention in the research community [120–129] for various applications. Advantageously, SMC material has excellent characteristics with respect to design freedom, magnetic isotropy, high saturation flux density, and eddy current suppression. However, the material is not as dense as an iron lamination stack, because otherwise the insulation between adjacent particles would be damaged, resulting in a relatively low relative permeability.

In summary, claw-pole machines have come a long way since their invention in the 19th century. They are all the more relevant today and can be found in various applications, notably as alternators as well as fan, pump, and stepper motors.

1.3 Contributions of this Thesis

Referring to the in part adverse characteristics of SFHP single-phase BLDC motors discussed in Subsections 1.1.2 and 1.2.2, this thesis makes the following contributions to the literature on SFHP single-phase BLDC motor design and analysis:

- Development of claw-pole motor designs with reduced cogging torque, smoothing the output torque and reducing its ripple to prevent potentially disturbing structure-borne and airborne noise.
- Cogging torque reduction with no (or little) increase to the manufacturing cost.
- Development of low cogging torque claw-pole motor designs which have balanced axial forces.
- Realization of the starting capability of claw-pole motors having at the same time maximum design freedom with respect to the claw-pole shapes.
- Investigation of the radial, axial, and tangential forces of the proposed single-phase BLDC claw-pole motor designs.
- Characterization of the thermal performances of different SFHP single-phase BLDC claw-pole motors.
- Accurate measurement of the cogging torque and hysteresis torque waveforms in the sub-milli-Newton meter range.
- Accurate determination of the iron losses (i.e., eddy current and hysteresis losses) of SFHP PM motors.

1.4 List of Publications

The work presented in this thesis has resulted in the following patent application[55] and *first author* publications. The papers are subjected to copyright by the *Institute of Electrical and Electronics Engineers (IEEE)*. The journal publications are extended versions of preceding conference publications (i.e., J1/C1, J2/C2, J3/C4).[56]

[55] The patent application was submitted to the European Patent Office on May 29, 2018 and published on December 4, 2019. In response to the extended European Search Report of December 3, 2018 a set of amended claims was submitted to the European Patent Office on May 20, 2020.

[56] J2 and J3 are open access publications.

Patent Application:

P1 **S. Leitner**, "Brushless Direct Current Motor," European Patent 3 576 267 A1, Dec. 4, 2019.

Journal Publications:

J1 **S. Leitner**, H. Gruebler, and A. Muetze, "Innovative Low-Cost Sub-Fractional HP BLDC Claw-Pole Machine Design for Fan Applications," in *IEEE Transactions on Industry Applications*, vol. 55, no. 3, pp. 2558–2568, May-Jun. 2019.

J2 **S. Leitner**, H. Gruebler, and A. Muetze, "Cogging Torque Minimization and Performance of the Sub-Fractional HP BLDC Claw-Pole Motor," in *IEEE Transactions on Industry Applications*, vol. 55, no. 5, pp. 4653–4664, Sep.-Oct. 2019.

J3 **S. Leitner**, G. Krenn, H. Gruebler, and A. Muetze, "Rheometer-Based Cogging and Hysteresis Torque and Iron Loss Determination of Sub-Fractional Horsepower Motors," in *IEEE Transactions on Industry Applications*, Apr. 2020.

Conference Publications:

C1 **S. Leitner**, H. Gruebler, and A. Muetze, "Low-Cost Sub-Fractional Horsepower Brushless Direct Current Claw-Pole Machine Topology for Fan Applications," *2018 IEEE Applied Power Electronics Conference and Exposition (APEC)*, San Antonio, TX, USA, 2018, pp. 1242–1248.

C2 **S. Leitner**, H. Gruebler, and A. Muetze, "Cogging Torque Minimization on a Mass-Produced Sub-Fractional Horsepower Brushless Direct Current Claw-Pole Motor," *2018 IEEE Energy Conversion Congress and Exposition (ECCE)*, Portland, OR, USA, 2018, pp. 6083–6089.

C3 **S. Leitner**, H. Gruebler, and A. Muetze, "Effects of Manufacturing Imperfections and Design Parameters on Radial Magnetic Forces in the BLDC Claw-Pole Motor," *2019 IEEE International Electric Machines and Drives Conference (IEMDC)*, San Diego, CA, USA, 2019, pp. 2167–2173.

C4 **S. Leitner**, G. Krenn, H. Gruebler, and A. Muetze, "Rheometer-Based Cogging Torque Measurement for Sub-Fractional HP Permanent Magnet Motors," *2019 IEEE International Transportation Electrification Conference and Expo (ITEC)*, Detroit, MI, USA, 2019, pp. 1–7.

C5 **S. Leitner**, H. Gruebler, and A. Muetze, "Low-Cost BLDC Claw-Pole Motor Design for Fan Applications with Reduced Cogging Torque and Balanced Axial Forces," *2020 IEEE Applied Power Electronics Conference and Exposition (APEC)*, New Orleans, LA, USA, 2020, pp. 279–284.

C6 **S. Leitner**, T. Kulterer, H. Gruebler, and A. Muetze, "Characterization of the Thermal Performance of Low-Cost Sub-FHP BLDC Claw-Pole Motor Designs," *2020 IEEE Energy Conversion Congress and Expo (ECCE)*, Detroit, MI, USA, 2020.

1.5 Thesis Outline

The thesis is subdivided into three major parts: Part I provides a broad introduction and overview of the BLDC claw-pole motor and the used techniques for analysis. Part II includes the contributions of this thesis to the research community, consisting of various analyses of the proposed BLDC claw-pole motor design improvements. Part III comprises the appendices in which additional analyses are presented. The individual chapters are organized as described below. Chapter summaries and conclusions are provided at the end of each chapter.

This chapter, *Chapter 1*, presents an introduction to the thesis topic. Starting with the context, the state-of-the-art is covered regarding brushless PM motors in general. The challenges concerning SFHP PM motors are pointed out and the cogging torque phenomenon is overviewed due to its importance concerning the understanding of the proposed low cogging torque designs. A review of iron losses and the history of claw-pole machines is given as well, and the contributions of this thesis are listed. The remainder is structured as follows:

Chapter 2 reviews the single-phase BLDC claw-pole motor topology, suitable for SFHP fan systems, which holds a central role in this thesis. Its structure and working principle are discussed. The punching layout for the claw-pole stator parts, which are punched and subsequently deep-drawn, are described, as are the possibilities of starting single-phase BLDC motors. Finally, the claw-pole motor topology is compared to the well-known salient-pole motor with a lamination stack; the latter is conventionally used in SFHP fan drives.

In *Chapter 3*, the modeling and experimental techniques used throughout this thesis are described. At first, the analytic modeling and the finite-element analysis are detailed. Then, the measurement setups are presented, including the investigation

of the cogging torque, hysteresis torque, iron losses, back-EMF, radial forces, axial forces, and thermal behavior.

Chapter 4 introduces the proposed single-phase BLDC claw-pole motor designs. Based on the *Baseline* claw-pole motor design, an overview of the proposed modifications, namely air-gap asymmetry, single-sided skew, V-skew, auxiliary slots, and combinations thereof, is given.

In *Chapters 5–8*, the proposed design modifications introduced in Chapter 4 are discussed and studied in great detail, focusing on their effects on the cogging torque and back-EMF waveforms.

Chapter 9 presents further rheometer-based experimental analyses of the claw-pole motor and the salient-pole motor. The focus is on the extraction of the cogging torque and hysteresis torque from the measured no-load torque waveforms, and the determination of the iron losses.

The *Conclusion*, *Chapter 10*, summarizes the findings of this thesis and provides an outlook on interesting future work.

Lastly, the *Appendices* are a conglomeration of additional analyses and information regarding various aspects presented and discussed in this thesis, especially *Chapters 5–9*.

Chapter 2

Single-Phase BLDC Claw-Pole Motor Topology – A Rediscovery

This chapter reviews the low-cost single-phase BLDC claw-pole motor topology, a niche concept that first prospered in the 1980s for SFHP fan applications and still used today. Serving as the Baseline, it provides the context of the proposed design modifications discussed in Chapters 5–8 when compared with the more conventional single-phase BLDC motor topologies (e.g., the salient-pole motor). First, the structure, working principle, and punching layout of the claw-pole motor are covered. Then, possible starting capability measures are overviewed. In the last part, a detailed topology comparison between the claw-pole motor and the salient-pole motor is provided.[1]

2.1 Structure and Working Principle

The following subsections briefly review the structure, electrical equivalent circuit, and commutation process of the low-cost single-phase BLDC claw-pole motor with a bifilar winding.[2]

2.1.1 Motor Structure

As opposed to other claw-pole machines (e.g., the well-known claw-pole alternator shown in Fig. 1.16), the dimensions of the single-phase BLDC claw-pole motor are so small that specially shaped steel sheets can form the stator claws. Fig. 2.1 illustrates a 3-D exploded view of the *Baseline* claw-pole motor detailing its structure. In fan

[1] Selected material of this chapter has also been published in [61, 130–132].
[2] The bifilar winding is described in Section 1.2 as well as Subsections 2.1.1, 2.1.2, and 2.1.3.

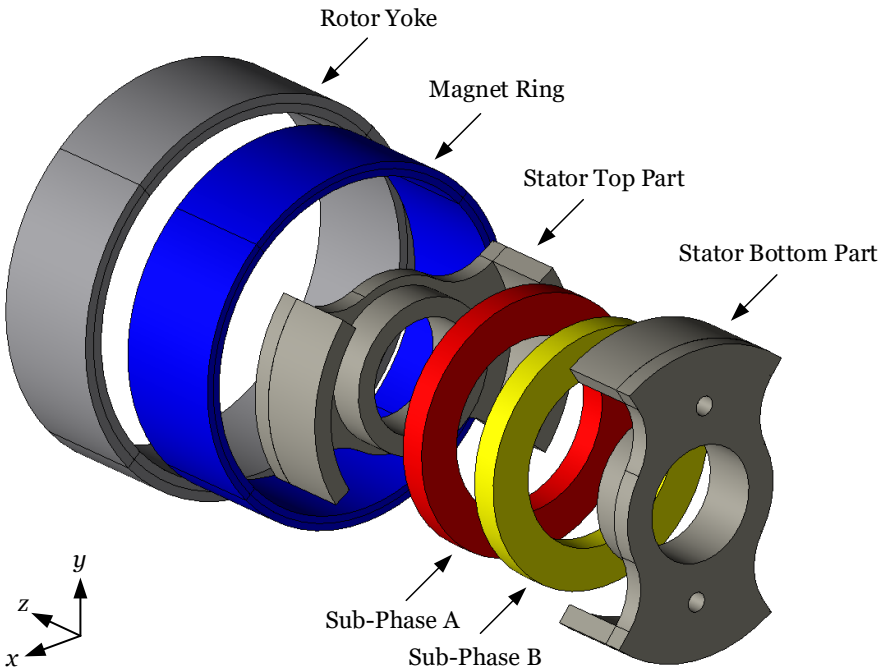

Fig. 2.1: 3-D exploded view of the *Baseline* claw-pole motor; visualized with JMAG® [91].

drives, it is typically realized as an outer-rotor motor.[3] The rotor comprises a bonded PM ring, with four poles radially magnetized on it, inside a rotor yoke for efficient flux guidance and mechanical stability. Central to the stator is the concentrated bifilar ring winding, consisting of sub-phases A and B on a coil former,[4] housed by two specially shaped steel sheet stator parts (i.e., the stator top and bottom parts) which are punched and subsequently deep-drawn. The bifilar winding is visualized (and also modeled) as two separate but concentric coils displaced axially. In practice, the sub-phases A and B are wound simultaneously and are hence intertwined. A detailed modeling thereof is not undertaken due to the immense computational burden but also because the influence is secondary for the analyses in this thesis.

Fig. 2.2 depicts a 3-D assembled view of the *Baseline* claw-pole motor for centered rotor and stator poles. The no-load flux density vector plot is shown in Fig. 2.2(a); Fig. 2.2(b) indicates the complex 3-D path of a flux line, where $\Phi_{p,PM}$ is the PM flux per pole.[5] Owing to the specially shaped stator parts, the flux has axial, radial,

[3] For other applications such as circulator pumps with a canned motor, inner-rotor variants are commonly used.

[4] For clarity, the coil former is not shown in Fig. 2.1.

[5] For illustration, any leakage flux is neglected.

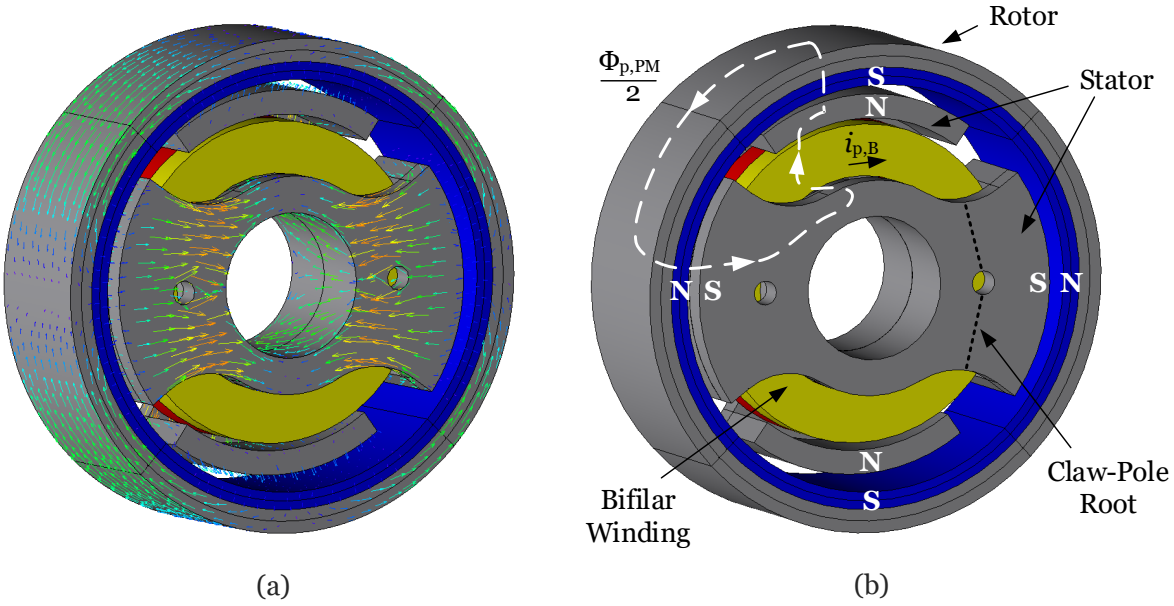

Fig. 2.2: Assembled view of the *Baseline* claw-pole motor: (a) no-load flux density vector plot and (b) indication of 3-D flux path; both visualized with JMAG® [91].

and tangential components: As indicated by the arrows in Figs. 2.2(a) and (b), the flux travels axially through the cylindrical portion of the stator parts (i.e., the stator yoke), bifurcates and passes radially by the claw-pole root and towards the claw-poles. Next, it passes through the air-gap and magnet until it splits again and travels through the rotor yoke in the tangential direction. The flux returns along the same path but in the reverse direction. (A detailed magnetic equivalent circuit of the claw-pole motor is presented and discussed in Appendix D.) The flux is concentrated in the claw-pole root indicated in Fig. 2.2(b); see also the yellow and orange flux density vectors in said region in Fig. 2.2(a). Thus, the claw-pole root is most prone to saturation, what must be avoided during the design. Hence, the torque of the claw-pole motor cannot be scaled in the axial direction but, instead, multiple stators can be arranged in series.

The claw-poles of the two stator parts, which lead to opposite sides of the coil, mesh such that a current in the ring winding generates a hetero-polar magnetic field in the air-gap. For clarification, the magnetic stator poles (due to the phase current $i_{p,B}$ in sub-phase B) and the magnetic rotor poles (due to the PMs) are marked in Fig. 2.2(b).

2.1.2 Electrical Equivalent Circuit

Fig. 2.3 shows the electrical equivalent circuit of a single-phase BLDC motor drive with a bifilar winding, where C is the DC-link capacitor and D is the diode that prevents current from flowing back into the source U_{DC}. Each of the sub-phases A

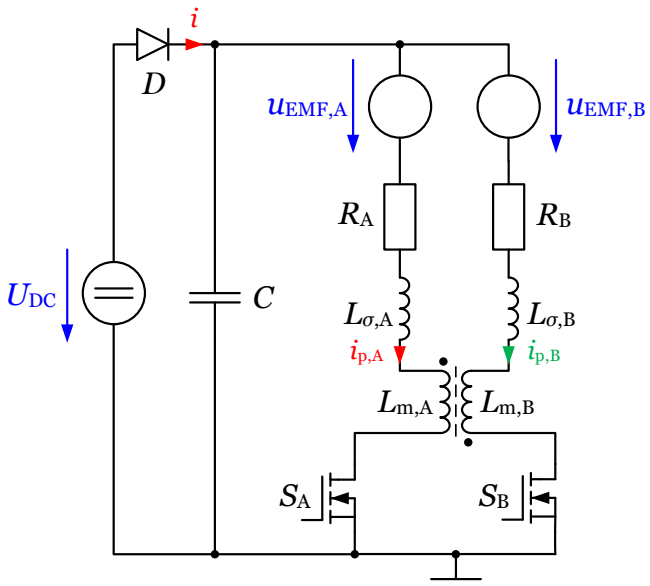

Fig. 2.3: Electrical equivalent circuit of a single-phase BLDC motor drive with a bifilar winding.

and B of the bifilar winding can principally be modeled by the single-phase electrical equivalent circuit presented in Fig. 1.6. The two sub-phases are oppositely coupled via the main inductance (the coupling factor ζ is typically between 0.8 and 1), as indicated by the dots next to $L_{\mathrm{m,A}}$ and $L_{\mathrm{m,B}}$ in Fig. 2.3.

Depending on the rotor position θ sensed by a Hall effect sensor, the bifilar winding is energized by the use of the power electronic switches S_{A} and S_{B} (see Subsection 2.1.3). For the studied fan application, the motor's nominal rms phase current is about 250 mA and the voltage rating is 13.5 V. Therefore, MOSFETs are most widely used as power electronic switches, in the form of discrete components or integrated driver circuits.[6]

[6] In practice, to meet the electromagnetic emission requirements, an LC-filter is often placed between the DC-link and the motor. In addition, a shunt resistor for diagnosis and over-current detection is typically placed in the current return path.

2.1.3 Commutation Process

As mentioned in Subsection 2.1.2, the switches S_A and S_B are turned on and off, depending on the rotor position θ sensed by a Hall effect sensor for proper phase current flow as discussed in Subsection 1.2.1. Based on the top part of Fig. 1.12, Fig. 2.4(a) shows the theoretical back-EMF and phase current waveforms of a bifilar winding as a function of θ. Ideally, rectangular current waveforms should be realized

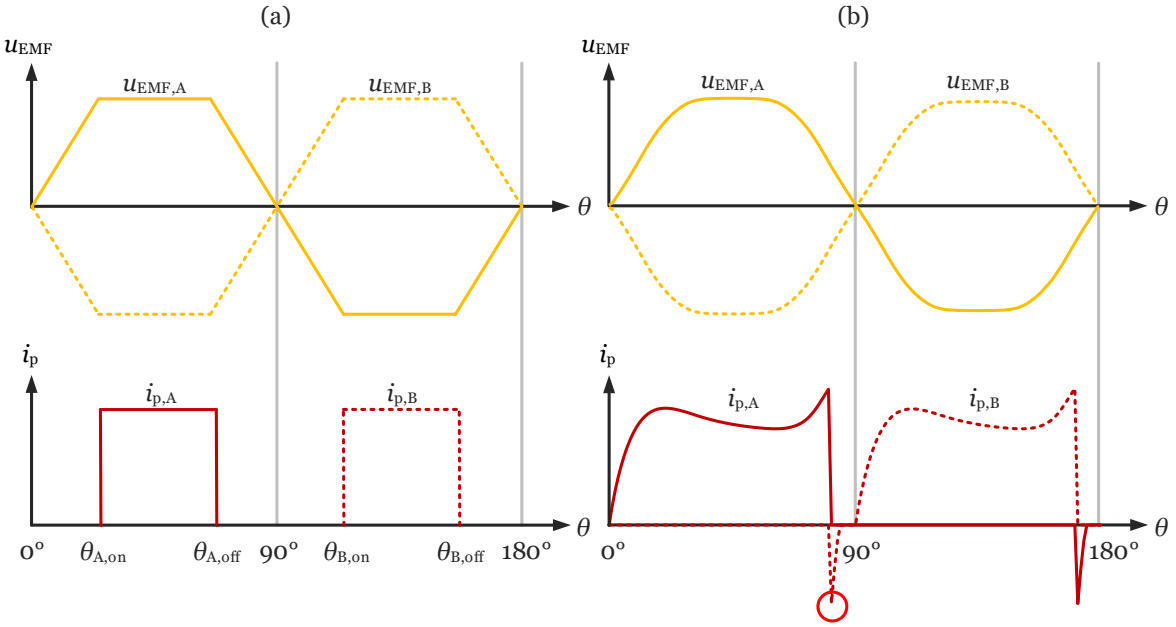

Fig. 2.4: Back-EMF and phase current waveforms: (a) theoretical and (b) real; the latter for open-loop control.

during the flat portion of the back-EMF to obtain constant torque for that interval, see the discussion in the context of Fig. 1.12. When the back-EMF $u_{EMF,A}$ is positive, sub-phase A is energized with U_{DC} at $\theta_{A,on}$ and turned off at $\theta_{A,off}$, causing a positive current flow of $i_{p,A}$. Sub-phase B is operated in the same way for the positive half-wave of $u_{EMF,B}$, causing $i_{p,B}$. The result is a unidirectional current flow into the motor (from top to bottom in Fig. 2.3).

However, the real waveforms deviate from the theoretical ones, especially those of the current when fed from a voltage source. Fig. 2.4(b) illustrates the real back-EMF and phase current waveforms of a bifilar winding for open-loop control,[7] illustrating the commutation process. The back-EMF has smooth transitions and the

[7] In open-loop control, the current waveform is not controlled, using, e.g., pulse-width modulation.

phase current rises exponentially according to the electric time constant. Hence, the switches must be turned on such that the phase current reaches the desired value in time. As mentioned before, the bifilar winding consists of two coupled coils. When one sub-phase is switched off, most of the stored magnetic energy is dissipated as a free-wheeling current in the other sub-phase, due to the coupling of $L_{m,A}$ and $L_{m,B}$ in Fig. 2.3. This results in negative current spikes indicated by the red circle in Fig. 2.4(b). The remaining magnetic energy, modeled by the leakage inductance L_σ in Fig. 2.3, is dissipated in the acting switch, known as the avalanche effect [7].

2.2 Punching Layout

This section discusses the manufacturing process of the claw-pole stator parts which are punched and subsequently deep-drawn steel sheets. Fig. 2.5(a) illustrates the *Baseline* steel sheet punching layout in which the solid lines represent the punching edges. The hatched sections are deep-drawn, along the dashed bending lines, into the positive or negative z-direction to yield the final stator part, a profile view of which is depicted in Fig. 2.5(b). (For reference, see also the final stator top and stator bottom parts in Fig. 2.1.) The parameters r_2 and r_3 are the inner and outer radii of the final stator part, r_1 and r_4 determine the lengths of the deep-drawn sections in the z-direction (the stator claw width is $w_{claw} \approx r_4 - r_3$ and the stator yoke width is $w_{s,yoke} \approx r_2 - r_1$), τ_p is the pole pitch, w_{stat} is the stator width, φ_m represents the circumferential angle in mechanical degrees, t_{steel} is the steel sheet thickness, φ_{cp} is the claw-pole angle defined by points I, II, and III, and SL is the symmetry line.[8]

Remark 1: While the axial claw width w_{claw} is theoretically not limited [as long as the structural requirements are met and saturation in the claw-pole root is prevented, see Fig. 2.2(b)] in this outer-rotor topology, since the claws lie on the outside stator perimeter, the stator yoke width $w_{s,yoke}$ inherently is. Alternatively, the stator yoke can be realized by a bushing onto which two "yokeless" stator parts are forced. Conversely, in case of an inner-rotor variant (see, e.g., [116–118]), w_{claw} is limited while $w_{s,yoke}$ is theoretically not restricted.

Remark 2: The selection of t_{steel} depends on both the maximum PM flux per

[8] In a claw-pole motor, the ratio φ_{cp}/τ_p can be closer to one than in a salient-pole motor because the latter requires a minimum slot opening ($w_{slot} = \tau_p - \varphi_{cp}$) for winding insertion. Decreasing slot openings decreases the cogging torque but at the same time increases the leakage flux.

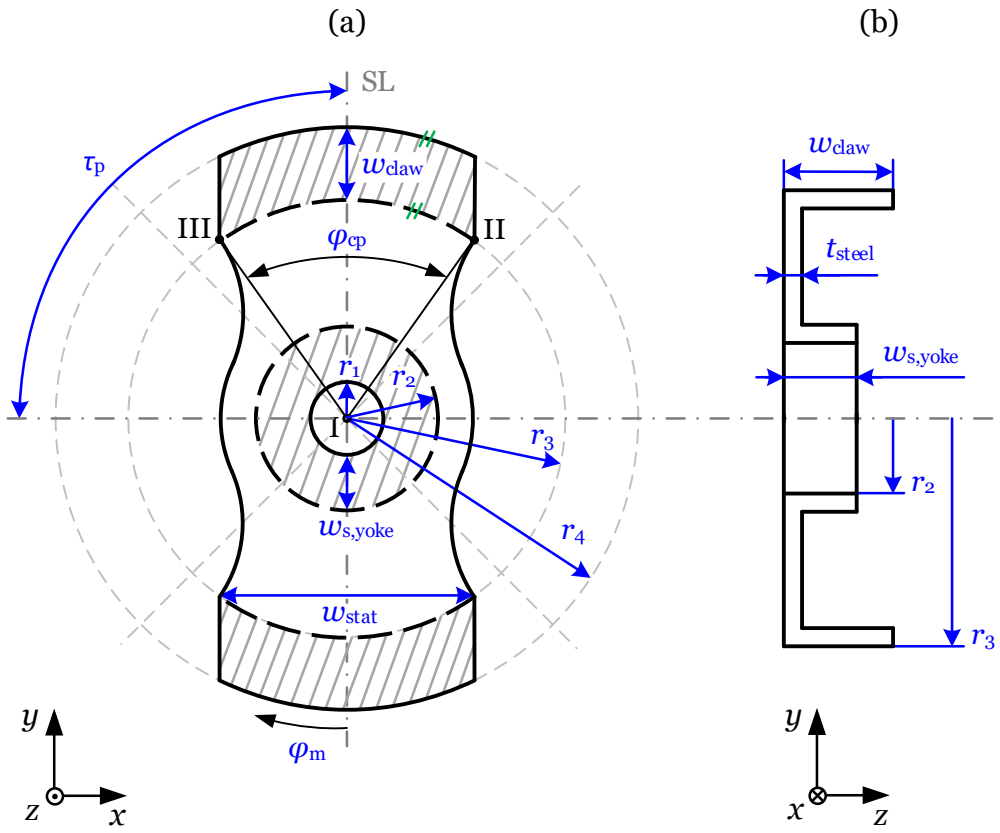

Fig. 2.5: *Baseline* stator part steel sheet punching layout: (a) before deep-drawing and (b) after deep-drawing.

pole $\Phi_{p,PM}$ [because the flux collected by a claw-pole is concentrated in the claw-pole root, indicated in Fig. 2.2(b), in which saturation must be avoided] and the maximum operating speed n_{max} [which is concomitant with the maximum eddy current losses for a chosen value of t_{steel}].

Remark 3: In practice, the actual length of w_{claw} and $w_{s,yoke}$ is reduced by about the size of t_{steel} due to material buckling caused by the bending or deep-drawing of the steel sheets.

Remark 4: Alternatively, the claw-pole stator parts can also be sintered, preferably from a soft magnetic composite (SMC) material. In this case, the scaling of the claw-pole motor is possible because excessive eddy current losses in the claw-pole root are a rather small problem.

2.3 Starting Capability

In general, single-phase BLDC motors cannot start autonomously owing to their alternating stator magnetic field. Hence, they are typically implemented with some kind of magnetic circuit imbalance, introducing space harmonics, to facilitate the starting and help provide sufficient cogging torque at positions of zero alignment torque [32, 33, 115]. Thereby, a defined parking position is created from which the motor can start by itself into a preferred direction of rotation.

Most commonly, single-phase BLDC motors with a lamination stack [see, e.g., the salient-pole motor depicted in Figs. 2.10(a) and 2.11(b)] are implemented with an asymmetric air-gap (e.g., tapered, uneven, stepped, notched, or with reluctance holes in the tooth-tips) to shift the magnetic symmetry axis. Fig. 2.6 illustrates a typical asymmetric air-gap of a salient-pole motor in which the air-gap length $\delta(\varphi_m)$ increases steadily along one stator pole:

$$\delta(\varphi_m) = \delta_{min} + \Delta\delta(\varphi_m), \tag{2.1}$$

where δ_{min} is the minimum air-gap length and $\Delta\delta(\varphi_m)$ denotes the widening of the air-gap length as a function of the circumferential angle φ_m. As a result, the

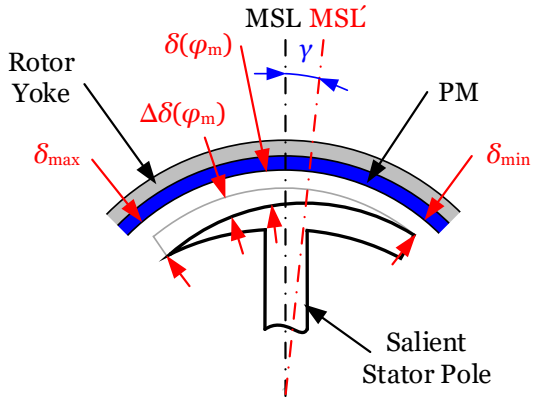

Fig. 2.6: Typical asymmetric air-gap of a salient-pole motor.

magnetic symmetry lines (MSL) of the stator, which are the rotor parking positions at standstill, are shifted by the angle γ from a central position towards the decreasing air-gap (see MSL′ in Fig. 2.6). The asymmetric air-gap increases the effective air-gap δ_{eff} [and hence the air-gap reluctance as per (D.1)], which decreases the PM flux per pole $\Phi_{p,PM}$. The effective air-gap can be approximated as $\delta_{eff} \approx \delta + \frac{\Delta\delta_{max}}{2}$. (The

air-gap permeance variations for symmetric and asymmetric air-gaps are presented in Appendix E.)

In contrast to the discussed asymmetric air-gap, single-phase BLDC claw-pole motor variants typically feature a symmetric air-gap but asymmetric claw-poles [133, 134] to realize a defined rotor parking position at standstill [see the claw-pole in Fig. 2.7(a)]. Alternatively, designs with symmetric claw-poles [see Fig. 2.7(b)] and

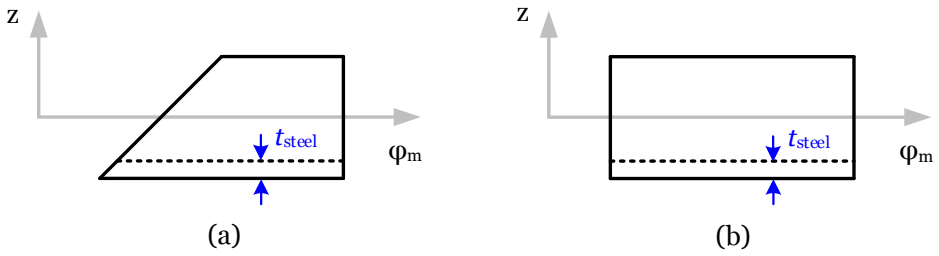

Fig. 2.7: Unrolled claw-poles: (a) asymmetric and (b) symmetric.

parking magnets offset by the angle γ have been proposed to facilitate the starting [11, 135], which is illustrated in Fig. 2.8. In this case, a yokeless PM rotor is forced by the

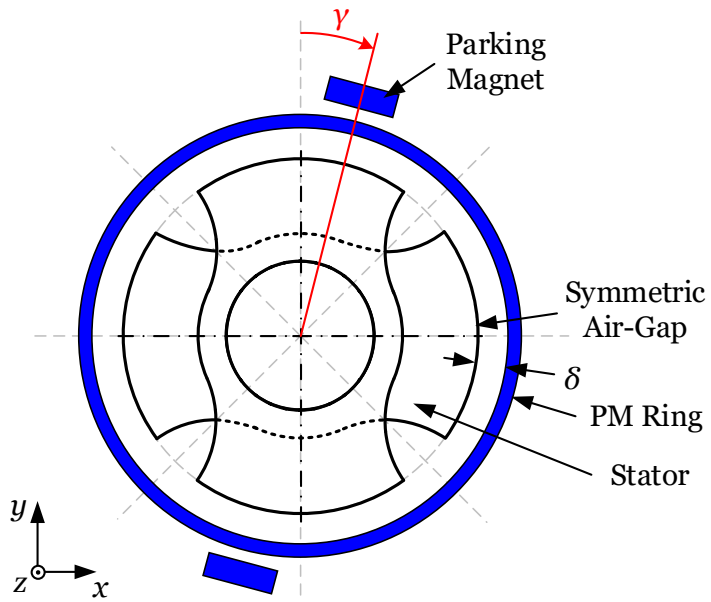

Fig. 2.8: Starting capability using parking magnets for motors with symmetric claw-poles.

parking magnets to rest at a defined position at standstill (i.e., the rotor aligns with the parking magnets) from which the motor can start.

Instead of using parking magnets [see Fig. 2.8] or asymmetric claw-poles [see Fig. 2.7(a)] like in conventional claw-pole motors, the claw-pole motor designs proposed in this thesis are implemented with symmetric claw-poles [see Fig. 2.7(b)] and air-gap asymmetry [see Fig. 2.6].[9] (The main reason is to obtain maximum design freedom with respect to the claw-poles for the implementation of cogging torque reduction measures.) Fig. 2.9 illustrates a claw-pole motor with an asymmetric air-gap, defined by points I, II, and III', in accordance with Fig. 2.5(a).

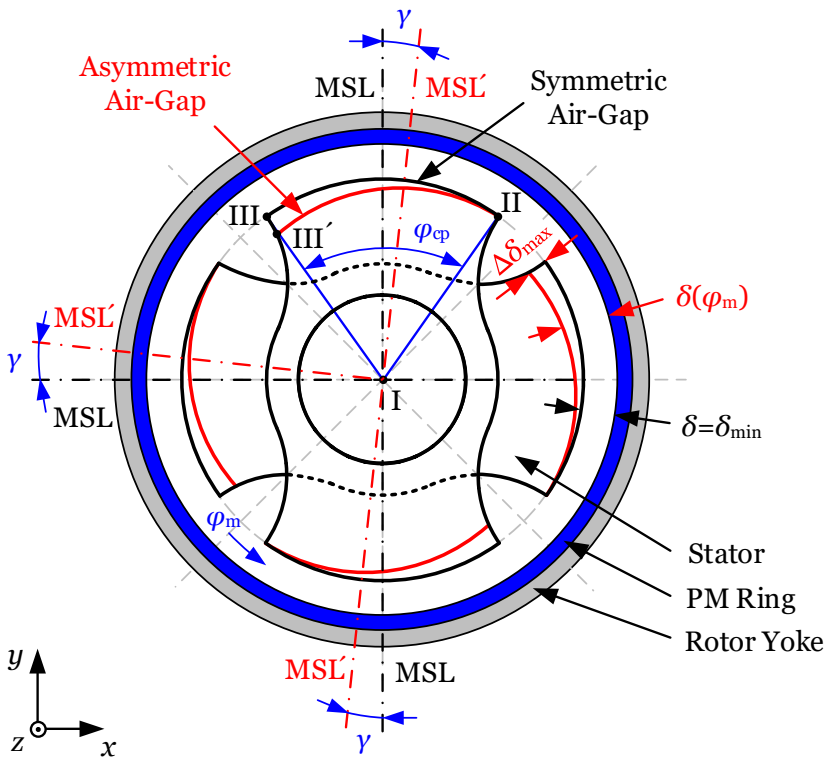

Fig. 2.9: Claw-pole motor with and without air-gap asymmetry.

As discussed in Section 5.4, the cogging torque waveform phase-shifts and changes when air-gap asymmetry is implemented. (See the discussion in the context of Fig. 5.3.) As a result, cogging torque is provided at the positions of zero alignment torque shown in Fig. 1.12. The actual starting torque, however, predominantly depends on the injected phase current at standstill.

[9] Other possibilities for air-gap asymmetry, such as the implementation of a stepped pole like sometimes used in motors with a lamination stack [57], are rather unsuitable for the claw-pole motor due to the concept of deep-drawn steel sheets. Concepts of reluctance notches or holes, as known from [115], could be implemented directly single-sided on the claw-pole surface shown in Fig. 2.7(b).

Remark 1: The implementation of a typical air-gap asymmetry in a SFHP BLDC claw-pole motor reduces the room for the winding by up to 10 %. (See the discussion in Appendix F.)

Remark 2: Implementing applications, which inherently have a relatively large air-gap (e.g., a circulator pump with a canned motor), with a single-phase motor with an asymmetric air-gap can be disadvantageous, because a large air-gap requires an even more pronounced air-gap asymmetry. This increases the effective air-gap δ_{eff} significantly and, in turn, reduces the PM flux per pole $\Phi_{\text{p,PM}}$.

2.4 Claw-Pole Motor versus Salient-Pole Motor

This section compares the widely used single-phase BLDC salient-pole motor (see, e.g., [25, 136, 137]) and the studied claw-pole motor variant. The focus is on the winding topology, the manufacturing process' simplicity, and the possible implementation of skewing.

Figs. 2.10(a) and (b) contrast the salient-pole motor (shown in a front view), which has a lamination stack, with the studied claw-pole motor (shown in a profile view) in terms of the winding pattern; both are four-pole four-slot motors.[10] While the salient-pole motor has, e.g., four bifilar windings on four salient poles connected in series, the claw-pole motor has a much simpler structure with one global ring winding on the machine axis between two stator parts. Hence, compared to the salient-pole motor, the claw-pole motor's number of windings is reduced (one instead of four), the winding itself is simpler (one ring winding instead of four windings on four salient poles), and the winding process is faster (linear instead of flyer winders[11]). Furthermore, the claw-pole motor's copper fill factor is higher (orthocyclic[12] instead of wild winding),[13] cheaper stator material can be used (DC01 steel instead of electrical steel),[14] and the number of components is reduced (two stator parts instead of interlocking laminations).

[10] SFHP fan drives typically feature single-phase BLDC motors with a low number of pole pairs p (e.g., $p = 2$) due to the low-cost manufacturing of the stator and the winding. Conversely, hard-disk drives usually have three-phase motors with higher pole pair and slot numbers, because such applications require low cogging torque and low output torque ripple.

[11] The manufacturing speed of linear or coil winders is up to twice as fast as that of flyer winders [138].

[12] Whether or not an orthocyclic winding can be realized depends on the wire diameter, see [139].

[13] The copper fill factor of linear or coil winders is up to twice as high as that of flyer winders [138].

[14] This, however, reduces the PM flux per pole $\Phi_{\text{p,PM}}$ for the same magnet and air-gap length.

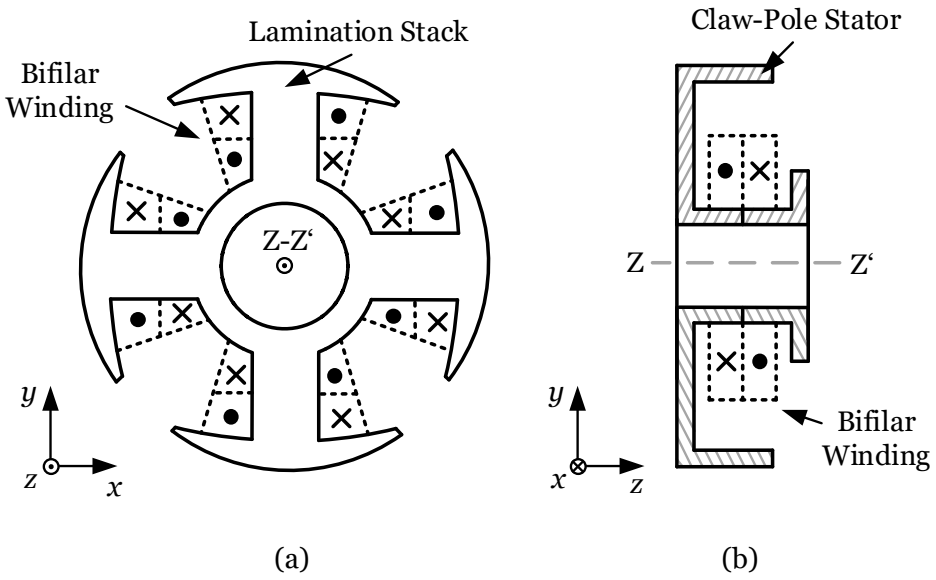

Fig. 2.10: Winding comparison: (a) salient-pole motor and (b) claw-pole motor; both have a bifilar winding. (For illustration, the coil former is not indicated.)

Figs. 2.11(a) and (b) contrast the pole-to-pole flux lines of the claw-pole motor and the salient-pole motor, where $\Phi_{p,PM}$ is the PM flux per pole. The indicated flux line

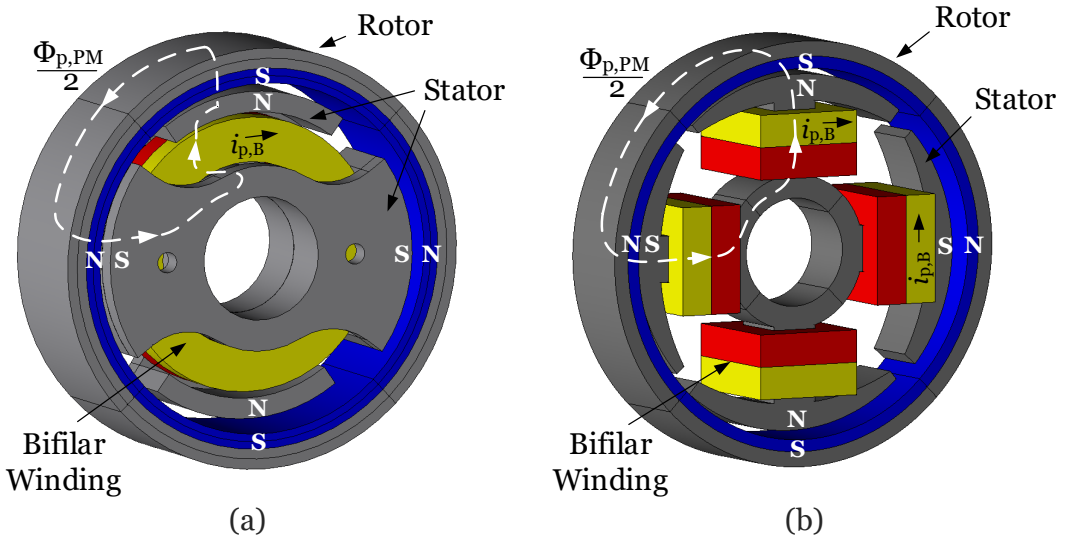

Fig. 2.11: Flux linkage comparison: (a) claw-pole motor and (b) salient-pole motor; visualized with JMAG® [91].

of the claw-pole motor inherently links with all the turns of the global ring winding, while the same flux line of the salient-pole motor only links with the turns of two

consecutive stator poles, i.e., halve the total number of turns in series. As a result, the salient-pole motor requires twice as many turns as the claw-pole motor to obtain the same back-EMF for consistent $\Phi_{p,PM}$.[15] At the same time, the excitation effort is reduced, as discussed in detail in Appendix C. The smaller excitation effort of the claw-pole motor is even more advantageous when the pole number and hence the number of claw-poles is increased [140]. For example, car alternators typically have 12 claw-poles, ancient hydro generators featured many more, e.g., 32 claw-poles.

Due to their slot-pole combination, both the claw-pole motor and the salient-pole motor have a large goodness factor [see (1.20), where $C_T = 4$ for $2p = 4$ and $Q = 4$], indicating a high inherent cogging torque. This often calls for cogging torque minimization measures to reduce the output torque ripple and even the output torque waveform, thereby preventing potential structure- or airborne noise.

However, in SFHP electric motors, like in the salient-pole motor with a lamination stack, skewing is typically either not possible or quite costly to implement (see Subsection 1.1.2). For example, using low-cost interlocking laminations typically prevents the implementation of a skew. Other methods, e.g., winding a welded skewed lamination stack, winding an unskewed stack and implementing skewing afterwards, using skewed magnets, realizing a stepped skewed with axially segmented magnets, or using a skewed magnetization fixture are often a disqualifier for mass-produced low-cost applications (see Subsection 1.2.3). These techniques can significantly increase the manufacturing complexity and cost, primarily due to the increased number of manufacturing steps [26]. Yet, implementing the motor designs with skewed claw-poles, as proposed in Chapter 4 and analyzed in detail in Chapters 5–8, affect neither the manufacturing process and cost (as the claws are punched skewed and then deep-drawn) nor the winding and winding process (as the ring winding wound on a coil former is placed between two already formed stator parts). Moreover, a uniform skew can be realized, compared to the stepped skew of axially segmented magnets or a lamination stack.

Chapter Summary and Conclusions:

- The single-phase BLDC claw-pole motor has a simple and cost-effective structure (simpler than the comparable salient-pole motor with a lamination stack), featuring one global ring winding between two punched and

[15] For cost reasons, the claw-pole motor often uses relatively lossy magnetic material, which reduces $\Phi_{p,PM}$ for the same PM rotor.

deep-drawn steel sheets.

- Its flux path is 3-D.
- The claw-pole motor can be realized with different starting capability measures, e.g., asymmetric air-gap, asymmetric poles, and parking magnets.
- Like the salient-pole motor, the claw-pole motor can be implemented with a bifilar winding and operated using a Hall sensor and two switches.
- While both motors can be implemented with air-gap asymmetry, the proposed low cogging torque designs with stator claw skewing (see Chapters 4–8) are unique features of the claw-pole motor which, as opposed to other motor topologies, come at no increase to the manufacturing cost owing to the proposed punching layouts.

Chapter 3

Modeling and Experimental Techniques

This chapter presents the modeling and experimental techniques used in this thesis. The modeling techniques include analytic and numerical analyses of different phenomena of the single-phase BLDC claw-pole motor such as cogging torque, back-EMF, magnetic forces, and iron losses. While certain effects can be studied with analytic methods, due to its complex geometry and 3-D flux and leakage paths, a 3-D finite-element model of the claw-pole motor is created as well. For verification of the analytic and numerical analyses, various experiments are performed. The experimental techniques include mostly investigations with a rheometer (i.e., cogging torque, hysteresis torque, iron loss, and axial force measurements), but also radial force, back-EMF, and thermal measurements with different test setups, all of which are described in this chapter.[1]

3.1 Modeling Techniques

This section presents the analytic and numerical modeling techniques used to study and describe characteristics of the different claw-pole motor designs. First, the analytic approaches used and the limits of their applicability are discussed. Second, the used numerical approach is introduced, i.e., the implemented 3-D finite-element model.

[1] Selected results of this chapter have also been published in [61, 130–132, 141–143].

3.1.1 Analytic Modeling and Relationships

Analytic modeling has a very long history in the design and operation of electric machines, and is still excessively used to this day, because the results cam typically be obtained quickly. Yet, the analytic solution of Maxwell's equations is limited to very simple shapes, and iterative approaches are necessary to consider saturation effects, which increases the computational time. Typically, many idealizations or assumptions are made such as linear material behavior and constant or sinusoidal distributions and waveforms, respectively. Hence, phenomena like saturation and material anisotropy are often neglected, as are the harmonic contents of the current, voltage, and flux density waveforms, because otherwise it is difficult to analytically solve the problem. For standard IHP electric machines and larger ones such as hydro- and turbogenerators, many empirical correction factors have been introduced in the literature [144] to account for nonideal phenomena. However, due to the small dimensions and diversity of FHP and SFHP electric machines, conventional design and calculation methods are largely not applicable because 3-D effects like, e.g., fringing and flux stray paths often dominate the operational behavior.

While analytic modeling of SFHP electric machines is not in the focus of this thesis, some useful analytic relationships and models are used for theoretical remarks, discussions of the principal behavior of certain quantities, and verification of the finite-element analysis (FEA) and experimental results, as detailed below.

Analytic Relationships

Different analytic relationships are utilized, which relate to

- the cogging torque [especially its minimization through skewing and auxiliary slots, see, e.g., (6.1) and (7.1)],
- the back-EMF [in connection with skewing, see, e.g., (6.2)],
- the iron losses [especially their main components, the hysteresis and eddy current losses, see, e.g., (1.23) and (1.24)],
- the radial forces [under certain conditions, see (P.1)–(P.7)],
- the axial forces [introduced by single-sided skewing, see, e.g., (8.1)], and
- the motion equation [as to the rheometer setup and analyses, see, e.g., (3.5)].

Analytic Models

Certain analytic models are developed and used, including

- the description of air-gap asymmetry for the proposed punching layouts [see Appendix G],
- the reduction of the winding room due to increasing air-gap asymmetry [see, Appendix F],
- the calculation of the phase current waveform [see Appendix B],
- the determination of a simple thermal model [see Appendix H],
- the determination of a magnetic equivalent circuit and from it an estimation of the phase inductance [see Appendix D],
- the estimation of unbalanced radial magnetic forces as a result of eccentricity [see Appendix I], and
- the estimation of radial claw deflection [see Appendix J].

3.1.2 3-D Finite-Element Analysis

The calculation of electric and magnetic fields typically requires numerical methods because for the majority of practical problems it is not possible to apply analytic solutions [145]. For the calculation of complex constructs such as electric machines, analytical methods are often unsuitable especially considering non-linear, non-homogeneous, and anisotropic materials and flux leakage effects like fringing [146]. Solving Maxwell's equations for practical objects and geometries, different numerical solution methods have been proposed including the finite-element, finite-difference, finite-integral, and boundary-element methods [144]. The finite-element method is one of the most important approximation method to solve differential equations [147]. Proposed in the 1940s, the finite-element method is utilized in very many engineering disciplines today. Initially used for structural analysis, it was first applied to solve electromagnetic problems between 1970 and 1980 [146].

A popular method for deriving the finite-element equations (i.e., the transform of a continuous problem into a discrete problem) is the Galerkin approach, being a special case of the method of weighted residuals [148]. Given the differential equation of the field problem

$$L_2(\phi_w) + f_s = 0, \tag{3.1}$$

where L_2 is a second order differential operator, ϕ_w is the wanted function, and f_s

presents the sources of the field problem, an approximated solution is inserted into (3.1), e.g., $\phi_w \approx \tilde{\phi}_w = \sum_{\nu=1}^{N_{node}} c_\nu w_\nu$, where N_{node} is the number of nodes of the element, c_ν are coefficients, and w_ν are the shape functions. Hence, the solution of the problem obtained by the approximation is not exact, yielding the residual $\mathbb{R}$:

$$L_2(\tilde{\phi}_w) + f_s = \mathbb{R}. \tag{3.2}$$

In the Galerkin method, the weighted error is forced to zero on the domain Ω

$$\int_\Omega \omega_w \left(L_2(\tilde{\phi}_w) + f_s \right) d\Omega \stackrel{!}{=} 0, \tag{3.3}$$

where ω_w presents the weighting functions, which typically have the same form as the shape functions w_ν [148] mentioned above. The result is a linear system of equations that can be solved more easily. (See [147, 148] for more detailed information.)

Finite-Element Modeling

In a finite-element model, the entire domain is discretized, i.e., divided into a finite number of subdomains called elements. For the analysis, Maxwell's equations are solved for every element considering certain boundary conditions (i.e., Dirichlet and Neumann boundary conditions as well as starting conditions for transient problems) to obtain a unique solution. Due to the finite character, the solution is an approximation, the accuracy of which depends on many factors most importantly the mesh size (or the number of elements), the shape of the elements (1-D: line; 2-D: triangle, quadrilateral; 3-D: tetrahedron, brick), and the number of nodes, which depends on the interpolation method (or order of the shape function, e.g., linear or quadratic). On the one hand, using many elements, especially in the case of 3-D models, can lead to very long computation times. On the other hand, finite-element simulations can reduce the number of prototypes significantly and hence save money building and testing the same.

In fact, studying the proposed claw-pole motor design improvements requires detailed 3-D FEA, in addition to analytic relationships, as the flux path in this motor is 3-D, saturation is likely to occur due to flux concentration in the claw-pole root [see Fig. 2.2(b)], and leakage effects are significant. Moreover, the accurate determination of the cogging torque waveform typically requires the finite-element method [33].[2]

[2] As discussed in Subsection 1.2.3, experimental cogging torque investigations are also necessary to verify the simulations since manufacturing influences and parameter uncertainties can significantly alter the cogging torque waveform.

Therefore, the proposed cogging torque reduction measures are applied to a finite-element model of the single-phase BLDC claw-pole motor to study their effects on the most important motor performance parameters.

Used Finite-Element Models

The software utilized in this thesis for the FEA is the JMAG Designer® from JSOL Corporation [91] (versions 16, 17, and 18). The models are implemented using both JMAG's geometry editor and Autodesk® Inventor®.

The finite-element model of the *Baseline* (see Figs. 2.1 and 2.2) for the electromagnetic analysis is shown in Fig. 3.1. A typical mesh used for the no-load simulations

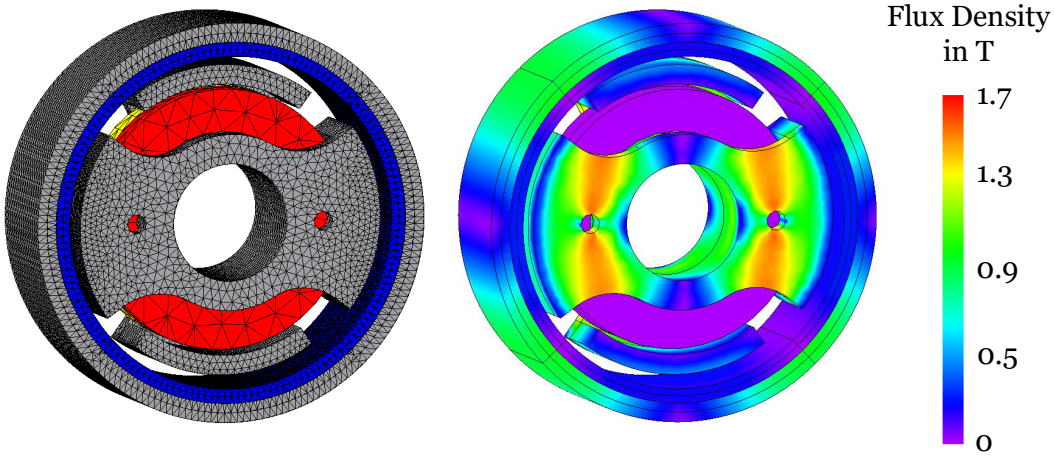

Fig. 3.1: 3-D finite-element model of the *Baseline*: (a) illustration of mesh and (b) no-load flux density contour plot for centered poles; visualized with JMAG® [91].

is illustrated in Fig. 3.1(a). The average number of elements is about 1,000,000 and the average number of nodes amounts to roughly 270,000. Depending on the type of analysis (e.g., eddy current, cogging torque, and back-EMF analyses) the mesh size is decreased or increased where needed, eddy current analyses requiring a very fine mesh. The mesh in the air-gap consists of five layers and the ring magnet is modeled specifying a linear decay of the magnetization as illustrated in Fig. P.2. The nodal force method is used to calculate the torque acting on magnetic materials. The rotor motion is specified in the rotation condition and the bifilar winding is modeled using FEM coils.[3] Voltage probes are used to determine the back-EMF in

[3]The FEM coil condition links the modeled coil with the electrical circuit, assuming a uniform

the no-load condition. For the load simulations, the electrical equivalent circuit from Fig. 2.3 is emulated. Fig. 3.1(b) depicts a no-load flux density contour plot of the *Baseline* claw-pole motor for centered poles. No-load simulations typically take up to 12 hours, load simulations up to 24 hours [Intel®Core™ i7-4790 CPU, 3.60 GHz, 4 cores, 32 GB memory, SMP[4]: 4].

Fig. 3.2 illustrates the finite-element model of the *Baseline* used for the thermal investigations. Thermal FEA is chosen over computational fluid dynamics (CFD) because the FEA models are already available from the electromagnetic analyses.

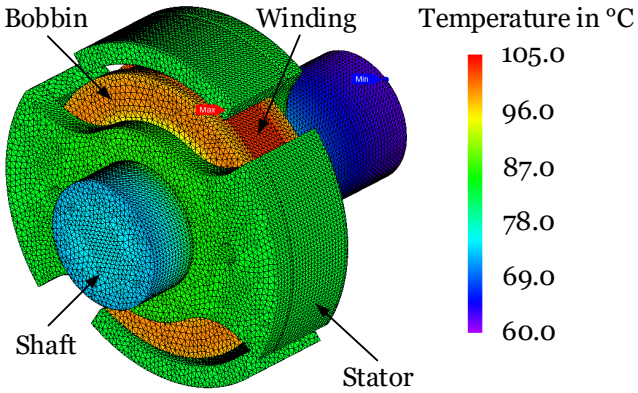

Fig. 3.2: Illustration of the mesh of the thermal finite-element model of the *Baseline*; visualized with JMAG® [91].

Heat transfer boundary conditions are set on the contact faces of the parts of the model, including the analysis model surroundings for which a reference temperature is preset. For the sake of simplicity, the heat transfer coefficients are generally assumed constant, i.e., temperature-invariant, in the simulations.[5]

As opposed to the electromagnetic finite-element model shown in Fig. 3.1, a unifilar winding (with the electrical resistance R) on a bobbin is supplied with different constant currents I_{DC}, leading to the dissipated power P_{Cu}. The related transient temperature rise and steady-state overtemperature of the winding ΔT are observed for different ambient temperatures T_A.

current distribution.

[4]JMAG Designer® allows for symmetric multiple processing (SMP), requiring multiple licenses.

[5]Selected measurement results have been used to adapt the heat transfer coefficient to the model surroundings, accounting for the convection effects. As a tradeoff, it is set to 30 W/m^2/K. The measurements at elevated ambient temperatures are performed to investigate to what extent this assumption holds true.

Remark: The FEA presented in Part II are multiply verified experimentally, showing very good congruity. Hence, those simulation results presented in this thesis, which are not verified experimentally, still provide for a high level of confidence.

3.2 Experimental Techniques

This section presents the experimental techniques utilized in this thesis to verify selected results of the FEA and used analytic relationships. Therefore, different prototype stators are manufactured and various investigations with a rheometer are performed to study the cogging torque,[6] hysteresis torque, iron losses, and axial forces. Moreover, the back-EMF and radial forces are measured using different test benches. In addition, thermal investigations are performed using a climate chamber.

3.2.1 Manufactured Prototype Stators

In accordance with the developed finite-element models, prototypes are built and tested to verify selected simulation results. Illustratively, Figs. 3.3(a) and (b) show prototypes of the *Baseline* claw-pole motor and the salient-pole motor. Due to eco-

(a) (b)

Fig. 3.3: Manufactured prototypes: (a) claw-pole stator and (b) salient-pole stator.

nomic reasons, the claw-pole stator parts are milled from free-cutting steel 11SM-

[6]The cogging torque has also been measured using a static approach as discussed in Appendix K. However, the static cogging torque measurement is inaccurate and hence unsuitable. Consequently, the torque measurements in this thesis are performed with the rheometer.

nPb37 instead of punching and subsequent deep-drawing steel sheets.[7] The salient-pole stator, which is solely used in Chapter 9, is realized with a 250-35A lamination stack [149]. The prototypes of the different claw-pole motors are depicted in Part II, in the respective sections about the experimental results.

3.2.2 Rheometer-Based Measurements

As rheometer-based investigations of electric machine characteristics (such as cogging torque, hysteresis torque, and iron losses) are unconventional, the used methodology is discussed in great detail below. After a short introduction to rheology, this subsection describes the used rheometer setup and elaborates upon the torque measurements with the rheometer.[8]

Introduction to Rheology

Rheology studies the flow and deformation behavior of viscoelastic materials [150]–[151]. Hence, rheometers are often used to determine the viscosity of fluids (e.g., water, milk, oil, ketchup, shampoo) and the elasticity of solids (e.g., gel, plastic, wood, metals), respectively. In electrical engineering, rheology is typically used in the electronics industry to study the behavior of pastes (e.g., solder, conductive, thick film), adhesives (e.g., surface mounted devices), and coatings (e.g., insulation, protection) [150].

The shear stress τ_s (in Pa) and the shear rate $\dot{\gamma}_s$ (in s^{-1}) are central to rheology, having the following relationship [151]:

$$\tau_s = \eta_v \, \dot{\gamma}_s, \tag{3.4}$$

where η_v is the dynamic viscosity (in $Pa \cdot s$). As a result, (3.4) allows for two different operating modes [150, 152]:

- controlled shear stress (CSS) and
- controlled shear rate (CSR).

For the cogging torque, hysteresis torque, and iron loss measurements performed with the rheometer, the CSR operating mode must be utilized, where the shear rate

[7] The used free-cutting steel 11SMnPb37 has similar magnetic characteristics as, e.g., a non-annealed DC03 steel, often used for deep-drawn steel components.

[8] Additional information on the torque and run-out accuracy can be found in Appendix L.

$\dot{\gamma}_s$ (or the rotational speed n) is the input and the shear stress τ_s (or the torque T, which is the quantity to be determined) is the output.[9]

Fig. 3.4 shows a block diagram of the measuring principle to perform CSR tests on the motor under test (MUT). Generally, the controller's input is the desired rotational

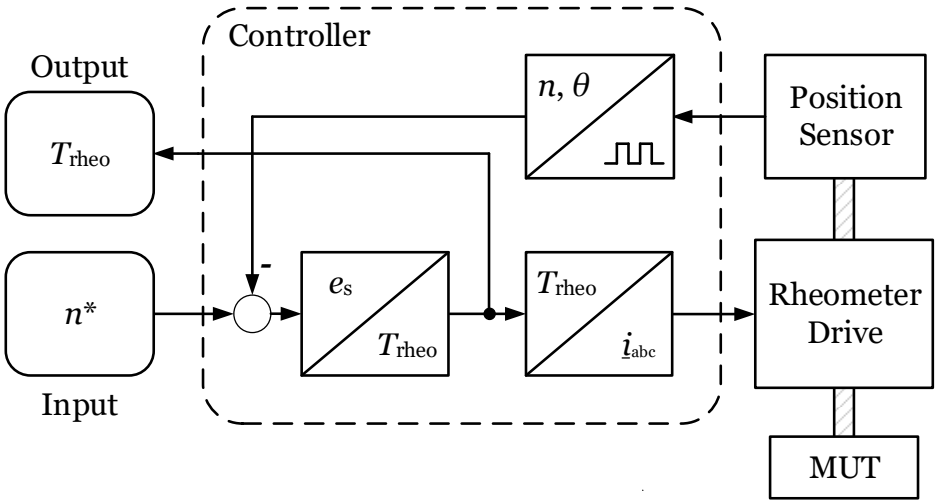

Fig. 3.4: Closed loop control of the rotational speed n for the controlled shear rate (CSR) measurement with the rheometer, as presented in [150].

speed n^* and the controller's output is the measured torque T_{rheo}. In a closed loop, the controller regulates the phase current system $\underline{i}_{abc}$ supplied to the electric motor of the rheometer drive, generating the torque T_{rheo}, such that the desired rotational speed n^* is maintained.[10] The position sensor is an incremental encoder whose signal is converted into a rotational speed n. In the CSR measurements, the parameter e_s is the speed control error, see Fig. 3.4.

Modified Rheometer Test Setup

Fig. 3.5(a) illustrates a typical rotational test on a liquid sample sandwiched between a lower stationary part and an upper rotary part to determine the necessary driving force to perform the preset rotation or oscillation.[11] Fig. 3.5(b) shows the adapted

[9] For the CSS operating mode, the input and output quantities are exchanged; hence, it is not suitable for torque investigations.

[10] See Appendix L for a discussion of the speed constancy.

[11] Possible configurations include capillary, coaxial cylinders, cone plate, parallel plate, or concentric spheres [153].

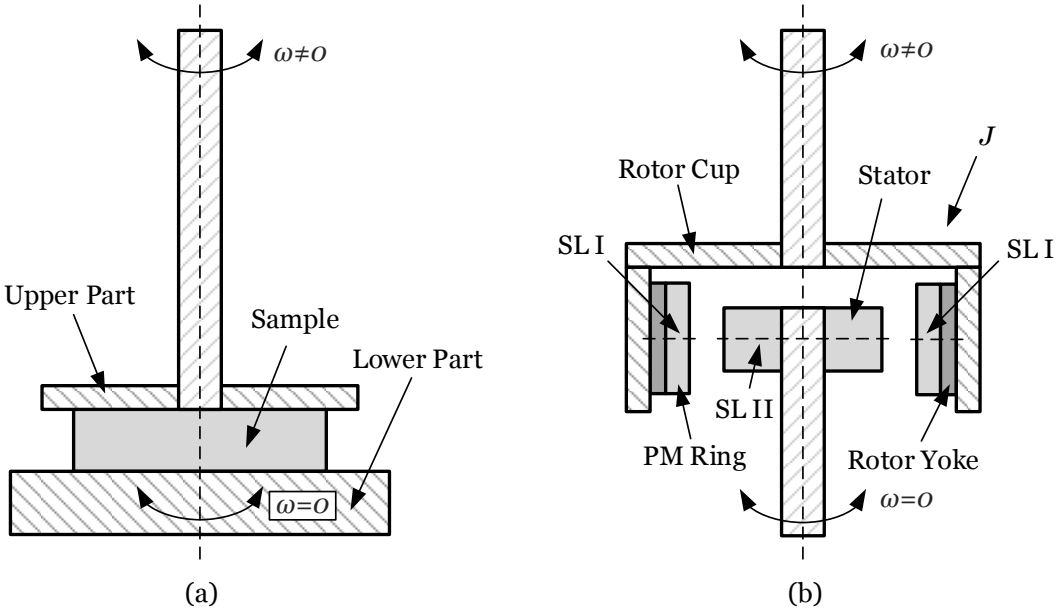

Fig. 3.5: (a) conventional rotational shear test on a sample with a rheometer and (b) adaptation of the setup to measure the cogging torque, hysteresis torque, and iron losses of SFHP outer-rotor motors.

setup to measure the cogging torque, hysteresis torque, and iron losses of SFHP outer-rotor motors,[12] e.g., the studied claw-pole and salient-pole motors exhibited in Fig. 2.11. Therefore, a rotor cup (which holds the PM ring and the rotor yoke) is attached to the upper rotary part ($\omega \neq 0$) of the rheometer, while the stator is fixed to the lower stationary part ($\omega = 0$); both are positioned coaxially with no shaft connection as depicted in Fig. 3.5(b). Hence, the described arrangement is non-contact, eliminating the influence of bearing friction of the MUT. The total inertia of the rotary part is denoted as J; SL I and SL II are the symmetry lines of the rotor and stator, respectively.

Fig. 3.6 shows the experimental rheometer test setup to measure the cogging torque, hysteresis torque, and the iron losses of SFHP PM motors. The rheometer MCR502 WESP from Anton Paar GmbH [152] is used to perform the measurements. It features an ultra-high resolution optical incremental encoder with an angular resolution of $< 10\,\text{nrad}$ and the torque resolution is $0.05\,\text{nN}\cdot\text{m}$. The measuring drive of the rheometer has a torque accuracy of $\pm 0.5\,\%$ with respect to the measured value

[12] The measuring method is not limited to outer-rotor motors, it can easily be applied to inner-rotor topologies as well.

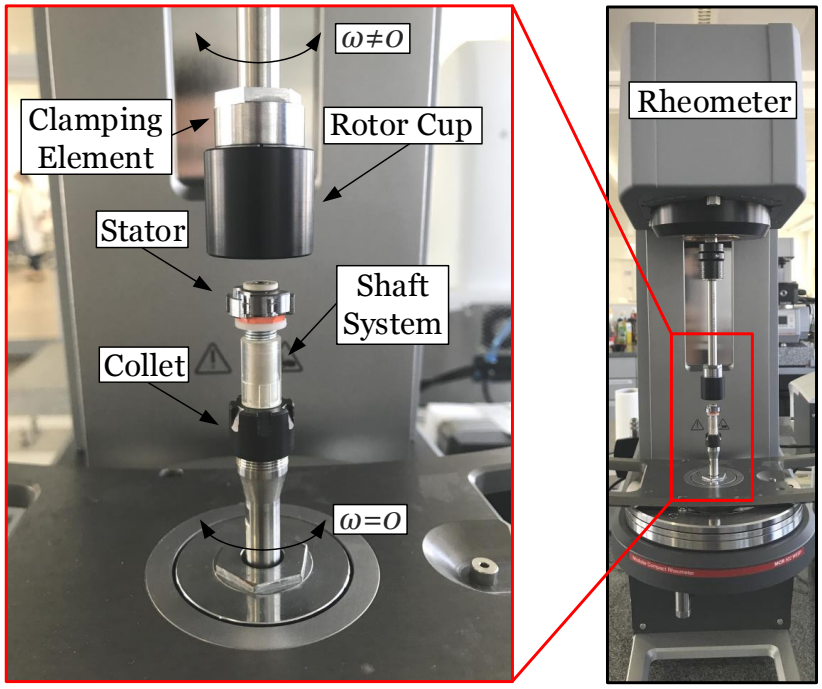

Fig. 3.6: Experimental rheometer test setup to measure the cogging torque, hysteresis torque, and iron losses of SFHP PM motors.

(but maximum $\pm 0.2\,\mu\mathrm{N}\cdot\mathrm{m}$) and the maximum rotational speed of the rheometer is 3000 rpm.[13] The rheometer features both axial and radial air bearings to practically eliminate the influence of bearing friction. The axial air bearing also features a capacitive force sensor which is utilized to capture axial forces. The electric motor driving the rheometer is a three-phase axial flux PM synchronous machine with an air-gap winding to avoid any cogging torque. This allows for an extremely accurate motion control.

As illustrated in Fig. 3.6, a clamping element attaches the rotor cup to the rotating shaft of the rheometer. The stator sits on a stationary shaft system fixed by a collet. Prior to the actual measurements, an automatic motor adjustment routine of the rheometer drive is performed to compensate for the residual friction of the air bearings and possible external magnetic fields which might interfere with the actual measurement. Then, for the measurements, the rotor and the stator need to be aligned such that their symmetry lines, SL I and SL II, coincide [see Fig. 3.5(b)]; this

[13] Rotational speeds up to 6000 rpm are possible using a dual rheometer, in which the lower part is also rotatable but operated into the opposite direction at 3000 rpm. Then, the relative speed between the upper and lower parts is 6000 rpm.

position is called magnetic symmetry in which no axial forces are acting on the rotor and stator, respectively. To this aim, the rotor is slowly pulled over the stator[14] until the axial force sensor, integrated in the axial air bearing of the rheometer, indicates zero force into the axial direction.

Generally, the following motion equation applies to the rheometer test setup depicted in Fig. 3.6:

$$J\frac{d\omega}{dt} = T_{\text{rheo}} - T_{\text{fric}} - T_{\text{c}} - T_{\text{hys}} - T_{\text{eddy}} - T_{\text{wind}}, \tag{3.5}$$

where J is the inertia of the rotating part of the measuring system [i.e., PM ring, rotor yoke, rotor cup, clamping element, and rotary system of the rheometer, see Fig. 3.5(b)], ω is the angular frequency ($\omega = 2\pi n/60$), T_{rheo} is the torque measured by the rheometer (see Fig. 3.4), T_{fric} is the friction torque, T_{c} is the cogging torque, T_{hys} is the hysteresis torque, T_{eddy} is the eddy current torque, and T_{wind} represents the windage torque.

Rheometer Measurement Techniques

At constant rotational speed n, the inertia related torque component $J\frac{d\omega}{dt}$ in (3.5) vanishes. (The validity of the assumption of constant speed is discussed in Appendix L.) Correspondingly, Fig. 3.7 illustrates a generic waveform of the measured no-load torque in the clockwise (CW) direction, identifying the different torque components to be expected in a PM motor, for constant rotational speed. Besides the cogging

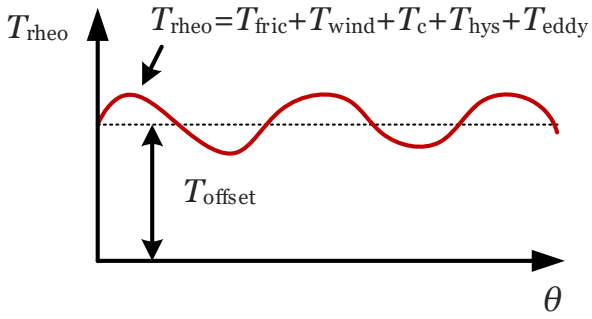

Fig. 3.7: Generic measured no-load torque waveform identifying the torque components to be expected in a PM motor, for constant rotational speed.

[14]The rotating shaft of the rheometer can be moved in the axial direction by means of a built-in stepper motor.

torque T_c, four parasitic torque components are distinguished between as mentioned previously:

1. Friction torque T_{fric},
2. Windage torque T_{wind},
3. Hysteresis torque T_{hys}, and
4. Eddy current torque T_{eddy};

all of which generally counteract the enforced rotation of the PM rotor somewhat. Other than the cogging torque, these parasitic torques can cause an offset T_{offset} in the measured torque, see Fig. 3.7. (Performing the measurement in the counter clockwise (CCW) direction, T_{offset} is negative.)

For the used rheometer test setup, T_{fric} can be neglected because 1) the rotor-stator arrangement is non-contact [see Figs. 3.5(b) and 3.6], 2) the utilized rheometer encompasses both axial and radial air bearings,[15] and 3) the residual friction is compensated for in an automatic motor adjustment routine of the rheometer drive prior to the measurement. The windage torque T_{wind} is also negligible for the studied motors and speeds. (See the estimation provided in Appendix M.)

Finally, for the no-load torque measurements performed with the rheometer at constant speed, (3.5) reduces to the following central equation:

$$T_{\text{rheo}} = T_c + T_{\text{hys}} + T_{\text{eddy}}. \tag{3.6}$$

Based on (3.6), the following two subsections show how the cogging torque, the hysteresis torque, and the iron losses of SFHP motors can be measured with the rheometer.

3.2.3 Cogging Torque and Hysteresis Torque Measurements

This subsection discusses how the cogging torque and the hysteresis torque can be extracted from the no-load torque waveforms measured, both in the CW and CCW directions using the rheometer shown in Fig. 3.6.

[15] Air bearings are known for having practically no friction. Hence, the air bearings eliminate the influence of friction of the measuring device to a large extent and also center the shaft as well as hold the rotating part. For comparison, ball bearings can exhibit friction torque of 0.05 to 0.5 mN·m [150], which clearly interferes with the torque range of interest, i.e., the sub-milli-Newton meter range.

Measurements at Low Speeds (n < 10 rpm)

For the cogging torque and hysteresis torque measurements, it is crucial to preset a very low constant rotational speed (e.g., $n = 1$ rpm) to avoid any eddy currents in the stator iron. As a result, the component T_{eddy} vanishes and (3.6) reduces to

$$T_{\text{rheo}} = T_{\text{c}} + T_{\text{hys}}, \tag{3.7}$$

where T_{hys} is the only parasitic torque component that cannot be eliminated. For illustration, Fig. 3.8 shows an exemplary no-load torque waveform of one of the proposed low cogging torque claw-pole motor designs (i.e., *Design 3* as studied in Chapter 7), measured with a rheometer at 1 rpm in the CW direction.

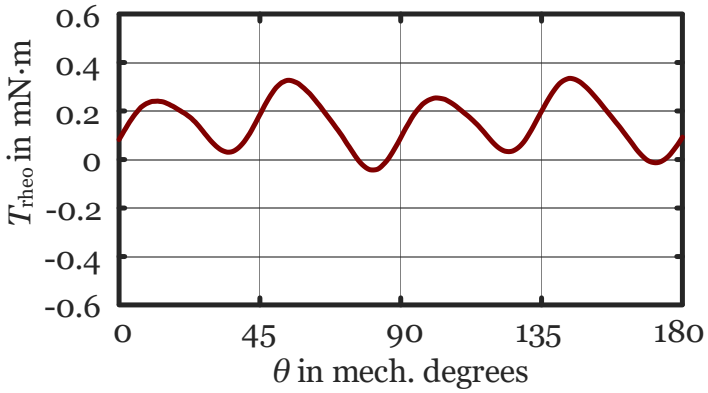

Fig. 3.8: Exemplary no-load torque waveform of a low cogging torque claw-pole motor design (*Design 3*) measured with a rheometer in the CW direction at 1 rpm.

According to (3.7), the measured no-load torque is a superposition of the cogging torque T_{c} and the hysteresis torque T_{hys} because of the very low speed. The cogging torque is inherently offset-free, see (1.16). Consequently, the observed positive offset T_{offset} in Fig. 3.8 is solely due to T_{hys} and, in fact, equals its average value $\overline{T}_{\text{hys}}$:

$$T_{\text{offset}} = \frac{1}{2\pi} \int_{\theta=0}^{\theta=2\pi} T_{\text{rheo}}\, d\theta = \overline{T}_{\text{hys}}. \tag{3.8}$$

Because of the stator slots, the hysteresis torque is not constant. Fortunately, the analyses with the rheometer not only allow determining its average value, but also its waveform: To separate the cogging torque and the hysteresis torque, measurements in the CW and CCW directions must be performed and evaluated as discussed in the following:

The cogging torque T_c can be determined by calculating pointwise the arithmetic average of the measured torque in the CW and CCW directions $T_{\text{rheo,CW}}$ and $T_{\text{rheo,CCW}}$, respectively:

$$T_c = \frac{T_{\text{rheo,CW}} + T_{\text{rheo,CCW}}}{2}. \tag{3.9}$$

Similarly, the hysteresis torque T_{hys}, which depends on the direction of rotation, can be determined as:

$$\left|T_{\text{hys}}\right| = \frac{\pm T_{\text{rheo,CW}} \mp T_{\text{rheo,CCW}}}{2}. \tag{3.10}$$

A detailed derivation of (3.9) and (3.10) based on (3.7) is provided in Appendix N. For an accurate evaluation, it is essential that the measured CW and CCW waveforms are in phase. Otherwise, the determined waveforms of T_c and T_{hys} are inaccurate. Hence, it is recommended to perform the CW and CCW measurements in a single measurement run.

3.2.4 Iron Loss Measurement

The iron losses of the prototypes are experimentally determined with the rheometer test setup exhibited in Fig. 3.6. A review of the iron loss mechanisms can be found in Subsection 1.2.4. The determination of the iron losses from the measured no-load torque waveforms and their subsequent separation into hysteresis and eddy current losses are discussed in the following:

Measurements at Elevated Speeds (n > 10 rpm)

For the iron loss determination, and hence no-load torque measurements at elevated rotational speeds, (3.6) holds true. Other than in (3.8) for constant low speeds, for constant elevated speeds, the offset of T_{rheo} consists of the average hysteresis and eddy current torque components $\overline{T}_{\text{hys}}$ and $\overline{T}_{\text{eddy}}$, respectively:

$$T_{\text{offset}} = \frac{1}{2\pi} \int_{\theta=0}^{\theta=2\pi} T_{\text{rheo}}\, d\theta = \overline{T}_{\text{hys}} + \overline{T}_{\text{eddy}}. \tag{3.11}$$

Given that T_{hys} is principally speed-invariant [see (9.2)] and T_{eddy} increases linearly with increasing speed [see (9.3)], the torque components can be separated. In fact, the

measured offset can be used to determine and separate the iron losses ($P_{\mathrm{fe}} = P_{\mathrm{offset}}$) of the motor under test for different speeds considering (9.2) and (9.3):

$$P_{\mathrm{offset}} = \omega\, T_{\mathrm{offset}} = \omega\,(\overline{T}_{\mathrm{hys}} + \overline{T}_{\mathrm{eddy}}) = \underbrace{\omega\,\sigma_{\mathrm{H}}\,\hat{B}^2\,V}_{\overline{P}_{\mathrm{hys}}} + \underbrace{\omega^2\,\sigma_{\mathrm{W}}\,\hat{B}^2 V}_{\overline{P}_{\mathrm{eddy}}}. \tag{3.12}$$

3.2.5 Axial Force Measurement

The axial forces of the manufactured prototype stator parts are investigated using the rheometer shown in Fig. 3.6. The built-in capacitive force sensor of the rheometer is used to measure the magnetic forces in the axial direction.

3.2.6 Back-EMF Measurement

The back-EMF waveforms of the manufactured prototype motors are measured using the test rig illustrated in Fig. 3.9. A slotless servomotor from Faulhaber (4490

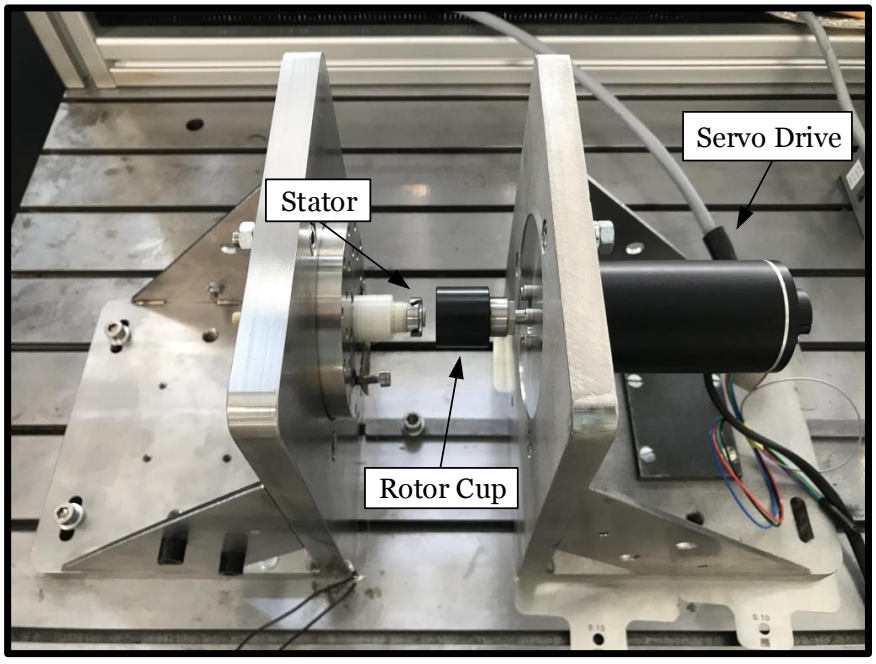

Fig. 3.9: Experimental test setup to measure the back-EMF.

H036 B) drives the rotor cup, which holds the PM ring and rotor yoke, while an HBM data recorder (Gen3i)–not shown in Fig. 3.9–is used to measure the back-EMF induced in the winding of the motor under investigation. Notice that the rotor-stator

arrangement is non-contact. For the measurements, the rotor cup is pulled over the stator by moving the right hand L-bracket.

3.2.7 Unbalanced Radial Magnetic Force Measurement

The unbalanced radial magnetic forces (URMFs) induced by an eccentricity are determined by means of a spring scale. Therefore, the static URMF measurement concept displayed in Fig. 3.10 is utilized.[16]

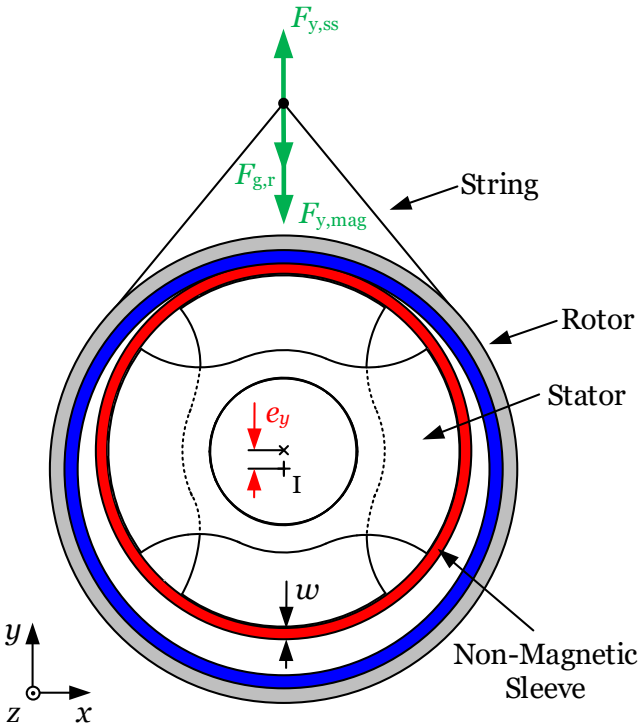

Fig. 3.10: Static URMF measurement concept.

To preset the eccentricity e_y, a non-magnetic paper sleeve of varying thickness w is placed in the air-gap δ, i.e., pulled over the stator, serving as a spacer between the fastened stator and the loose rotor. (The necessary paper sleeve thickness can be determined as $w = \delta - e_y$ for a given e_y.) From the position shown in Fig. 3.10, where one rotor pole is attracted to one stator claw-pole, the increasing spring scale force $F_{y,ss}$ is applied to the rotor into the y-direction until a deflection is achieved. The

[16] The measuring concept was inspired by the test setup presented in [154] but modified for the measurement of SFHP PM motors in which the forces are particularly small.

static URMF $F_{y,mag}$, resulting from the preset eccentricity, can then be determined as

$$F_{y,mag} = F_{y,ss} - F_{g,r}, \tag{3.13}$$

where the gravitational force on the rotor is $F_{g,r} = m_{rot}\, g$, m_{rot} is the mass of the rotor, and g is the gravitational acceleration. In accordance with Fig. 3.10, the test setup is shown in Fig. 3.11.

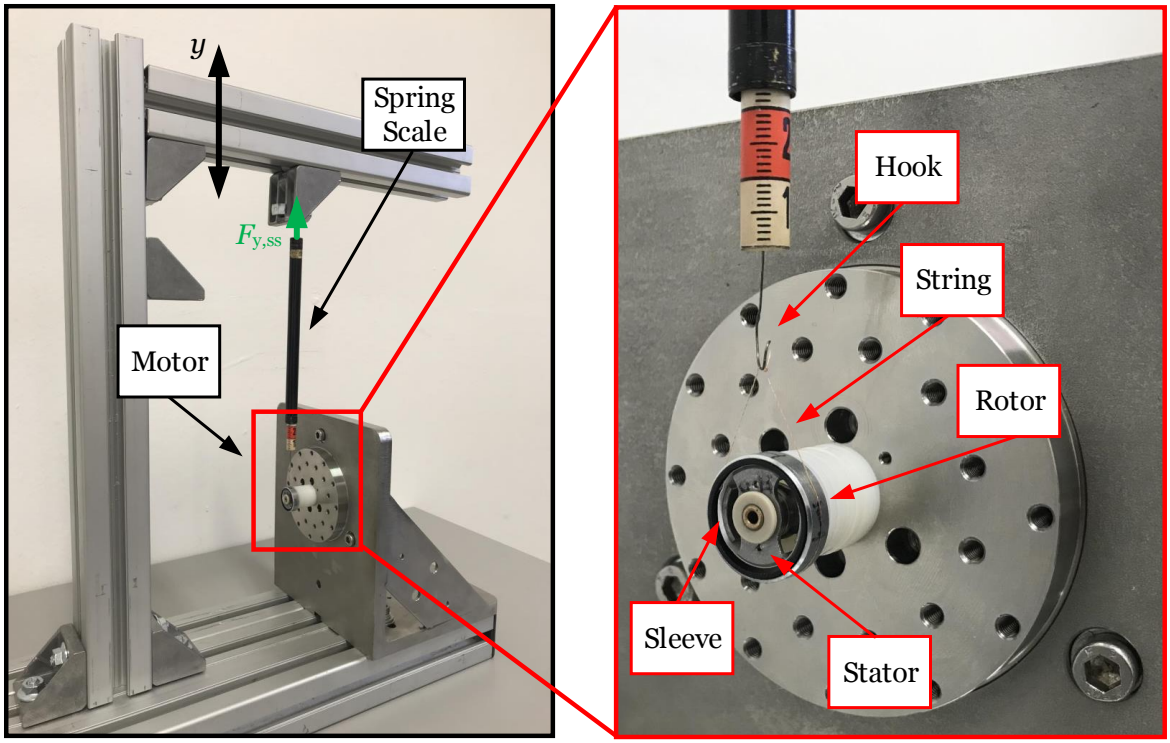

Fig. 3.11: Test setup to measure the URMF caused by static eccentricity.

3.2.8 Thermal Measurement

To study the thermal performances of the proposed claw-pole motors, various measurements in a climate chamber are performed. The schematic of the test setup is illustrated in Fig. 3.12. For the thermal investigations, the prototype claw-pole stators are equipped with a thermocouple (Type K, class 1) placed on the bottom of the coil former, over which the coil is wound. The winding is supplied from a DC source (BK Precision 9115 DC power supply) with a constant current I_{DC}, while a data recorder (HBM Gen3i) measures the input power by tracking both the input

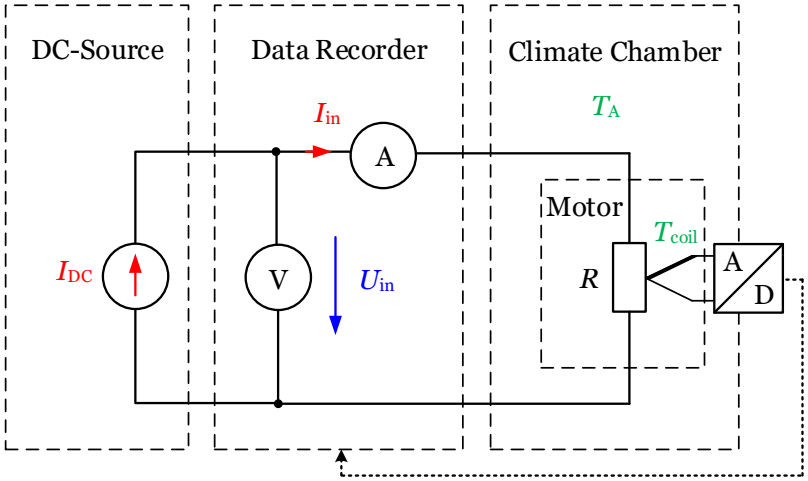

Fig. 3.12: Schematic test setup for the thermal measurements.

voltage U_{in} and the input current I_{in}, as exhibited in Fig. 3.12. While the voltage can be measured directly with the data recorder, the current is measured using a current transducer (LEM IT 65-S Ultrastab). The winding temperature T_{coil} measured with the thermocouple is evaluated by a programmable logic controller and fed into the data recorder via a CAN-bus interface.

The measurement setup is shown in Figs. 3.13(a) and (b), where the climate cham-

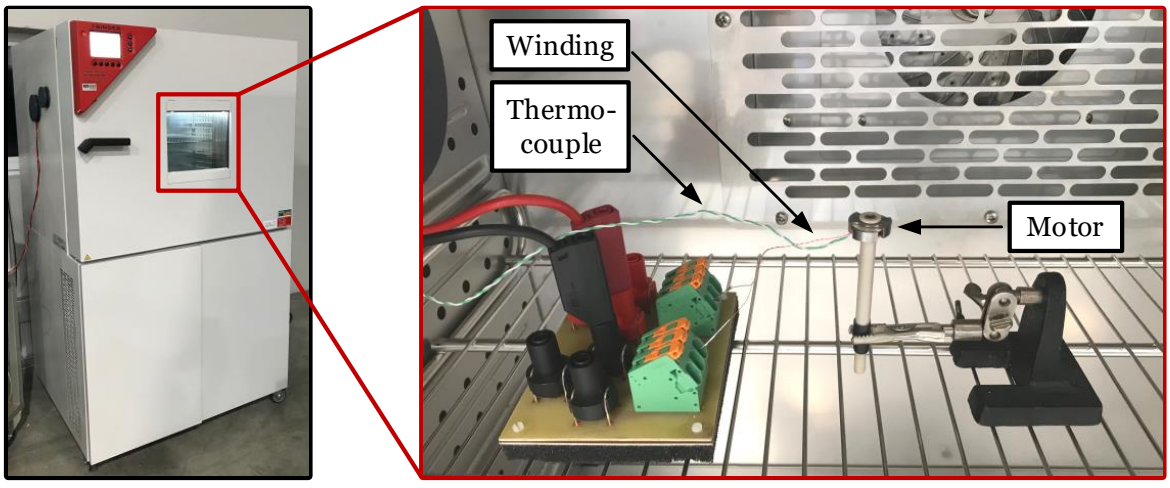

(a) (b)

Fig. 3.13: Temperature measurements: (a) climate chamber and (b) test setup.

ber (Dynamic Climate Chamber MK 115 from Binder GmbH) is used to set the

ambient temperature T_A, measured at a sufficient distance from the motor.[17]

Chapter Summary and Conclusions:

- The main modeling technique to study the proposed claw-pole motor design improvements is the 3-D FEA.
- Analytic relationships and models are used for discussion and verification of the 3-D FEA and experiments.
- The prototype claw-pole stator parts are milled from free-cutting steel.
- The main experimental technique used for verification of the 3-D FEA is the rheometer-based measurement, studying the cogging torque, hysteresis torque, iron losses, and axial forces.
- The measurements of the back-EMF, unbalanced radial magnetic forces, and the thermal characteristics are performed with different test setups.

[17] The thermocouple mounted on the bottom of the coil former is calibrated by a PT1000 temperature sensor which is used to measure the ambient temperature T_A in the proximity of the investigated stators when no current flows in the coil.

Chapter 4

Overview of the Proposed BLDC Claw-Pole Motor Designs

This chapter overviews the proposed claw-pole motor designs (i.e., Designs 0–5) and briefly discusses their characteristics and differences, respectively.[1] *While the Design 0 primarily enables the starting capability of the claw-pole motor through an asymmetric air-gap, the Designs 1–5 relate to different claw-pole designs which reduce and alter the cogging torque waveform. Although the claw-pole motor design improvements are implemented on outer-rotor variants, they can also be applied to inner-rotor types. All of the proposed design modifications can be considered at the stage of punching the steel sheets and subsequent deep-drawing thereof, to yield the desired claw-pole shapes, at no increase to the manufacturing cost.*[2]

4.1 *Design 0:* Air-Gap Asymmetry

Fig. 4.1 illustrates the *Design 0*. Based on the *Baseline* claw-pole design shown in Figs. 2.1 and 2.2, it is proposed to implemented air-gap asymmetry to facilitate the starting, see $\Delta\delta_{\text{max}}$ indicated in Fig. 4.1. As per Section 2.3, air-gap asymmetry is chosen over claw-pole asymmetry (or some other kind of magnetic circuit imbalance) because the former allows for maximum design freedom with respect to the claw-pole shape, which is important for the *Designs 1–5*. (While *Design 0* alters the air-gap of the *Baseline*, the *Designs 1–5* presented in the following alter the claw-pole shape.)[3]

[1] A profound discussion of the *Designs 0–5* is provided in Part II.

[2] Selected material of this chapter have also been published in [61, 130–132, 141, 142].

[3] Eventually, implementing the *Baseline* with any of the *Designs 1–5*, *Design 0* must be implemented as well for starting capability.

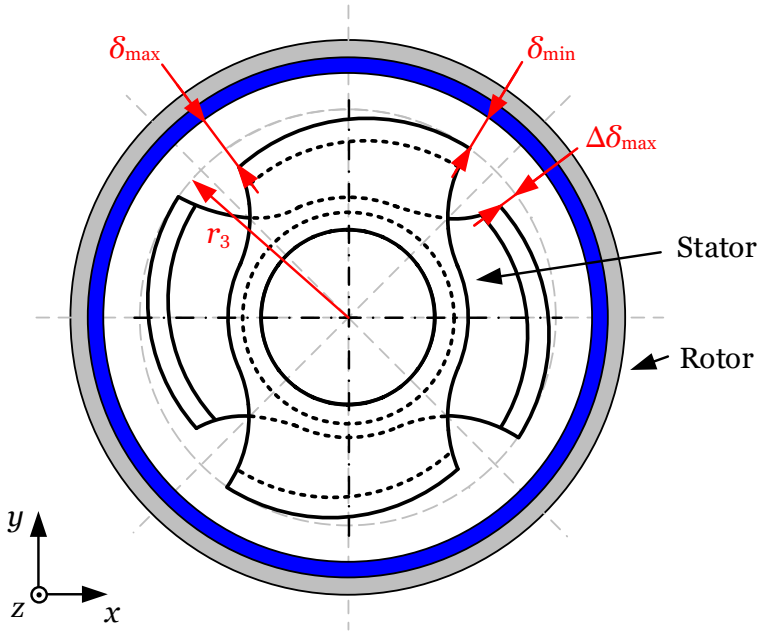

Fig. 4.1: Schematic illustration of *Design 0* which, when compared with the *Baseline*, features air-gap asymmetry $\Delta\delta_{rel}$.

Air-gap asymmetry is defined as $\Delta\delta_{max} = \delta_{max} - \delta_{min}$, where δ_{min} and δ_{max} are the minimum and maximum air-gap lengths, see Fig. 4.1. The implementation of air-gap asymmetry and its effects on the cogging torque, back-EMF, output torque, and radial forces are studied in Chapter 5. For comparability, the relative air-gap asymmetry $\Delta\delta_{rel}$, which is based on the outer stator radius r_3 shown in Fig. 4.1, is used in the analysis: $\Delta\delta_{rel} = \frac{\Delta\delta_{max}}{r_3}$. The finite-element models and prototypes in which air-gap asymmetry is implemented, i.e., *Design 0*, are denoted as *D0* with the relative air-gap asymmetry $\Delta\delta_{rel}$ in brackets, e.g., *D0(1.8%)*. [A relative air-gap asymmetry of 0 %, i.e., *D0(0%)*, is equivalent to the *Baseline*.]

4.2 *Design 1:* Single-Sided Skew

Fig. 4.2 illustrates the *Design 1*. Based on the *Baseline* claw-pole design shown in Figs. 2.1 and 2.2, it is proposed to implement a single-sided skew to the claw-poles to reduce the cogging torque. The cogging torque decreases with increasing skewing

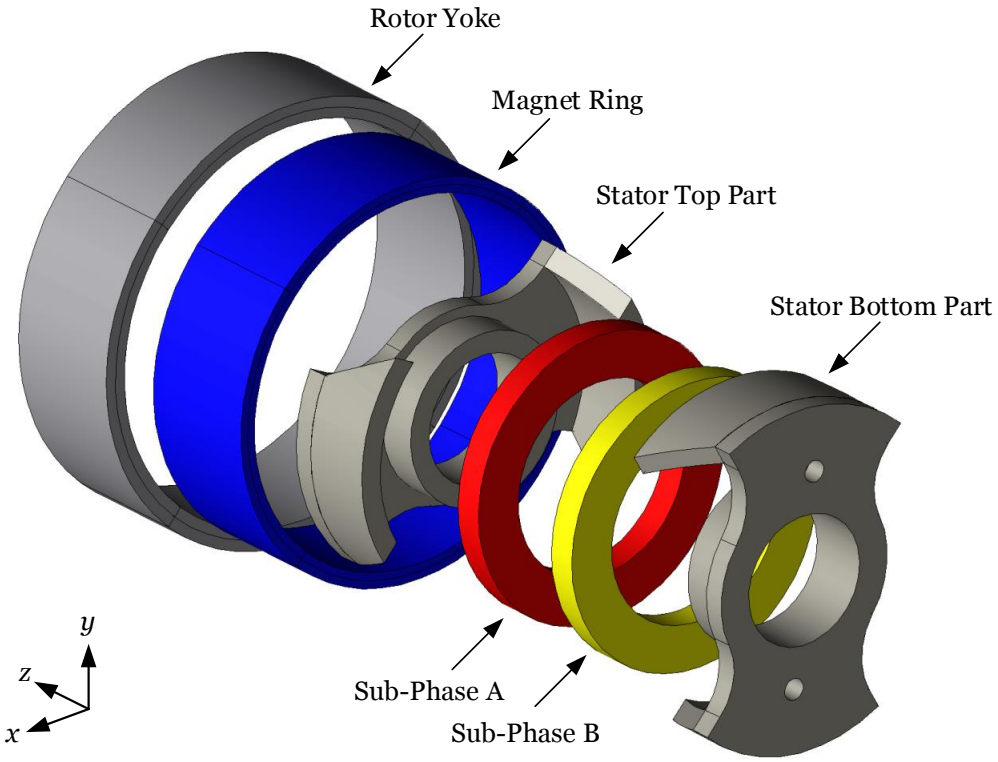

Fig. 4.2: 3-D exploded view of *Design 1* which features claw-poles with a single-sided skew; visualized with JMAG® [91].

angle ξ_{skew}, as does the back-EMF.[4] The implementation of a single-sided skew and its effects are studied in Chapter 6. Finite-element models and prototypes in which a single-sided skew, i.e., *Design 1*, is implemented are generally denoted as *D1* with the skewing angle ξ_{skew} in brackets, e.g., *D1(30°)*. A combined design consisting of, e.g., the *Design 0* with $\Delta\delta_{\text{rel}} = 1.8\,\%$ and the *Design 1* with $\xi_{\text{skew}} = 30°$, is denoted as *D01(1.8%,30°)*.

4.3 *Design 2:* Auxiliary Slots

Fig. 4.3 illustrates the *Design 2*. Based on the *Baseline* claw-pole design shown in Figs. 2.1 and 2.2, it is proposed to implement the claw-poles with auxiliary slots to modulate the frequency of the cogging torque. (In further consequence, auxiliary slots can enhance the effect of skewing to a large extent because the optimal skewing

[4] As discussed in the context of *Design 4* and *Design 5*, a single-sided skew induces axial forces proportional to the output torque T_{o}, the extent of which increases with increasing ξ_{skew}.

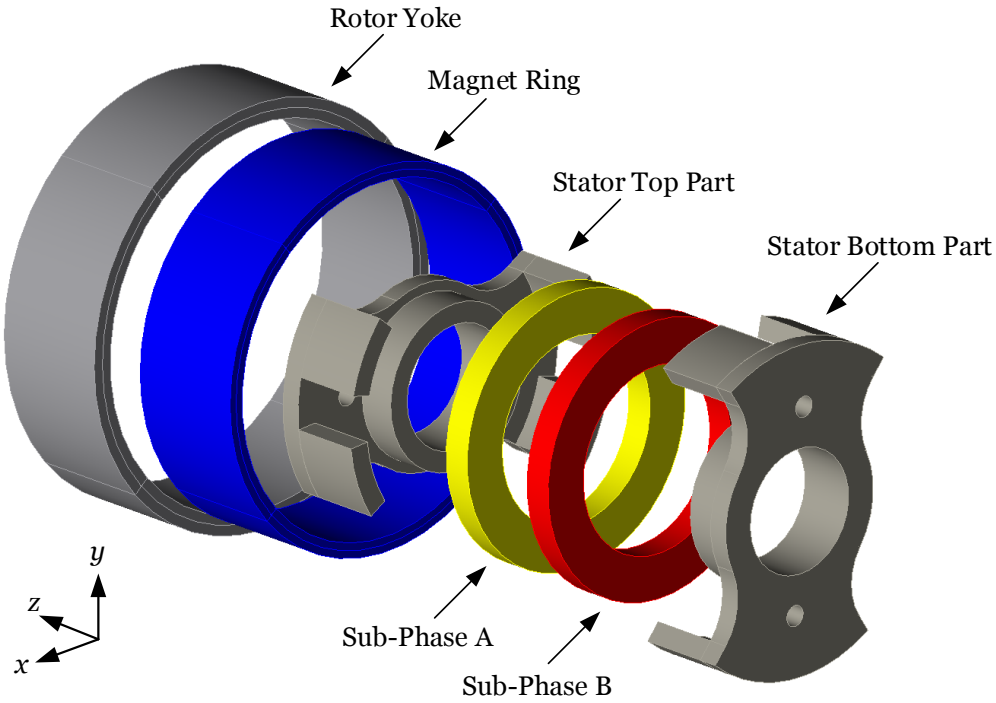

Fig. 4.3: 3-D exploded view of *Design 2* which features claw-poles with auxiliary slots; visualized with JMAG® [91].

angle can be reduced, see *Design 3* in Section 4.4.) For modulation, the auxiliary slots are most effective when they are identical to the actual slots, see Section 7.1. However, due to the auxiliary slots, the PM flux per pole $\Phi_{p,PM}$ and, as a result, the back-EMF are reduced. For proper cogging torque modulation, the number of auxiliary slots generally depends on the slot-pole combination which is discussed, along with their implementation and the resulting effects, in Chapter 7. Finite-element models and prototypes in which auxiliary slots, i.e., *Design 2*, are implemented are denoted as *D2*. A combined design consisting of, e.g., the *Design 0* with $\Delta\delta_{rel} = 1.8\,\%$ and the *Design 2*, is denoted as *D02(1.8%)*.[5]

4.4 *Design 3:* Single-Sided Skew with Auxiliary Slots

Fig. 4.4 illustrates the *Design 3*, which is a combination of *Design 1* and *Design 2*. Thereby, the cogging torque frequency is modulated due to the auxiliary slots which

[5] In the designs presented in this thesis which feature auxiliary slots, the auxiliary slots are always designed to be identical to the actual slots for an effective modulation of the cogging torque.

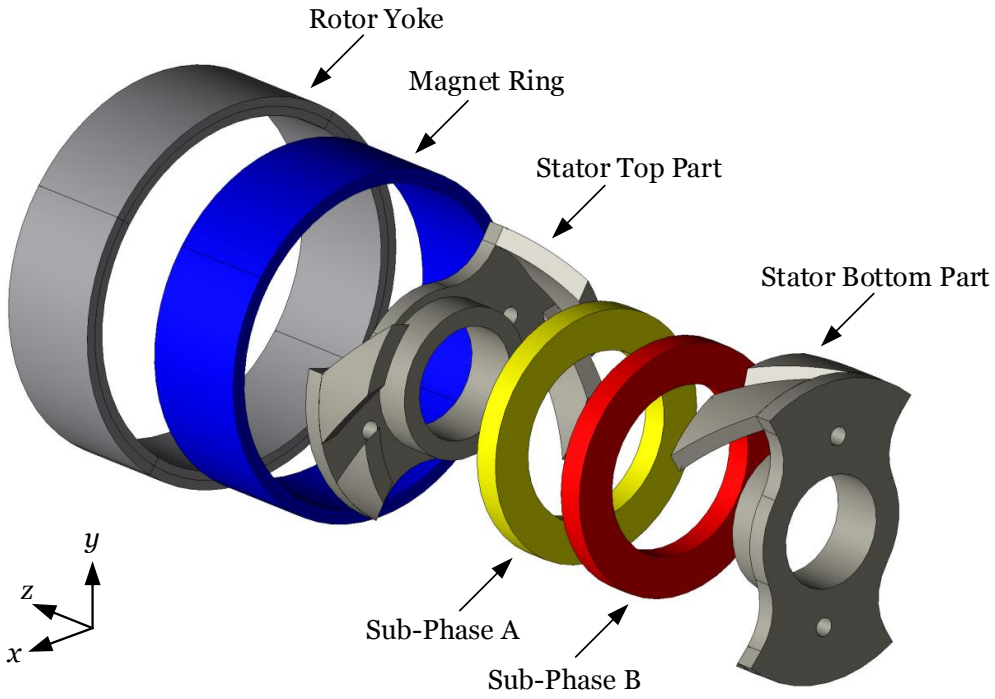

Fig. 4.4: 3-D exploded view of *Design 3* which features claw-poles with a single-sided skew and auxiliary slots; visualized with JMAG® [91].

makes the implemented skew much more effective in reducing the cogging torque.[6] The realization of a single-sided skew with auxiliary slots and its effects are studied in Chapter 7. Finite-element models and prototypes in which a single-sided skew with auxiliary slots, i.e., *Design 3*, is implemented are denoted as *D3*. A combined design consisting of, e.g., the *Design 0* with $\Delta\delta_{\text{rel}} = 1.8\,\%$ and the *Design 3* with $\xi_{\text{skew}} = 45°$, is denoted as *D03(1.8%,45°)*.

4.5 *Design 4:* V-Skew

Fig. 4.5 illustrates the *Design 4* which is a further development of *Design 1*. It features V-skewed claw-poles in which positive and negative skewing angles ξ_{skew} are realized halfway through the axial length of the motor. Thereby, the axial forces induced by the skewing are balanced. The implementation of a V-skew and its effects

Hence, specific labeling as to details of the auxiliary slots is omitted.

[6] As discussed in the context of *Design 4* and *Design 5*, a single-sided skew induces axial forces proportional to the output torque T_{o}, the extent of which increases with increasing ξ_{skew}.

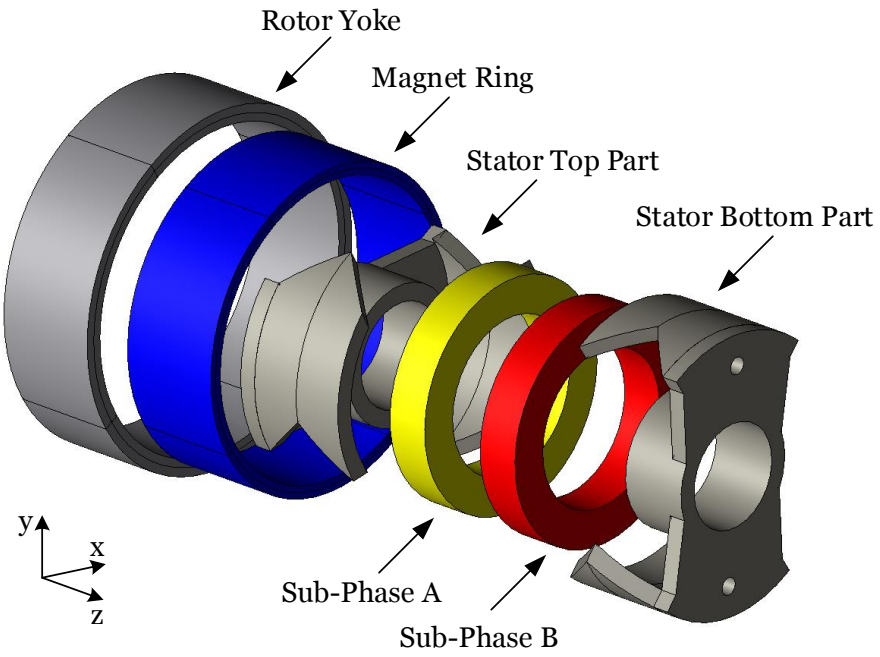

Fig. 4.5: 3-D exploded view of *Design 4* which features claw-poles with a V-skew; visualized with JMAG® [91].

are studied in Chapter 8. Finite-element models and prototypes in which a V-skew, i.e., *Design 4* with, e.g., $\xi_{\text{skew}} = 30°$, is implemented are denoted as *D4(30°)*.

4.6 *Design 5:* V-Skew with Auxiliary Slots

Fig. 4.6 illustrates *Design 5*, which is a combination of *Design 2* and *Design 4*. Thereby, the cogging torque is both modulated and reduced but, at the same time, the axial forces are balanced. The implementation of a V-skew with auxiliary slots and its effects are studied in Chapter 8. Finite-element models and prototypes in which a V-skew with auxiliary slots, i.e., *Design 5*, is implemented, e.g., with $\xi_{\text{skew}} = 30°$, are denoted as *D5(30°)*.

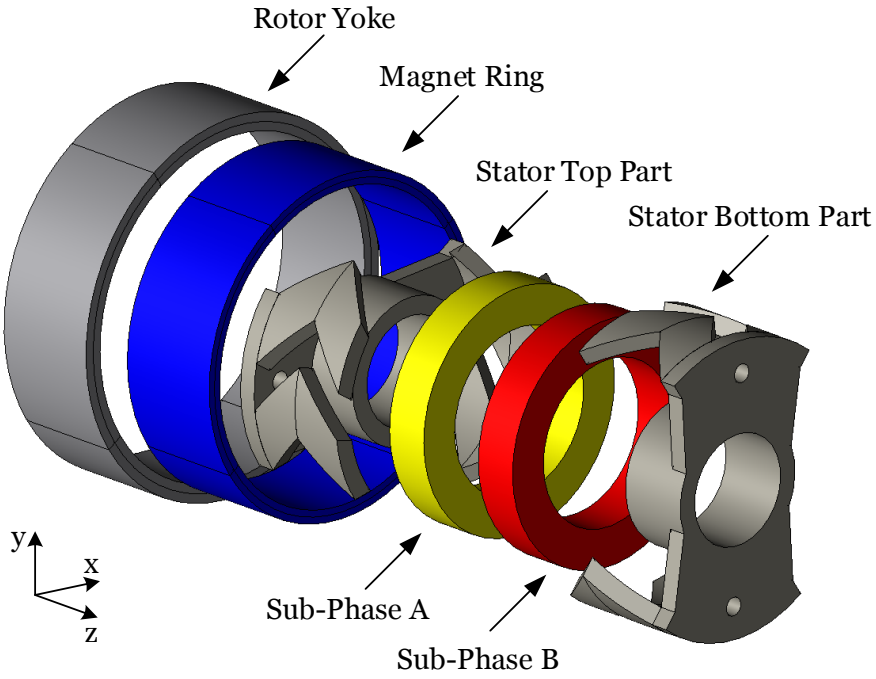

Fig. 4.6: 3-D exploded view of *Design 5* which features claw-poles with a V-skew and auxiliary slots; visualized with JMAG® [91].

Chapter Summary and Conclusions:

- The proposed single-phase BLDC claw-pole motor designs, i.e., *Designs 0–5*, can be implemented at no increase to the manufacturing cost.
- The asymmetric air-gap in *Design 0* facilitates the starting.
- The single-sided skew in *Design 1* reduces the cogging torque.
- The auxiliary slots in *Design 2* can modulate the cogging torque.
- The single-sided skew combined with auxiliary slots in *Design 3* can modulate and reduce the cogging torque.
- The V-skew in *Design 4* can reduce the cogging torque and balance the axial magnetic forces.
- The V-skew combined with auxiliary slots in *Design 5* can modulate and reduce the cogging torque, and balance the axial magnetic forces.

Part II

The Proposed BLDC Claw-Pole Motor Designs

Overview of Studied Designs

CLAW-POLE DESIGN[7]	EXPANSION
Baseline, *Baseline**	baseline design with straight claws
D0	design with air-gap asymmetry ($\Delta\delta_{\text{rel}}$)
D1	design with a single-sided skew (ξ_{skew})
D2	design with auxiliary slots ($w_{\text{aux,slot}}$)
D3	design with auxiliary slots ($w_{\text{aux,slot}}$) and a single-sided skew (ξ_{skew})
D4	design with a V-skew ($\pm\xi_{\text{skew}}$)
D5	design with auxiliary slots ($w_{\text{aux,slot}}$) and a V-skew ($\pm\xi_{\text{skew}}$)
D0(1.8%)	*D0* with $\Delta\delta_{\text{rel}} = 1.8\,\%$
D0(4.2%)	*D0* with $\Delta\delta_{\text{rel}} = 4.2\,\%$
D0(7.7%)	*D0* with $\Delta\delta_{\text{rel}} = 7.7\,\%$
D0(12.5%)	*D0* with $\Delta\delta_{\text{rel}} = 12.5\,\%$
D01(1.8%,30°)	*D0* and *D1* with $\Delta\delta_{\text{rel}} = 1.8\,\%$ and $\xi_{\text{skew}} = 30°$
D02(1.8%)	*D0* and *D2* with $\Delta\delta_{\text{rel}} = 1.8\,\%$ and $w_{\text{aux,slot}} = \delta_{\text{claw}}$
D03(1.8%,45°)	*D0* and *D3* with $\Delta\delta_{\text{rel}} = 1.8\,\%$, $w_{\text{aux,slot}} = \delta_{\text{claw}}$, and $\xi_{\text{skew}} = 45°$
D1(30°), *D1*(30°)*	*D1* with $\xi_{\text{skew}} = 30°$
D1(45°)*	*D1* with $\xi_{\text{skew}} = 45°$
D3(45°)	*D3* with $w_{\text{aux,slot}} = \delta_{\text{claw}}$ and $\xi_{\text{skew}} = 45°$
D4(30°)*	*D4* with $\xi_{\text{skew}} = \pm 30°$
D4(45°)*	*D4* with $\xi_{\text{skew}} = \pm 45°$
D5(30°)*	*D5* with $w_{\text{aux,slot}} = \delta_{\text{claw}}$ and $\xi_{\text{skew}} = \pm 30°$
D5(45°)*	*D5* with $w_{\text{aux,slot}} = \delta_{\text{claw}}$ and $\xi_{\text{skew}} = \pm 45°$
D5(55°)*	*D5* with $w_{\text{aux,slot}} = \delta_{\text{claw}}$ and $\xi_{\text{skew}} = \pm 55°$

[7] In the designs marked with "*", the axial stator length $l_{\text{ax,s}}$ is 8 mm instead of 5.8 mm.

SALIENT-POLE DESIGN	**EXPANSION**
S0(2.8%)	design with $\Delta\delta_{\text{rel}} = 2.8\,\%$

Overview of Analyses

Table 4.3: Overview of Analyses – I.

Design	Analysis	Location
Baseline	cogging or no-load torque	Sections 5.4, 7.6, 8.6, and 9.1
	back-EMF	Sections 5.5, 7.7, and 8.7
	phase current	Section 5.6 and Appendix B
	output torque	Sections 5.6 and 6.6
	radial magnetic forces	Section 5.7 and Appendix O
	air-gap flux density	Appendix R
	phase inductance	Appendix S
	leakage	Appendix S
	iron losses	Sections 7.10 and 9.2
	thermal performance	Section 7.12
	axial forces	Section 8.8
	hysteresis torque	Section 9.1
	air-gap permeance	Appendix E
D0	cogging or no-load torque	Sections 5.4, 6.4, and 9.1 and Appendix K
	back-EMF	Sections 5.5 and 6.5
	phase current	Sections 5.6 and 7.11
	output torque	Sections 5.6, 6.6, and 7.11
	radial magnetic forces	Section 5.7
	iron losses	Section 9.2
	efficiency	Section 7.11
	phase resistance	Appendix F
	hysteresis torque	Section 9.1
	air-gap permeance	Appendix E

Table 4.4: Overview of Analyses – II.

Design	Analysis	Location
D1	cogging or no-load torque	Sections 6.4 and 8.6 and Appendix K
	back-EMF	Sections 6.5 and 8.7
	output torque	Section 6.6
	axial forces	Section 8.8
D2	cogging or no-load torque	Section 7.6
	back-EMF	Section 7.7
	phase current	Section 7.11
	output torque	Section 7.11
	air-gap flux density	Appendix R
	phase inductance	Appendix S
	leakage	Appendix S
	iron losses	Section 7.10
	efficiency	Section 7.11
	thermal performance	Section 7.12
D3	cogging or no-load torque	Section 7.6
	back-EMF	Section 7.7
	phase current	Section 7.11
	output torque	Section 7.11
	air-gap flux density	Appendix R
	phase inductance	Appendix S
	leakage	Appendix S
	iron losses	Section 7.10
	efficiency	Section 7.11
	thermal performance	Section 7.12
D4	cogging torque	Section 8.6
	back-EMF	Section 8.7
	axial forces	Section 8.8
D5	cogging torque	Section 8.6
	back-EMF	Section 8.7
	axial forces	Section 8.8
S0	cogging or no-load torque	Section 9.1
	hysteresis torque	Section 9.1
	iron losses	Section 9.2

Chapter 5

Air-Gap Asymmetry (*D0*)

This chapter discusses air-gap asymmetry and its application to the Baseline claw-pole motor. It is shown how air-gap asymmetry can be implemented in the punching layout of the claw-pole stator parts at no increase to the manufacturing cost. The effects of the asymmetric air-gap are then studied mostly through 3-D finite-element simulations for the example case claw-pole motor, the performance specifications and system parameters of which are presented in Tables A.1 and A.2.[1]

5.1 Air-Gap Asymmetry – Principle

The single-phase BLDC claw-pole motor is implemented with air-gap asymmetry to facilitate the starting. As per Section 2.3, air-gap asymmetry is chosen over claw-pole asymmetry (or some other kind of magnetic circuit imbalance) because air-gap asymmetry allows for maximum design freedom with respect to the shape of the claw-pole, which is important for the *Designs 1–5*. The principle of air-gap asymmetry is discussed in detail in Sections 2.3 and 4.1.

5.2 Air-Gap Asymmetry – Steel Sheet Punching Layout

The following shows how to account for an asymmetric air-gap in the steel sheet punching layout of the claw-pole motor. Given the *Baseline* punching layout in Fig. 2.5(a), Fig. 5.1(a) shows how to realize air-gap asymmetry, where d_{asym} is the necessary x-axis displacement to implement a certain air-gap asymmetry and r'_3 is an auxiliary radius. Points I′ and III′ indicate the altered points of interest defined in

[1] Selected results of this chapter have also been published in [61, 130, 141].

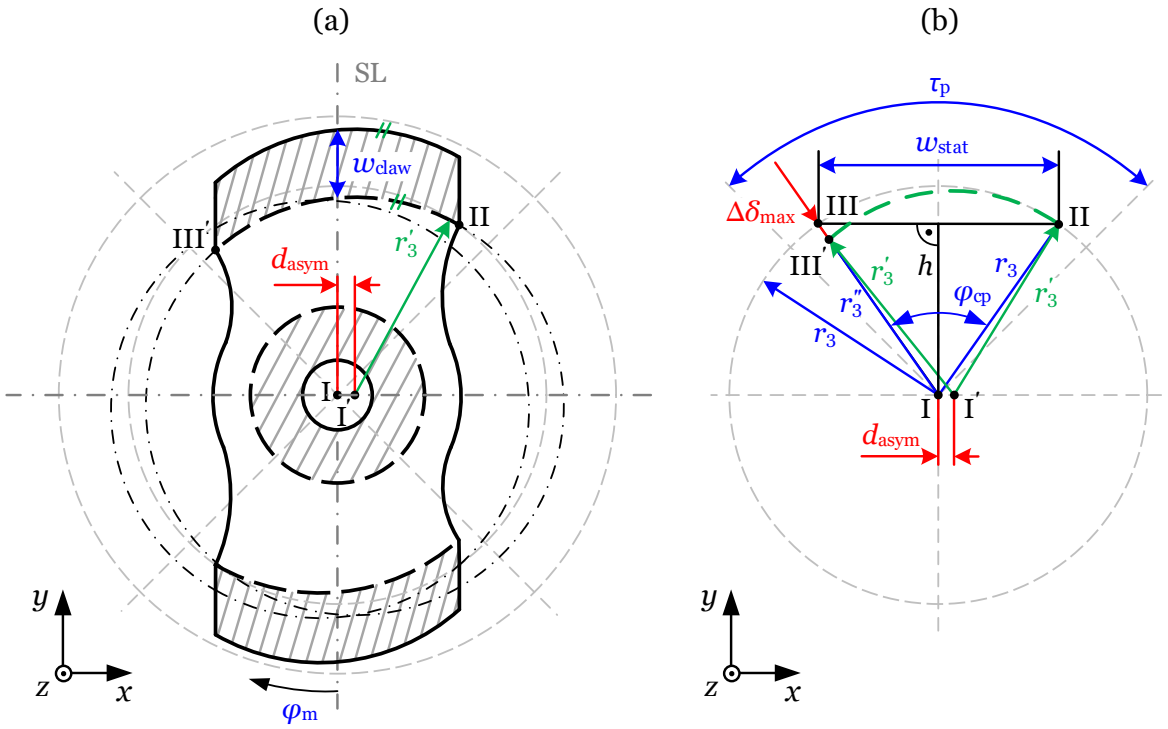

Fig. 5.1: (a) steel sheet punching layout for the realization of air-gap asymmetry (*Design 0*) and (b) definition of the geometric parameters.

Fig. 2.5(a). SL is the symmetry line and the parameters indicated in Fig. 5.1(a) have origin, i.e., point I, symmetry. Fig. 5.1(b) offers a more detailed view of the upper claw-pole in Fig. 5.1(a), showing the geometric parameters.

As per Section 2.3 and shown in Fig. 4.1, the characteristic parameter of the air-gap asymmetry is the widening of the air-gap $\Delta\delta_{\max}$, as shown in Fig. 5.1(b):

$$\Delta\delta_{\max} = r_3 - r_3''. \tag{5.1}$$

To implement $\Delta\delta_{\max}$ for the given parameters r_3 and φ_{cp}, the x-axis displacement d_{asym} [see Figs. 5.1(a) and (b)] can be calculated utilizing trigonometric identities:

$$d_{\mathrm{asym}} = \frac{r_3''^2 - h^2 - \frac{w_{\mathrm{stat}}^2}{4}}{2\,r_3'' \cos\left(\frac{\varphi_{\mathrm{cp}}}{2} + 90^\circ\right) - w_{\mathrm{stat}}}, \tag{5.2}$$

where

$$h = r_3 \cos\left(\frac{\varphi_{\mathrm{cp}}}{2}\right), \tag{5.3a}$$

$$r_3'' = r_3 - \Delta\delta_{\max}, \tag{5.3b}$$

$$w_{\mathrm{stat}} = 2\,r_3 \sin\left(\frac{\varphi_{\mathrm{cp}}}{2}\right). \tag{5.3c}$$

A step-by-step derivation of (5.2) is presented in Appendix G.

Remark 1: Although necessary in single-phase BLDC motors to enable the starting, an asymmetric air-gap acts essentially as an enlarged effective air-gap ($\delta_{\text{eff}} \approx \delta + \frac{\Delta\delta_{\text{max}}}{2}$), increasing the air-gap reluctance, see (D.1). Thereby, the PM flux per pole $\Phi_{\text{p,PM}}$ is reduced for the same PM, as is the average output torque $\overline{T}_{\text{o}}$ when the same phase current is supplied. The air-gap permeance variation for symmetric and asymmetric air-gaps is discussed in Appendix E.

Remark 2: Implementing an asymmetric air-gap, the stator top and bottom parts shown in Fig. 2.1 must be manufactured with mirror-symmetry, requiring two different punching dies. The same holds true for a claw-pole motor implemented with asymmetric claw-poles instead of an asymmetric air-gap, as shown in Fig. 2.7(a).

5.3 Finite-Element Models

To study the effects of the air-gap asymmetry, finite-element models, in which different values of $\Delta\delta_{\text{max}}$ are implemented, are developed. As mentioned in Section 4.1, the relative air-gap asymmetry $\Delta\delta_{\text{rel}} = \frac{\Delta\delta_{\text{max}}}{r_3}$ is used for comparability, where $r_3 = 8\,\text{mm}$ for all designs. Illustratively, Fig. 5.2 contrasts two finite-element models with widely differing values of $\Delta\delta_{\text{rel}}$, i.e., *D0(1.8%)* and *D0(12.5%)*.

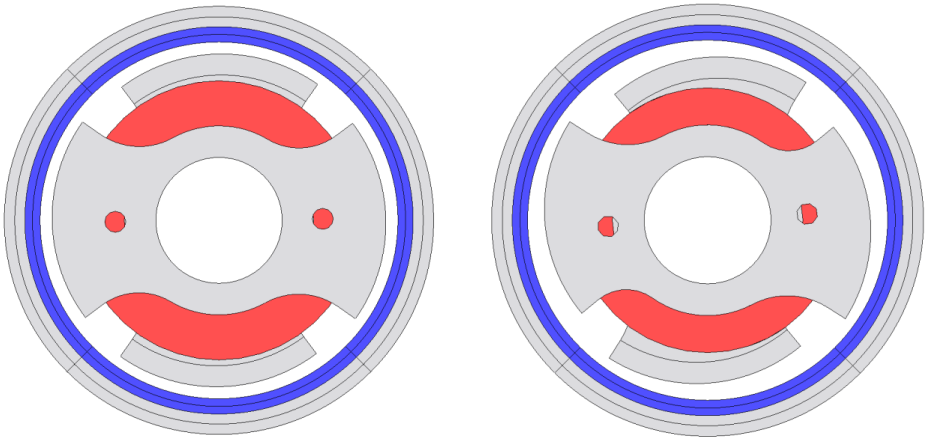

(a) *D0(1.8%)* (b) *D0(12.5%)*

Fig. 5.2: Finite-element models to study the effect of air-gap asymmetry (*Design 0*); visualized with JMAG® [91].

Remark: Comparing Figs. 5.2(a) and (b), it is evident that increasing $\Delta\delta_{\text{rel}}$ reduces the room for the winding. This is discussed in detail in Appendix F.

5.4 Analysis of the Cogging Torque

Starting from the *Baseline*, which has a symmetric air-gap and hence a symmetric cogging torque waveform, Fig. 5.3 shows the change in the cogging torque waveform for increasing air-gap asymmetry, see *D0(1.8%)–D0(12.5%)*. The air-gap asymmetry

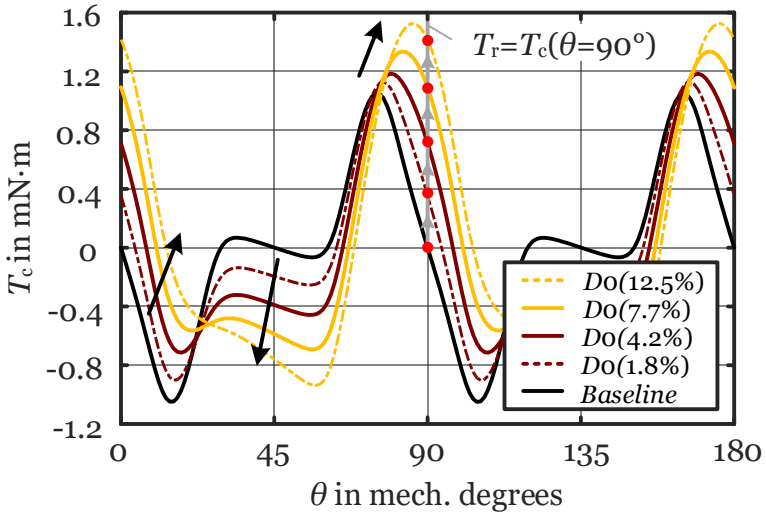

Fig. 5.3: Change in the calculated cogging torque waveform for increasing air-gap asymmetry and determination of the resulting cogging torque at $\theta = 90°$.

affects the cogging torque waveform twofold:

1. the positive and negative half-cycles are not identical anymore, i.e., the waveform becomes asymmetric; and
2. the zero-crossings of the *Baseline* at $\theta = k \cdot 45°$ (where $k \in \mathbb{Z}$) are shifted to larger angles θ, described by the angle γ in Fig. 2.9 by which the magnetic symmetry line is shifted (MSL → MSL').

As a result:

- The zero cogging torque "plateau" of the *Baseline* at $\theta = 45°$ shifts to negative torque values for increasing $\Delta\delta_{\text{rel}}$. [See the arrow in Fig. 5.3 at $\theta \approx 45°$.]
- More importantly, the zero positions of the cogging torque of the *Baseline* at $\theta = k \cdot 90°$ (where $k \in \mathbb{Z}$) show positive resulting cogging torque at the current zero-crossing T_r for increasing $\Delta\delta_{\text{rel}}$. [See Fig. 5.3, where $T_c(\theta = 90°) = T_r$.]

Increasing $\Delta\delta_{\text{rel}}$ increases the positive peak value of the cogging torque but decreases the negative one. [See the arrows in Fig. 5.3 at $\theta \approx 10°$ and $\theta \approx 70°$.]

Fig. 5.4 shows the order analysis of selected waveforms from Fig. 5.3 [i.e., the *Baseline*, *D0(4.2%)*, *D0(12.5%)*], where k is the harmonic order. Most significantly, the cogging torque's first order harmonic component (i.e., $T_{\text{c},1}$) increases with increasing $\Delta\delta_{\text{rel}}$, while the other harmonics slightly decrease or do not change notably.

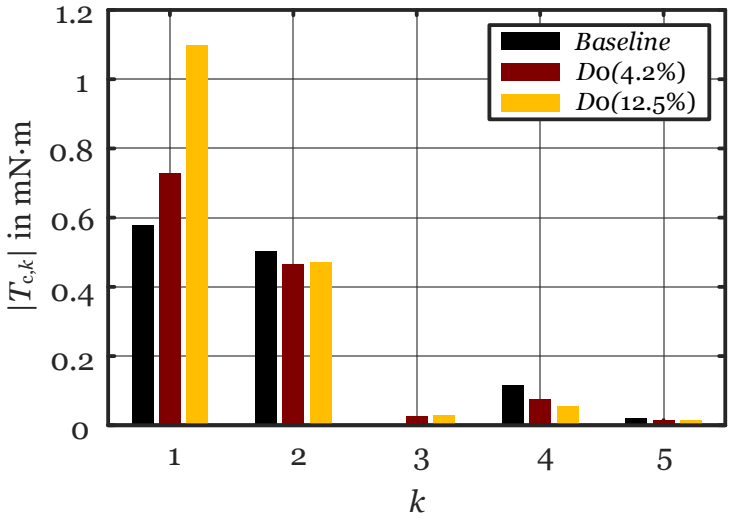

Fig. 5.4: Order analysis of three selected cogging torque waveforms from Fig. 5.3.

Remark: When relating k to the rotational frequency of the rotor, a factor of four must be considered as the cogging torque waveform repeats itself four times per rotor revolution, due to the motor's slot-pole combination. Hence, $T_{\text{c},1}$ and $T_{\text{c},2}$ correspond to fourth and eighth order harmonic components of the rotational frequency.

Fig. 5.5 shows the resulting cogging torque at the current zero-crossing T_{r} obtained from Fig. 5.3 for increasing $\Delta\delta_{\text{rel}}$. T_{r} increases non-linearly with increasing air-gap asymmetry. The change in the cogging torque waveform for increasing $\Delta\delta_{\text{rel}}$ (see Fig. 5.3) must be taken into account because the cogging torque is superposed upon the alignment torque in the load condition, forming a complex output torque waveform (see Section 5.6).

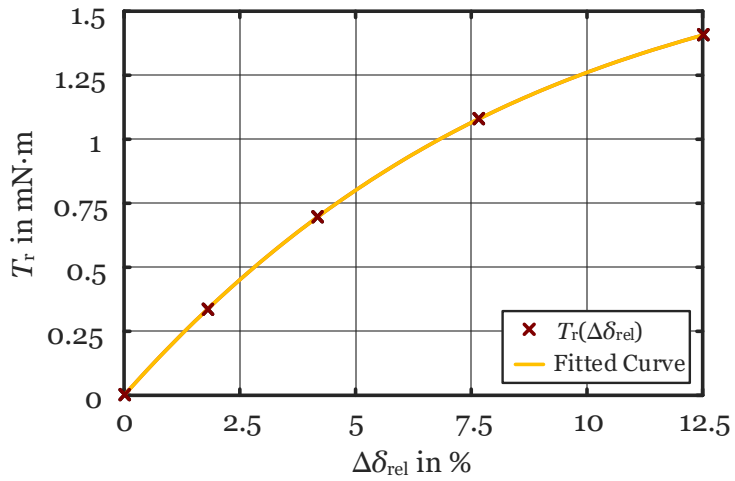

Fig. 5.5: Calculated resulting cogging torque at the current zero-crossing T_r for different values of $\Delta\delta_{rel}$.

5.5 Analysis of the Back-EMF

Starting from the *Baseline*, which has a symmetric air-gap and hence a symmetric back-EMF waveform, Fig. 5.6 depicts the change in the back-EMF waveforms for increasing air-gap asymmetry, i.e., *D0(1.8%)–D0(12.5%)*, in accordance with Fig. 5.3. Most notably, the asymmetric air-gap manifests itself in an asymmetric back-EMF

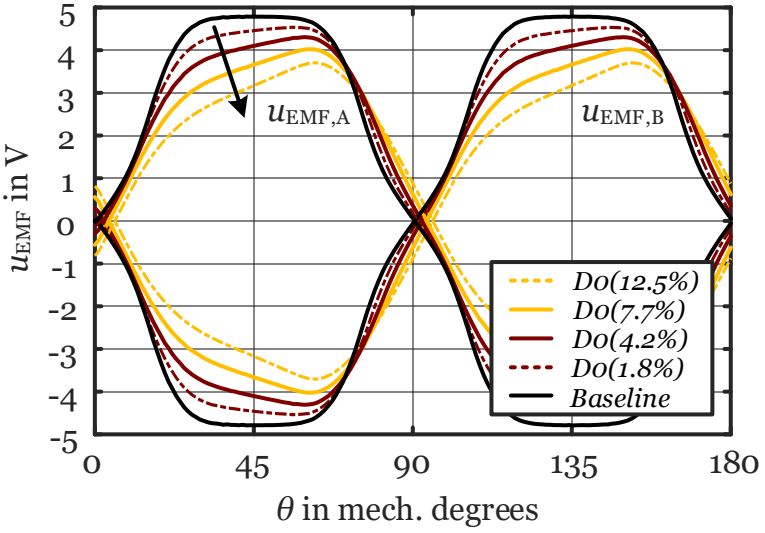

Fig. 5.6: Change in the calculated back-EMF waveforms of sub-phases A and B for increasing air-gap asymmetry at 5500 rpm.

waveform with reduced peak value.[2]

Fig. 5.7 presents the order analysis of three selected back-EMF waveforms from Fig. 5.6, i.e., the *Baseline*, *D0(4.2%)*, and *D0(12.5%)*. As expected, compared to the

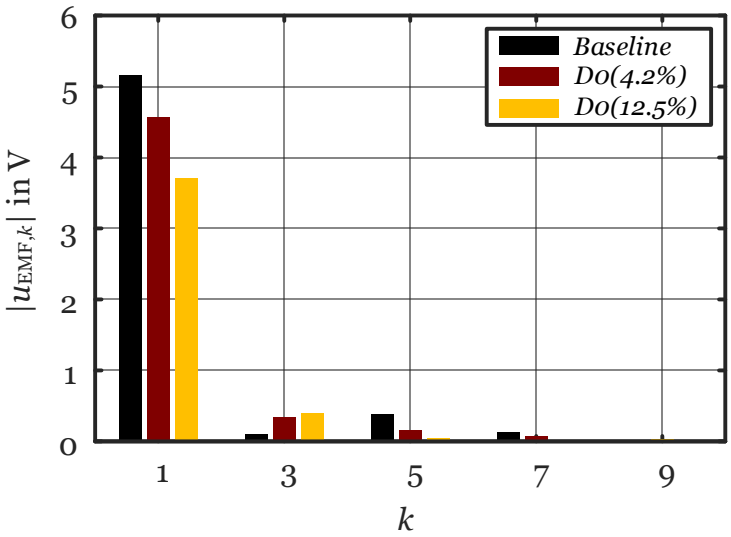

Fig. 5.7: Order analysis of three selected back-EMF waveforms from Fig. 5.6.

Baseline, $u_{EMF,1}$ and $u_{EMF,5}$ reduce in *D0(4.2%)* and *D0(12.5%)*, while $u_{EMF,3}$ increases slightly. The reduction in the back-EMF's first order harmonic component is due to the increase in the effective air-gap, causing a reduction in the PM flux per pole $\Phi_{p,PM}$, see Section 2.3. According to [136], which studies the salient-pole motor shown in Fig. 2.11(b), the asymmetric back-EMF causes a local increase in the phase current in the region of the lower back-EMF (indicated by the arrow in Fig. 5.6) when the same voltage is supplied to the winding, as studied in Section 5.6. Similar to the cogging torque waveforms, the back-EMF waveforms undergo a slight phase shift for increasing $\Delta\delta_{rel}$ (see Fig. 5.6). Therefore, to obtain smooth current waveforms and not deteriorate the torque ripple substantially, the speed-dependent commutation angles (see θ_{on} and θ_{off} in Fig. 2.4) need to be adapted when air-gap asymmetry is implemented [137].

Remark: In light of the back-EMF reduction shown in Fig. 5.6, the smallest $\Delta\delta_{rel}$ possible should be chosen. However, increasing $\Delta\delta_{rel}$ provides useful cogging torque, which can reduce the output torque ripple (see Section 5.6).

[2]Qualitatively, the change in the back-EMF, caused by the air-gap asymmetry of the claw-poles, is the same as that in the salient-pole motor shown in Fig. 2.11(b) when implemented with air-gap asymmetry, as studied, e.g., in [136].

5.6 Analysis of the Output Torque

To illustrate the usefulness of an asymmetric air-gap, the phase current and output torque waveforms of the *Baseline* and *D0(1.8%)* are presented in Figs. 5.8 and 5.9. The applied voltage is constant and the commutation angles are $\theta_{on} = 0°$ and $\theta_{off} = 80°$ for every half-wave of the back-EMF, see Fig. 2.4(b).

As shown in Fig. 5.8, due to the single-sided decrease in the back-EMF of *D0(1.8%)* illustrated in Fig. 5.6, the phase current i_p increases in the same region because of the larger difference between the supplied voltage and the back-EMF. The resulting

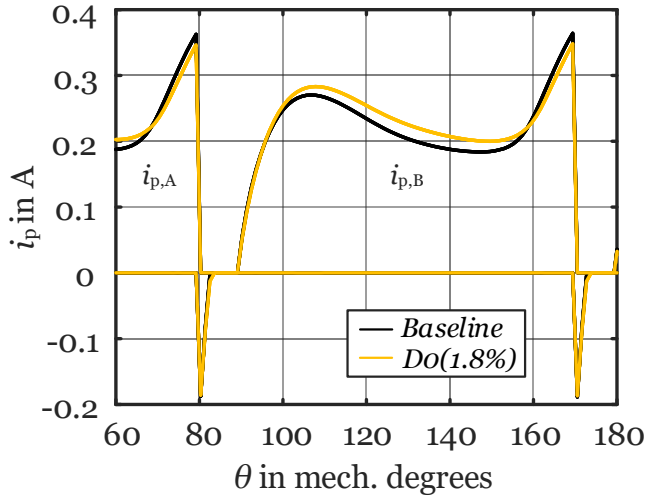

Fig. 5.8: Simulated phase current waveforms of the *Baseline* and *D0(1.8%)*.

output torque T_o is displayed in Fig. 5.9.[3] As per (1.15), the *Baseline* has an output torque ripple T_{rip} of about 106 %, because 1) the zero-crossings of the phase current and the cogging torque coincide and 2) breaking torque occurs, see the dashed circle in Fig. 5.9, since the cogging torque is larger than the torque as per (1.14) at the beginning of the commutation. Compared to the *Baseline*, the output torque ripple is significantly reduced down to about 80 % in *D0(1.8%)*. Owing to the asymmetric air-gap, the cogging torque is altered and phase-shifted, see Fig. 5.3, providing cogging torque in the region indicated by the dashed circle in Fig. 5.9. The obtained average output torques are almost the same, amounting to 1.07 mN · m for the *Baseline* and

[3] As mentioned in Subsection 1.2.1, the simulated output torque is essentially the superposition of the cogging torque and the alignment torque, where the latter is due to the currents flowing in sub-phases A and B.

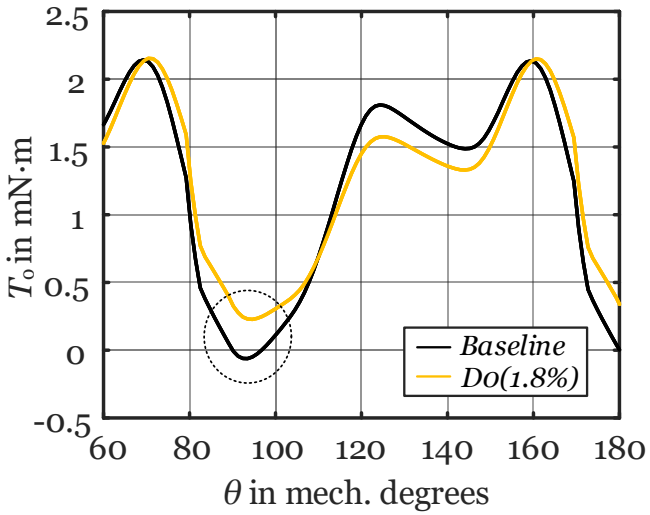

Fig. 5.9: Simulated output torque waveforms of the *Baseline* and *D0(1.8%)*.

1.096 mN · m for *D0(1.8%)*, the latter being 2.4 % higher than the former due to the slight increase in the phase current and absent breaking torque.

Notice that the asymmetric air-gap not only facilitates the starting but also reduces the output torque ripple by about 25 %. In general, the harmonics of the output torque change when air-gap asymmetry is implemented as a result of the altered cogging torque waveform.

5.7 Analysis of the Unbalanced Radial Magnetic Forces

This section studies the no-load[4] radial magnetic forces present in the *Baseline*, *D0(1.8%)*, and *D0(7.5%)* under different conditions as they can trigger resonances of the drive system or adjacent construction elements. The focus is on the formation of unbalanced radial magnetic forces (URMFs) caused by the static eccentricity e [see Fig. P.1(a)], which is studied through simulations and experiments. The maximum eccentricity considered in the following simulations is $e = 0.2\,\text{mm}$, which yields a maximum relative eccentricity ε_{max} of 0.4 for $\delta = 0.5\,\text{mm}$ according to (P.8). (Additional radial force analyses of the *Baseline* are presented in Appendix O, studying the effect of eccentricity for misaligned stator parts and different magnetization patterns, as well as non-uniform magnetization for concentric rotor-stator arrangements.)

The calculation procedure of the radial magnetic forces is discussed in Appendix P,

[4] According to [40], the armature reaction field can be neglected for the analysis of radial magnetic forces in surface-mounted PM motors.

as is the model of the magnetization with the transition angle α. The URMF amplitude caused by eccentricity is estimated analytically in Appendix I. In Appendix J, potential radial claw-pole deflection caused by the radial magnetic forces in the air-gap is studied.

Calculated URMF Caused by Eccentricity – *Baseline*

Fig. 5.10 shows both the radial and tangential air-gap flux density distributions, B_r and B_t, of the *Baseline* when $\theta = 0°$ and $\varepsilon \in [0, 0.2, 0.4]$. As expected, when the rotor-

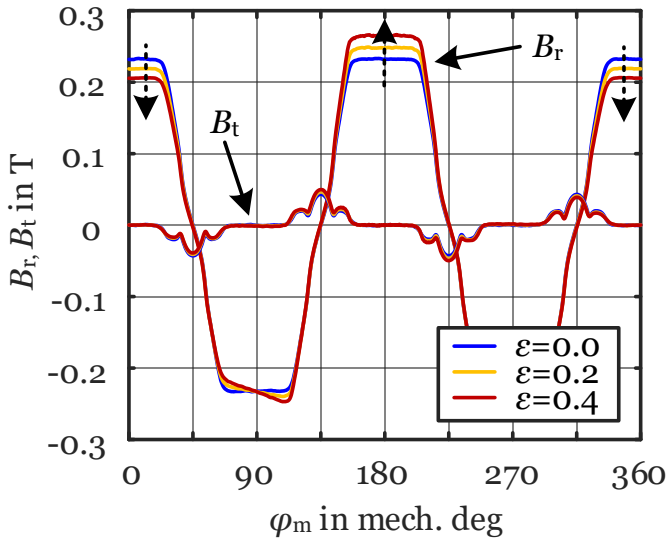

Fig. 5.10: Analysis of eccentricity for the *Baseline*: radial and tangential air-gap flux density distributions, when $\theta = 0°$ and $\alpha = 24°$.

stator arrangement is concentric (i.e., $\varepsilon = 0$), the peaks of B_r are of equal magnitude. However, for increasing eccentricity (i.e., $\varepsilon > 0$), B_r increases with decreasing air-gap and vice versa, as indicated by the dashed arrows in Fig. 5.10. (The smallest air-gap is at $\varphi_m = 180°$.) B_t, on the other hand, is rather invariant to the studied eccentricities.

Fig. 5.11 shows the corresponding local radial and tangential magnetic tractions, f_r and f_t, calculated according to (P.1)–(P.2). Similar to B_r in Fig. 5.10, f_r increases with decreasing air-gap and vice versa, indicated by the dashed arrows, while f_t changes only marginally. Since f_t determines the cogging torque [see (P.2) and (1.18)], this means that the cogging torque is hardly affected by the studied eccentricity.

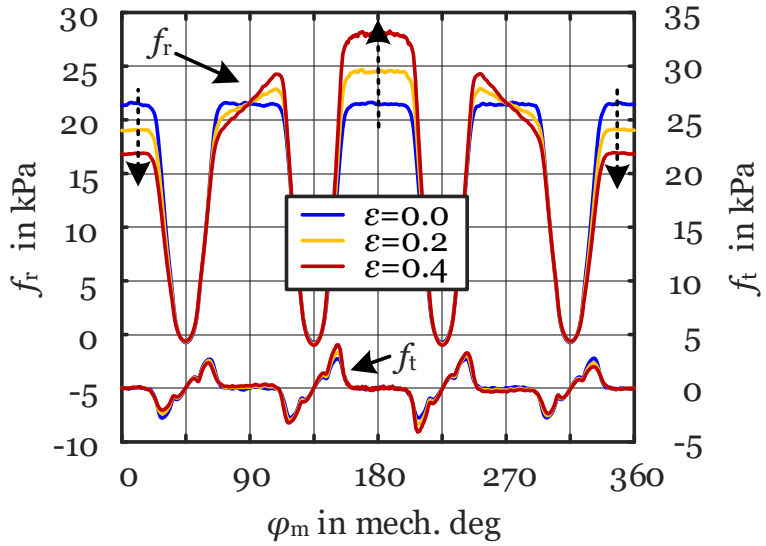

Fig. 5.11: Analysis of eccentricity for the *Baseline*: radial and tangential magnetic tractions, when $\theta = 0°$ and $\alpha = 24°$.

Figs. 5.12, 5.13, and 5.14 show the results of the URMF analysis of the *Baseline* using (P.3)–(P.7), when $\varepsilon \in [0, 0.2, 0.4]$. Fig. 5.12 shows the x- and y-components of the URMFs, while Fig. 5.13 depicts the resulting URMFs, both as functions of the rotor position θ. In Fig. 5.14, the loci of the URMFs are illustrated for the studied eccentricities.

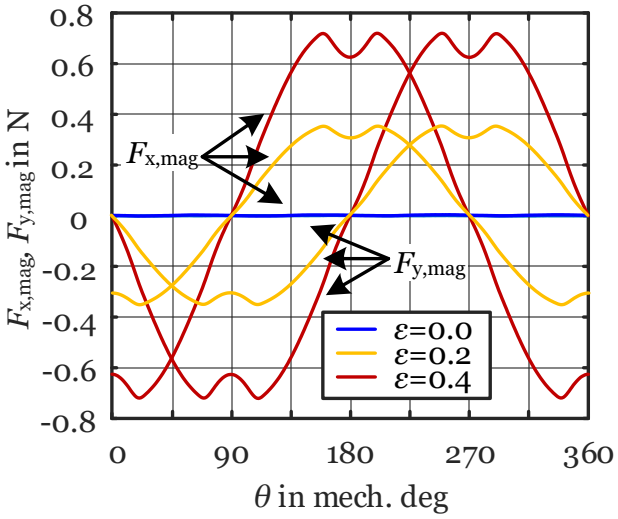

Fig. 5.12: Analysis of eccentricity for the *Baseline*: x- and y-components of the URMF as functions of θ, when $\alpha = 24°$.

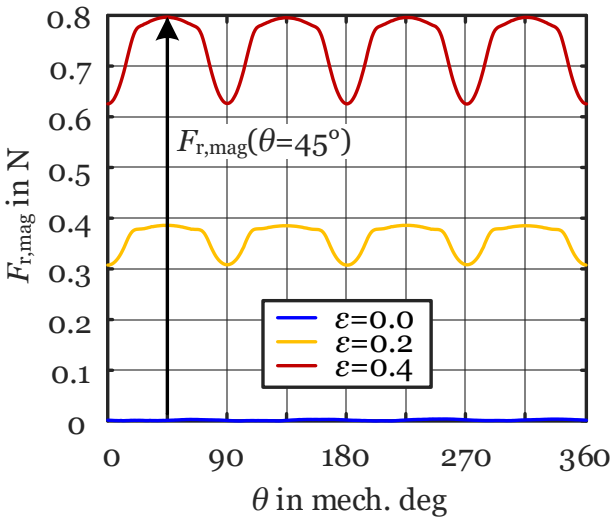

Fig. 5.13: Analysis of eccentricity for the *Baseline*: resultant URMFs as functions of θ, when $\alpha = 24°$.

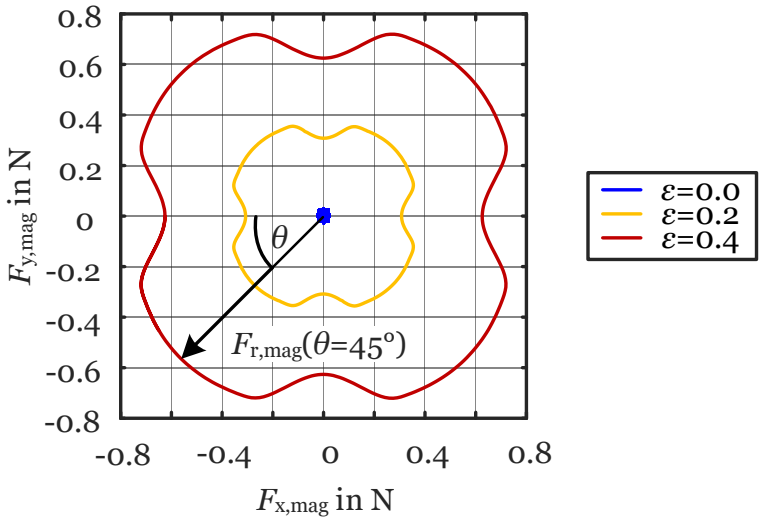

Fig. 5.14: Analysis of eccentricity for the *Baseline*: loci of URMFs, when $\alpha = 24°$.

It is evident from Figs. 5.12, 5.13, and 5.14 that the URMFs are zero when $\varepsilon = 0$. However, when $\varepsilon > 0$, the URMFs increase linearly[5] with increasing eccentricity (as described in [40]) and rotate synchronously with the rotor [37], see Fig. 5.14. For $\varepsilon = 0.4$, the URMF peak value is 0.8 N.

Despite of its symmetric structure, the calculated URMFs of the *Baseline* form a quadrupole, featuring a fourth harmonic of the rotational frequency, and not a

[5]Theoretically, the URMFs increase with the square of the eccentricity. However, for small eccentricities, their increase is approximately linear for increasing eccentricities, see Appendix I.

circular behavior as predicted in [40]. Hence, the URMFs pulsate four times per revolution ($f_{\mathrm{URMF}} = 4\,n/60$). Depending on the rotational speed, resonances of the drive system or adjacent construction elements can be triggered.

Calculated URMF Caused by Eccentricity – *D0*

For the investigations of *D0*, similar to Figs. 5.10 and 5.11, Figs. 5.15 and 5.16 show B_r and B_t as well as f_r and f_t, when $\theta = 0°$, $\varepsilon \in [0, 0.4]$, and $\Delta\delta_\mathrm{rel} \in [0, 1.8, 7.5]$ %; the dashed arrows indicate increasing $\Delta\delta_\mathrm{rel}$. For *D0(1.8%)* when $\varepsilon = 0$, both B_r and f_r

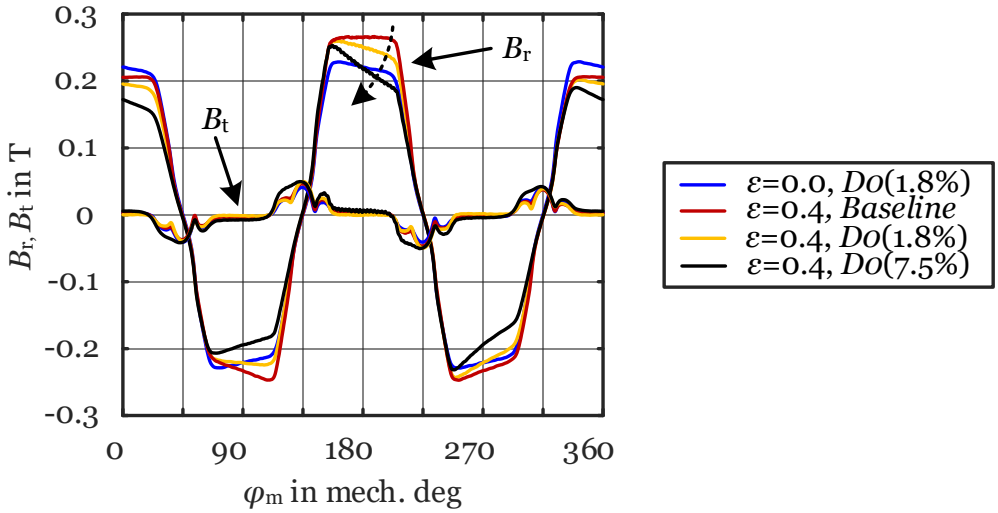

Fig. 5.15: Analysis of eccentricity for *D0*: radial and tangential air-gap flux density distributions, when $\theta = 0°$ and $\alpha = 24°$.

show peaks of equal magnitude but asymmetric shape due to the asymmetric air-gap and hence incrementally increasing air-gap reluctance over the claw-pole, see Appendix E. Introducing eccentricity for *D0(1.8%)*, when $\varepsilon = 0.4$, B_r and f_r increase with decreasing air-gap, while B_t and f_t change slightly. As expected, for *D0(7.5%)* when $\varepsilon = 0.4$, the described asymmetry in B_r and f_r is more pronounced.

Similar to Figs. 5.12, 5.13, and 5.14, Figs. 5.17, 5.18, and 5.19 show the results of the URMF analysis of *D0*. For *D0(1.8%)* when $\varepsilon = 0$, the URMFs are zero despite the air-gap asymmetry. Introducing eccentricity for *D0(1.8%)*, when $\varepsilon = 0.4$, URMFs with a peak value of 0.67 N occur featuring asymmetric waveforms due to the asymmetric

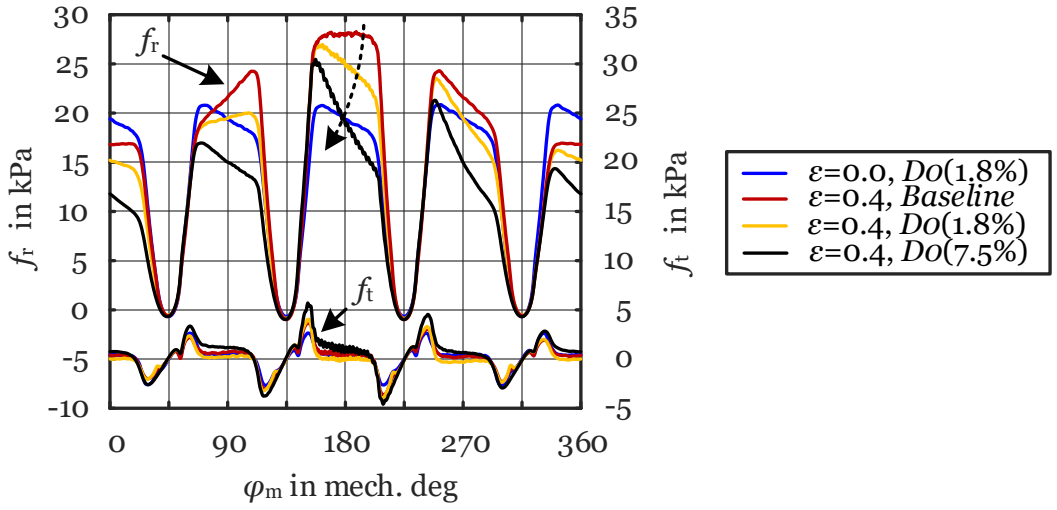

Fig. 5.16: Analysis of eccentricity for *D0*: radial and tangential magnetic tractions, when $\theta = 0°$ and $\alpha = 24°$.

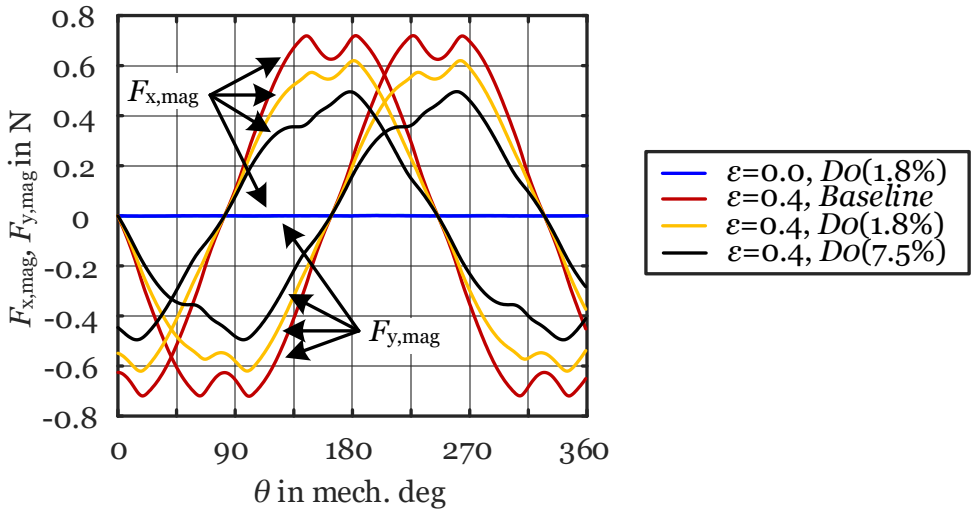

Fig. 5.17: Analysis of eccentricity for *D0*: *x*- and *y*-components of the URMF as functions of θ, when $\alpha = 24°$.

air-gaps. The URMF distribution of *D0* is still quadrupole-like but of different shape and lower magnitude compared to the *Baseline*. Increasing $\Delta\delta_{rel}$ increases the effective air-gap length, which reduces the average air-gap flux density. Hence, the URMF magnitude of, e.g, *D0(7.5%)* is about 22 % lower than that of *D0(1.8%)* for equal eccentricity, as displayed in Fig. 5.19. Again, the URMFs pulsate four times per revolution (similar to the results presented in Fig. 5.14). The reduced magnitude can be beneficial in terms of noise, but increasing air-gap asymmetry also reduces

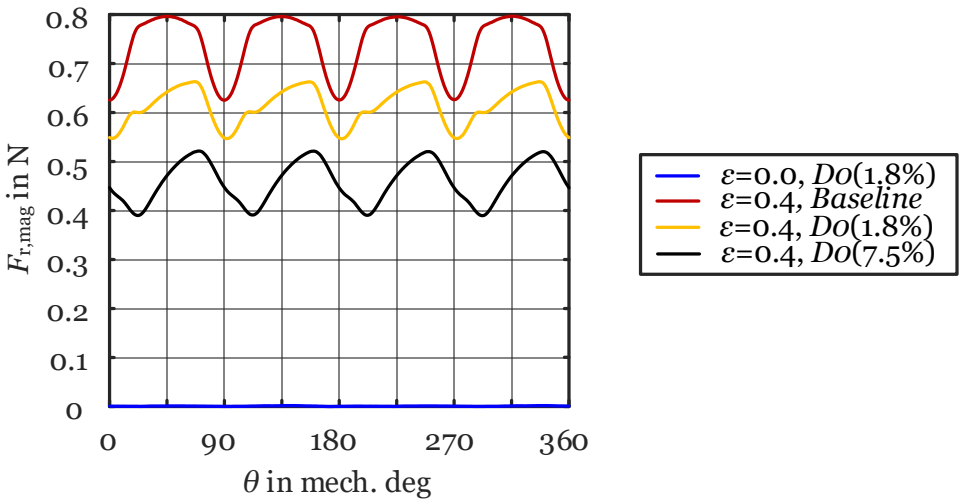

Fig. 5.18: Analysis of eccentricity for *D0*: resultant URMF (b) as functions of θ, when $\alpha = 24°$.

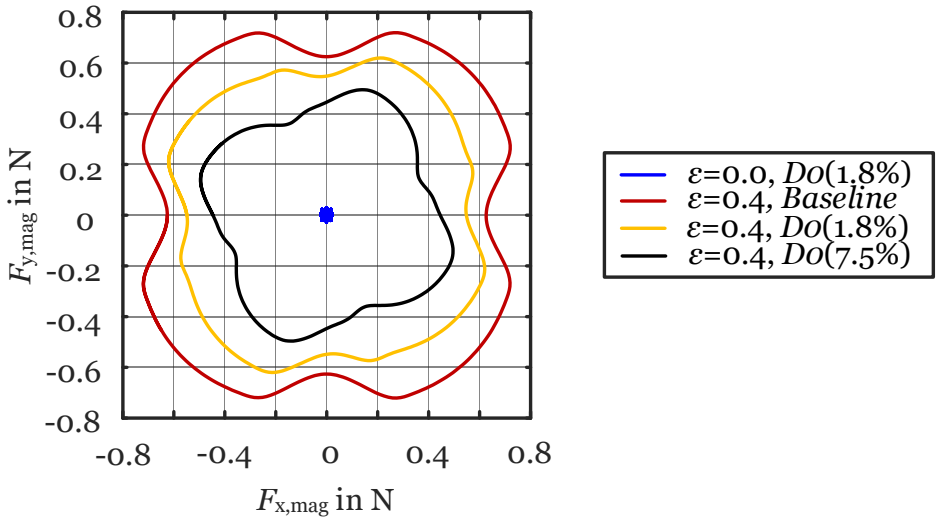

Fig. 5.19: Analysis of eccentricity for *D0*: loci of URMFs, when $\alpha = 24°$.

the PM flux per pole $\Phi_{p,PM}$, as discussed in Section 2.3.

Further URMF analyses results are presented in Appendix O, studying the effects of misaligned stator parts, different magnetization patterns, and non-uniform magnetization. The results show that misaligned stator parts and different magnetization patterns slightly change the URMF distributions, which only occur in combination with eccentricity. A non-uniform magnetization, on the other hand, causes URMFs even for concentric rotor-stator arrangements.

Measured URMF Caused by Eccentricity – *Baseline* and *D0(1.8%)*

The URMF measurement results are presented in the following, verifying selected calculated URMFs from Figs. 5.14 and 5.19. The relative eccentricities to be studied are $\varepsilon \in [0, 0.4, 0.8]$, which are realized by sleeve thicknesses of $w \in [0.1, 0.3, 0.5]$ mm for $\delta = 0.5$ mm, see Subsection 3.2.7.

Fig. 5.20 shows the measured URMF of the *Baseline* for different eccentricities. The

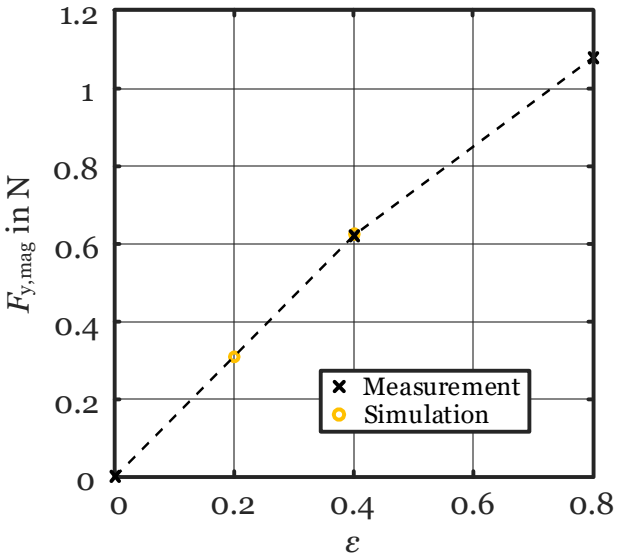

Fig. 5.20: Analysis of eccentricity: Measured and simulated URMFs of the *Baseline*.

simulation results from Fig. 5.14 for the rotor position $\theta = 90°$, where $F_{x,mag} = 0$ and $\varepsilon \in [0.2, 0.4]$, are indicated for comparison. As mentioned before and discussed in Appendix I, theoretically, the URMFs increase with the square of the eccentricity. However, for small eccentricities, this increase is approximately linear. Notice that the URMF $F_{y,mag}$ increases linearly with increasing eccentricity ε at first but then decreases for high values of ε similar to the results presented in [154]. The observed decrease may be explained by iron saturation for large values of ε; iron saturation is neglected in the theoretical calculations in Appendix I. Yet, the simulated URMFs are in excellent congruity with the measured ones.

Similarly, Fig. 5.21 shows the measured URMF of *D0(1.8%)* for different eccentricities. The corresponding simulation result from Fig. 5.19 for the rotor position $\theta = 90°$, where $F_{x,mag} = 0$ and $\varepsilon = 0.4$, is indicated for comparison.

As expected and similar to Fig. 5.20, the measured static URMF increases essen-

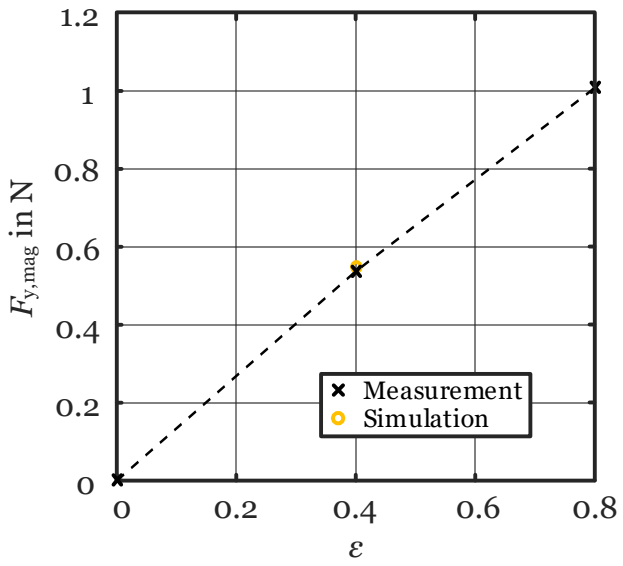

Fig. 5.21: Analysis of eccentricity: Measured and simulated URMFs of *D0(1.8%)*.

tially linearly with increasing ε. A small saturation effect can be identified for large eccentricities similar to [154]. When $\varepsilon = 0.4$, the simulated URMF $F_{y,mag}$ of *D0(1.8%)* is in congruity with the measured one.

Chapter Summary and Conclusions:

- The asymmetric air-gap (*Design 0*) can be implemented in the steel sheet punching layout at no increase to the manufacturing cost.
- An asymmetric air-gap causes asymmetric back-EMF and cogging torque waveforms.
- It can facilitate the starting, by creating a parking position for the rotor at standstill, and provide cogging torque at positions of zero alignment torque during operation, which reduces the output torque ripple.
- Eccentricity induces a quadrupole-like URMF distribution, featuring a major fourth harmonic of the rotational frequency, which can trigger resonances of the drive system or adjacent construction elements.
- An asymmetric air-gap slightly changes the shape of the URMF distribution, as do stator part misalignments and different magnetization patterns.
- A non-uniform magnetization pattern, in which the pole pairs are not equally strong, has the same effect as eccentricity.
- Since the manufactured motors are neither perfectly concentric nor feature

uniform magnetizations, the effects of both eccentricity and non-uniform magnetization typically overlap to some extent.

Chapter 6

Single-Sided Skew (*D1*)

This chapter discusses the application of skewing to the single-phase BLDC claw-pole motor to reduce the cogging torque. It is shown how a single-sided skew can be implemented in the punching layout of the claw-pole stator parts at no increase to the manufacturing cost. The effects of a single-sided skew are studied through 3-D finite-element simulations and experiments for the example case claw-pole motor, the performance specifications and system parameters of which are presented in Tables A.1 and A.2.[1]

6.1 Single-Sided Skew – Principle

As per Subsection 1.2.3, skewing can reduce the cogging torque of a PM motor. Therefore, the claw-poles are implemented with a single-sided skew as illustrated in Fig. 6.1. Due to the obtained parallelogram-like shape, the claw-pole area is the same for the *Baseline* and *Design 1*.[2]

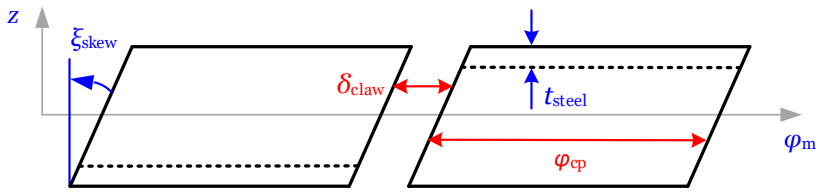

Fig. 6.1: Two consecutive poles of the unrolled claw-pole stator perimeter with implemented single-sided skew (*Design 1*).

[1] Selected results of this chapter have also been published in [61, 130].
[2] The inter-claw distance can be calculated as $\delta_{claw} = \tau_p - \varphi_{cp}$.

Predominantly, skewing acts as an "averaging filter" changing the cogging torque waveform in (1.19) to the following:

$$T_{\mathrm{c,skew}} = \frac{1}{\xi_{\mathrm{skew}}} \sum_{k=1}^{\infty} \int_{0}^{\xi_{\mathrm{skew}}} T_k \sin(kN_{\mathrm{p}}Q\theta + \varphi_k) d\theta, \tag{6.1}$$

where, in addition to the parameters already defined in the context of (1.19), ξ_{skew} is the skewing angle and N_{p} is the number of cogging torque periods during a slot pitch rotation [28].

Disadvantageously, skewing generally reduces the back-EMF due to increased leakage[3] and hence reduced PM flux per pole $\Phi_{\mathrm{p,PM}}$. The skewing factor $k_{\mathrm{skew},k}$ [33], describing the reduction in the respective harmonics of the back-EMF, is defined as

$$k_{\mathrm{skew},k} = \frac{\sin(k\,p\,\xi_{\mathrm{skew}}/2)}{k\,p\,\xi_{\mathrm{skew}}/2}, \tag{6.2}$$

where k is the harmonic order of the back-EMF.[4] A reduction in the back-EMF causes an increase in the phase current for the same voltage supplied to the winding.

Theoretically, to completely eliminate the cogging torque requires to skew by the mechanical angle ξ'_{skew} equal to the spatial period of the cogging torque λ'_{c}:

$$\xi'_{\mathrm{skew}} = \lambda'_{\mathrm{c}} = \frac{360^\circ}{\mathrm{LCM}(2p, Q)}. \tag{6.3}$$

Due to the sub-optimal slot-pole combination and low slot number of the *Baseline* (see Fig. 2.1), this skewing angle is extremely large, i.e., $\xi'_{\mathrm{skew}} = 90^\circ$. Realizing such a large skewing angle would a) deteriorate the motor performance significantly, because the first order harmonic of the back-EMF would be reduced by more than 36 % as per (6.2), b) be detrimental in single-phase motors with asymmetric magnetic design for starting capability (see Chapter 5), because the starting capability would theoretically be lost, and c) be both impractical and unrealistic for manufacturing, considering the small dimensions of the motor and its short axial length.

Remark: While typically desirable in three-phase PM motors, fully eliminating the cogging torque can be detrimental in single-phase variants. As discussed in Chapter 5, the cogging torque can be altered and phase-shifted, by implementing

[3] For constant φ_{cp}, the leakage flux increases with increasing ξ_{skew} due to the reduction in the inter-claw distance, see Appendix Q.

[4] In (6.2), the skewing angle ξ_{skew} is multiplied by the number of pole pairs, because ξ_{skew} is defined as a mechanical angle.

an asymmetric air-gap, such that a parking position is realized (from which the motor can start) and the torque ripple can be reduced (by providing cogging torque at positions of zero alignment torque, see Fig. 5.3). Hence, the implementation of skewing is clearly a tradeoff between a) reducing the cogging torque to even the output torque and reduce its ripple, and b) increasing the output torque ripple by reducing the designed cogging torque at $\theta = 90°$ too much. Hence, it is often advantageous to implement a partial skew in single-phase motors, reducing the cogging torque to some extent. (Implementing very large skewing angles in single-phase PM motors does also not make sense from a performance point of view.) Nevertheless, due to manufacturing imperfections and tolerances, the cogging torque can never be fully eliminated, merely minimized.

In the following sections, a partial skew of $\xi_{\text{skew}} = 30°$ (which is much smaller than the skewing angle of $\xi'_{\text{skew}} = 90°$) is implemented as a tradeoff between reasonable cogging torque reduction and minimum performance deterioration.[5]

6.2 Single-Sided Skew – Steel Sheet Punching Layout

The following discusses the implementation of stator claws which feature a single-sided skew in the steel sheet punching layout of the claw-pole motor. Based on the punching layout of the *Baseline* shown in Fig. 2.5(a), Fig. 6.2 illustrates how to realize skewed stator claws, where ξ_{skew} is the skewing angle in mechanical degrees, d_{skew} is the necessary x-axis displacement, w_{claw} is the stator claw width in the z-direction after bending, and r_3 is the outer stator radius. The parameter d_{skew} can be calculated for given w_{claw} and ξ_{skew} as follows:

$$d_{\text{skew}} = w_{\text{claw}} \tan(\xi_{\text{skew}}). \tag{6.4}$$

Using d_{skew} and w_{claw}, the point IV in Fig. 6.2 can be determined from which r_3 bounds the geometry to be punched. SL is the symmetry line and the parameters indicated in Fig. 6.2 have origin (i.e., point I) symmetry. For the final claw-pole motors, stator claw skewing and air-gap asymmetry (see Fig. 5.1) are eventually combined. For clarity, a combined drawing of the punching layouts is omitted.

[5] A skewing angle of $\xi_{\text{skew}} = 30°$ is chosen due to the following tradeoff: 1) the cogging torque is reduced significantly by about 25 %, 2) the first order harmonic component of the back-EMF is marginally reduced by about 1 %, and 3) the cogging torque of about 0.3 mN·m at $\theta = 90°$ ($\Delta\delta_{\text{rel}} = 1.8$ %, see Fig. 5.5) is hardly affected.

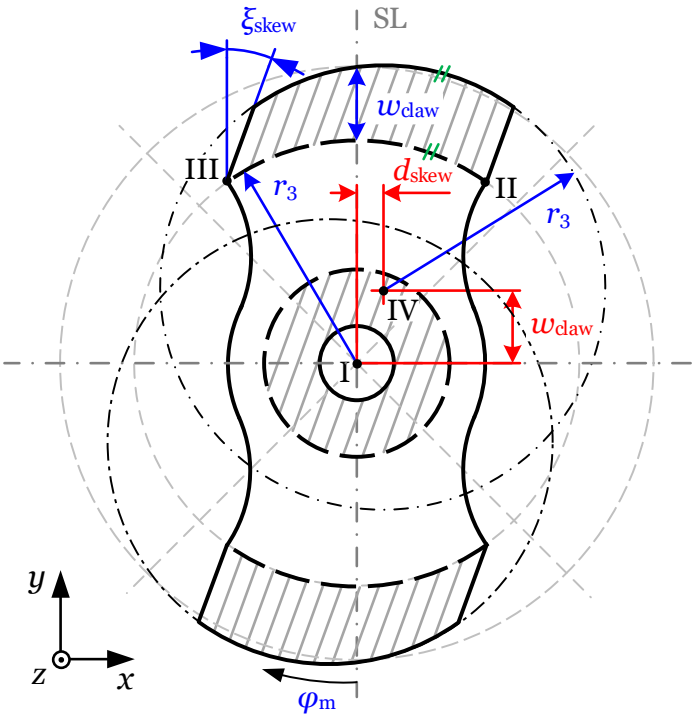

Fig. 6.2: Steel sheet punching layout for the realization of a single-sided skew (*Design 1*).

Remark: During assembly, depending on the implemented skewing angle ξ_{skew}, the symmetry lines of the two stator parts (see SL in Fig. 6.2) must be displaced by an angle other than 90° to yield coextensive inter-claw regions. In addition, as ξ_{skew} is increased for constant claw-pole angle φ_{cp}, the inter-claw region becomes smaller and the corresponding leakage flux increases, see δ^*_{claw} in Appendix Q. Therefore, depending on φ_{cp} (but also the air-gap length δ), a tradeoff exists between the positive effect of skewing in reducing the cogging torque and the increase in leakage flux.

6.3 Finite-Element Models and Prototypes

Fig. 6.3 shows the finite-element models used to study the effect of a single-sided skew of 30°.[6] Therefore, *D0(1.8%)* is compared with *D01(1.8%,30°)*, both of which are implemented with an asymmetric air-gap of $\Delta\delta_{rel} = 1.8\,\%$ for starting capability.

[6] As mentioned in Section 6.1, a skewing angle of $\xi_{skew} = 30°$ is chosen as a tradeoff between maximum cogging torque reduction and minimum performance deterioration.

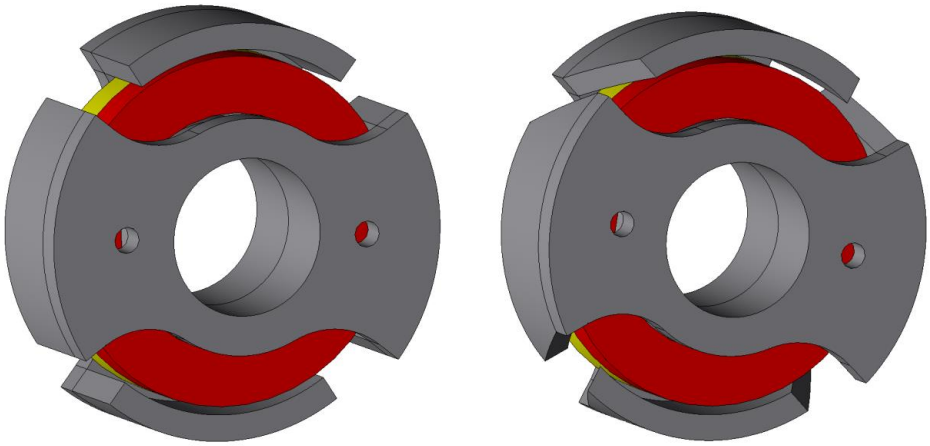

(a) *D0(1.8%)* (b) *D01(1.8%,30°)*

Fig. 6.3: Finite-element models to study the effect of a single-sided skew *(Design 1)*; visualized with JMAG® [91].

Fig. 6.4 depicts the manufactured prototype stator parts of *D0(1.8%)* and *D01(1.8%,30°)* based on the finite-element models from Fig. 6.3.

Fig. 6.4: Prototype stator parts milled from free-cutting steel 11SMnPb37 to investigate *Design 1*.

6.4 Analysis of the Cogging Torque

The effect of a single-sided skew (*Design 1*) on the cogging torque is studied below. 3-D finite-element simulations are performed, which are subsequently verified by no-load torque measurements with the rheometer as per Subsection 3.2.2.

Simulation Results

Fig. 6.5 shows the effect of a single-sided skew on the calculated cogging torque waveform. Compared to *D0(1.8%)*, implementing a single-sided skew of 30° in

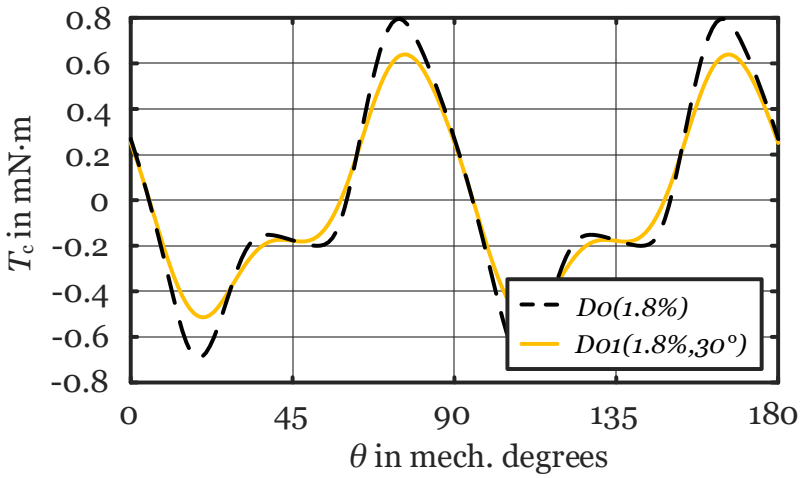

Fig. 6.5: Simulated cogging torque waveforms of *D0(1.8%)* and *D01(1.8%,30°)*.

D01(1.8%,30°) effectively reduces the cogging torque peak-to-peak value of *D0(1.8%)* by 23 % (from 1.5 mN · m to 1.15 mN · m).[7] Also, the cogging torque waveform becomes smoother, as the amplitudes of the harmonics are reduced substantially. Fortunately, the designed torque of about 0.3 mN · m at $\theta = 90°$ is hardly reduced.

Fig. 6.6 displays the order analysis of the calculated cogging torque waveforms from Fig. 6.5, where the implemented single-sided skew successfully reduces all harmonic components. While the first order harmonic component $T_{c,1}$ is reduced by about 13 %, the higher order harmonics are reduced by 31 %, 50 %, and 80 %, respectively, in ascending order. It can be concluded that higher order harmonics are reduced more significantly than lower order harmonics.

Remark: When relating k to the rotational frequency of the rotor, a factor of four must be considered as the cogging torque waveform repeats itself four times per rotor revolution, due to the motor's slot-pole combination. Hence, $T_{c,1}$ and $T_{c,2}$ correspond to fourth and eighth order harmonic components of the rotational frequency.

[7] Compared to the *Baseline*, implementing a single-sided skew of 30° in *D1(0 %,30°)* causes a similar reduction in the cogging torque.

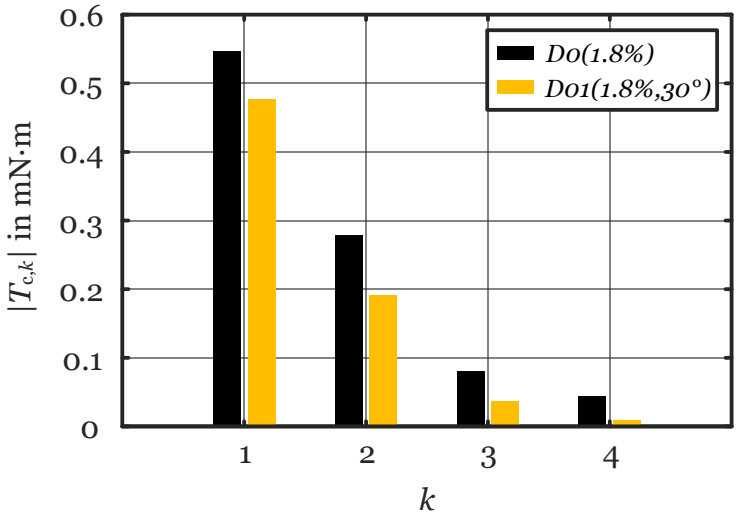

Fig. 6.6: Order analysis of the simulated cogging torque waveforms from Fig. 6.5.

Experimental Results

Fig. 6.7 shows the measured no-load torque waveforms of *D0(1.8%)* and *D01(1.8%,30°)* using the rheometer in the CCW direction. Compared to *D0(1.8%)*, the implemented

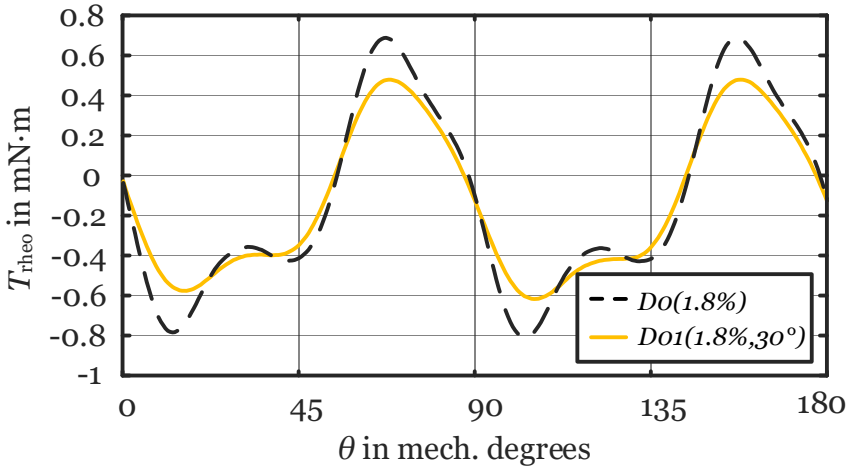

Fig. 6.7: Measured no-load torque waveforms of *D0(1.8%)* and *D01(1.8%,30°)* using a rheometer CCW at 1 rpm.

single-sided skew of 30° in *D01(1.8%,30°)* reduces the torque peak-to-peak value of *D0(1.8%)* by more than 28 % in the measurements (from 1.47 mN · m to 1.05 mN · m), confirming the simulation results presented in Fig. 6.5. The effectiveness of the proposed single-sided skew is evident. The differences of the saddle point torque

at $\theta \approx 45°$ is $-0.2\,\mathrm{mN \cdot m}$ in the simulations and $-0.4\,\mathrm{mN \cdot m}$ in the measurements, which is attributed to the measurement-related hysteresis torque[8] phenomenon discussed in detail in Subsection 9.2.1.

Fig. 6.8 shows the order analysis of the measured torque waveforms from Fig. 6.7. Notice the offset torque component $T_{\mathrm{rheo},0}$ in the measured waveform, which remains

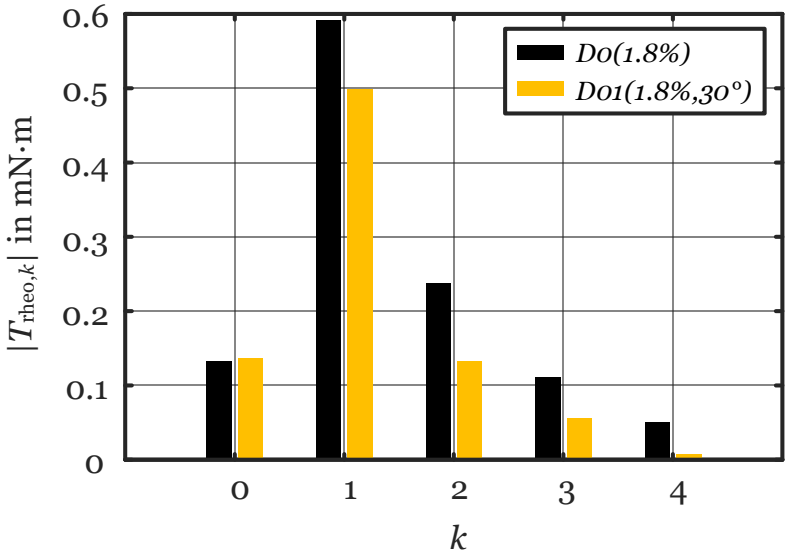

Fig. 6.8: Order analysis of the measured torque waveforms from Fig. 6.7.

the same for both motors. Again, this offset is due to the mentioned hysteresis torque discussed in detail in Subsection 9.2.1 and hence not part of the cogging torque.[8] (Performing no-load torque measurements in the CW and CCW directions, (3.9) and (3.10) can be used to separate the cogging torque and the hysteresis torque, as discussed in Subsection 9.1.2.) In close congruity with the simulation results, the harmonic components are significantly reduced when a single-sided skew of 30° is applied in *D01(1.8%,30°)*.

[8] In the performed FEA, a hysteresis model for the stator iron is not included because a) the focus is on the cogging torque and b) the necessary measurement data is not available.

6.5 Analysis of the Back-EMF

The effect of a single-sided skew (*Design 1*) on the back-EMF is studied below. 3-D finite-element simulations are performed, which are subsequently verified by measurements with the test setup shown in Fig. 3.9. Using (6.2), a theoretical reduction of the back-EMF's first order harmonic component of 4.5 % can be predicted for $\xi_{\text{skew}} = 30°$.

Simulation Results

Fig. 6.9 shows the effect of a single-sided skew on the calculated back-EMF waveform. Compared to *D0(1.8%)*, implementing a single-sided skew of 30° in *D01(1.8%,30°)* marginally affects the back-EMF waveform.

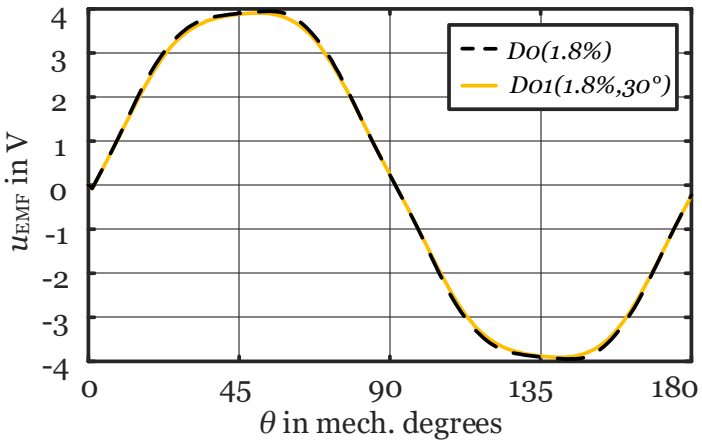

Fig. 6.9: Simulated back-EMF of *D0(1.8%)* and *D01(1.8%,30°)* at 5500 rpm.

Fig. 6.10 shows the order analysis of the calculated back-EMF waveforms from Fig. 6.9, where the implemented single-sided skew in *D01(1.8%,30°)* reduces the first order harmonic component $u_{\text{EMF},1}$ by only 1.7 % (from 4.21 V to 4.14 V).[9] Due to this reduction, the average output torque is hardly affected, see Section 6.6.

[9] This reduction is less than the expected 4.5 % based on (6.2). The reason is that, given the relatively large inter-pole region of the PM ring, the implemented skew reduces the $\Phi_{\text{p,PM}}$ only slightly.

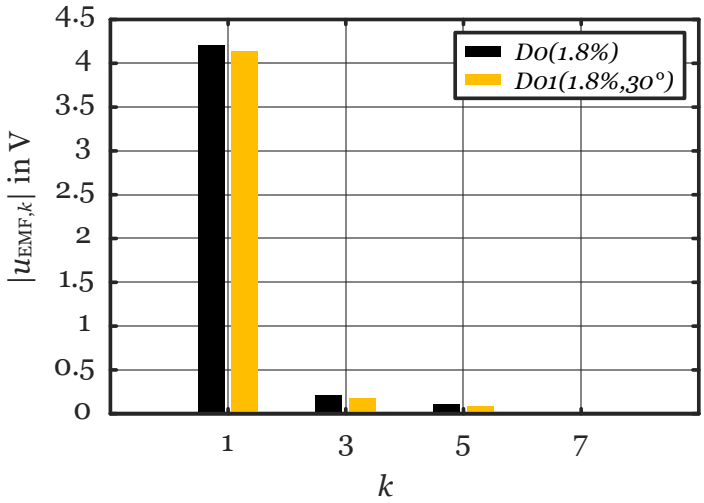

Fig. 6.10: Order analysis of the calculated back-EMF waveforms from Fig. 6.9.

Experimental Results

Fig. 6.11 shows the measured back-EMF waveforms of *D0(1.8%)* and *D01(1.8%,30°)*. In conformity with the simulation results, the implemented single-sided skew of 30° alters the back-EMF waveform only marginally.

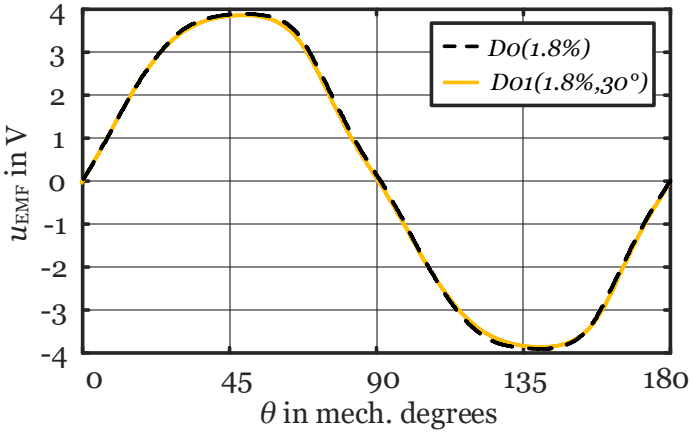

Fig. 6.11: Measured back-EMF of *D0(1.8%)* and *D01(1.8%,30°)* at 5500 rpm.

Fig. 6.12 shows the order analysis of the measured back-EMF waveforms from Fig. 6.11, where the implemented single-sided skew reduces the back-EMF's first order harmonic component $u_{EMF,1}$ by only 1.87 % (from 4.07 V to 4.00 V). This reduction conforms well with the simulation results. Compared with the experiments, $u_{EMF,3}$ is slightly more pronounced in the simulations. This is due to the fact that the exact

magnetization of the PMs is not known and can hence not be modeled exactly.

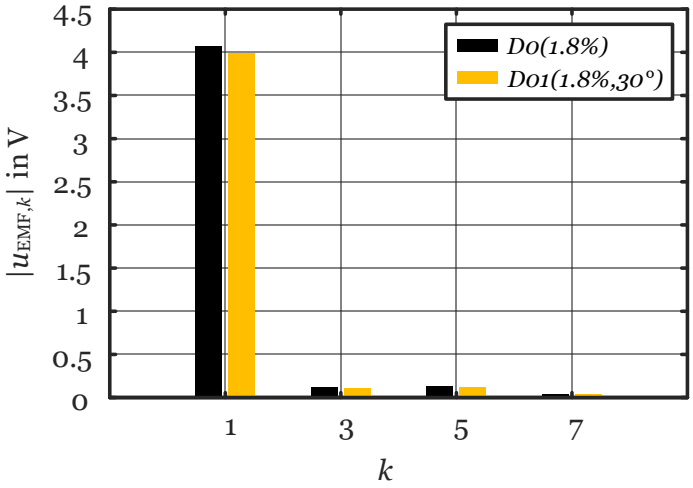

Fig. 6.12: Order analysis of the measured back-EMF waveforms from Fig. 6.11.

6.6 Analysis of the Output Torque

This section studies the effect of a single-sided skew (*Design 1*) on the output torque waveform,[10] comparing the *Baseline*, *D0(1.8%)*, *D1(30°)*, and *D01(1.8%,30°)*.

Fig. 6.13 contrasts the output torque waveforms of the *Baseline* and *D1(30°)*. The

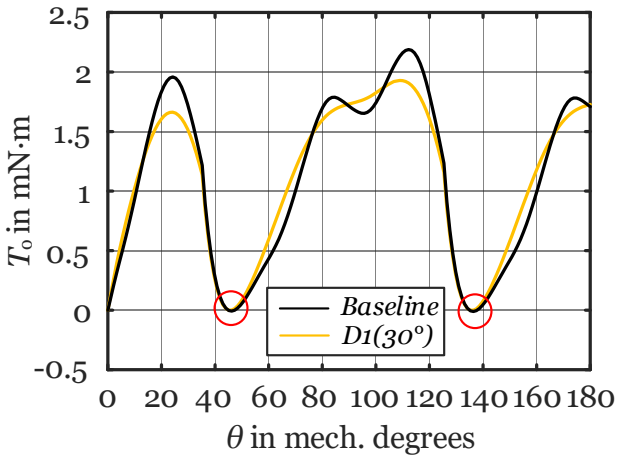

Fig. 6.13: Output torque ripple reduction caused by a single-sided skew (*Design 1*) for a symmetric air-gap.

single-sided skew of 30° in *D1(30°)* can reduce the output torque ripple of the *Baseline* by 11.9 % and also smooth the output torque waveform (higher torque harmonics are demonstrably reduced). Yet, since both motors have a symmetric air-gap, zero output torque positions exist, see the red circles in Fig. 6.13, where a false-start into the wrong direction can occur or friction-related standstill at low speeds.

The output torque waveforms of *D0(1.8%)* and *D01(1.8%,30°)* are compared in Fig. 6.14. Again, the single-sided skew of 30° in *D01(1.8%,30°)* can smooth the output torque waveform (i.e., reduce higher torque harmonics) and reduce the output torque ripple of *D0(1.8%)* by 11.4 %. The average output torque $\overline{T}_o = 1.135\,\mathrm{mN\cdot m}$ for *D0(1.8%)*, which hardly changes (it is reduced by 0.4 %) when the single-sided skew of 30° is implemented in *D01(1.8%,30°)*. Due to the realized air-gap asymmetry of $\Delta\delta_{rel} = 1.8\,\%$ in both designs, no zero output torque positions are present [compare the red circles of Figs. 6.13 and 6.14]. Contrasting the *Baseline* with *D01(1.8%,30°)*,

[10] As mentioned in Subsection 1.2.1, the simulated output torque is essentially the superposition of the cogging torque and the alignment torque, where the latter is due to the currents flowing in sub-phases A and B.

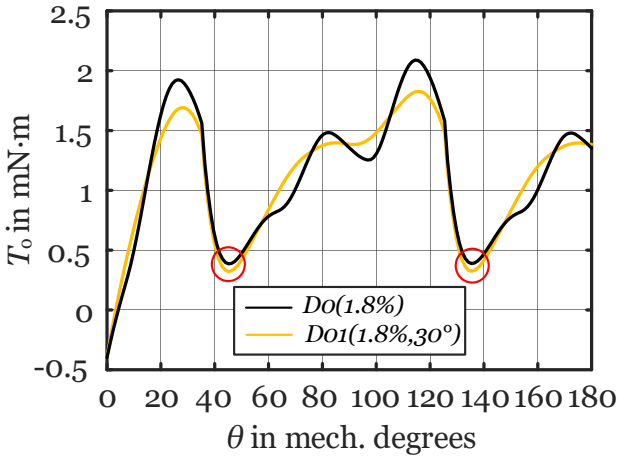

Fig. 6.14: Output torque ripple reduction caused by a single-sided skew (*Design 1*) for an asymmetric air-gap.

the output torque ripple is successfully reduced by about 31 % combining an air-gap asymmetry of 1.8 % and a single-sided skew of 30°.

Chapter Summary and Conclusions:

- In general, a single-sided skew (*Design 1*) reduces the cogging torque but at the same time the back-EMF.
- The proposed partial skew of 30° in *D01(1.8%,30°)* marginally reduces the back-EMF by 1.7 % in the simulations and 1.9 % in the measurements but significantly reduces the cogging torque by 23 % in the simulation and 28 % in the measurements.
- The single-sided skew of 30° in *D01(1.8%,30°)* can reduce the output torque ripple by almost 12 %, in combination with an asymmetric air-gap even by 31 %, while the average output torque hardly changes.

Chapter 7

Auxiliary Slots (*D2*) and Single-Sided Skew with Auxiliary Slots (*D3*)

This chapter illustrates how the introduction of one auxiliary slot per claw-pole (Design 2) can double the cogging torque fundamental frequency, which makes skewing much more effective in reducing the cogging torque. Then, the combination of a single-sided skew with auxiliary slots (Design 3) is elaborated upon, showing great potential for cogging torque reduction. The next discussion point is how the proposed measures can be implemented in the punching layout of the Baseline at no increase to the manufacturing cost. The effects of auxiliary slots with and without a single-sided skew are studied through 3-D finite-element simulations and experiments of the claw-pole motor, the performance specifications and system parameters of which are presented in Tables A.1 and A.2.[1]

7.1 Auxiliary Slots – Principle

As discussed in Subsection 1.2.3, auxiliary slots can modulate the permeance variation in the air-gap. In fact, introducing auxiliary slots creates an additional cogging torque waveform $T_{\mathrm{c,aux}}$ phase-shifted from (1.19), which results from the interaction of the PMs with the new artificial slots [28]:

$$T_{\mathrm{c,aux}} = \sum_{k=1}^{\infty} T_k \sin\left(kQ\left[\theta + \frac{2\pi}{Q(N_{\mathrm{n}}+1)}\right] + \varphi_k\right), \tag{7.1}$$

where, in addition to the parameters defined in (1.19), N_{n} is the number of auxiliary slots per claw-pole. Consequently, the total cogging torque $T_{\mathrm{c,tot}}$ is the superposition

[1] Selected results of this chapter have also been published in [131, 132, 155].

of (1.19) and (7.1):

$$T_{\mathrm{c,tot}} = T_{\mathrm{c}} + T_{\mathrm{c,aux}}. \tag{7.2}$$

As shown in (7.3), implementing the *Baseline* (in which $Q = 4$) with one auxiliary slot per claw-pole (*Design 2*), i.e., $N_{\mathrm{n}} = 1$, the first order harmonic component (which has typically the largest amplitude) and all other odd components of the cogging torque of the *Baseline* are theoretically eliminated, while essentially the even order harmonics (which have typically smaller amplitudes) add up:

$$\begin{aligned} T_{\mathrm{c,tot}} &= \sum_{k=1}^{\infty} T_k \sin(k4\theta + \varphi_k) + T_k \sin\left(k4\left[\theta + \frac{\pi}{4}\right] + \varphi_k\right) \\ &= \underbrace{T_1 \sin(4\theta + \varphi_1) + T_1 \sin(4\theta + \pi + \varphi_1)}_{=0} + T_2 \sin(8\theta + \varphi_2) + T_2 \sin(8\theta + 2\pi + \varphi_2) + \\ &\quad \underbrace{T_3 \sin(12\theta + \varphi_3) + T_3 \sin(12\theta + 3\pi + \varphi_3)}_{=0} + T_4 \sin(16\theta + \varphi_4) + T_4 \sin(16\theta + 4\pi + \varphi_4) + \\ &\quad \underbrace{T_5 \sin(20\theta + \varphi_5) + T_5 \sin(20\theta + 5\pi + \varphi_5)}_{=0} + T_6 \sin(24\theta + \varphi_6) + T_6 \sin(24\theta + 6\pi + \varphi_6) + \dots . \end{aligned} \tag{7.3}$$

Fig. 7.1 shows two consecutive poles of the unrolled stator perimeter of a claw-pole motor with one auxiliary slot per pole (*Design 2*). The bridge can enhance the mechanical stability and prevent claw-deformation during the deep-drawing process.

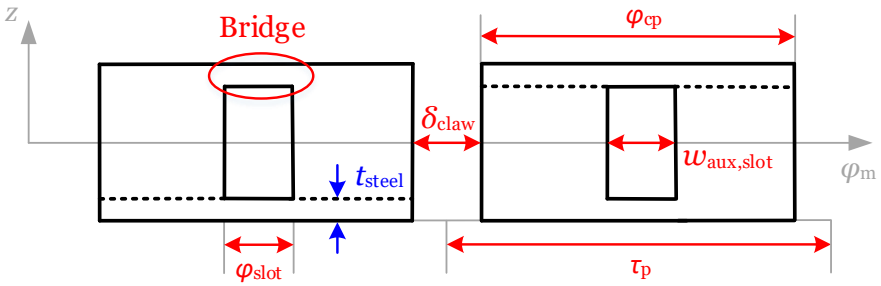

Fig. 7.1: Two consecutive poles of the unrolled stator perimeter of a claw-pole motor with one auxiliary slot per pole (*Design 2*).

Realizing one auxiliary slot per claw-pole, the number of slots is doubled, i.e., $Q^* = 8$, where Q^* is the new number of slots. Thereby, as per (6.3), the cogging torque

spatial period and hence the skewing angle to completely eliminate the cogging torque are halved compared to the *Baseline* ($\xi^*_{\text{skew}} = \lambda^*_{\text{c}} = \frac{\xi'_{\text{skew}}}{2} = \frac{\lambda'_{\text{c}}}{2} = 45°$).

Introducing auxiliary slots modulates the permeance variation in the circumferential direction around the stator, making skewing much more effective as discussed later in this section. However, total cancelation of the odd harmonics cannot be achieved as the electromagnetic characteristics of the auxiliary slots are never identical with those of the actual slots, causing the coefficients T_k and φ_k in (1.19) and (7.1) to not be exactly the same. Yet, the first order harmonic frequency of the cogging torque is modulated due to the artificial increase in the number of slots.

Remark: Introducing a number of auxiliary slots other than $N_{\text{n}} = 1$ (i.e., $N_{\text{n}} \geq 2$, where $N_{\text{n}} \in \mathbb{N}$) cannot effectively eliminate the first order harmonic and hence largest component of the cogging torque of the *Baseline*. In fact, for single-phase BLDC motors, in which the slot and pole numbers coincide, the best choice is always $N_{\text{n}} = 1$. (One possibility being a claw-pole motor variant featuring three [or more] claws per stator part [instead of the two claws shown in Fig. 2.5(a)] arranged in a spoke-like fashion, yielding to six slots and six poles.) Yet, especially in three-phase BLDC motors, in which the number of slots is typically higher than the number of poles, a different number of auxiliary slots may be beneficial so as to effectively modulate the cogging torque and make skewing more effective in reducing the cogging torque. In addition, N_{n} may be subject to practical limitations due to the motor dimensions. (The number of auxiliary slots per claw pole is limited geometrically.)

7.2 Auxiliary Slots – Steel Sheet Punching Layout

The following shows how to account for auxiliary slots in the steel sheet punching layout of the claw-pole motor. Based on the punching layout of the *Baseline* depicted in Fig. 2.5(a), Fig. 7.2 shows how to include one auxiliary slot per claw-pole (*Design 2*), where $w_{\text{aux,slot}}$ is the width of the auxiliary slots and φ_{slot} is the slot angle. Optimally, the width of the auxiliary slot should be equal to that of the actual slot [28], i.e., $w_{\text{aux,slot}} = \delta_{\text{claw}}$, where δ_{claw} is the inter-claw distance. Eventually, $w_{\text{aux,slot}}$ can be

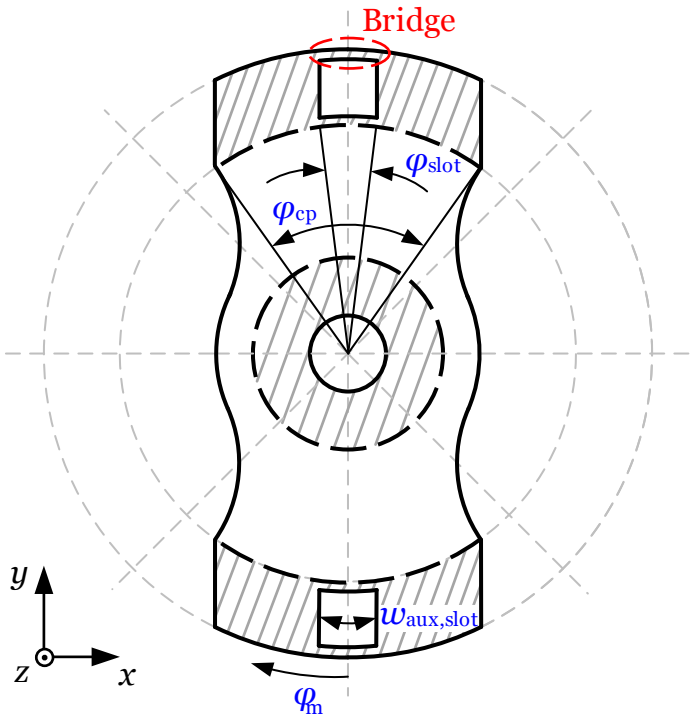

Fig. 7.2: Steel sheet punching layout for the realization of auxiliary slots (*Design 2*).

determined from τ_p, φ_{cp}, and r_3 as

$$\tau_p = \frac{360^\circ}{2p}, \tag{7.4}$$

$$\varphi_{slot} = \tau_p - \varphi_{cp}, \tag{7.5}$$

$$w_{aux,slot} = r_3 \, \varphi_{slot} \frac{2\pi}{360^\circ}. \tag{7.6}$$

Remark: Depending on the motor rating and, in turn, the dimensions of the stator parts characterized by the axial claw width w_{claw}, the proposed bridge in Fig. 7.2 can enhance the mechanical stability and avoid claw deformation during the deep-drawing process.

7.3 Single-Sided Skew with Auxiliary Slots – Principle

As discussed in Section 7.1, the implementation of one auxiliary slot per claw-pole (*Design 2*) can double the cogging torque first order harmonic frequency, halving the skewing angle to completely eliminate the cogging torque (i.e., $\xi^*_{skew} = 45^\circ$). As the

next step, using (6.1), a single-sided skew of ξ^*_{skew} is applied to (7.2):

$$\begin{aligned} T_{\text{c,skew}} &= \frac{1}{\xi^*_{\text{skew}}} \sum_{k=1}^{\infty} \int_0^{\xi^*_{\text{skew}}} T_{\text{c,tot}}\, d\theta \\ &= \frac{1}{\xi^*_{\text{skew}}} \sum_{k=1}^{\infty} \int_0^{\xi^*_{\text{skew}}} T_k \sin(kN_{\text{p}}Q^*\theta + \varphi_k)\, d\theta, \\ &= \frac{1}{\xi^*_{\text{skew}}} \sum_{k=1}^{\infty} \frac{T_k}{kN_{\text{p}}Q^*} [-\cos(kN_{\text{p}}Q^*\xi^*_{\text{skew}} + \varphi_k) + \cos(\varphi_k)], \end{aligned} \tag{7.7}$$

where $T_{\text{c,tot}}$ is represented as a new Fourier series. Theoretically, the cogging torque is eliminated when $\xi^*_{\text{skew}} = \frac{\pi}{4} = 45°$, $N_{\text{p}} = 1$, and $Q^* = 8$:

$$T_{\text{c,skew}} = \frac{4}{\pi} \sum_{k=1}^{\infty} \frac{T_k}{k8} \left[-\cos\left(\frac{k8\pi}{4} + \varphi_k \right) + \cos(\varphi_k) \right] = 0. \tag{7.8}$$

Fig. 7.3 shows two consecutive poles of the unrolled stator perimeter of a claw-pole motor with a single-sided skew and one auxiliary slot per claw-pole.

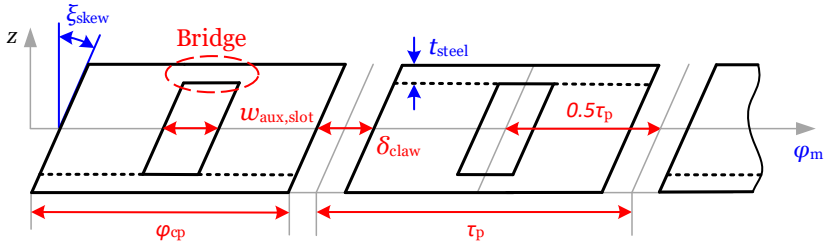

Fig. 7.3: Two consecutive poles of the unrolled stator perimeter of a claw-pole motor with a single-sided skew and one auxiliary slot per claw-pole (*Design 3*).

Applying the proposed cogging torque reduction methods in practice will not completely eliminate the cogging torque due to manufacturing imperfections and tolerances [53]. Moreover, the PM magnetization pattern (e.g., radial, parallel, or polar anisotropic) significantly influences the amplitudes of the cogging torque harmonics T_k. On the one hand, implementing a single-sided skew with auxiliary slots (*Design 3*) will reduce the PM flux per pole $\Phi_{\text{p,PM}}$ indicated in Fig. 2.2(a). This eventually causes a reduction in the back-EMF (see Section 7.7) due to the reduction in the average absolute air-gap flux density $|\overline{B}_\delta|$ (see Appendix R). On the other hand, the eddy current losses are reduced in *Design 2* and *Design 3*, owing to the axial slit in the claw-poles, which partly prevents the eddy currents (see Section 7.10).

Remark: Alternatively, a design with doubly skewed claw-poles (i.e., a positive skewing angle at one claw-pole edge and a negative skewing angle at the other edge), leading to the trapezoidal claw-pole shape found in IHP alternators, prevents the realization of the proposed skewed auxiliary slots. Implementing doubly skewed claw-poles with straight auxiliary slots is less effective in reducing the cogging torque than *Design 3* because the latter exhibits a smoother air-gap permeance variation.

7.4 Single-Sided Skew with Auxiliary Slots – Steel Sheet Punching Layout

The following shows how to account for a single-sided skew with auxiliary slots (*Design 3*) in the punching layout. Based on the punching layout of *Design 2* in Fig. 7.2, Fig. 7.4 illustrates how auxiliary slots can be combined with a single-sided skew. The x-axis displacement d_{skew} can be calculated from the desired skewing angle

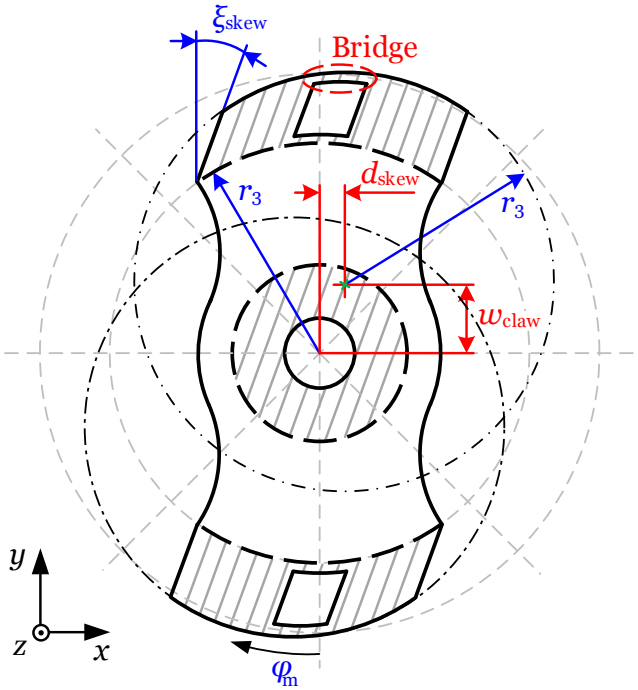

Fig. 7.4: Steel sheet punching layout for the realization of a single-sided skew with auxiliary slots (*Design 3*).

ξ_{skew} and w_{claw} according to (6.4). The bridge indicated can enhance the mechanical stability and prevent claw-deformation during the deep-drawing process.

Remark: The practical realization of a certain skewing angle ξ_{skew} may be subject to restrictions of the deep-drawing process, especially t_{steel}, the motor's axial length determined by w_{claw}, and φ_{cp}. As discussed in Chapter 6, when skewing is applied to the stator claws, the inter-claw distance δ_{claw} reduces for constant φ_{cp}. Hence, the width of the auxiliary slot must be adapted to equal that of the actual slot.

7.5 Finite-Element Models and Prototypes

Fig. 7.5 shows the finite-element models used to study the effects of auxiliary slots (*Design 2*) and their combination with a single-sided skew (*Design 3*). To better

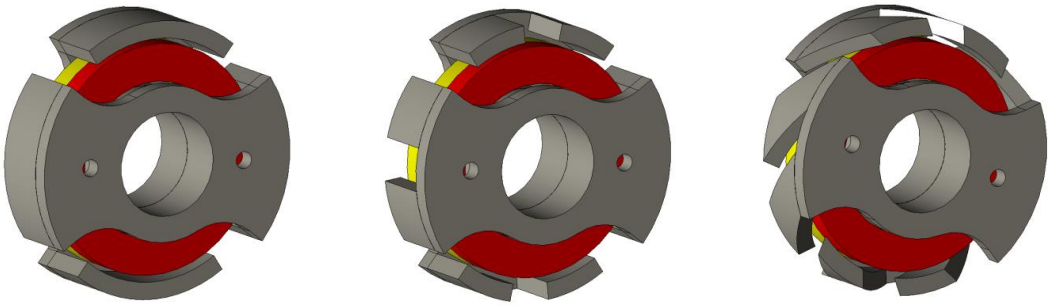

(a) *Baseline* (b) *D2* (c) *D3(45°)*

Fig. 7.5: Finite-element models to study the influence of auxiliary slots (*Design 2*) and a single-sided skew with auxiliary slots (*Design 3*); visualized with JMAG® [91].

illustrate the underlying concept of the design improvements, an asymmetric air-gap is not implemented at first. (For the analysis of the output torque in Section 7.11, an asymmetric air-gap of $\Delta\delta_{\text{rel}} = 1.8\,\%$ is implemented.)

Fig. 7.6 exhibits the manufactured prototype stator parts of the *Baseline*, *D2*, and *D3(45°)* in accordance with the finite-element models from Fig. 7.5.

Baseline *D2* *D3(45°)*

Fig. 7.6: Prototype stator parts milled from free-cutting steel 11SMnPb37 to investigate *Design 2* and *Design 3*.

7.6 Analysis of the Cogging Torque

The effect of one auxiliary slot per claw-pole (*Design 2*) and its combination with a single-sided skew of 45° (*Design 3*) on the cogging torque of the *Baseline* is studied below.[2] 3-D finite-element simulations are performed, which are subsequently verified by measurements with the rheometer shown in Fig. 3.6.

Simulation Results

Fig. 7.7 contrasts the simulated cogging torque waveforms of the *Baseline*, *D2*, and *D3(45°)*. As predicted in Section 7.1, the auxiliary slots introduced in *D2* successfully double the first order harmonic frequency of the cogging torque of the *Baseline*. Com-

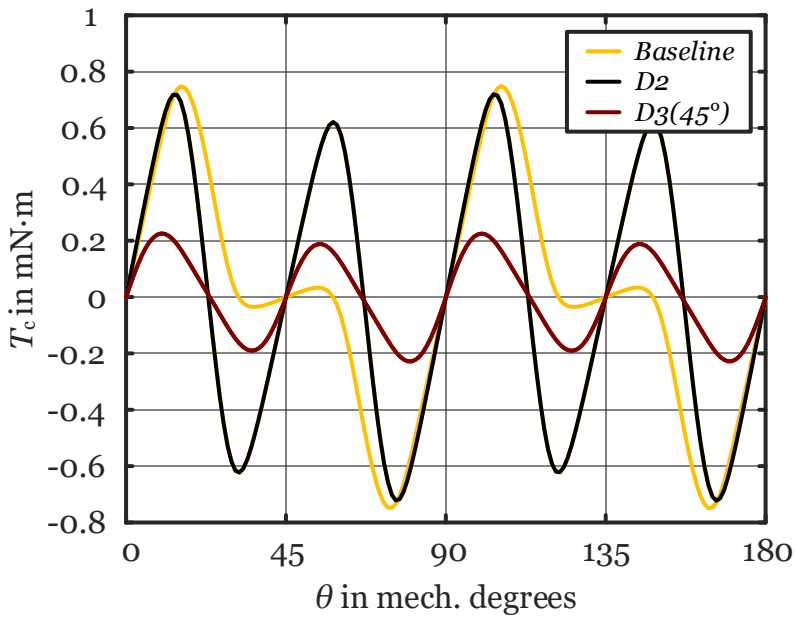

Fig. 7.7: Simulated cogging torque waveforms of the *Baseline*, *D2*, and *D3(45°)*.

bining auxiliary slots with a single-sided skew of $\xi_{\text{skew}} = 45°$ in *D3(45°)* successfully reduces the peak-to-peak value of the cogging torque of the *Baseline* by 70 % in the simulations [from 1.5 mN · m to 0.45 mN · m].

Fig. 7.8 shows the order analysis of the calculated cogging torque waveforms from Fig. 7.7, where k is the order of the cogging torque harmonics. As predicted in

[2] For reasons of clarity, air-gap asymmetry is not considered in this section. However, in Section 7.11, in which the output torque is studied in the load-condition, air-gap asymmetry is considered.

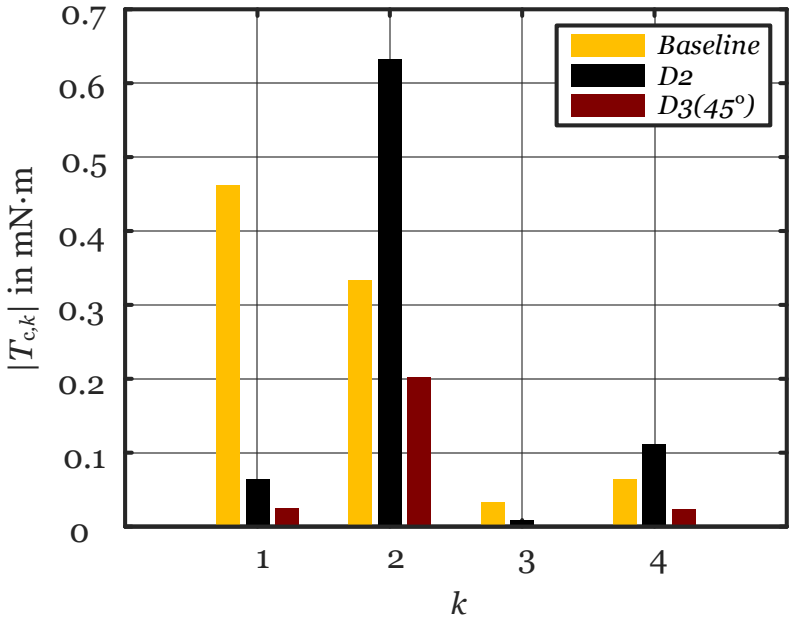

Fig. 7.8: Order analysis of the calculated cogging torque waveforms from Fig. 7.7.

(7.3), the first order harmonic component $T_{c,1}$ of the *Baseline* is almost canceled (it is reduced by 86 %) when auxiliary slots are introduced in *D2*, while the second order harmonic component $T_{c,2}$ is almost doubled (it is increased by 89 %).[3] In *D3(45°)*, in which a single-sided skew of $\xi_{skew} = 45°$ is applied to the stator claws in addition to auxiliary slots, the dominant even order harmonics $T_{c,2}$ and $T_{c,4}$ are then reduced by 68 % and 79 %, respectively, compared with *D2*.

Remark: When relating k to the rotational frequency of the rotor, a factor of four must be considered as the cogging torque waveform repeats itself four times per rotor revolution, due to the motor's slot-pole combination. Hence, $T_{c,1}$ and $T_{c,2}$ correspond to fourth and eighth order harmonic components of the rotational frequency.

Experimental Results

Fig. 7.9 depicts the measured no-load torque waveforms of the *Baseline*, *D2*, and *D3(45°)*, which are in close congruity with the simulated cogging torque waveforms shown in Fig. 7.7. Minor asymmetries and differences in the amplitudes occur due to manufacturing imperfections and lack of knowledge of the real magnetization of the PM. Similar to Fig. 6.7, a hysteresis torque related offset is present in the

[3] While a cogging torque modulation is expected to cause an amplitude reduction, the cogging torque peak-to-peak value is hardly changed for the studied radial magnetization pattern and α.

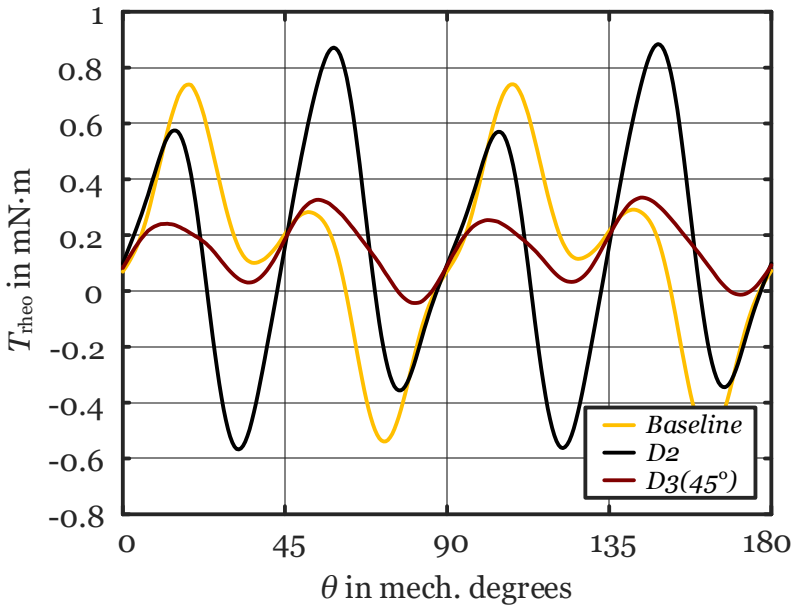

Fig. 7.9: Measured no-load torque waveforms of the *Baseline*, *D2*, *D3(45°)* using a rheometer CW at 1 rpm.

measurements, as discussed in Subsection 9.2.1. As anticipated, the implemented auxiliary slots in *D2* successfully double the cogging torque first order harmonic frequency of the *Baseline* and, due to the implemented single-sided skew in *D3(45°)*, the cogging torque of *D2* is significantly reduced. In the measurements, the peak-to-peak no-load torque of the *Baseline* is reduced by 70 % in *D3(45°)* [from 1.28 mN · m to 0.38 mN · m], which is in excellent congruity with the simulation results.

Fig. 7.10 illustrates the order analysis of the measured waveforms from Fig. 7.9. The offset components $T_{\text{rheo},0}$ are not part of the respective cogging torque and can be attributed to the measurement-related hysteresis torque phenomenon, as discussed in Subsection 9.2.1.[4] Similar to the simulation results, the first order harmonic component $T_{\text{rheo},1}$ of the *Baseline* is significantly reduced in *D2*, while the second order harmonic $T_{\text{rheo},2}$ doubles. Finally, the torque harmonics of *D2* are significantly reduced in *D3(45°)*, owing to the implemented single-sided skew of 45°.

[4]Performing no-load torque measurements in the CW and CCW directions, (3.9) and (3.10) can be used to separate the cogging torque and the hysteresis torque, as discussed in Subsection 9.1.2.

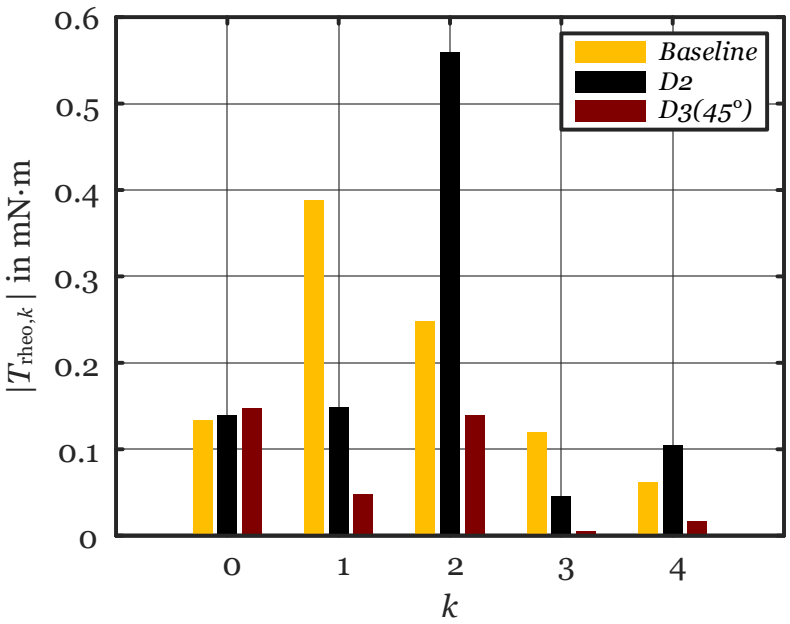

Fig. 7.10: Order analysis of the measured torque waveforms from Fig. 7.9.

7.7 Analysis of the Back-EMF

The effect of one auxiliary slot per claw-pole (*Design 2*) and its combination with a single-sided skew of 45° (*Design 3*) on the back-EMF of the *Baseline* is studied below. 3-D finite-element simulations are performed, which are subsequently verified by measurements with the test setup shown in Fig. 3.9. It is expected that, as iron is removed from each claw-pole as part of the cogging torque reduction, the PM flux per pole $\Phi_{\mathrm{p,PM}}$ will be reduced in *D2* and *D3(45°)*, causing a reduction in the back-EMF due to the increased rotor leakage flux.

Simulation Results

Fig. 7.11 depicts the simulated back-EMF waveforms of the *Baseline*, *D2*, and *D3(45°)*. Implementing auxiliary slots in *D2* reduces the back-EMF peak value of the *Baseline* by about 12 %. The realization of a single-sided skew of $\xi_{\mathrm{skew}} = 45°$ in addition to auxiliary slots in *D3(45°)* causes narrower peaks leading to more rounded back-EMF transitions. (The latter conforms well with the behavior described in [38] as a result of skewing.)

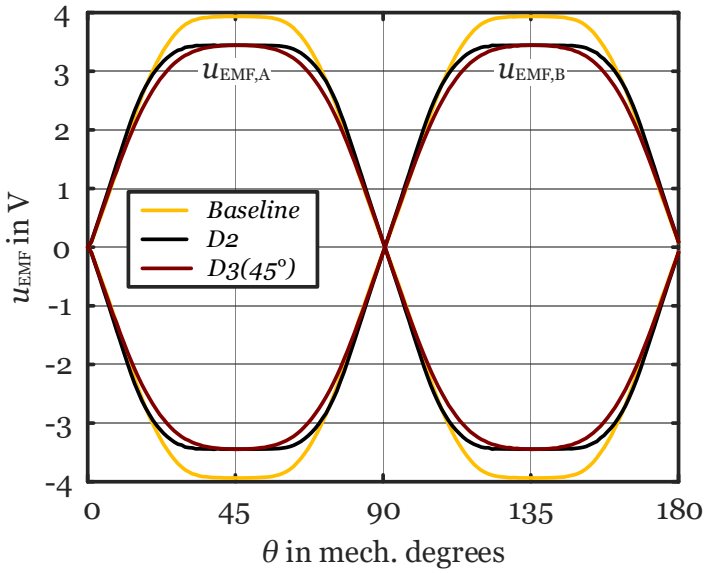

Fig. 7.11: Simulated back-EMF waveforms of the *Baseline*, *D2*, and *D3(45°)* at $n = 5500$ rpm.

Fig. 7.12 illustrates the order analysis of the back-EMF waveforms from Fig. 7.11. The implemented auxiliary slots in *D2* cause a reduction in the back-EMF's first

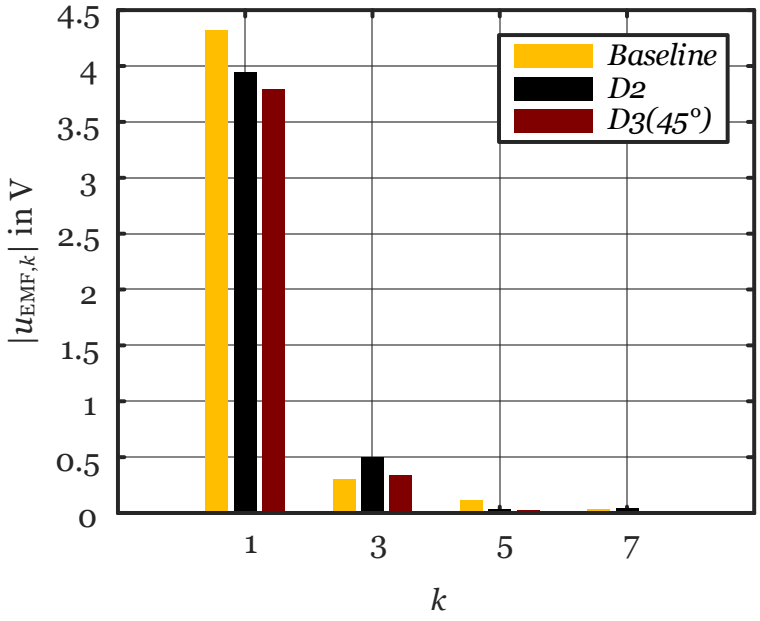

Fig. 7.12: Order analysis of the calculated back-EMF waveforms from Fig. 7.11.

order harmonic component $u_{EMF,1}$ of the *Baseline* of 8.8 % (and an increase in $u_{EMF,3}$). Implementing a single-sided skew of $\xi_{skew} = 45°$ in addition to auxiliary slots in

D3(45°) causes an additional reduction in $u_{\mathrm{EMF},1}$ of about 3.8 %, yielding a total reduction of about 12 % compared with the *Baseline* [from 4.32 V to 3.94 V to 3.79 V].

Remark: Considering the predicted back-EMF reduction, the rms phase current will increase when the same voltage is applied to the winding.

Experimental results

Fig. 7.13 shows the measured back-EMF waveforms of the *Baseline*, *D2*, and *D3(45°)*. In conformity with the simulation results, the implemented auxiliary slots in *D2*

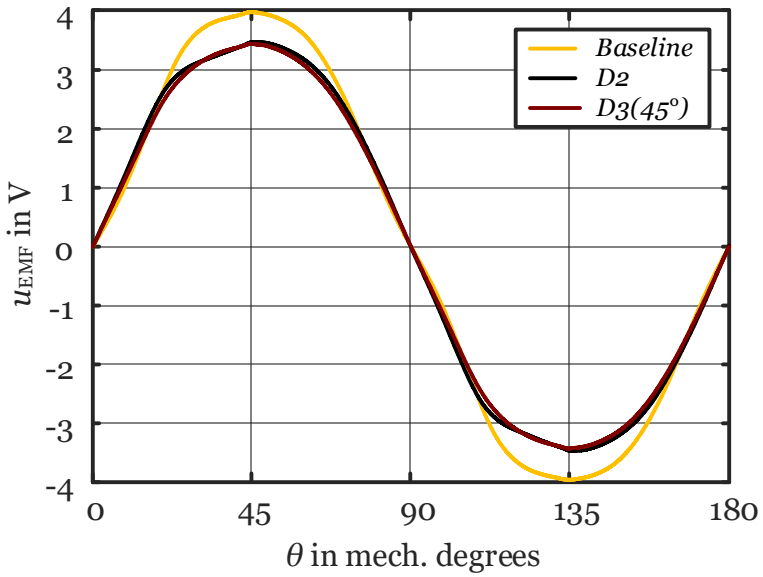

Fig. 7.13: Measured back-EMF waveforms of the *Baseline*, *D2*, and *D3(45°)* at $n = 5500$ rpm.

reduce the back-EMF peak value of the *Baseline* by 12.8 % in the measurements. As in the simulations, implementing a stator claw skewing of $\xi_{\mathrm{skew}} = 45°$ in *D3(45°)* causes narrower peaks leading to more rounded back-EMF transitions. The trapezoidal character of the back-EMF waveform is less pronounced in the measurement.

Fig. 7.14 exhibits the order analysis of the measured back-EMF waveforms from Fig. 7.13. Compared with the *Baseline*, the auxiliary slots in *D2* cause a reduction in the back-EMF's first order harmonic component $u_{\mathrm{EMF},1}$ of about 10 % (from 4.05 V to 3.64 V). Implementing a stator claw skewing of 45° in *D3(45°)* yields a total reduction in $u_{\mathrm{EMF},1}$ of 12.3 %, which is in excellent congruity with the simulation results. Compared with the experiments, the third order harmonic components are more

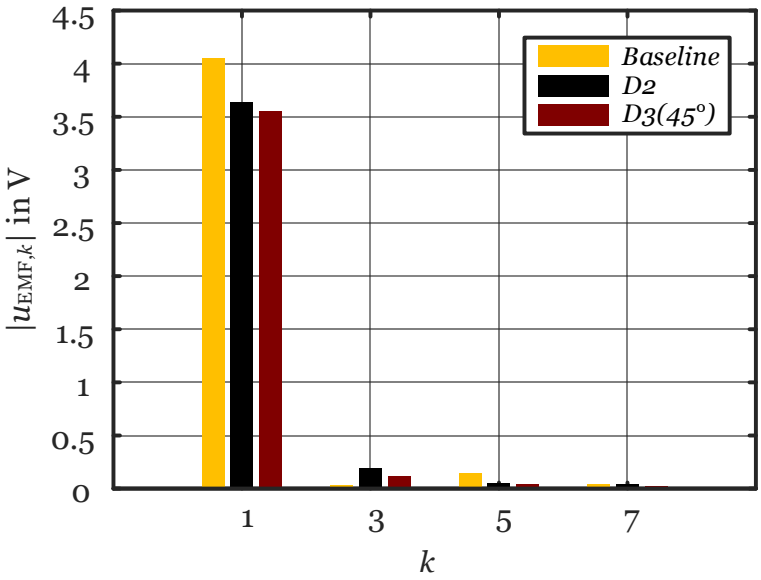

Fig. 7.14: Order analysis of the measured back-EMF waveforms from Fig. 7.13.

pronounced in the simulations. This is because the exact magnetization state of the PM is not fully known and can hence not be modeled exactly.

7.8 Analysis of the Air-Gap Flux Density Distribution

The air-gap flux density distributions of the *Baseline*, *D2*, and *D3(45°)* are studied in Appendix R, with respect to the radial and tangential components, as well as the absolute value. The auxiliary slots in *D2* and *D3(45°)* cause local drops in the radial flux density in the middle of the auxiliary slots and additional tangential components in the same locations. The average values are 148 mT, 136 mT, and 140 mT in the *Baseline*, *D2*, and *D3(45°)*, respectively.

7.9 Analyses of the Phase Inductance and Leakage Flux Ratios

The phase inductance and leakage flux ratios of the *Baseline*, *D2*, and *D3(45°)* are studied in Appendix S. For the unsaturated case, the phase inductance L_{ph} is 6 mH, 5.7 mH, and 6.2 mH for the *Baseline*, *D2*, and *D3(45°)*, respectively. For currents larger than 1 A, L_{ph} decreases significantly down to approximately 3 mH. The stator leakage ratios λ_{s} amount to 54.9 %, 55.9 %, and 62.7 % for the *Baseline*, *D2*, and

D3(45°), respectively, for the unsaturated case. For currents larger than 1 A, λ_s increases by up to 7 %. The calculated rotor leakage ratios λ_r are 14.6 %, 16.5 %, and 19.9 % for the *Baseline*, *D2*, and *D3(45°)*.

7.10 Analyses of the Eddy Current and Hysteresis Losses

The stator of the claw-pole motor typically consists of two solid stator parts instead of a laminated core [25, 136, 137]. Hence, in addition to the hysteresis losses, it is important to account for eddy current effects in the two stator parts when designing this type of motor as the eddy current losses strongly vary with both the speed n and the steel sheet thickness t_{steel}, and can significantly impact the performance of the motor. Therefore, the eddy current losses in the stator parts are estimated in the no-load condition for the maximum rotational speed through 3-D finite-element simulations.[5]

In the following, the average eddy current losses $\overline{P}_{eddy}$ and hysteresis losses $\overline{P}_{hys}$ of the *Baseline*, *D2*, and *D3(45°)* are calculated in the no-load condition at $n = 5500$ rpm. It is anticipated that, owing to the auxiliary slots in the claw-poles, the eddy current losses will decrease in *D2* and *D3(45°)*. Moreover, the hysteresis losses are anticipated to be about the same for the studied stators, as they share similar iron volume and are exposed to the same operating frequency.

Fig. 7.15 illustrates a snapshot of the computed current density contour plots of the stator parts of the *Baseline*, *D2*, and *D3(45°)*. The formation of eddy currents differ for the three designs due to the auxiliary slots. At large, $\overline{P}_{eddy}$ is calculated as 220 mW, 204 mW, and 198 mW in the *Baseline*, *D2*, and *D3(45°)*, respectively. Compared with the *Baseline*, $\overline{P}_{eddy}$ is reduced by 7.3 % in *D2* and 10 % in *D3(45°)*.

The calculated hysteresis losses are approximately the same for all three stators, amounting to about 10 mW for the *Baseline*, *D2*, and *D3(45°)*.[6] This can be explained by the fact that the motors are operated at the same rotational speed n and share roughly the same stator iron mass [$m_{Fe} \approx 3$ g for the *Baseline*, *D2*, and *D3(45°)*]. Notice

[5] The eddy current and hysteresis losses in the rotor can be neglected since the flux therein is essentially constant.

[6] The used calculation method is based on the separation of major and minor loops of the respective flux density waveforms. A detailed hysteresis model of the used iron material is not available.

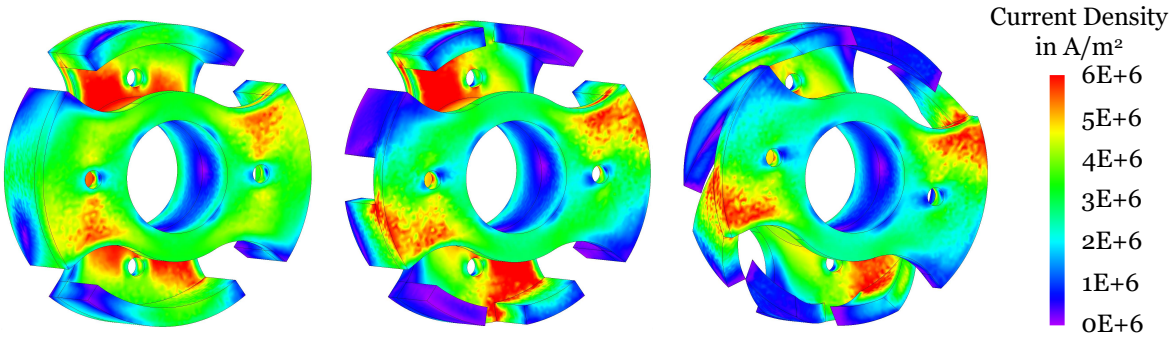

(a) *Baseline* (b) *D2* (c) *D3(45°)*

Fig. 7.15: Current density contour plots of the *Baseline*, *D2*, and *D3(45°)* in the no-load eddy current analysis for $n = 5500$ rpm; visualized with JMAG® [91].

that the calculated hysteresis losses $\overline{P}_{\text{hys}}$ are significantly lower than the calculated eddy current losses $\overline{P}_{\text{eddy}}$. ($\overline{P}_{\text{hys}}$ amounts to about 5 % of $\overline{P}_{\text{eddy}}$.)

Remark: As per Section 9.2, the measured iron losses are significantly larger than the simulated ones. Extrapolating the measured total iron losses for $n = 5500$ rpm yields 695 mW, which is three times larger than the simulated losses of the *Baseline* amounting to 230 mW. (The measured and simulated eddy current losses amount to 613 mW and 220 mW, respectively; the measured and simulated hysteresis losses amount to 82 mW and 10 mW, respectively.) The discrepancy can be caused by material parameter uncertainties in the finite-element model, partly caused by the manufacturing process.

7.11 Analysis of the Output Torque

This section addresses the operation of the *Baseline*, *D2*, and *D3(45°)* in the load condition. To avoid zero output torque positions, they are implemented with a relative air-gap asymmetry of $\Delta\delta_{\text{rel}} = 1.8\,\%$, leading to *D0(1.8%)*, *D02(1.8%)*, and *D03(1.8%,45°)*. The phase current i_{p}, the output torque T_{o}, the average output torque $\overline{T}_{\text{o}}$, and the output torque ripple T_{rip} are investigated.[7]

Fig. 7.16 shows the calculated phase current waveforms of *D0(1.8%)*, *D02(1.8%)*, and *D03(1.8%,45°)*, including the current spike indicated with the red circle which is characteristic for the bifilar winding (see Subsection 2.1.3). The applied voltage is

[7] For the analysis, online iron loss calculation is not included in light of the tremendous computational burden. As an approximation, the iron losses are accounted for when calculating the efficiency.

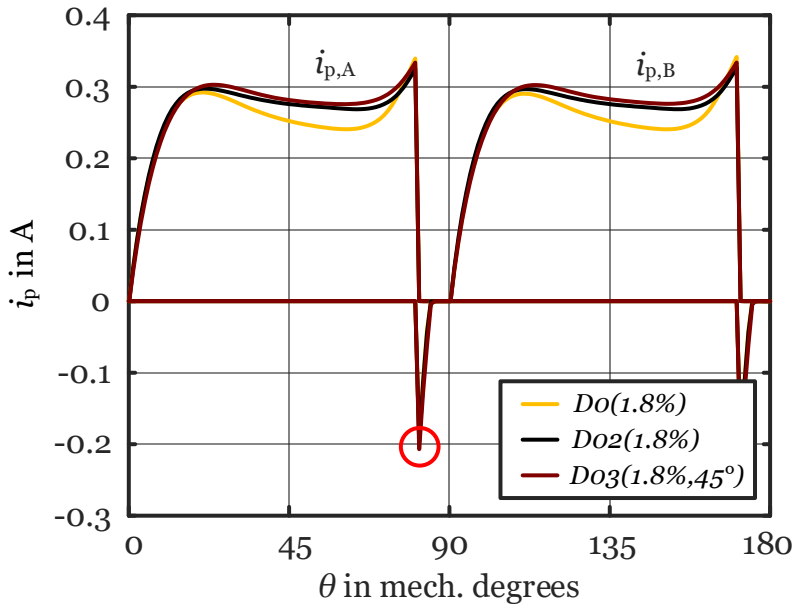

Fig. 7.16: Simulated phase current waveforms of *D0(1.8%)*, *D02(1.8%)*, and *D03(1.8%,45°)* at $n = 5500$ rpm.

constant and the commutation angles are $\theta_{on} = 0°$ and $\theta_{off} = 80°$ for every half-wave of the back-EMF, see Subsection 2.1.3. The respective rms phase current values of *D0(1.8%)*, *D02(1.8%)*, and *D03(1.8%,45°)* are presented in Table 7.1. Because of the decrease in the back-EMF displayed in Fig. 7.11, the drawn rms phase current I_p slightly increases by 5.2 % and 7 %, in *D02(1.8%)* and *D03(1.8%,45°)*, compared with *D0(1.8%)*. In the cases of *D02(1.8%)* and *D03(1.8%,45°)*, the rectangular-like current shape is more pronounced.

Table 7.1: Load Condition Analysis

	I_p	T_{rip}	$\overline{T}_o$	η
	mA	mN·m	mN·m	%
D0(1.8%)	243.3	1.77	1.15	35.8
D02(1.8%)	255.9	1.81	1.14	33.8
D03(1.8%,45°)	260.3	1.47	1.10	32.7

Fig. 7.17 exhibits the output torque waveforms[8] of *D0(1.8%)*, *D02(1.8%)*, and *D03(1.8%,45°)*. The resulting output torque ripples and average torques are also presented in Table 7.1. The introduction of auxiliary slots in *D02(1.8%)* slightly

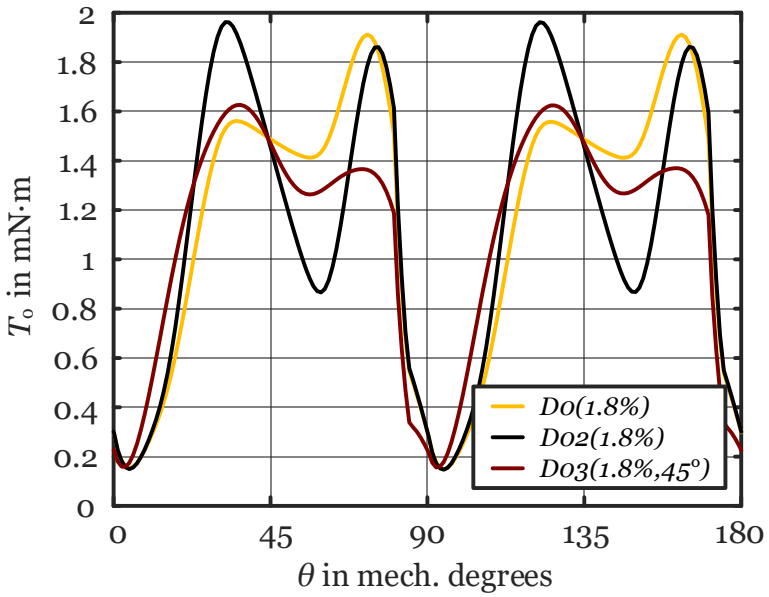

Fig. 7.17: Simulated output torque waveforms of *D0(1.8%)*, *D02(1.8%)*, and *D03(1.8%,45°)* at $n = 5500$ rpm.

increases the output torque ripple for the studied magnetization pattern, where $\alpha = 24°$. [For $\alpha = 28°$, the output torque ripple is reduced by almost 19 %.] However, *D03(1.8%,45°)*, which features auxiliary slots and a single-sided skew of $\xi_{\text{skew}} = 45°$, shows a successful reduction in the output torque ripple of 17 %, compared with *D0(1.8%)*. [For $\alpha = 28°$, the output torque ripple is reduced by almost 33 %.] As presented in Table 7.1, the average output torque $\overline{T}_o$ of *D0(1.8%)* only decreases marginally by 0.9 % and 4.4. %, respectively, when the cogging torque reduction methods are implemented in *D02(1.8%)* and *D03(1.8%,45°)*.

Fig. 7.18 illustrates the order analysis of the calculated output torque waveforms from Fig. 7.17. The zero order harmonic components equal the average output torques of *D0(1.8%)*, *D02(1.8%)*, and *D03(1.8%,45°)*, see $\overline{T}_o$ in Table 7.1. Compared to *D0(1.8%)*, the auxiliary slots in *D02(1.8%)* reduce $T_{o,1}$ by 26 % but increase $T_{o,2}$ by

[8] As mentioned in Subsection 1.2.1, the simulated output torque is essentially the superposition of the cogging torque and the alignment torque, where the latter is due to the currents flowing in sub-phases A and B.

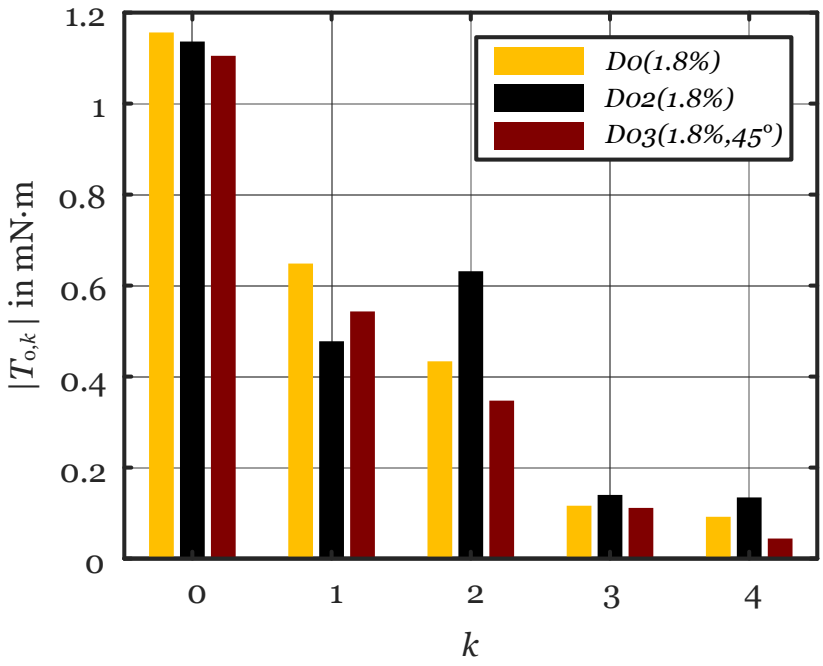

Fig. 7.18: Order analysis of the calculated output torque waveforms from Fig. 7.17.

45 %. ($T_{o,3}$ and $T_{o,4}$ are increased by 20 % and 46 %, respectively.) Yet, more importantly, the single-sided skew of 45° in addition to auxiliary slots in *D03(1.8%,45°)* successfully reduces $T_{o,1}$ and $T_{o,2}$ of *D0(1.8%)* by 16 % and 20 %, respectively. ($T_{o,3}$ and $T_{o,4}$ are reduced by 4 % and 52 %, respectively.) The higher order harmonic components of the output torque are notably reduced in *D03(1.8%,45°)*, too.

Remark 1: Again, when relating k to the rotational frequency of the rotor, a factor of four must be considered. Hence, $T_{o,1}$ and $T_{o,2}$ correspond to fourth and eighth order harmonic components of the rotational frequency.

Using the eddy current and hysteresis losses calculated in Section 7.10, the efficiencies of *D0(1.8%)*, *D02(1.8%)*, and *D03(1.8%,45°)* are estimated for $n = 5500$ rpm as follows:

$$\eta \approx \frac{\omega \overline{T}_o}{\omega \overline{T}_o + I_p^2 R + \overline{P}_{eddy} + \overline{P}_{hys}}. \tag{7.9}$$

The computed efficiencies of *D0(1.8%)*, *D02(1.8%)*, and *D03(1.8%,45°)* are 35.8 %, 33.8 %, and 32.7 %, respectively, see Table 7.1. It can be concluded that the implemented cogging torque reduction methods sightly reduce the calculated efficiency by 2–3 percentage points.

Remark 2: As per Section 9.2 and remarked in Section 7.10, the measured iron losses are significantly larger than the simulated ones (by a factor of 3 for $n =$

5500 rpm). Taking the extrapolated measured iron losses into account (P_{fe} = 695 mW for n = 5500 rpm), the efficiency of *D0(1.8%)* is reduced down to 28.6 %. Similar effects can be expected for *D02(1.8%)* and *D03(1.8%,45°)*.

Remark 3: The simulated average output torque $\overline{T}_o$ of *D0(1.8%)*, listed in Table 7.1, is verified analytically in the following using (1.12) and (1.13). As per (1.12), the average linear current density over a pole pitch of *D0(1.8%)* can be calculated as[9]

$$\overline{A}_{\tau_p} = \frac{2pz_Q I_{p,av}}{2\pi r_s} = \frac{2 \cdot 2 \cdot 208 \cdot 220\,\text{mA}}{2\pi \cdot 8\,\text{mm}} = 3641 \frac{\text{A}}{\text{m}}. \tag{7.10}$$

The average output torque $\overline{T}_o$ is the same as the average electromagnetic torque $\overline{T}_{em}$, because the average value of the cogging torque is zero (neglecting the hysteresis torque). Using (1.13), the average output torque can be estimated as[10]

$$\begin{aligned} \overline{T}_o = \overline{T}_{em} &= 2\pi r_s^2 l_{ax} \overline{A}_{\tau_p} \overline{B}_{\delta,PM} \\ &= 2\pi \cdot (8\,\text{mm})^2 \cdot 5.25\,\text{mm} \cdot 3641 \frac{\text{A}}{\text{m}} \cdot 0.148\,\text{T} = 1.14\,\text{mN} \cdot \text{m}, \end{aligned} \tag{7.11}$$

which is in good congruity with the simulated $\overline{T}_o$ of *D0(1.8%)*, listed in Table 7.1.

7.12 Analysis of the Thermal Behavior

This section investigates the steady-state and transient thermal performances of the *Baseline*, *D2*, and *D3(45°)* because, due to the removal of iron material in *D2* and *D3(45°)*, the iron cooling surfaces of all three stators differ. For the thermal analyses, the ratio of the overtemperature in Kelvin to the total loss in Watts is determined, as described in [33]. The overtemperature refers to the winding compared to the ambient temperature. Thereby, the overall thermal behavior of the motor can be determined by rather simple analysis. As discussed in Appendix H, the corresponding thermal equivalent circuit comprises only one thermal resistance and one thermal capacitance, the parameters of which are determined in this section. Both 3-D finite-element and experimental analyses are carried out to determine the equivalent thermal resistances and capacitances.[11] The used measurement setup is illustrated

[9] $z_Q = N$, $2p = 4$, $I_{p,av}$ = 220 mA (according to Fig. 7.16), r_s = 8 mm.

[10] r_s = 8 mm, $\overline{B}_{\delta,PM}$ = 148 mT (see Appendix R), $l_{ax} \approx$ 5.25 mm (average of w_{claw} and l_{PM}).

[11] The measurement results have been used to adapt the combined heat transfer coefficient h_{th} in the finite-element model, which characterizes the heat transfer to the analysis model surroundings. As discussed in Subsection 3.1.2, h_{th} is assumed constant and set to 30 W/m^2/K for the simulations.

in Figs. 3.13(a) and (b). (Additional thermal analyses are presented in Appendix T, including the investigation of the transient temperature drop of the *Baseline* for different input losses, the influence of the rotor cup on the thermal performance of the motor, and the thermal characterization of the winding alone.)

Finite-Element Model

Fig. 7.19 illustrates the finite-element model used to study the thermal performance of the *Baseline*, which is described in detail in Subsection 3.1.2.

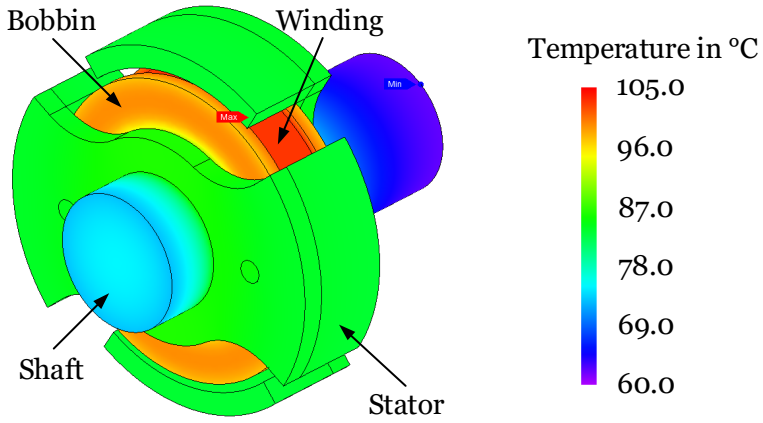

Fig. 7.19: Thermal finite-element model of the *Baseline*; visualized with JMAG® [91].

Simulation and Experimental Results

Fig. 7.19 shows the steady-state thermal contour plot of the *Baseline* for $T_A = 60°C$ and $P_{Cu} = 1\,W$.[12] As expected, the winding is the hottest part with a temperature T_{coil} of about 100°C while the stator parts have a temperature of about 85°C. Dissipating a power of 1 W in the motor winding causes an overtemperature of the winding of about 40 K, which leads, according to (H.1), to an equivalent thermal resistance R_{th} of approximately 40 K/W. A detailed analysis is presented in the following:

Fig. 7.20 exhibits the simulated and measured transient temperatures of the *Baseline* for $I_{DC} = 0.6\,A$ at $T_A = 30°C$. The temperature increases from 30°C to about 69°C. As the electrical resistance of the winding increases with increasing temperature,

[12] The maximum losses to be expected in the claw-pole motor are below 1 W, consisting mostly of copper losses.

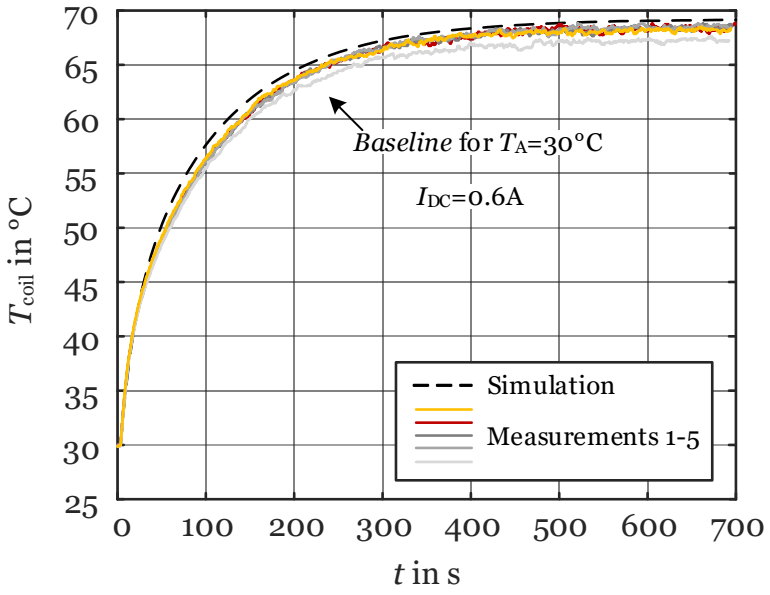

Fig. 7.20: Calculated and measured transient temperatures of the *Baseline*.

the input power is not constant for a constant current. In fact, the measured input power has been used as an input for the simulations. The dissipated steady-state losses amount to P_{cu} = 0.92 W. Several measurements are performed for repeatability, where the stator is disassembled and subsequently reassambled. The measurement and simulation results are in good agreement. Based on the transient temperature rise, the approximate thermal time constants τ_{th} can be determined. The *Baseline* reaches 63.2 % of the steady-state temperature within 60 s.

Fig. 7.21 shows the calculated and measured steady-state temperatures of the *Baseline* for different input losses and two different values of T_A. As expected, the steady-state temperature of the winding increases linearly with increasing P_{cu}. (For illustration, the results are interpolated linearly based on a least squares approximation.) As per (H.1), the equivalent thermal resistance is determined to $R_{th,A}$ = 42.4 K/W in the simulations for both ambient temperatures. The measured value of $R_{th,A}$, on the other hand, decreases slightly with increasing ambient temperature (by about 5 % for a ΔT_A of 30 K). This can be attributed to the heat transfer coefficients being temperature-dependent (they increase somewhat with increasing temperature). The results are presented in Table 7.2. Given the decreasing trend of $R_{th,A}$, as per (H.1) and (H.2), a steady-state winding temperature of below 140°C can be predicted for an ambient temperature of T_A = 100°C and P_{cu} = 1 W.

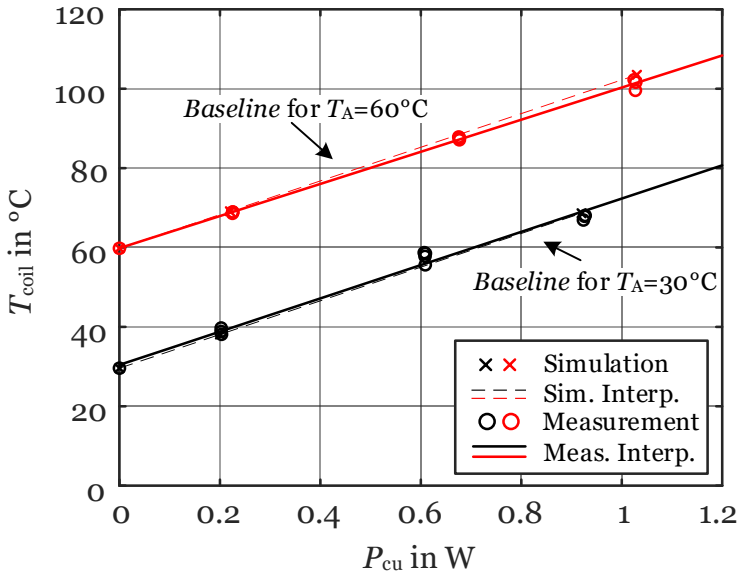

Fig. 7.21: Calculated and measured steady-state temperatures of the *Baseline*.

Table 7.2: Thermal Resistances of the *Baseline*, *D2*, and *D3(45°)*

	Simulation			Measurement		
T_A	$R_{th,Baseline}$	$R_{th,D2}$	$R_{th,D3(45°)}$	$R_{th,Baseline}$	$R_{th,D2}$	$R_{th,D3(45°)}$
°C	K/W	K/W	K/W	K/W	K/W	K/W
30	42.4	43.3	43.8	42.6	45.0	45.1
60	42.4	43.3	43.8	40.5	43.9	42.6

Based on the determined thermal time constants and resistances, the thermal heat capacitance C_{th} is calculated using (H.3). From the simulations, the thermal capacitance is estimated to $C_{th,A} = 1.42\,W \cdot s/K$ for $R_{th,A} = 42.4\,K/W$ and $\tau_{th,A} = 60\,s$. The thermal capacitances as determined from the simulations and measurements are presented in Table 7.3. The thermal capacitances determined from the measured

Table 7.3: Thermal Capacitances of the *Baseline*, *D2*, and *D3(45°)*

	Simulation			Measurement		
T_A	$C_{th,Baseline}$	$C_{th,D2}$	$C_{th,D3(45°)}$	$C_{th,Baseline}$	$C_{th,D2}$	$C_{th,D3(45°)}$
°C	K/W	K/W	K/W	K/W	K/W	K/W
30	1.42	1.43	1.45	1.77	1.54	1.59
60	1.42	1.43	1.45	1.93	1.69	1.79

temperatures generally increase with increasing ambient temperature (e.g., by 9 % for a ΔT_A of 30 K). This is explained by the thermal capacitance being a function of the temperature. (Note that, since the input losses are not constant during the transients due to the increase in the ohmic resistance of the winding, the determined value of τ_{th} is an approximate value.)

The calculated and measured steady-state temperatures of *D2* and *D3*(45°) are displayed in Figs. 7.22 and 7.23 for the studied input losses and ambient temperatures, showing good congruity. As expected, the steady-state temperatures increase

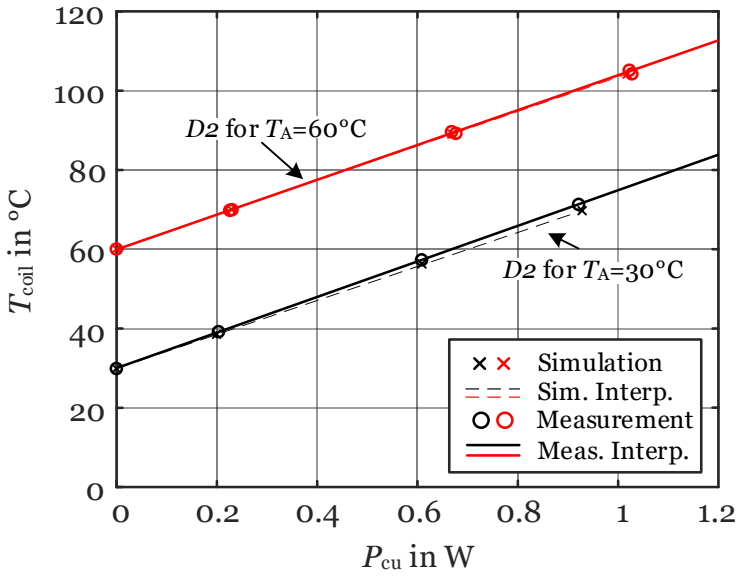

Fig. 7.22: Calculated and measured steady-state temperatures of *D2*.

linearly with increasing input losses, similar to Fig. 7.21. The respective thermal resistances of *D2* and *D3(45°)* are presented in Table 7.2, which are slightly higher than that of the *Baseline* (by 2–3 %). Again, the thermal resistances obtained from the measured temperatures slightly decrease with increasing ambient temperature. The determined equivalent thermal capacitances of *D2* and *D3(45°)* are also slightly higher than that of the *Baseline* (by 1–2 %), and they increase somewhat with increasing ambient temperature in the experiments, see Table 7.3.

Appendix T presents additional thermal analyses, the results of which are briefly summarized in the following: The transient temperature drop of the *Baseline* for different input losses essentially shows the inverse behavior of Fig. 7.20. By removing the claw-poles of the *Baseline*, the measured thermal resistance is determined to

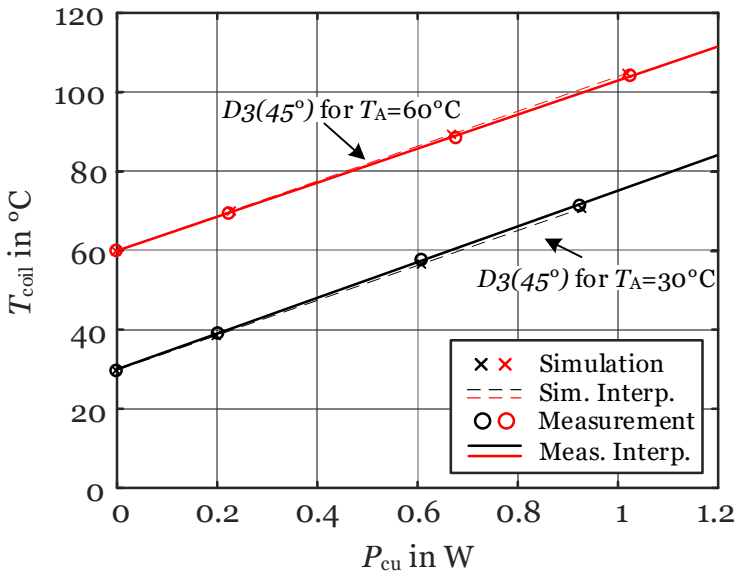

Fig. 7.23: Calculated and measured steady-state temperatures of *D3(45°)*.

43.2 K/W, similar to *D2* and *D3(45°)* at T_A = 60°C. When the rotor is placed on top of the stator, the thermal resistance increases by about 15 % to 50 K/W as the rotor builds a heat trap. Similar results have been obtained for the *Baseline*, *D2*, and *D3(45°)*. The thermal resistance of the winding alone, when placed on a wooden plate, is 70.3 K/W and 58.5 K/W for ambient temperatures of 30°C and 60°C, respectively.

Chapter Summary and Conclusions:

- The implementation of one auxiliary slot per claw-pole (*Design 2*), which is the same as the actual slot, can effectively modulate the cogging torque.
- The realized single-sided skew of 45° in addition to auxiliary slots (*Design 3*) can reduce the cogging torque of the *Baseline* by 70 % in both the simulations and measurements, at no increase to the manufacturing cost owing to the proposed punching layout.
- However, concurrently, the back-EMF peak value is reduced by about 12 %.
- The stator and rotor leakages increase by 14 % and 36 %, respectively, but the eddy current losses can be reduced by 10 % due to the auxiliary slots.
- The output torque ripple is reduced by 17 % and the efficiency is reduced by 8.6 %, while the average output torque hardly decreases because the drawn phase current increases.
- The *Baseline*, *Design 2*, and *Design 3* show similar thermal performance.

Hence, the proposed cogging torque reduction measures do not cause excessive heating.

Chapter 8

V-Skew (*D4*) and V-Skew with Auxiliary Slots (*D5*)

This chapter discusses the realization of V-skewed claw-poles (Design 4) to compensate for the axial forces induced by a single-sided skew such as in Design 1 and Design 3. Also, the implementation of auxiliary slots in addition to V-skewed claw-poles (Design 5) is investigated. It is shown how V-skewed claw-poles and V-skewed claw-poles with auxiliary slots can be realized in the steel sheet punching layout at no increase to the manufacturing cost. The effects are studied through 3-D finite-element simulations and experiments. The performance specifications and system parameters of the example case motors are presented in Tables A.1 and A.2.[1,2]

8.1 V-Skew – Principle

The implementation of a single-sided skew (independent of whether the rotor or the stator is skewed) generally causes axial magnetic forces F_a proportional to the tangential forces F_t and hence the output torque T_o [36]:

$$F_\mathrm{a} = F_\mathrm{t} \tan(\xi_\mathrm{skew}) = \frac{T_\mathrm{o}}{r_\delta} \tan(\xi_\mathrm{skew}), \tag{8.1}$$

where ξ_skew is the skewing angle and r_δ is the air-gap radius. As per (8.1), the extent of the axial forces increases with increasing ξ_skew. [The formation of axial forces induced by different skewing possibilities is discussed in Appendix U.]

[1] However, for the following analyses, the axial length of the claw-pole stator is increased to the same length as that of a comparable salient-pole motor of similar size (see e.g., [25]), taking the end-winding into account to yield more design flexibility with respect to the claw-pole shape. Thereby, the room for the winding is increased.

[2] Selected results of this chapter have also been published in [143].

Significant cogging torque reduction in SFHP single-phase PM motors, which typically have a low number of poles and slots, requires relatively large skewing angles (e.g., 30° or 45°) as discussed in the context of *Design 1* and *Design 3*. Implementing skewing angles between 30° and 45° yields axial forces in the range of the tangential forces [see *D1* in Fig. 6.3(b), where $F_\mathrm{a} = F_\mathrm{t}$ for $\xi_\mathrm{skew} = 45°$]. This can be especially unfavorable for single-phase PM motors, which are characterized by a large torque ripple, because then the axial forces also pulsate heavily, see (8.1).[3] Such pulsating axial forces indeed pose additional stress on the bearing system, decreasing its lifetime, and may induce disturbing noise.

To avoid the heavily fluctuating axial forces caused by a single-sided skew and still reduce the cogging torque, V-skewed claw-poles (*Design 4*) can be implemented. Fig. 8.1 shows an unrolled stator perimeter of a claw-pole motor with a V-skew.

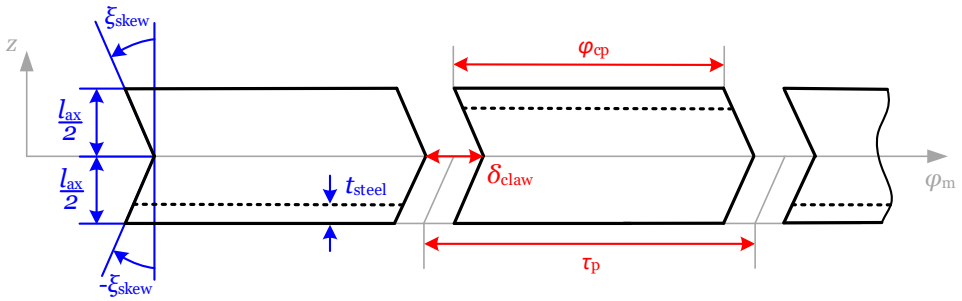

Fig. 8.1: Two consecutive poles of the unrolled stator perimeter of a claw-pole motor implemented with a V-skew (*Design 4*).

Owing to their V-shaped claw-pole edges, where positive and negative skewing angles are realized halfway through the axial length of the motor l_ax, the axial forces induced by the skewing are balanced as illustrated for one claw-pole edge below:

$$\begin{aligned} F_\mathrm{a} = \sum_{i=1}^{2} F_{\mathrm{a},i} = F_{\mathrm{a},1} + F_{\mathrm{a},2} &= \int_{-\frac{l_\mathrm{ax}}{2}}^{0} f_\mathrm{t} \tan(\xi_\mathrm{skew})\, dz + \int_{0}^{\frac{l_\mathrm{ax}}{2}} f_\mathrm{t} \tan(-\xi_\mathrm{skew})\, dz \\ &= f_\mathrm{t} \tan(\xi_\mathrm{skew}) \left[0 - \left(-\frac{l_\mathrm{ax}}{2}\right)\right] + f_\mathrm{t} \tan(-\xi_\mathrm{skew}) \left[\frac{l_\mathrm{ax}}{2} - 0\right] \\ &= f_\mathrm{t} \left[\tan(\xi_\mathrm{skew}) \frac{l_\mathrm{ax}}{2} + \tan(-\xi_\mathrm{skew}) \frac{l_\mathrm{ax}}{2}\right] \\ &= f_\mathrm{t} \frac{l_\mathrm{ax}}{2} \left[\tan(\xi_\mathrm{skew}) - \tan(\xi_\mathrm{skew})\right] = 0. \end{aligned} \tag{8.2}$$

[3] Considering a typical peak output torque of about 2 mN · m (see, e.g., Figs. 5.9 and 7.17), yields peak axial forces of about 0.25 N, when $\xi_\mathrm{skew} = 45°$ and $r_\delta = 8$ mm.

8.2 V-Skew – Steel Sheet Punching Layout

Based on the punching layout of the *Baseline* shown in Fig. 2.5(a), Fig. 8.2 illustrates how to account for a V-skew, in which positive and negative skewing angles (i.e., $\pm\xi_{\text{skew}}$) are realized halfway through the axial length of the motor.

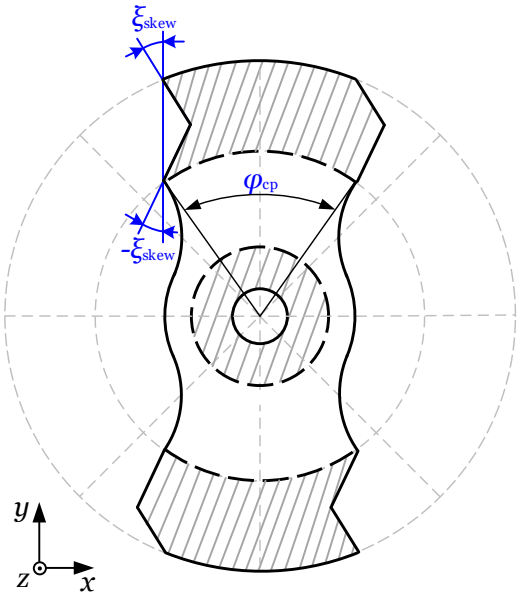

Fig. 8.2: Steel sheet punching layout for the realization of a V-skew (*Design 4*).

Remark 1: Implementing a V-skew, the stator top and bottom parts must be manufactured with mirror-symmetry, such that the stator parts mesh appropriately and identical inter-claw regions are obtained.

Remark 2: Depending on φ_{cp}, the motor should be designed such that the two stator parts can be assembled easily without having to tilt one of the stator parts. Hence, the maximum skewing angle is limited for a constant claw-pole angle φ_{cp}.

8.3 V-Skew with Auxiliary Slots – Principle

Based on *Design 2*, the V-skewed claw-poles shown in Fig. 8.1 can also be implemented with auxiliary slots to modulate the cogging torque frequency, as derived in (7.1). Fig. 8.3 shows two consecutive poles of the unrolled stator perimeter of a claw-pole motor with a V-skew and auxiliary slots.

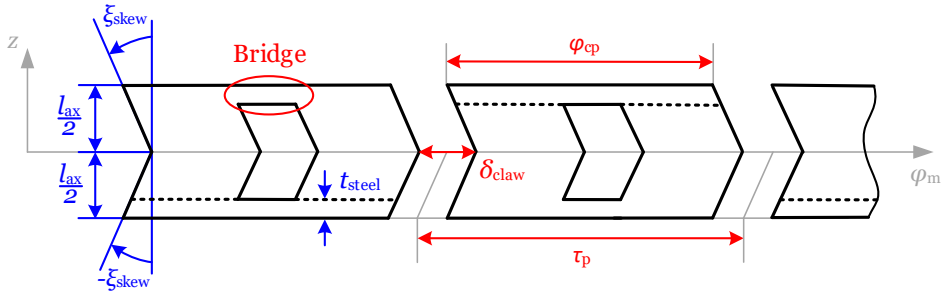

Fig. 8.3: Two consecutive poles of the unrolled stator perimeter of a claw-pole motor implemented with a V-skew and auxiliary slots (*Design 5*).

As discussed in Chapter 7, optimally, the auxiliary slots should have the same shape and width as the actual slots and should be located right in the middle of the claw-pole. Again, the bridge indicated in Fig. 8.3 can prevent claw deformation during the deep-drawing process. Auxiliary slots can modulate the cogging torque to help reduce the cogging torque by skewing like in *Design 3*. Hence, it is expected that implementing a V-skew with auxiliary slots (*Design 5*) can reduce the cogging torque more effectively than only V-skewed claw-poles (*Design 4*).

8.4 V-Skew and Auxiliary Slots – Steel Sheet Punching Layout

Based on the punching layout of *Design 4* in Fig. 8.2, Fig. 8.4 shows how to implement V-skewed claw-poles with auxiliary slots.

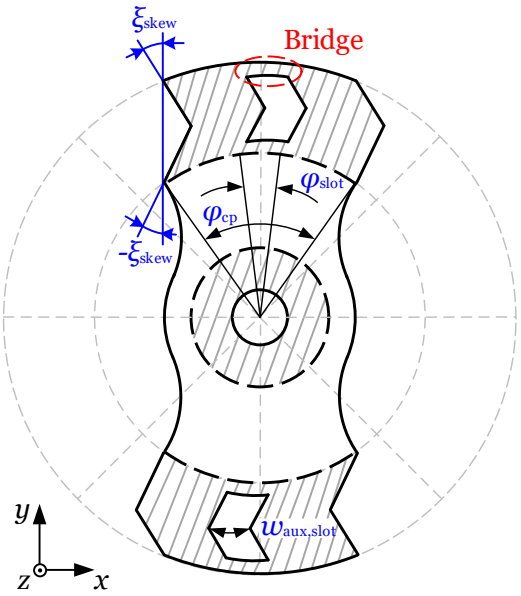

Fig. 8.4: Steel sheet punching layout for the realization of a V-skew with auxiliary slots (*Design 5*).

Remark: See *Remark 1* and *Remark 2* in Section 8.2.

8.5 Finite-Element Models and Prototypes

Fig. 8.5 shows the finite-element models used to study the effects of a V-skew (*Design 4*) and its combination with auxiliary slots (*Design 5*). The presented models are implemented with increased axial length compared to those used in Chapters 5, 6, and 7, to obtain more design flexibility with respect to the claw-pole shape. The axial length is equal to that of a comparable salient-pole motor of similar size (see e.g., [25]), taking the length of its end-winding into account. Hence, the models which have increased axial length are denoted with an asterisks: *Baseline**, *D1*(45°)*, *D4*(30°)*, and *D5*(30°)*.

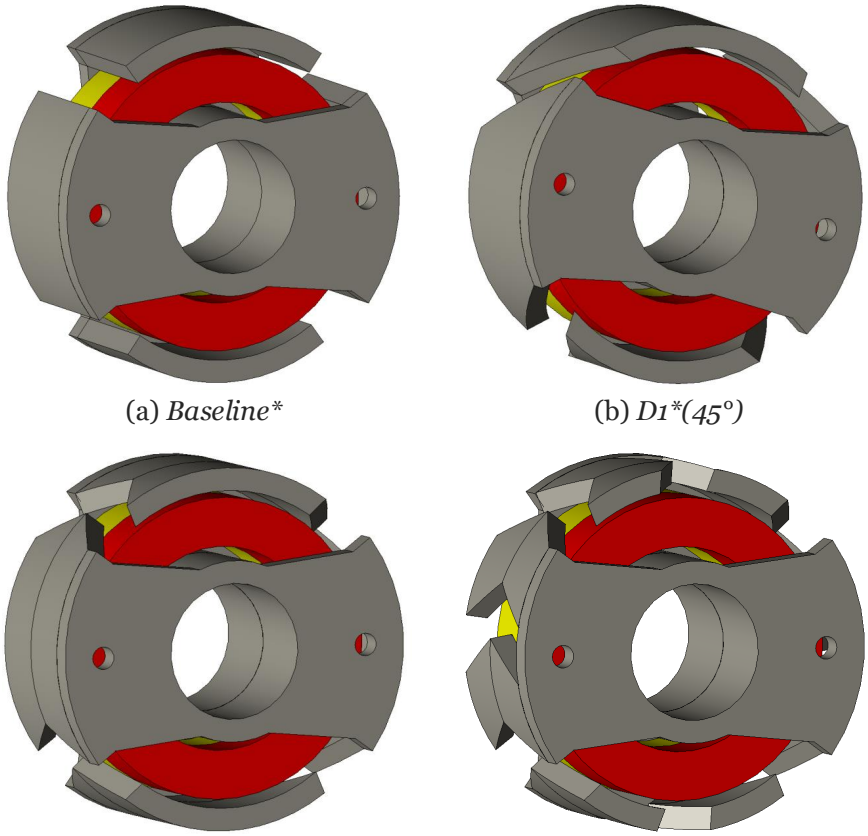

(a) *Baseline** (b) *D1*(45°)*

(c) *D4*(30°)* (d) *D5*(30°)*

Fig. 8.5: Finite-element models to study the effects of a V-skew (*Design 4*) and a V-skew with auxiliary slots (*Design 5*); visualized with JMAG® [91].

Fig. 8.6 exhibits the manufactured prototype stator parts of the *Baseline**, *D1*(45°)*, *D4*(30°)*, and *D5*(30°)* in accordance with the finite-element models from Fig. 8.5.

*Baseline** *D1*(45°)* *D4*(30°)* *D4*(45°)*

Fig. 8.6: Prototype stator parts milled from free-cutting steel 11SMnPb37 to investigate *Design 4* and *Design 5*.

8.6 Analysis of the Cogging Torque

The effect of a V-skew (*Design 4*) and a V-skew with auxiliary slots (*Design 5*) on the cogging torque is studied below. 3-D finite-element simulations are performed, which are subsequently verified by measurements with the rheometer.

Simulation Results

Fig. 8.7 shows the computed cogging torque waveforms of the *Baseline**, *D1*(30°)*, *D4*(30°)*, and *D4*(45°)*. Given the *Baseline**, which has a peak value of 0.8 mN · m, the

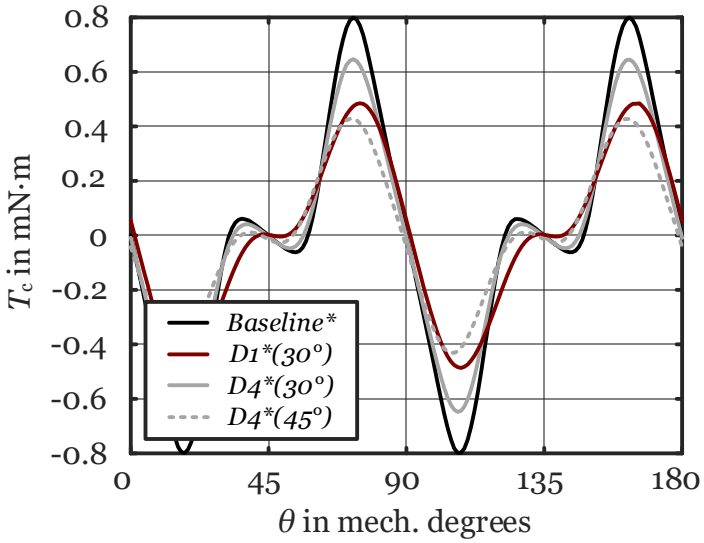

Fig. 8.7: Computed cogging torque waveforms of the *Baseline**, *D1*(30°)*, *D4*(30°)*, and *D4*(45°)*.

cogging torque is reduced by 39.4 % in *D1*(30°)*. However, *D4*(30°)*, which has the same skewing angle, can reduce the cogging torque of the *Baseline** by only 19.2 %, since the effective skewing reaches only halfway through the axial length of the motor (see Fig. 8.1). [However, as discussed in Section 8.8, unlike *D1*(30°)*, *D4*(30°)* has compensated axial forces.] To yield about the same cogging torque reduction as *D1*(30°)*, the skewing angle must be increased, see *D4*(45°)* in Fig. 8.7.

Fig. 8.8 shows the computed cogging torque waveforms of the *Baseline**, *D5*(30°)*, and *D5*(55°)*. Compared to the *Baseline**, the cogging torque is reduced by 19.7 % and 44 % in *D5*(30°)* and *D5*(55°)*, respectively. As expected, auxiliary slots can modulate the cogging torque. Contrary to expectations, *D4*(30°)* is more effective in reducing

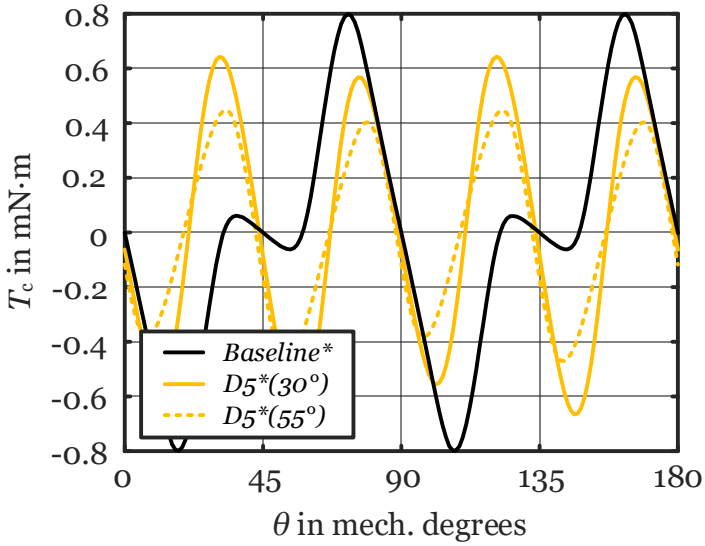

Fig. 8.8: Computed cogging torque waveforms of the *Baseline**, *D5*(30°)*, and *D5*(55°)*.

the cogging torque peak-to-peak value than *D5*(30°)*,[4] contrasting Figs. 8.7 and 8.8. Increasing the skewing angle further, see *D5*(55°)*, can yield a similar reduction. This behavior can be attributed to the pitch of the maximum radial magnetization (see Fig. P.2) being in the range of a V-skewed claw-pole half [see Fig. 8.5(d)]. In a motor in which the PMs on the rotor have a parallel magnetization pattern, *D5*(30°)* may be more effective than *D4*(30°)* in reducing the cogging torque.

Experimental Results

Fig. 8.9 shows the measured cogging torque waveforms[5] of the *Baseline** and *D1*(45°)*. The cogging torque peak value of the *Baseline**, which is about 0.45 mN · m, is reduced by about 67 % in *D1*(45°)* due to the single-sided skew.

[4] This is true for the studied motor dimensions and radial magnetization pattern in which $\alpha = 24°$. In other designs, *D5*(30°)* may be more effective in reducing the cogging torque than *D4*(30°)*.

[5] The cogging torque is extracted from the measured no-load torque waveforms in the CW and CCW directions, as discussed in Subsection 3.2.3 in detail.

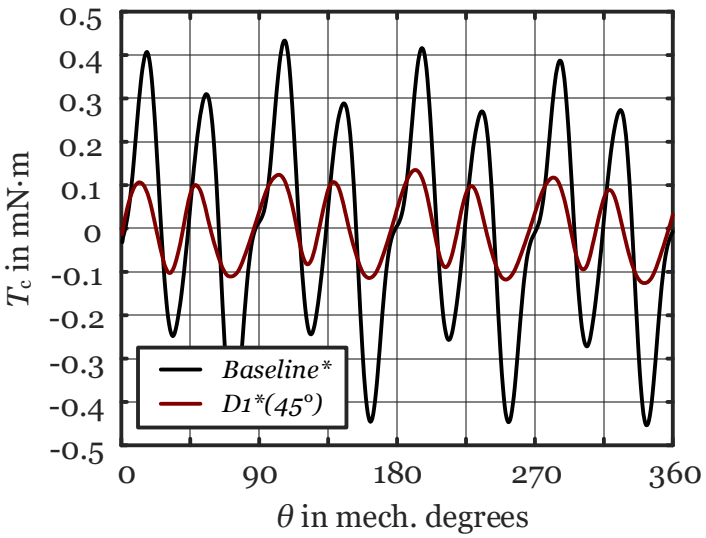

Fig. 8.9: Measured cogging torque waveforms of the *Baseline** and *D1*(45°)*.

Fig. 8.10 exhibits the measured cogging torque waveforms[5] of the *Baseline**, *D4*(30°)*, and *D4*(45°)*. The implemented V-skews in *D4*(30°)* and *D4*(45°)* can reduce the

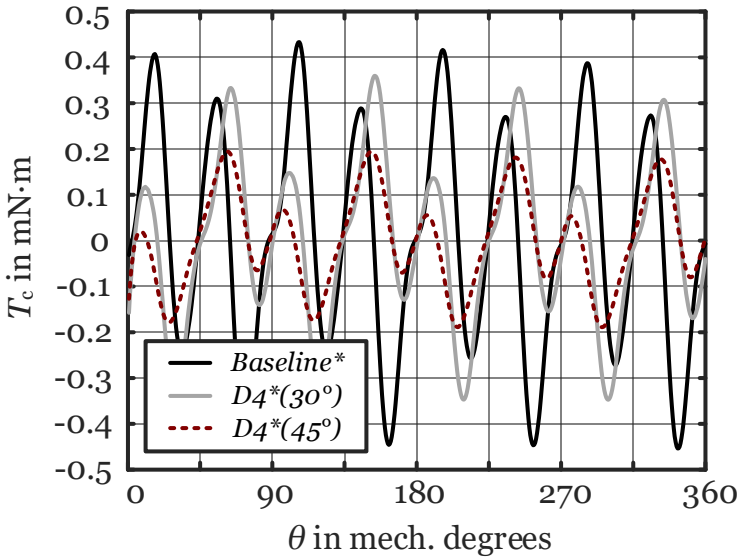

Fig. 8.10: Measured cogging torque waveforms of the *Baseline**, *D4*(30°)*, and *D4*(45°)*.

measured cogging torque of the *Baseline** by 22.2 % and 56.4 %, respectively. The measured cogging torque waveforms deviate notably from the simulated ones in amplitude and harmonic content. This may be caused by material parameter uncertainties such as those introduced by the manufacturing of the prototypes.

8.7 Analysis of the Back-EMF

The effect of a V-skew (*Design 4*) and its combination with auxiliary slots (*Design 5*) on the back-EMF is studied below through 3-D finite-element simulations.

Simulation Results

Fig. 8.11 illustrates the computed back-EMF waveforms of the *Baseline**, *D1*(30°)*, *D4*(30°)*, and *D4*(45°)*. The computed back-EMF of the *Baseline** has a peak value

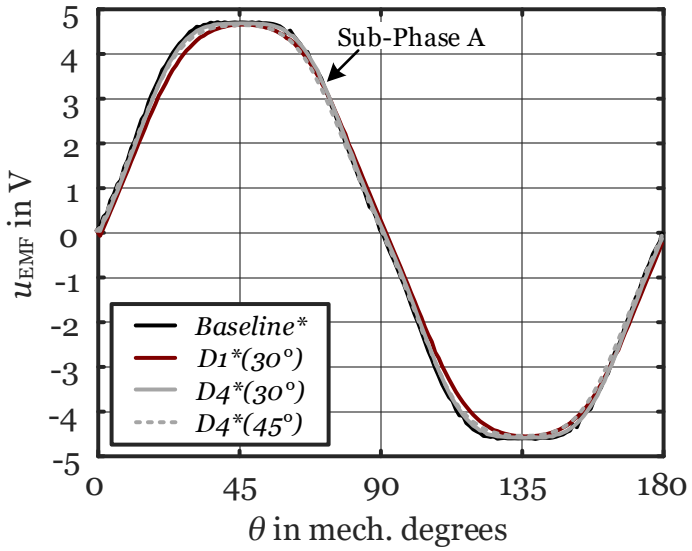

Fig. 8.11: Computed back-EMF waveforms of *Baseline**, *D1*(30°)*, *D4*(30°)*, and *D4*(45°)*.

of 4.65 V, which is reduced by 1.1 % in *D1*(30°)* due to the implemented single-sided skew of $\xi_{\text{skew}} = 30°$. However, the back-EMF reductions in *D4*(30°)* and *D4*(45°)* amount to only 0.36 % and 1.3 %, respectively. Hence, compared to *D1*(30°)*, the leakage flux is significantly reduced in *D4*(30°)* for the same skewing angle.

Fig. 8.12 depicts the computed back-EMF waveforms of the *Baseline**, *D5*(30°)*, *D5*(45°)*, and *D5*(55°)*. Due to the auxiliary slots in *D5*(30°)*, the back-EMF peak value of the *Baseline** is reduced by 20 %. For increasing ξ_{skew}, the back-EMF can have serious dips in *D5*(45°)* and *D5*(55°)* due to the auxiliary slots and implemented V-skew, which can adversely affect the current and hence the motor performance.

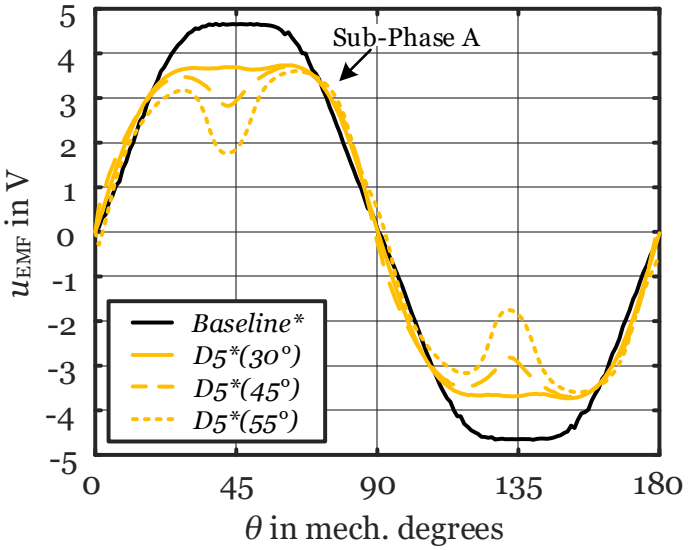

Fig. 8.12: Computed back-EMF waveforms of the *Baseline**, *D5*(30°)*, *D5*(45°)*, and *D5*(55°)*.

8.8 Analysis of the Axial Forces

The effect of a V-skew (*Design 4*) and its combination with auxiliary slots (*Design 5*) on the axial forces is studied for the no-load condition below. 3-D finite-element simulations are performed, which are subsequently verified by measurements with the rheometer shown in Fig. 3.6.

Simulation Results

Fig. 8.13 shows the computed axial forces of the *Baseline**, *D1*(30°)*, *D4*(30°)*, and *D5*(30°)* in the no-load condition. In congruity with (8.1), the axial forces of the *Baseline** are essentially zero. The single-sided skew in *D1*(30°)*, however, exhibits heavily fluctuating axial forces of the same shape as the cogging torque, with a peak value of 36.5 mN. [See (8.1), where the axial forces have the same shape as the cogging torque, since $T_o = T_c$ in the no-load condition.] Unlike *D1*(30°)*, both *D4*(30°)* and *D5*(30°)* have compensated axial forces, similar to those of the *Baseline**, and still reduce the cogging torque.[6]

[6]The axial forces of the *Baseline*, *D4*(30°)*, and *D5*(30°)* in Fig. 8.13 are not exactly zero due to geometric and numerical errors.

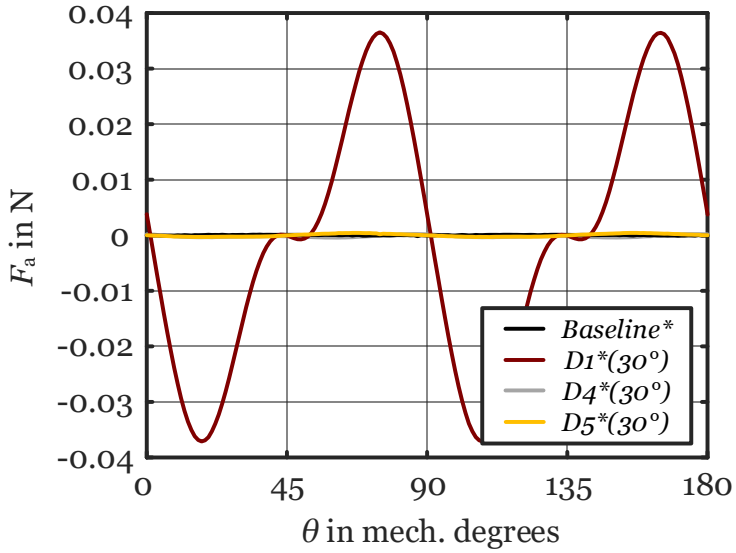

Fig. 8.13: Computed axial forces of the *Baseline**, *D1*(30°)*, *D4*(30°)*, and *D5*(30°)*.

Fig. 8.14 depicts the order analysis of selected calculated axial forces from Fig. 8.13, where k is the harmonic order. While the harmonics of the *Baseline** and *D4*(30°)* are

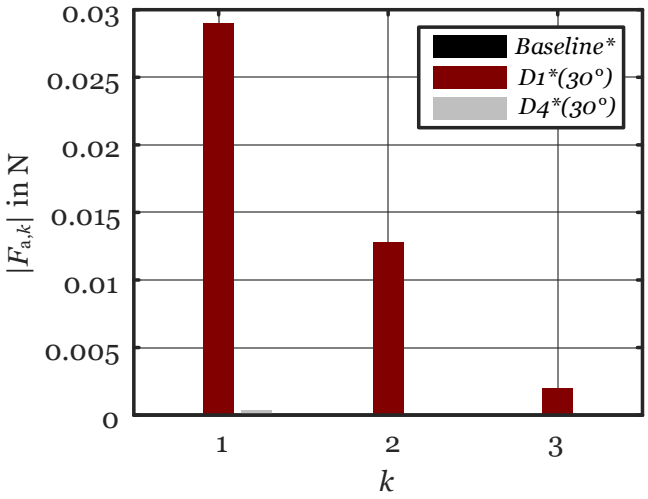

Fig. 8.14: Order analysis of selected computed waveforms from Fig. 8.13.

essentially zero, the induced axial forces in *D1*(30°)*–as a result of the single-sided skew–consist of distinct first, second, and third order harmonic components. This corresponds to fourth, eighth, and twelfth order harmonic components with respect to the one revolution of the motor, due to its slot-pole combination.

Experimental Results

Fig. 8.15 exhibits the order analysis in pu of the measured axial forces of the *Baseline**, *D1*(30°)*, and *D4*(30°)* depicting the first, second, and third harmonic components in accordance with Fig. 8.14.[7]

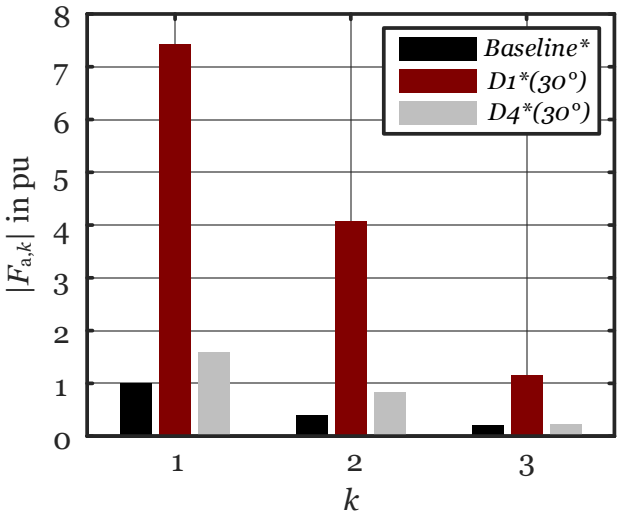

Fig. 8.15: Order analysis of the measured axial forces of *Baseline**, *D1*(30°)*, and *D4*(30°)*.

As opposed to the simulation results, the measured axial forces in the fabricated prototype of the *Baseline** are not exactly zero. This may be due to manufacturing imperfections and uncertainties, or inaccuracies and misalignments in the test setup. However, compared to the *Baseline**, the first, second, and third order harmonic components of the axial forces increase at least sevenfold in *D1*(30°)*. In *D4*(30°)*, yet, the axial forces induced in *D1*(30°)* caused by the single-sided skew are reduced by at least 78 % due to the V-shape of the claw-poles, and still reduce the cogging torque.

[7] The order analysis is presented in pu because the measured axial forces deviated from the simulated ones in amplitude and harmonic content, featuring distinct low order harmonics which may result from misalignments in the test setup. To still allow for a comparison with the simulation results, the harmonic components of interest have been extracted from the measured axial forces.

Chapter Summary and Conclusions:

- The implementation of a single-sided skew (*Design 1*) induces axial magnetic forces proportional to the output torque.
- The proposed V-skew (*Design 4*) has (ideally) balanced axial forces.
- Combining the V-skew with auxiliary slots (*Design 5*) can modulate and reduce the cogging torque, while (ideally) having balanced axial forces.
- Due to the positive and negative skewing angles in *Design 4* and *Design 5*, the effect of the cogging torque reduction is reduced, because the effective skewing reaches only halfway through the axial length of the motor.

Chapter 9

Further Rheometer-Based Experimental Analyses

This chapter expands on the theory developed in Subsections 3.2.2, 3.2.3, and 3.2.4, and on the investigations in Chapters 5–8, by further experimentally investigating the cogging torque, the hysteresis torque, and the iron losses of SFHP PM motors in detail.[1] *Therefore, the measured no-load torque waveforms of two claw-pole motor designs, the Baseline and D0(1.8%), are elaborated upon. In addition, a salient-pole motor design, referred to as S0(2.8%) which has a relative air-gap asymmetry of* 2.8%*, is investigated for comparison. First, it is shown how the cogging torque and the hysteresis torque waveforms can be extracted from the measured no-load torque waveforms in the CW and CCW directions at a speed of 1 rpm. The obtained cogging torque waveforms are compared with those obtained from 3-D finite-element simulations. Second, it is shown how the investigation of the measured no-load torque waveforms at elevated speeds enables an iron loss determination and separation, by studying the change in the observed offset torque.*[2]

9.1 Cogging Torque and Hysteresis Torque Determination

This section presents the determined cogging torque and hysteresis torque waveforms of the claw-pole motors *Baseline* and *D0(1.8%)*, see Fig. 3.3(a), and the salient-

[1] In contrast to the measured no-load torque waveforms from Figs. 6.7 and 7.9 in Chapters 6 and 7, which are a superposition of the cogging torque and the hysteresis torque, this chapter shows how to separate the cogging torque from the hysteresis torque. Yet, the measured torque waveforms from Figs. 8.9 and 8.10 in Chapter 8 are obtained based on the methods presented in this chapter.

[2] Selected results of this chapter have also been published in [142, 156].

pole motor *S0(2.8%)*, see Fig. 3.3(b). Therefore, the no-load torque waveforms in the CW and CCW are measured at very low speed and subsequently used to extract the cogging torque and hysteresis torque waveforms.

9.1.1 No-Load Torque Measurements at Very Low Speed

For the no-load torque measurements, the rheometer is operated in the CSR mode (see Subsection 3.2.2) at a very low rotational speed of $n = 1\,\text{rpm}$ in the CW and CCW directions consecutively. A full rotor rotation ($0° \leq \theta \leq 360°$) is divided into 600 measuring points, which results in an angular resolution of 0.6°, sufficient to detect the expected torque harmonics. Based on Fig. 3.6, Figs. 9.1(a) and (b) show the respective test setups of the claw-pole motor and the salient-pole motor [see Figs. 3.3(a) and (b)] used in this chapter. (The measured runout accuracies are reported in Appendix L.)

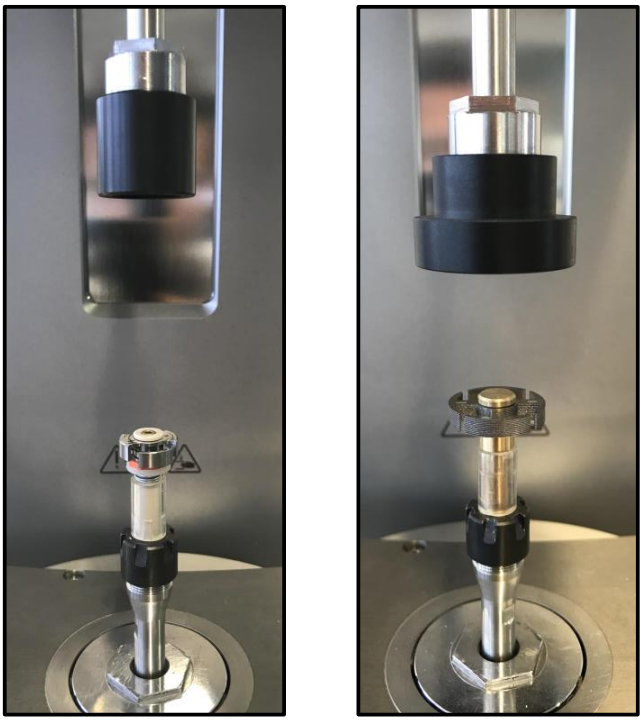

(a) (b)

Fig. 9.1: Rheometer test setups: (a) claw-pole motor and (b) salient-pole motor.

Analysis of the No-Load Torque of the *Baseline*

Fig. 9.2 shows the measured no-load torque waveforms of the *Baseline* [see Fig. 9.1(a)] in the CW and CCW directions. The CW and CCW torque waveforms are very

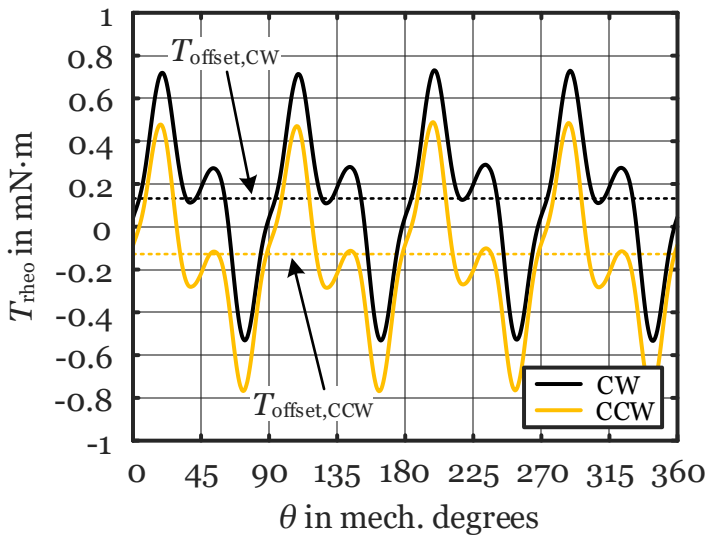

Fig. 9.2: Measured no-load torque waveforms of the *Baseline* at $n = 1$ rpm in the CW and CCW directions.

similar; yet, they are offset to a certain extent. The offset torque component T_{offset} is $+0.14\,\text{mN}\cdot\text{m}$ for the CW direction and $-0.139\,\text{mN}\cdot\text{m}$ for the CCW direction. This offset is solely caused by the hysteresis torque[3] which is acting against the direction of rotation causing losses, see Subsections 3.2.2 and 9.2.1. As per (3.8), the offset is equal to the average hysteresis torque ($T_{offset,CW} = \overline{T}_{hys,CW} = +0.14\,\text{mN}\cdot\text{m}$ and $T_{offset,CCW} = \overline{T}_{hys,CCW} = -0.139\,\text{mN}\cdot\text{m}$).

Analysis of the No-Load Torque of *D0(1.8%)*

Fig. 9.3 shows the measured no-load torque waveforms of *D0(1.8%)* [see Fig. 9.1(a)] in the CW and CCW directions. While also offset ($T_{offset,CW} = \overline{T}_{hys,CW} = +0.1424\,\text{mN}\cdot\text{m}$ and $T_{offset,CCW} = \overline{T}_{hys,CCW} = -0.1421\,\text{mN}\cdot\text{m}$), the CW and CCW torque waveforms differ obviously for *D0(1.8%)* which has an asymmetric air-gap. The results indicate that, while the absolute value of T_{offset} is essentially the same for the CW and CCW

[3] This is due to the very low rotational speed of $n = 1$ rpm and hence the absence of eddy current effects.

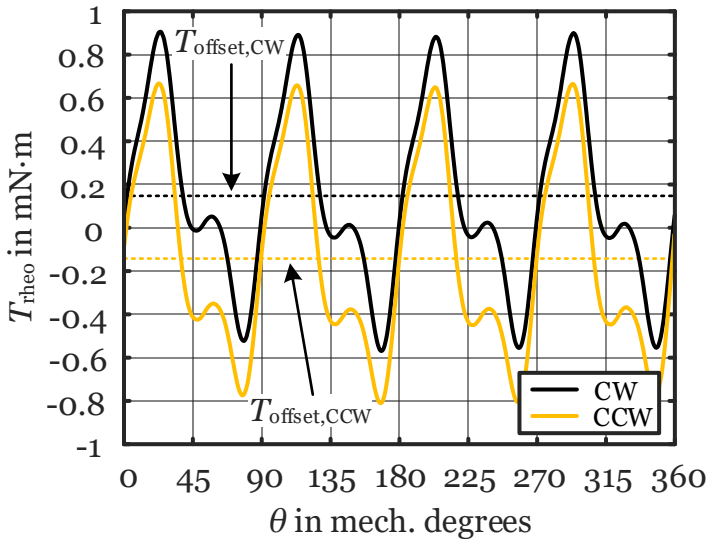

Fig. 9.3: Measured no-load torque waveforms of *D0(1.8%)* at $n = 1$ rpm in the CW and CCW directions.

directions (and hence $\overline{T}_{\text{hys}}$), the actual hysteresis torque waveform T_{hys} differs for the CW and CCW directions. The hysteresis torque waveform is investigated in Subsection 9.1.2 in detail.

Analysis of the No-Load Torque of *S0(2.8%)*

Fig. 9.4 shows the measured no-load torque waveforms of *S0(2.8%)* [see Fig. 9.1(b)] in the CW and CCW directions. As expected, the measured waveforms for the CW and CCW directions slightly differ and are offset ($T_{\text{offset,CW}} = \overline{T}_{\text{hys,CW}} = +0.0848\,\text{mN}\cdot\text{m}$ and $T_{\text{offset,CCW}} = \overline{T}_{\text{hys,CCW}} = -0.0850\,\text{mN}\cdot\text{m}$).

Notice that $\overline{T}_{\text{hys}}$ of *S0(2.8%)* is about 40 % lower than that of *D0(1.8%)*. This is due to the high quality steel (i.e., M250-35A) used for *S0(2.8%)* compared to the free-cutting steel (i.e., 11SMnPb37) used for *D0(1.8%)*; the free-cutting steel features a larger hysteresis area and hence larger hysteresis losses for the same operating frequency, see (1.24). The reduced run-out accuracy of the salient-pole motor setup in Fig. 9.1(b) compared to that of the claw-pole motor in Fig. 9.1(a), as reported in Subsection 3.2.2, is reflected in a marginal asymmetry in the measured torque peaks. (The peaks slightly decrease from left to right.)

Remark: As mentioned in Chapter 5, an asymmetric air-gap is often introduced in single-phase PM motors for self-starting capability, by which a preferred rotational

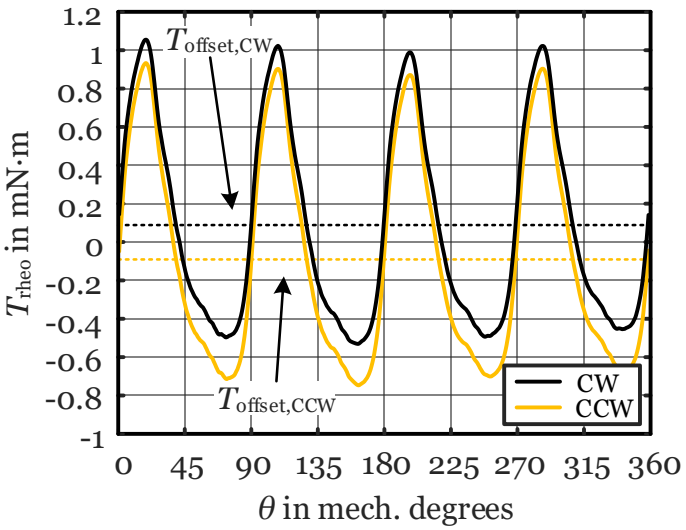

Fig. 9.4: Measured no-load torque waveforms of *S0(2.8%)* at $n = 1$ rpm in the CW and CCW directions.

direction is created. Hence, experimentally investigating unidirectional single-phase PM motors with an asymmetric magnetic design, it is important to consider the measured no-load torque waveform in the designed rotational direction of the motor [for both *D0(1.8%)* and *S0(2.8%)* this is the respective CCW waveform in Figs. 9.3 and 9.4], as the motor typically cannot operate in the reverse direction.

9.1.2 Cogging Torque and Hysteresis Torque Analyses

Based on Subsection 3.2.3, this subsection presents the extracted cogging torque and hysteresis torque waveforms based on the measured CW and CCW torque waveforms in Figs. 9.2, 9.3, and 9.4. As the no-load torque measured by the rheometer T_{rheo} represents the superposition of the cogging torque and the hysteresis torque for very low speeds, a separation thereof can be carried out according to (3.9) and (3.10). In addition, the experimentally determined cogging torque waveforms are compared with those obtained from 3-D finite-element simulations.

Analysis of the Cogging Torque and the Hysteresis Torque of the *Baseline*

As per (3.9) and (3.10), Fig. 9.5 shows the determined cogging torque T_{c} and hysteresis torque T_{hys} waveforms of the *Baseline* based on the measured torque waveforms from Fig. 9.2, which are indicated by the dashed lines for reference. Notice that T_{hys} is

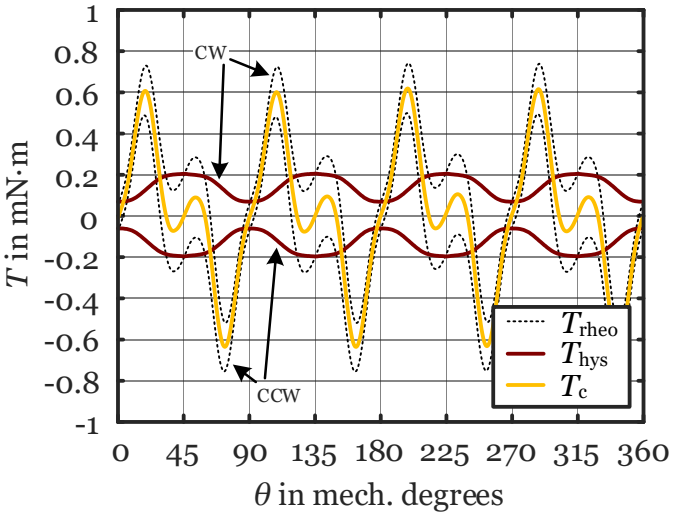

Fig. 9.5: Determination of the cogging and hysteresis torque of the *Baseline* based on T_{rheo} from Fig. 9.2 using (3.9) and (3.10).

rotor position-dependent as a result of the stator slots;[4] yet, its average value $\overline{T}_{\text{hys}}$ is equal to the offset determined in Fig. 9.2. As expected and discussed in the context of (1.17) and (1.16), the average of T_{c} is zero. For comparison, Fig. 9.6 contrasts the experimentally determined cogging torque of the *Baseline* from Fig. 9.5 with the simulated one. The waveforms generally agree well; yet, the measured peak-to-peak value is about 17 % lower than the simulated one obtained from 3-D FEA.

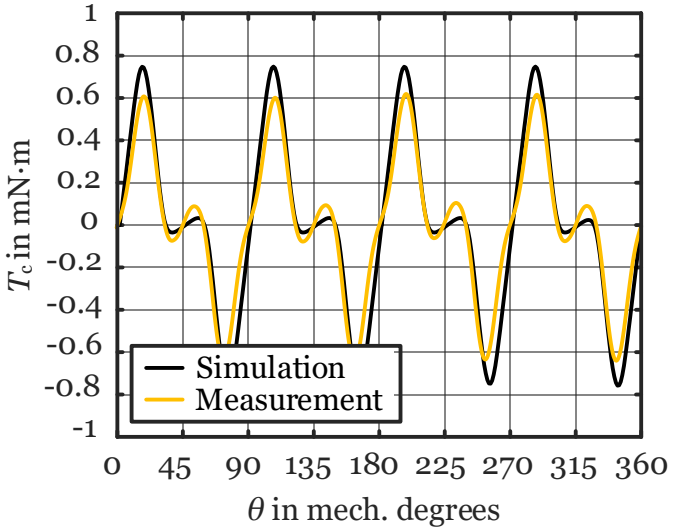

Fig. 9.6: Simulated cogging torque waveform of the *Baseline* from 3-D finite-element simulations versus measured cogging torque from Fig. 9.5.

[4] A PM motor without slots has a constant hysteresis torque, similar to a hysteresis motor.

Analysis of the Cogging Torque and the Hysteresis Torque of *D0(1.8%)*

Fig. 9.7 shows the determined T_c and T_{hys} of *D0(1.8%)* based on Fig. 9.3. Again, T_{hys} is rotor position-dependent, $\overline{T}_{hys}$ is equal to the offset in Fig. 9.3, and $\overline{T}_c$ is zero.

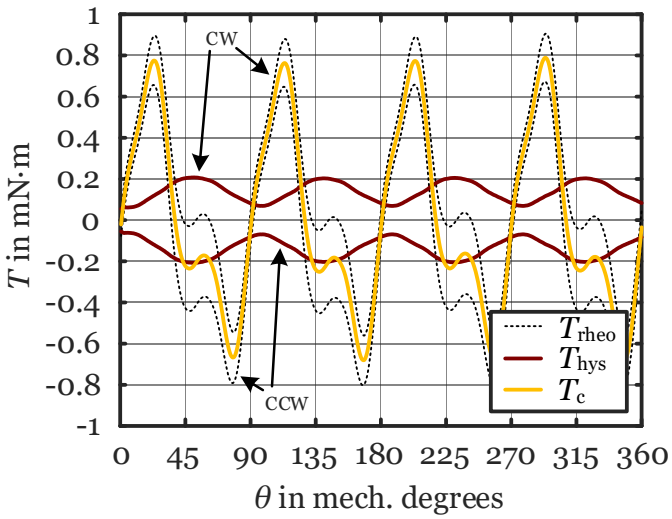

Fig. 9.7: Determination of the cogging and hysteresis torque of *D0(1.8%)* based on T_{rheo} from Fig. 9.3 using (3.9) and (3.10).

For comparison, Fig. 9.8 contrasts the measured cogging torque from Fig. 9.7 with the simulated one, showing a peak-to-peak deviation below 2 %.

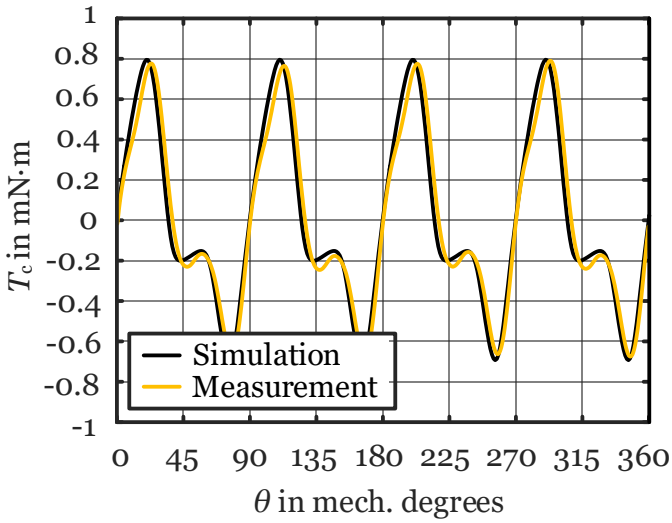

Fig. 9.8: Simulated cogging torque waveform of *D0(1.8%)* from the 3-D finite-element simulations versus measured cogging torque from Fig. 9.7.

Analysis of the Cogging Torque and the Hysteresis Torque of *S0(2.8%)*

Fig. 9.9 depicts the determined T_c and T_{hys} of *S0(2.8%)*. T_{hys} is slightly rotor position-dependent and $\overline{T}_{hys}$ is equal to the offset determined in Fig. 9.4. The measured T_c is in close congruity with the simulations, see Fig. 9.10. The peak-to-peak value of the measured cogging torque is about 7 % higher than the simulated one. The differences are attributed to the influence of the interlocking as identified in measurements of a salient-pole motor with glued laminations not reported in this thesis.

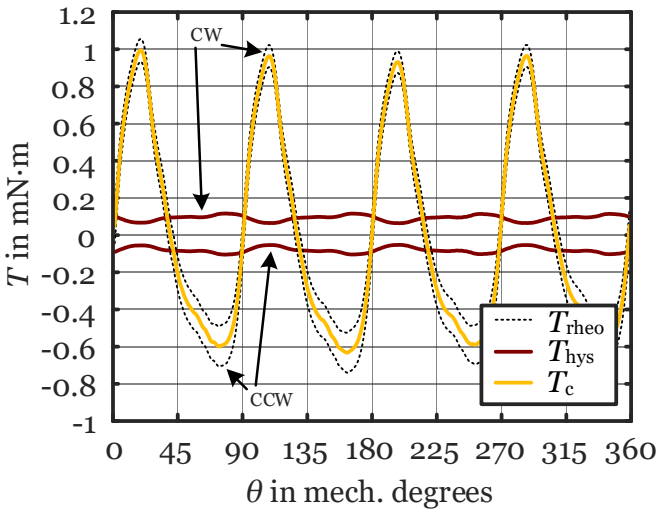

Fig. 9.9: Determination of the cogging and hysteresis torque of *S0(2.8%)* based on T_{rheo} from Fig. 9.4 using (3.9) and (3.10).

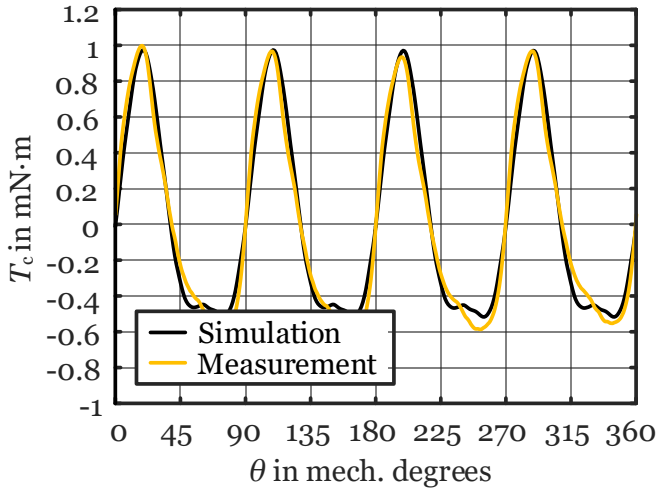

Fig. 9.10: Simulated cogging torque of *S0(2.8%)* from the 3-D finite-element simulations versus measured cogging torque from Fig. 9.9.

9.2 Iron Loss Determination

Based on Subsection 3.2.4, this section discusses the experimental iron loss determination of SFHP PM motors using a rheometer. First, the torque measurement–based iron loss determination is introduced, as are the terms hysteresis torque and eddy current torque. Second, the iron losses of *D0(1.8%)* and *S0(2.8%)* are determined and analyzed.

9.2.1 Torque Measurement–Based Iron Loss Determination

While most iron loss measurement and separation methods are power-based (see Subsection 1.2.4), the investigations in this thesis are torque-based as discussed in Subsection 3.2.4. This method relies on extremely accurate torque and speed measurements to determine the losses, using the following well-known relationship:

$$P = \omega T, \tag{9.1}$$

with the power P, the angular speed ω, and the torque T. As per (3.12), the iron loss separation into hysteresis and eddy current losses is also torque-based. The following overviews these loss mechanisms as they are important for the interpretation of the results in Subsection 9.2.2.

Hysteresis Torque

As the PM rotor rotates past the stator during operation, the stator iron magnetization state changes constantly according to the material's hysteresis curve due to the alternating flux in the stator. The associated losses are called hysteresis losses P_{hys}, see (1.24). They strongly depend on the magnetic material used, especially on the coercivity H_{co}. While hard magnetic materials feature high values of H_{co}, causing a large hysteresis area, soft magnetic materials show rather small H_{co} values, featuring a small hysteresis area. As discussed in the context of (1.24), the hysteresis losses increase with an increasing hysteresis area [144].

During rotation, the hysteresis torque T_{hys} is generated because the direction of the magnetic field of the PMs differs from that of a subset of the magnetic dipoles in the stator iron. In fact, T_{hys} always counteracts the direction of rotation. This is illustrated for the hysteresis force F_{hys} in the linear model in Fig. 9.11. F_{hys} is

caused by the magnetic dipoles indicated in red, as they counteract the direction of movement; the latter is indicated by the linear speed v. Multiplying F_{hys} and v by the air-gap radius r_δ yields the rotating quantities T_{hys} and ω, respectively.

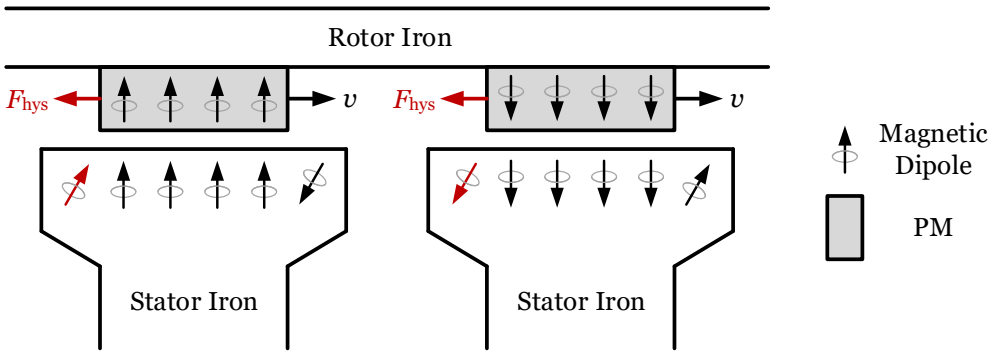

Fig. 9.11: Hysteresis torque generation mechanism using a linear model of a PM motor. (The illustration is inspired by [157].)

The hysteresis torque can be identified as an offset in the measured no-load torque waveform [157]. However, due to the stator slots, T_{hys} is not constant, it is rotor position–dependent. Based on (9.1) and (1.22), the hysteresis torque T_{hys} can be obtained from the hysteresis losses P_{hys} and ω as follows [144]:

$$T_{\text{hys}} = \frac{P_{\text{hys}}}{\omega} = \frac{\sigma_{\text{H}}\,\omega\,\hat{B}^2\,V}{\omega} = \sigma_{\text{H}}\,\hat{B}^2\,V, \tag{9.2}$$

where σ_{H} is a material-specific hysteresis loss coefficient, $\hat{B}$ is the amplitude of the sinusoidal flux density, and V is the iron volume. As per (9.2), T_{hys} is principally speed-invariant.

Eddy Current Torque

As the PM rotor rotates past the stator during operation, the alternating flux in the stator iron material also causes eddy currents, resulting in eddy current losses P_{eddy}. Based on (9.1) and (1.22), an eddy current torque T_{eddy} can be calculated from the eddy current losses P_{eddy} as follows [144]:

$$T_{\text{eddy}} = \frac{P_{\text{eddy}}}{\omega} = \frac{\sigma_{\text{W}}\,\omega^2\,\hat{B}^2\,V}{\omega} = \sigma_{\text{W}}\omega\,\hat{B}^2\,V, \tag{9.3}$$

where, in addition to the parameters defined in the context of (9.2), σ_{W} is a material-specific eddy current loss coefficient. While T_{hys} is principally speed-invariant according to (9.2), the eddy current torque T_{eddy}, however, increases linearly with

increasing speed. Hence, other than T_{hys}, T_{eddy} contributes to the measured offset torque T_{offset} for $n \neq 0$. Besides the speed, T_{eddy} and P_{eddy} strongly depend on the conductivity of the iron material and whether it is laminated or not.

9.2.2 No-Load Torque Measurements at Elevated Speeds

This subsection presents the rheometer-based iron loss determination and separation of SFHP PM motors, using *D0(1.8%)* and *S0(2.8%)* as example cases. As discussed in Section 9.2 and in the context of (3.12), the no-load iron losses can be determined investigating the speed-dependency of the offset torque T_{offset}. Since T_{hys} is largely speed-invariant and T_{eddy} increases linearly with increasing speed, a torque separation and an iron loss separation can be carried out (see Subsection 3.2.4).

Analysis of the Iron Losses of *D0(1.8%)*

Fig. 9.12 shows the offset torque determined in the CW direction $T_{\text{offset,CW}}$ of *D0(1.8%)* as a function of the rotational speed n. Starting from about 0.14 mN·m at 1 rpm, $T_{\text{offset,CW}}$ increases linearly with increasing n. As discussed in the context of (3.8),

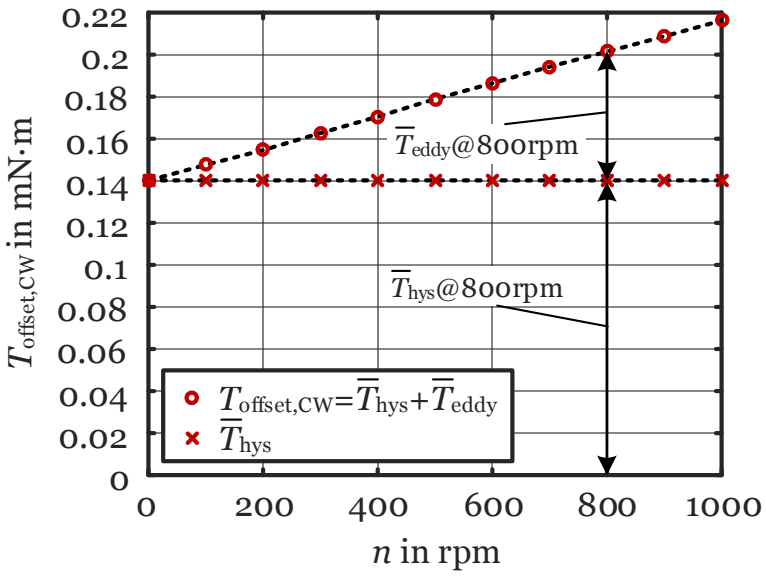

Fig. 9.12: Measured offset torque of *D0(1.8%)* versus rotational speed including torque separation.

the offset at very low speeds is solely due to the average hysteresis torque ($T_{\text{offset}} = \overline{T}_{\text{hys}}$). Since T_{hys} is largely speed-invariant and can be assumed constant as per

(9.2), the linear increase in $T_{\text{offset,CW}}$ can be attributed to the average eddy current torque $\overline{T}_{\text{eddy}}$, see (9.3). As a result, $T_{\text{offset,CW}}$ can be separated into $\overline{T}_{\text{hys}}$ and $\overline{T}_{\text{eddy}}$, which is exemplarily indicated in Fig. 9.12 for $n = 800\,\text{rpm}$ [$\overline{T}_{\text{hys}} \approx 0.14\,\text{mN}\cdot\text{m}$ and $\overline{T}_{\text{eddy}} \approx 0.06\,\text{mN}\cdot\text{m}$].

Based on the measured offset torque $T_{\text{offset,CW}}$ from Fig. 9.12, Fig. 9.13 shows the corresponding average iron losses $P_{\text{offset,CW}}$ as a function of the speed n calculated according to (9.1).[5] Using (9.2), (9.3), and (3.12), a separation of the average hysteresis and eddy current losses can be carried out, as exemplarily indicated in Fig. 9.13 for $n = 800\,\text{rpm}$ [$P_{\text{hys}} \approx 12\,\text{mW}$ and $P_{\text{eddy}} \approx 5\,\text{mW}$].

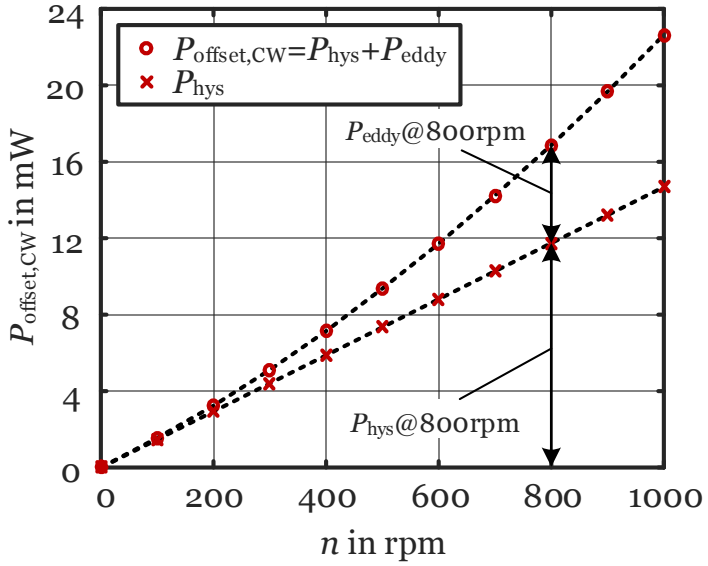

Fig. 9.13: Average iron loss determination and separation of *D0(1.8%)*.

Remark: Extrapolating the measured iron losses of *D0(1.8%)* for $n = 5500\,\text{rpm}$ yields about 695 mW, of which 613 mW are eddy current and 82 mW are hysteresis losses. The measured iron losses are about three times higher than the simulated ones: As per Section 7.10, the simulated eddy current losses are 220 mW and the simulated hysteresis losses are about 10 mW. The discrepancy can be attributed to parameter uncertainties (including manufacturing influences).

[5] Using [158], the maximum expanded measurement uncertainty for $n = 1000\,\text{rpm}$ is $\pm 188\,\mu\text{W}$.

Analysis of the Iron Losses of *S0(2.8%)*

Similar to Fig. 9.12, Fig. 9.14 shows $T_{\text{offset,CW}}$ of *S0(2.8%)* as a function of n which, as expected, increases linearly with increasing speed. The separation of $T_{\text{offset,CW}}$ into

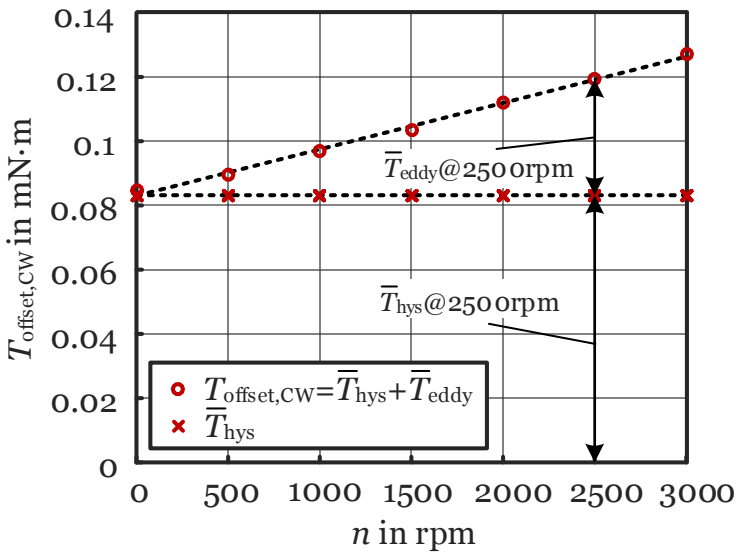

Fig. 9.14: Measured offset torque of *S0(2.8%)* versus rotational speed including torque separation.

$\overline{T}_{\text{hys}}$ and $\overline{T}_{\text{eddy}}$ is exemplarily indicated for $n = 2500\,\text{rpm}$ [$\overline{T}_{\text{hys}} \approx 0.08\,\text{mN}\cdot\text{m}$ and $\overline{T}_{\text{eddy}} \approx 0.04\,\text{mN}\cdot\text{m}$].

Based on the measured offset torque from Fig. 9.14, Fig. 9.15 shows the corresponding average iron losses of *S0(2.8%)* as a function of n.[6] Again, a separation of the average hysteresis and eddy current losses can be made, which is exemplarily illustrated for $n = 2500\,\text{rpm}$ [$P_{\text{hys}} \approx 22\,\text{mW}$ and $P_{\text{eddy}} \approx 10\,\text{mW}$].

Remark: For comparison, the iron losses of *S0(2.8%)* have also been determined using the well-known Steinmetz equation presented in (1.21), with the following parameters, which have been extracted from the M250-35A datasheet [149], assuming a flux density amplitude of 1.4 T based on the 3-D finite-element simulations: $k_{\text{s}} = 43.4\,\text{W/m}^3$, $\alpha_{\text{s}} = 1.3$, and $\beta_{\text{s}} = 2.1$. With this approach, the iron losses are underestimated by about 50 % over the whole frequency range, compared to those determined with the rheometer. The differences can be attributed mostly to parameter uncertainties (e.g., due to manufacturing influences) but also to non-ideal

[6] Using [158], the maximum expanded measurement uncertainty for $n = 3000\,\text{rpm}$ is $\pm 326\,\mu\text{W}$.

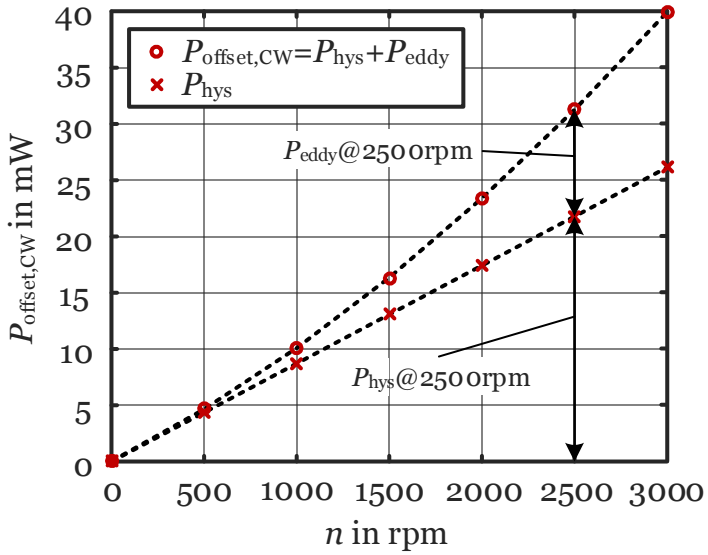

Fig. 9.15: Average iron loss determination and separation of *S0(2.8%)*.

flux density waveforms. Indeed, increases of iron losses of up to 50 % caused by manufacturing influences have been reported in the literature, for an overview see, e.g., [159].

Chapter Summary and Conclusions:

- The measured no-load torque waveforms in the CW and CCW directions show positive and negative offsets, respectively, because the hysteresis and eddy current effects counteract the rotation enforced by the rheometer.
- These waveforms are generally a superposition of the cogging torque, hysteresis torque, and eddy current torque. (For very low speeds, eddy current effects can be neglected.)
- In motors with asymmetric air-gaps, it is important to consider the measured no-load torque waveform in the designed rotational direction, because the CW and CCW waveforms can differ significantly.
- Building the average and difference of the CW and CCW waveforms for low speeds, the cogging torque and hysteresis torque can be extracted.
- The hysteresis torque is not constant due to the slotting of the stator.
- The observed offset torque component is solely caused by the hysteresis and eddy current torque components because the cogging torque is inherently offset-free.

- Investigating said offset torque for different speeds enables a torque separation as the hysteresis torque is speed-invariant and the eddy current torque increases linearly with increasing speed. As a result, the corresponding iron losses can be determined using $P = \omega T$.
- Advantageous is the fact that, other than with material samples, all parameter uncertainties (including manufacturing influences) are inherently accounted for in the measured iron losses since the actual motor is tested.
- The measured iron losses of *D0(1.8%)* are about three times higher than the simulated ones, see Section 7.11. This increase in the iron losses reduces the efficiency of *D0(1.8%)* from 35.8 % to 28.6 % for the operating point considered.

Chapter 10

Conclusion

This thesis aims to develop single-phase brushless direct current (BLDC) motor designs in which the cogging torque can be reduced at no increase to the manufacturing cost to reduce the output torque fluctuations and ripple, which can lead to structure-borne and airborne noise. In this regard, the claw-pole motor topology is identified as a suitable motor concept. The proposed design improvements are studied analytically, through finite-element analysis, and by means of different experiments in detail, determining their effects on selected motor performance parameters of key interest: the cogging torque, the back-EMF, the output torque, the air-gap flux density, the inductance, the thermal behavior, the eddy currents, the radial forces, and the axial forces. The results indicate that the motor performance parameters are generally interdependent. Hence, there is always a trade-off between reducing the cogging torque and, concurrently, reducing the average output torque, efficiency, and back-EMF, or increasing the axial forces.

The findings show that an asymmetric air-gap can facilitate the starting and, at the same time, provide maximum design freedom concerning the claw-pole shapes for the implementation of cogging torque reduction measures. Realizing a single-sided skew is a good tradeoff between significant cogging torque reduction and marginal back-EMF reduction; yet, axial forces are induced which may reduce the bearing systems's lifetime and cause noise. The selected introduction of auxiliary slots can successfully modulate the cogging torque, making skewing much more effective in reducing the cogging torque. The implementation of a V-skew can successfully balance the axial forces but, compared to a single-sided skew, the cogging torque reduction is less pronounced because the effective skewing extends to only half-way through the axial length of the motor. (A summary of the main quantitative results is provided in the subsequent chapter.) The results also indicate that a rheometer

is suitable for accurate 1) cogging torque and hysteresis torque measurement in the sub-milli-Newton meter range; and 2) iron loss determination including all manufacturing influences of the motor.

Although it is hardly possible, it should be noted that fully eliminating the cogging torque of this single-phase BLDC motor would compromise its starting capability realized by the asymmetric air-gap. Since the cogging torque, the alignment torque, and potential unbalanced radial and axial magnetic forces of the studied claw-pole motor have the same dominant harmonic components (especially the fourth harmonic of the rotational frequency), a source separation in a noise and vibration analysis may be challenging. Unless soft magnetic composite (SMC) materials are used, scaling of the claw-pole motor concept is generally limited, because eddy current effects can deteriorate the motor performance. Axial scaling is limited due to potential saturation in the claw-pole root. However, by arranging multiple motors in series in the axial direction, the output torque can be scaled linearly.

Future work may investigate prototype stator parts which are 3-D printed or made out of punched and subsequently deep-drawn steel sheets, instead of milled stator parts. Furthermore, the proposed claw-pole motor designs should be investigated in the actual application, particularly regarding their structure- and airborne noise. In addition to the rheometer-based measurements, further axial force measurements should be considered, using an adequate miniature force sensor.

This thesis shows that cogging torque reduction does not always involve additional fabrication operations and an increased manufacturing cost. The proposed single-phase BLDC claw-pole motor designs with low cogging torque may help prevent disturbing structure-borne noise or airborne noise.

Summary of Main Quantitative Results

Table 10.1: Designs with a single-sided skew.

	T_c Reduction	u_{EMF} Reduction	T_{rip} Reduction
Baseline	-	-	-
D1(30°)	−25 %	−2 %	−12 %
D3(45°)	−70 %	−12 %	−17 %

Table 10.2: Designs with a V-skew.

	T_c Reduction	u_{EMF} Reduction	F_a Presence
*Baseline**	-	-	no
D1(30°)*	−40 %	−1 %	yes
D4(30°)*	−20 %	≈ 0 %	no
D4(45°)*	−50 %	−1 %	no
D5(30°)*	−20 %	−20 %	no

Symbols

SYMBOL	UNIT	NAME
α	°	magnetization decaying angle
α_p	-	pole coverage
α_s	-	Steinmetz frequency exponent
β	rad	angle related to the law of cosines
β_s	-	Steinmetz flux density exponent
γ	°	angle of the magnetic symmetry line
γ_{el}	S/m	electrical conductivity
$\dot{\gamma}_s$	s^{-1}	shear rate
Γ_δ	m^2	air-gap annulus area
∂_c	m	contour
δ	m	radial air-gap length
δ_{claw}	m	inter-claw distance
δ^*_{claw}	m	effective inter-claw distance due to skewing
δ_{eff}	m	effective radial air-gap length
δ_{max}	m	maximum air-gap length
δ_{min}	m	minimum air-gap length
δ_{slot}	m	slot air-gap length
$\Delta\delta$	m	widening of the air-gap length
$\Delta\delta_{max}$	m	maximum air-gap widening
$\Delta\delta_{rel}$	%	relative air-gap asymmetry
ΔM	A/m	change in magnetization
ΔT	K	temperature rise
ε	-	relative eccentricity
ε_{max}	-	maximum relative eccentricity
ζ	-	coupling factor of the bifilar winding
η	%	efficiency

SYMBOL	UNIT	NAME
η_v	$\mathrm{Pa \cdot s}$	dynamic viscosity
θ	°	rotor position
θ_el	°	electrical angle
θ_on	°	turn-on angle
$\theta_\mathrm{A,on}$	°	turn-on angle of sub-phase A
$\theta_\mathrm{B,on}$	°	turn-on angle of sub-phase B
θ_off	°	turn-off angle
$\theta_\mathrm{A,off}$	°	turn-off angle of sub-phase A
$\theta_\mathrm{B,off}$	°	turn-off angle of sub-phase B
$\Theta_{\delta,i_\mathrm{p}}$	A	stator magnetomotive force
$\Theta_\mathrm{\delta,PM}$	A	rotor magnetomotive force
λ	rad^{-1}	exponent of the Ansatz function for the homogeneous solution
λ'_c	°	spatial period of the cogging torque
λ^*_c	°	spatial period of the cogging torque due to auxiliary slots
λ_r	%	rotor leakage flux ratio
λ_s	%	stator leakage flux ratio
μ	$\mathrm{V \cdot s/(A \cdot m)}$	permeability
μ_0	$\mathrm{V \cdot s/(A \cdot m)}$	permeability of free space
μ_fe	$\mathrm{V \cdot s/(A \cdot m)}$	permeability of iron material
μ_s	m	coefficient of static friction torque
μ_rec	-	relative recoil permeability of the PM
ν	-	index variable
ξ_skew	°	skewing angle
ξ'_skew	°	skewing angle to completely eliminate the cogging torque
ξ^*_skew	°	reduced skewing angle due to auxiliary slots
σ_H	-	material-dependent hysteresis loss coefficient
σ_W	-	material-dependent eddy current loss coefficient
τ_s	Pa	shear stress
τ_el	s	electrical time constant
τ_th	s	thermal time constant

SYMBOL	UNIT	NAME
τ_p	m	pole pitch
φ_slot	°	slot angle
φ_cp	°	claw-pole angle
φ_off	°	angle of stator part misalignment
φ_k	°	cogging torque phase of harmonic k
φ_m	°	circumferential angle in a stator coordinate system
ϕ	V · s	flux
ϕ_r	V · s	rotor yoke flux
ϕ_s	V · s	stator yoke flux
ϕ_w	-	wanted function
$\tilde{\phi}_\mathrm{w}$	-	approximation of the wanted function
Φ_net	V · s	coil net flux through
$\Phi_\mathrm{p,PM}$	V · s	PM flux per pole
Ψ_c	V · s	flux linkage of one coil
$\hat{\Psi}_\mathrm{c}$	V · s	maximum flux linkage of one coil
ω	rad/s	angular frequency
ω_el	rad/s	electrical frequency
ω_w	-	weighting function
Ω	m, m^2, m^3	finite-element domain
a	-	coefficient related to the law of cosines
A	A/m	linear current density
$\boldsymbol{A}_\mathrm{c}$	-	area vector of the coil
$\overline{A}_{\tau_\mathrm{p}}$	A/m	average linear current density over a pole pitch
$\overline{A}_{\tau_\mathrm{p},\mathrm{CP}}$	A/m	average linear current density of the claw-pole motor
$\overline{A}_{\tau_\mathrm{p},\mathrm{SP}}$	A/m	average linear current density of the salient-pole motor
A_pole	m^2	pole area
A_p	A	coefficient no. 1 of the Ansatz function for the particular solution no. 2
A_slot	A/m	local linear current density of the slot
A_th	m^2	equivalent heat transfer surface area
A_tot	m^2	total winding window area
b	-	coefficient related to the law of cosines
b_w	m	winding window width

SYMBOL	UNIT	NAME
B	T	flux density
$\hat{B}$	T	flux density peak value
$\lvert\overline{B}_\delta\rvert$	T	average absolute air-gap flux density
B_{δ,i_p}	T	air-gap flux density caused by the phase current
$\hat{B}_{\delta,i_\mathrm{p}}$	T	maximum air-gap flux density caused by the phase current
$B_{\delta,\mathrm{PM}}$	T	air-gap flux density caused by the PM
$\hat{B}_{\delta,\mathrm{PM}}$	T	maximum air-gap flux density caused by the PM
$\overline{B}_{\delta,\mathrm{PM}}$	T	average air-gap flux density caused by the PM
B_m	T	magnetic flux density in the PM
B_p	A	coefficient no. 2 of the Ansatz function for the particular solution no. 2
B_r	T	radial flux density component
B_rem	T	remanence flux density of the PM
B_t	T	tangential flux density component
c	-	coefficient related to the law of cosines
c_ν	-	coefficients of the Ansatz function
c_eddy	-	eddy current coefficient
c_hys	-	hysteresis coefficient
c_w	m	winding clearance
C	F	DC-link capacitor
C_th	W · s/K	thermal capacitance
$C_{\mathrm{th},\_}$	W · s/K	thermal capacitance of a certain design
C_T	-	goodness factor
d_asym	m	x-axis displacement related to air-gap asymmetry
d_cu	m	wire copper diameter
d_r	m	rotor diameter
d_skew	m	x-axis displacement related to skewing
d_wire	m	wire outer diameter
$d\theta$	°	differential rotor angle
$d\varphi_\mathrm{m}$	rad	differential circumferential angle
$d\Gamma_\delta$	m^2	differential area of air-gap annulus
$d\omega$	rad	differential angular frequency

SYMBOL	UNIT	NAME
$d\Omega$	m, m^2, m^3	differential element of the finite-element domain
ds	m	differential length element
dt	s	differential time
dz	m	differential length element in the z-direction
dB	T	differential flux density element
$d\mathcal{R}$	H^{-1}	differential magnetic reluctance
D	-	diode
e	mm	static eccentricity
e_s	rpm	speed control error
e_y	mm	eccentricity in the y-direction
E	Pa	Young's Modulus
f	Hz	frequency
f_r	N/m^2, Pa	radial force density or magnetic traction
f_s	-	sources of the field problem
f_t	N/m^2, Pa	tangential force density or magnetic traction
f_{URMF}	s^{-1}	frequency of the unbalanced radial magnetic forces
f_x	N/m^2, Pa	x-axis force density or magnetic traction
f_y	N/m^2, Pa	y-axis force density or magnetic traction
$\overline{F}$	N	average Lorentz force
F_δ	N	force in the air-gap over one pole
F_a	N	axial magnetic force
$F_{a,i}$	N	axial magnetic force components i
$F_{a,k}$	N	axial magnetic force harmonic k
$F_{g,m}$	N	gravitational force of the additional mass
$F_{g,r}$	N	gravitational force of the rotor
F_{hys}	N	hysteresis force
F_r	N	radial magnetic force
F_t	N	tangential magnetic force
$F_{r,mag}$	N	resulting radial magnetic force
$F_{x,mag}$	N	resulting x-axis magnetic force
$F_{y,mag}$	N	resulting y-axis magnetic force
$F_{y,ss}$	N	spring scale magnetic force in the y-direction
g	m/s^2	gravitational constant

SYMBOL	UNIT	NAME
g_1	V	perturbation function no. 1
g_2	V	perturbation function no. 2
g_3	V	perturbation function no. 3
h	m	height related to air-gap asymmetry
h_m	m	radial magnet height
h_th	W/m^2/K	equivalent heat transfer coefficient
h_w	m	winding window height
H	A/m	magnetic field
H_{δ,i_p}	A/m	magnetic field in the air-gap caused by the phase current
$H_{\delta,\mathrm{PM}}$	A/m	magnetic field in the air-gap caused by the PM
H_co	A/m	magnetic coercivity of the PM
$H_\mathrm{fe,s}$	A/m	magnetic field in the stator iron
$H_\mathrm{fe,r}$	A/m	magnetic field in the rotor iron
H_m	A/m	magnetic field in the PM
i	A	current
$\underline{i}_\mathrm{abc}$	A	phase current system
i_eddy	A	eddy current
i_hom	A	homogeneous solution of the current
i_p	A	phase current
$i_\mathrm{p,A}$	A	current of sub-phase A
$i_\mathrm{p,B}$	A	current of sub-phase B
i_part1	A	particular solution no. 1 of the current
i_part2	A	particular solution no. 2 of the current
i_part3	A	particular solution no. 3 of the current
I	A	rms current
I_area	m^4	area moment of inertia of a flattened claw-pole
I'_area	m^4	exact area moment of inertia of one claw-pole
I_DC	A	DC current
I_in	A	input current
I_m	A	equivalent magnetization current
I_p	A	rms phase current
I	-	origin

SYMBOL	UNIT	NAME
I′	-	altered origin
II	-	point no. 1 defining the air-gap
III	-	point no. 2 defining the air-gap
III′	-	point defining the asymmetric air-gap
IV	-	point defining the implemented skew
J	$\mathrm{kg \cdot m^2}$	mass moment of inertia
k	-	harmonic order of the studied waveform
k_c	-	arbitrary constant
k_mech	-	mechanical fill factor
k_s	-	Steinmetz factor
$k_{\mathrm{skew},k}$	-	skewing factor for the harmonic k
k_w	-	winding factor (bifilar vs. unifilar)
K_1	A	constant no. 1 of the Ansatz function for the homogeneous solution
K_2	A	constant no. 2 of the Ansatz function for the particular solution no. 1
l_ax	m	axial length of the machine
$l_\mathrm{ax,s}$	m	axial length of the stator
$l_\mathrm{ax,r}$	m	axial length of the rotor
$l_\mathrm{fe,s}$	m	length of iron path in the stator
$l_\mathrm{fe,r}$	m	length of iron path in the rotor
l_PM	m	axial length of the PM
L	H	inductance
L_2	-	second order differential operator
L_σ	H	leakage inductance
$L_{\sigma,\mathrm{A}}$	H	leakage inductance inductance of sub-phase A
$L_{\sigma,\mathrm{B}}$	H	leakage inductance inductance of sub-phase B
L_m	H	main inductance
$L_\mathrm{m,A}$	H	main inductance of sub-phase A
$L_\mathrm{m,B}$	H	main inductance of sub-phase B
L_ph	H	phase inductance
m	-	relative change in magnetization
m_add	kg	additional mass

SYMBOL	UNIT	NAME
m_{Fe}	kg	iron mass
m_{rot}	kg	rotor mass
M	N · m	bending moment
M_{r}	A/m	radial magnetization
M_{ro}	A/m	maximum radial magnetization
n	rpm	rotational speed
n^*	rpm	desired rotational speed
n_{max}	rpm	maximum rotational speed
N	-	number of turns
N_{cs}	-	number of coils in series per phase
N_{n}	-	number of auxiliary slots per pole
N_{node}	-	number of nodes of the finite-element
N_{p}	-	number of cogging torque periods during a slot pitch rotation
N_{pole}	-	number of turns per salient-pole
N_{tot}	-	total number of turns in series per phase
N_{A}	-	number of turns of sub-phase A
N_{B}	-	number of turns of sub-phase B
p	-	number of pole pairs
$\mathcal{P}$	V · s/A	magnetic permeance
$\mathcal{P}_{\mathrm{min}}$	V · s/A	minimum magnetic permeance
$\mathcal{P}_{\mathrm{max}}$	V · s/A	maximum magnetic permeance
$\mathcal{P}_{\mathrm{slot}}$	V · s/A	slot permeance
P	W	power
P_{Cu}	W	copper losses
P_{eddy}	W	eddy current losses
$\overline{P}_{\mathrm{eddy}}$	W	average eddy current losses
P_{fe}	W	iron losses
P_{hys}	W	hysteresis losses
$\overline{P}_{\mathrm{hys}}$	W	average hysteresis losses
P_{i}	W	inner power
P_{offset}	W	iron losses determined from the offset torque
$P_{\mathrm{offset,CW}}$	W	iron losses in the CW direction

SYMBOL	UNIT	NAME
P_{wind}	W	windage losses
q	N/m	line load
Q	-	number of slots
Q^*	-	number of slots including auxiliary slots
r	m	radius of the additional mass
r_δ	m	air-gap radius
r_1	m	stator part inner radius before bending
r_2	m	stator part inner radius after bending
r_2''	m	auxiliary radius no. 1 related to the winding model
r_3	m	stator part outer radius after bending
r_3'	m	auxiliary radius no. 1 related to the air-gap asymmetry
r_3''	m	auxiliary radius no. 2 related to the air-gap asymmetry
r_4	m	stator part outer radius before bending
r_d	m	dummy radius
r_s	m	stator radius
$\mathbb{R}$	-	residual
$\mathcal{R}$	H^{-1}	magnetic reluctance
$\mathcal{R}_\delta$	H^{-1}	magnetic reluctance of the air-gap
$\mathcal{R}_{\delta,\text{claw}}$	H^{-1}	magnetic reluctance of the inter-claw region
$\mathcal{R}_\text{claw}$	H^{-1}	magnetic reluctance of the claw
$\mathcal{R}_\text{leak,slot}$	H^{-1}	magnetic slot leakage reluctance
$\mathcal{R}_\text{m,sys}$	H^{-1}	magnetic system reluctance
$\mathcal{R}_\text{mag}$	H^{-1}	magnetic reluctance of the magnet
$\mathcal{R}_\text{tot}$	H^{-1}	total magnetic reluctance
$\mathcal{R}_\text{yoke}$	H^{-1}	magnetic reluctance of the rotor yoke
$\mathcal{R}_\text{zyl}$	H^{-1}	magnetic reluctance of the cylindrical portion of the claw-pole stator part
R	Ω	phase resistance
R_A	Ω	resistance of sub-phase A
R_B	Ω	resistance of sub-phase B
R_th	K/W	thermal resistance

SYMBOL	UNIT	NAME
$R_{\text{th,\_}}$	K/W	thermal resistance of the design _
S_{A}	-	switch sub-phase A
S_{B}	-	switch sub-phase B
t	s	time
t_{steel}	m	steel sheet thickness
t^*_{steel}	m	altered steel sheet thickness
T	N · m	torque
$\hat{T}$	N · m	output torque maximum value
$\check{T}$	N · m	output torque minimum value
T_{A}	°C	ambient temperature
T_{c}	N · m	cogging torque
$\overline{T}_{\text{c}}$	N · m	average cogging torque
$T_{\text{c,aux}}$	N · m	cogging torque due to auxiliary slots
$T_{\text{c},k}$	N · m	cogging torque component of harmonic k
$T_{\text{c,skew}}$	N · m	cogging torque after skewing
$T_{\text{c,tot}}$	N · m	total cogging torque
T_{coil}	°C	winding temperature
T_{eddy}	N · m	eddy current torque
$\overline{T}_{\text{eddy}}$	N · m	average eddy current torque
T_{em}	N · m	instantaneous electromagnetic torque
$\overline{T}_{\text{em}}$	N · m	average electromagnetic torque
T_{f}	N · m	friction torque of the slide bearing
T_{fric}	N · m	friction torque
T_{hys}	N · m	hysteresis torque
$\overline{T}_{\text{hys}}$	N · m	average hysteresis torque
$\overline{T}_{\text{hys,CCW}}$	N · m	average hysteresis torque in the CCW direction
$\overline{T}_{\text{hys,CW}}$	N · m	average hysteresis torque in the CW direction
T_k	N · m	cogging torque amplitude of harmonic k
T_{o}	N · m	output torque
$\overline{T}_{\text{o}}$	N · m	average output torque
T_{offset}	N · m	offset torque

SYMBOL	UNIT	NAME
$T_{\text{offset,CW}}$	N · m	offset torque measured in the CW direction
$T_{\text{offset,CCW}}$	N · m	offset torque measured in the CCW direction
T_{r}	N · m	resulting cogging torque at current zero-crossing
T_{rip}	%	torque ripple
T_{rheo}	N · m	rheometer torque
$T_{\text{rheo,CCW}}$	N · m	rheometer torque in the CCW direction
$T_{\text{rheo,CW}}$	N · m	rheometer torque in the CW direction
$T_{\text{rheo},k}$	N · m	rheometer torque amplitude of harmonic k
T_{wind}	N · m	windage torque
u_{EMF}	V	back-EMF
$\hat{u}_{\text{EMF}}$	V	back-EMF maximum value
$u_{\text{EMF,A}}$	V	back-EMF of sub-phase A
$u_{\text{EMF,B}}$	V	back-EMF of sub-phase B
$u_{\text{EMF,c}}$	V	back-EMF induced in one coil
$\hat{u}_{\text{EMF,c}}$	V	maximum back-EMF induced in one coil
$u_{\text{EMF,CP}}$	V	back-EMF of the claw-pole motor
$u_{\text{EMF,SP}}$	V	back-EMF of the salient-pole motor
$u_{\text{EMF},k}$	V	back-EMF amplitude of harmonic k
u_{inv}	V	inverter voltage
U_{DC}	V	DC-link voltage
U_{in}	V	input voltage
U_{inv}	V	maximum inverter voltage
v	m/s	linear speed
V	m^3	volume
w	m	thickness of non-magnetic sleeve
w_ν	-	shape functions
$w_{\text{aux,slot}}$	m	auxiliary slot width
w_{claw}	m	axial stator claw width
w_{hys}	J/m^3	specific magnetic loss energy
$w_{\text{s,yoke}}$	m	axial stator yoke width
w_{slot}	m	slot opening
w_{stat}	m	stator part width
W_{co}	J	magnetic co-energy

SYMBOL	UNIT	NAME
x	-	x-axis
y	-	y-axis
y_{max}	m	maximum claw deflection in the y-axis
z	-	z-axis
z_c	-	variable
z_Q	-	total number of conductors per slot

Acronyms and Abbreviations

ACRONYM	EXPANSION
1-D	one-dimensional
2-D	two-dimensional
3-D	three-dimensional
AC	alternating current
BDC	brushed direct current
BLDC	brushless direct current
BLAC	brushless alternating current
CSR	controlled shear rate
CSS	controlled shear stress
CW	clockwise
CCW	counter clockwise
CPU	central processing unit
DC	direct current
EMF	electromotive force
EU	European Union
FEA	finite-element analysis
FEM	finite-element method
FHP	fractional horsepower
GmbH	Gesellschaft mit begrenzter Haftung
HP	horsepower
IEC	International Electrotechnical Commission
IEEE	Institute of Electrical and Electronics Engineers
IHP	integral horsepower
LCM	least common multiple
LED	light emitting diode

ACRONYM	EXPANSION
LS	left side
MCR	modular compact rheometer
MEC	magnetic equivalent circuit
MMF	magnetomotive force
MOSFET	metal-oxide semiconductor field-effect transistor
MUT	motor under test
MSG	Mechatronic Systems GmbH
MSL	magnetic symmetry line
MSL'	altered magnetic symmetry line
NdFeB	neodymium iron boron
N	north pole
NVH	noise, vibration, and harshness
OP	operating point
pu	per unit
PM	permanent-magnet
PWM	pulse-width modulation
rad	radians
rms	root mean square
rpm	rounds per minute
RS	right side
S	south pole
SFHP	sub-fractional horsepower
SL	symmetry line
SL I	symmetry line of the rotor
SL II	symmetry line of the stator
SPL	sound pressure level
SMC	soft magnetic composite
SMP	symmetric multiple processing
SMnPb	sulfur manganese lead
URMF	unbalanced radial magnetic force
US	United States
VW	Volkswagen
WESP	with exposed support plate

ACRONYM	EXPANSION
ZVEI	Zentralverband Elektro- und Elektronikindustrie e.V.

ABBREVIATION	EXPANSION
sin.	sinusoidal
rec.	rectangular
trap.	trapezoidal
vol.	volume
no.	number
pp.	pages

Bibliography

[1] P. Waide and C. U. Brunner, "Energy-efficiency policy opportunities for electric motor-driven systems," International Energy Agency (IEA), Tech. Rep., 2011.

[2] A. Hasanbeigi, "Infographic: The profile of energy use in industrial motor systems," Apr. 2017. [Online]. Available: https://www.globalefficiencyintel.com/new-blog/2017/infographic-energy-industrial-motor-systems

[3] M. Jordan, "With more than 100 actuators - the new S-Class," 2013, [Accessed: Jun. 20, 2020]. [Online]. Available: https://blog.mercedes-benz-passion.com/2013/07/mit-uber-100-kleinen-stellmotoren-die-neue-s-klasse/

[4] A. Muetze, S. Leitner, H. Gruebler, and F. Krall, "Performance improvements of auxiliary drives for automotive pump and fan applications," *Elektrotechnik und Informationstechnik, https://doi.org/10.1007/s00502-020-00797-7*, Apr. 2020.

[5] A. Kunz, M. Kunz, H. Vollert, and M. Förster, "Electromechanical brake booster for all drive concepts and automated driving," *ATZ worldwide*, vol. 120, no. 4, pp. 58–61, Apr. 2018.

[6] A. Reul, K. Fecke, and H. Stobrawe, "Adjustable oil pump for the lubrication of transmission," *ATZ worldwide*, vol. 116, no. 12, pp. 30–35, Nov. 2014.

[7] H. Hembach, "Systematic comparison of BLDC motor concepts for small automotive wet-running water pump applications," Ph.D. dissertation, Bundeswehr Universität München, Neubiberg, Nov. 2007 (in German).

[8] mag - The Magazine of ebm-papst. (2014) What to look out for in vehicle LED headlights. [Nov. 21, 2018]. [Online]. Available: https://mag.ebmpapst.com/en/products/fans/what-to-look-out-for-in-vehicle-led-headlights_8380/

[9] J. Hirt, "Cooling and dehumidification of LED headlights," *ATZ worldwide*, vol. 116, no. 5, pp. 52–55, May 2014. [Online]. Available: https://doi.org/10.1007/s38311-014-0178-z

[10] ebm-papst. (2019) Seat ventilation. [Apr. 15, 2019]. [Online]. Available: https://www.ebmpapst.com/en/overview-industries/automotive/references/seat_climatisation_compact_fan/seatventilation_compactfan.html

[11] Wolfgang Fehrenbacher, "Kleinlueftereinheit, insbesondere zur Verwendung als Leitnerplattenluefter," EP 0 908 630 A1, April 1999.

[12] C. Kinnaird, "How many electric motors are in your car?" Mar. 2018, [Accessed: Feb. 08, 2019]. [Online]. Available: https://e2e.ti.com/blogs_/b/behind_the_wheel/archive/2018/03/29/how-many-electric-motors-are-in-your-car#

[13] S. Hofmann, "Noise, Vibration, and Harshness - Characteristics of Sub-Fractional Horsepower Fan Drives," Master's thesis, Electric Drives and Machines Institute - Graz University of Technology, 2019.

[14] Volkswagen Aktiengesellschaft. (2019) erWin. Accessed on Nov. 19, 2019. [Online]. Available: https://erwin.volkswagen.de/erwin/showHome.do

[15] ——. (2019) Annual Report 2018. Accessed on Feb. 19, 2020. [Online]. Available: https://www.volkswagenag.com/en/InvestorRelations/news-and-publications/Annual_Reports.html

[16] OICA. Estimated worldwise automobile producion from 2000 to 2018 (in million vehicles). Chart. [Feb., 26, 2020]. [Online]. Available: https://www.statista.com/statistics/262747/worldwide-automobile-production-since-2000/

[17] P. Zeller, *Handbook of vehicle acoustics*. Berlin Heidelberg New York: Springer-Verlag, 2009 (in German).

[18] H. D. Stölting, E. Kallenbach, and W. Amrhein, *Handbook of small electric drives*, 4th ed. München: Hanser Verlag, 2011 (in German).

[19] H. Moczala, *Small electric machines*, 2nd ed. 7044 Ehningen bei Böblingen: Expert Verlag, 1993 (in German).

[20] F. Bielert, "Zusatzaggregate - Akustische Anforderungen, Volkswagen Konzernnorm VW 82 469," Jul. 2014.

[21] H. Le-Huy, R. Perret, and R. Feuillet, "Minimization of torque ripple in brushless dc motor drives," *IEEE Transactions on Industry Applications*, vol. IA-22, no. 4, pp. 748–755, Jul. 1986.

[22] J. F. Gieras, *Permanent Magnet Motor Technology*. Florida, USA: CRC Press: Taylor & Francis Group, LLC, 2010.

[23] S. Dunkl, A. Muetze, and G. Schoener, "Design constraints of small single-phase permanent magnet brushless dc drives for fan applications," *IEEE Transactions on Industry Applications*, vol. 51, no. 4, pp. 3178–3186, Jul. 2015.

[24] A. Lelkes and M. Bufe, "BLDC motor for fan application with automatically optimized commutation angle," in *2004 IEEE 35th Annual Power Electronics Specialists Conference (IEEE Cat. No.04CH37551)*, vol. 3, Jun. 2004, pp. 2277–2281 Vol.3.

[25] H. Gruebler, S. Leitner, A. Muetze, and G. Schoener, "Improved switching strategy for a single-phase brushless direct current fan drive and its impact on efficiency," *IEEE Transactions on Industry Applications*, vol. 54, no. 6, pp. 6050–6059, Nov. 2018.

[26] R. Krishnan, *Permanent Magnet Synchronous and Brushless DC Motor Drives*. Boca Raton, FL, USA: CRC Press: Taylor & Francis Group, LLC, 2010.

[27] Z. Q. Zhu and D. Howe, "Influence of design parameters on cogging torque in permanent magnet machines," *IEEE Transactions on Energy Conversion*, vol. 15, no. 4, pp. 407–412, Dec. 2000.

[28] N. Bianchi and S. Bolognani, "Design techniques for reducing the cogging torque in surface-mounted pm motors," *IEEE Transactions on Industry Applications*, vol. 38, no. 5, pp. 1259–1265, Sep. 2002.

[29] Gui-Jia Su and J. W. McKeever, "Low-cost sensorless control of brushless dc motors with improved speed range," *IEEE Transactions on Power Electronics*, vol. 19, no. 2, pp. 296–302, Mar. 2004.

[30] C.-L. Xia, *Permanent Magnet Brushless DC Motor Drives and Controls*. Singapore: Wiley, 2012.

[31] Ji-Hoon Jang, Seung-Ki Sul, Jung-Ik Ha, K. Ide, and M. Sawamura, "Sensorless drive of surface-mounted permanent-magnet motor by high-frequency signal injection based on magnetic saliency," *IEEE Transactions on Industry Applications*, vol. 39, no. 4, pp. 1031–1039, 2003.

[32] A. Binder, *Electric machines and drives*. Berlin Heidelberg: Springer-Verlag, 2012 (in German).

[33] J. R. Hendershot and T. J. E. Miller, *Design of Brushless Permanent-Magnet Machines*, 2nd ed. Florida, USA: Motor Design Books LLC, 2010.

[34] "Direct-drive permanent magnet generators for high-power wind turbines: benefits and limiting factors," *IET Renewable Power Generation*, vol. 6, no. 1, pp. 1–8, Jan. 2012.

[35] J. F. Gieras and M. Wing, *Permanent Magnet Motor Technology*. Marcel Dekker Inc., 2002.

[36] G. Müller, K. Vogt, and B. Ponick, *Calculation of electric machines*, 6th ed. Wiley-VCH, 2008 (in German).

[37] G. H. Jang, J. W. Yoon, N. Y. Park, and S. M. Jang, "Torque and unbalanced magnetic force in a rotational unsymmetric brushless dc motors," *IEEE Transactions on Magnetics*, vol. 32, no. 5, pp. 5157–5159, Sep. 1996.

[38] D. Hanselman, *Brushless Permanent Magnet Motor Design*, 2nd ed. Ohio 45036, USA: Magna Physics Publishing, 2006.

[39] T. Koenig and T. Wilharm, "Reducing magnetic noise of an auxiliary water pump drive," in *Innovative Small Drives and Micro-Motor Systems; 9. ETG/GMM Symposium*, 2013, pp. 1–6.

[40] Sang-Moon Hwang, Kyung-Tae Kim, Weui-Bong Jeong, Yoong-Ho Jung, and Beom-Soo Kang, "Comparison of vibration sources between symmetric and asymmetric hdd spindle motors with rotor eccentricity," *IEEE Transactions on Industry Applications*, vol. 37, no. 6, pp. 1727–1731, Nov. 2001.

[41] (2018) Melexis announces new automotive-grade fan driver ics for small applications. [Online]. Available: https://www.melexis.com/en/news/2017/28dec2017-us168-new-automotive-grade-fan-driver-ic

[42] "Field-oriented BLDC motor controller with 16 bit CPU," 2020. [Online]. Available: https://www.elmos.com/produkte/motor-control-ics/brushless-dc-motor-controller-ic/bldc-motor-controller/e52306-soc-1.html

[43] "Highly integrated, automotive state machine controller for the soundless control of BLDC motors," 2017. [Online]. Available: www.haptic.ro/highly-integrated-automotive-state-machine-controller-soundless-control-bldc-motors/

[44] B. Dehez, F. Baudart, and Y. Perriard, "Comparison of FPCB windings of BLDC machines with paralelly and radially magnetized rotor poles," in *2014 17th International Conference on Electrical Machines and Systems (ICEMS)*, 2014, pp. 3331–3337.

[45] P. Ragot, M. Markovic, and Y. Perriard, "Analytical determination of the phase inductances of a brushless dc motor with faulhaber winding," *IEEE Transactions on Industry Applications*, vol. 46, no. 4, pp. 1360–1366, May 2010.

[46] B. Dehez, F. Baudart, M. Markovic, and Y. Perriard, "Theoretical and experimental investigation of flex-pcb air-gap windings in slotless bldc machines," *IEEE Transactions on Industry Applications*, vol. 50, no. 5, pp. 3153–3160, Jan. 2014.

[47] G. Burnand, A. Thabuis, D. M. Araujo, and Y. Perriard, "Novel optimized shape and topology for slotless windings in BLDC machines," *IEEE Transactions on Industry Applications*, vol. 56, no. 2, pp. 1275–1283, Apr./Mar. 2020.

[48] F. Schwenker, "Aspects of high performance flat external rotor motors," in *Innovative Small Drives and Micro-Motor Systems; 12. ETG/GMM Symposium*, Sep. 2019, pp. 152–155.

[49] A. Arkkio, "Time-stepping finite element analysis of induction motors," in *International Conferenc on Electrical Machines (ICEM)*, 1988.

[50] Z. Q. Zhu and D. Howe, "Analytical prediction of the cogging torque in radial-field permanent magnet brushless motors," *IEEE Transactions on Magnetics*, vol. 28, no. 2, pp. 1371–1374, Mar. 1992.

[51] D. Lin, S. L. Ho, and W. N. Fu, "Analytical prediction of cogging torque in surface-mounted permanent-magnet motors," *IEEE Trans. Mag.*, vol. 45, no. 9, pp. 3296–3302, Sep. 2009.

[52] D. Zarko, D. Ban, and T. A. Lipo, "Analytical solution for cogging torque in surface permanent-magnet motors using conformal mapping," *IEEE Trans. Mag.*, vol. 44, no. 1, pp. 52–65, Jan. 2008.

[53] M. S. Islam, S. Mir, and T. Sebastian, "Issues in reducing the cogging torque of mass-produced permanent-magnet brushless dc motor," *IEEE Transactions on Industry Applications*, vol. 40, no. 3, pp. 813–820, May 2004.

[54] Z. Q. Zhu, J. T. Chen, L. J. Wu, and D. Howe, "Influence of stator asymmetry on cogging torque of permanent magnet brushless machines," *IEEE Transactions on Magnetics*, vol. 44, no. 11, pp. 3851–3854, Nov. 2008.

[55] Sang-Moon Hwang, Jae-Boo Eom, Geun-Bae Hwang, Weui-Bong Jeong, and Yoong-Ho Jung, "Cogging torque and acoustic noise reduction in permanent magnet motors by teeth pairing," *IEEE Transactions on Magnetics*, vol. 36, no. 5, pp. 3144–3146, Sep. 2000.

[56] Z. Q. Zhu, S. Ruangsinchaiwanich, and D. Howe, "Synthesis of cogging-torque waveform from analysis of a single stator slot," *IEEE Transactions on Industry Applications*, vol. 42, no. 3, pp. 650–657, May 2006.

[57] S. Bentouati, Z. Q. Zhu, and D. Howe, "Influence of design parameters on the starting torque of a single-phase pm brushless dc motor," *IEEE Transactions on Magnetics*, vol. 36, no. 5, pp. 3533–3536, Sep. 2000.

[58] Z. Q. Zhu, "A simple method for measuring cogging torque in permanent magnet machines," in *2009 IEEE Power Energy Society General Meeting*, July 2009, pp. 1–4.

[59] F. Caricchi, F. G. Capponi, F. Crescimbini, and L. Solero, "Experimental study on reducing cogging torque and no-load power loss in axial-flux permanent-magnet machines with slotted winding," *IEEE Transactions on Industry Applications*, vol. 40, no. 4, pp. 1066–1075, Jul. 2004.

[60] M. Popescu, E. Tudor, S. Nicolaie, C. I. Ilie, L. Popovici, and C. Dumitru, "Experimental results regarding cogging torque reduction for the permanent magnet synchronous motors pmsm," in *2019 11th International Symposium on Advanced Topics in Electrical Engineering (ATEE)*, Mar. 2019, pp. 1–4.

[61] S. Leitner, H. Gruebler, and A. Muetze, "Low-cost sub-fractional horsepower brushless direct current claw-pole machine topology for fan applications," in *2018 IEEE Applied Power Electronics Conference and Exposition (APEC)*, Mar. 2018, pp. 1242–1248.

[62] L. Xiao, J. Li, R. Qu, Y. Lu, R. Zhang, and D. Li, "Cogging torque analysis and minimization of axial flux pm machines with combined rectangle-shaped magnet," *IEEE Transactions on Industry Applications*, vol. 53, no. 2, pp. 1018–1027, Mar. 2017.

[63] F. Aghili, M. Buehler, and J. M. Hollerbach, "Experimental characterization and quadratic programming-based control of brushless-motors," *IEEE Transactions on Control Systems Technology*, vol. 11, no. 1, pp. 139–146, Jan. 2003.

[64] T. Kikuchi and T. Kenjo, "In-depth learning of cogging/detenting torque through experiments and simulations," *IEEE Transactions on Education*, vol. 41, no. 4, Nov 1998.

[65] C. Schlensok, D. V. Riesen, B. Schmuelling, M. C. Schoening, and K. Hameyer, "Cogging-torque analysis on permanent-magnet machines by simulation and measurement," *tm - Technisches Messen*, vol. 74, no. 7-8, pp. 393–401, Jun. 2007.

[66] V. Simon-Sempere, M. Burgos-Payan, and J. Cerquides-Bueno, "Cogging torque measurement using the electromotive force in surface-mounted permanent-magnet motors," *IEEE Transactions on Magnetics*, vol. 51, no. 7, pp. 1–10, Jul. 2015.

[67] L. Ferraris, F. Franchini, and E. Poskovic, "The cogging torque measurement through a new validated methodology," in *2017 11th IEEE International Conference on Compatibility, Power Electronics and Power Engineering (CPE-POWERENG)*, Apr. 2017, pp. 398–403.

[68] M. Aydin and M. Gulec, "Reduction of cogging torque in double-rotor axial-flux permanent-magnet disk motors: A review of cost-effective magnet-skewing techniques with experimental verification," *IEEE Transactions on Industrial Electronics*, vol. 61, no. 9, pp. 5025–5034, Sep. 2014.

[69] A. Krings, "Iron losses in electrical machines - influence of material properties, manufacturing processes, and inverter operation," Ph.D. dissertation, KTH Royal Institute of Technology Sweden, 2014.

[70] C. P. Steinmetz, "On the law of hysteresis (part ii.) and other phenomena of the magnetic circuit," *Transactions of the American Institute of Electrical Engineers*, vol. IX, no. 1, pp. 619–758, Jan. 1892.

[71] H. Jordan, *The ferromagnetic constants for weak alternating fields*. Elektrische Nachrichtentechnik, vol. 1, p. 8, 1924 (in German).

[72] A. Emadi, *Advanced Electric Drive Vehicles*. CRC Press: Taylor & Francis Group, LLC, 2014.

[73] Cogent Power Inc. (2020) Thin gauge non-oriented steels. Accessed on Jun. 3, 2020. [Online]. Available: https://cogent-power.com/products/non-oriented-electrical-steel/thin-non-oriented-fully-processed-electrical-steels

[74] A. Krings and J. Soulard, "Experimental characterization of magnetic materials for electrical machine applications," in *2015 IEEE Workshop on Electrical Machines Design, Control and Diagnosis (WEMDCD)*, Mar. 2015, pp. 85–89.

[75] *Methods of measurement of the magnetic properties of electrical steel strip and sheet by means of an Epstein frame*, International Standard IEC 60404-2 Std., 2008.

[76] A. Mouillet, J. L. Ille, M. Akroune, and M. A. Dami, "Magnetic and loss characteristics of nonoriented silicon-iron under unconventional conditions," *IEE Proceedings - Science, Measurement and Technology*, vol. 141, no. 1, pp. 75–78, Jan 1994.

[77] R. Kaczmarek, M. Amar, and F. Protat, "Iron loss under PWM voltage supply on Epstein frame and in induction motor core," *IEEE Transactions on Magnetics*, vol. 32, no. 1, pp. 189–194, Jan. 1996.

[78] H. Kapeller, B. Plassnegger, and J. V. Gragger, "Iron-loss modeling based on a loss-separation approach in modelica," *IEEE Transactions on Magnetics*, vol. 54, no. 3, pp. 1–4, Mar. 2018.

[79] M. Bali, H. D. Gersem, and A. Muetze, "Determination of original nondegraded and fully degraded magnetic properties of material subjected to mechanical cutting," *IEEE Transactions on Industry Applications*, vol. 52, no. 3, pp. 2297–2305, May 2016.

[80] M. Bali and A. Muetze, "Influences of CO2 laser, FKL laser, and mechanical cutting on the magnetic properties of electrical steel sheets," *IEEE Transactions on Industry Applications*, vol. 51, no. 6, pp. 4446–4454, Nov. 2015.

[81] *Methods of measurement of the magnetic properties of electrical steel strip and sheet by means of a single sheet tester*, International Standard IEC 60404-3 Std., 2002.

[82] N. Nencib, S. Spornic, A. Kedous-Lebouc, and B. Cornut, "Macroscopic anisotropy characterization of SiFe using a rotational single sheet tester," *IEEE Transactions on Magnetics*, vol. 31, no. 6, pp. 4047–4049, Nov. 1995.

[83] M. Nakano, H. Nishimoto, K. Fujiwara, and N. Takahashi, "Improvements of single sheet testers for measurement of 2-d magnetic properties up to high flux density," *IEEE Transactions on Magnetics*, vol. 35, no. 5, pp. 3965–3967, Sep. 1999.

[84] U. Aydin, F. Martin, P. Rasilo, A. Belahcen, A. Haavisto, D. Singh, L. Daniel, and A. Arkkio, "Rotational single sheet tester for multiaxial magneto-mechanical effects in steel sheets," *IEEE Transactions on Magnetics*, vol. 55, no. 3, pp. 1–10, Mar. 2019.

[85] *Methods of measurement of the magnetic properties of magnetically soft metallic and powder materials at frequencies in the range 20Hz to 200kHz by the use of ring specimens*, International Standard IEC 60404-6 Std., 2003.

[86] G. Bramerdorfer and D. Andessner, "Accurate and easy-to-obtain iron loss model for electric machine design," *IEEE Transactions on Industrial Electronics*, vol. 64, no. 3, pp. 2530–2537, Mar. 2017.

[87] H. Gruebler, F. Krall, S. Leitner, and A. Muetze, "Loss-surface-based iron loss prediction for fractional horsepower electric motor design," in *2018 20th European Conference on Power Electronics and Applications (EPE'18 ECCE Europe)*, Sep. 2018, pp. P.1–P.8.

[88] *Rotating electrical machines - part 2-1: standard methods for determining losses and efficiency from tests (excluding machines for traction vehicles)*, International Standard IEC 60034-2-1 Std., 2007.

[89] "IEEE guide: Test procedures for synchronous machines part i–acceptance and performance testing part ii-test procedures and parameter determination for dynamic analysis," *IEEE Std 115-1995*, pp. 1–198, Apr. 1996.

[90] J. Richter, A. Dollinger, and M. Doppelbauer, "Iron loss and parameter measurement of permanent magnet synchronous machines," in *2014 International Conference on Electrical Machines (ICEM)*, 2014, pp. 1635–1641.

[91] JSOL Corporation. JMAG-Designer, FEA Software for Electromechanical Design. [May, 19, 2018]. [Online]. Available: https://jmag-international.com/products/jmag-designer/index.html

[92] H. Janocha, *Actuators*. Berlin Heidelberg: Springer-Verlag, 2004.

[93] J. D. Gibbs and E. Fesquet, *Brit. Patent Nr. 238*, 1889.

[94] C. Bratiloveanu, D. Anghelus, and I. Boldea, "A comparative investigation of three pm-less mw power range wind generator topologies," in *2012 13th International Conference on Optimization of Electrical and Electronic Equipment (OPTIM)*, 2012, pp. 535–543.

[95] M. von Dolivo-Dobrowolsky, "Power transmission with alternating currents of different phase (three-phase current)," *Elektrotechnische Zeitschrift*, pp. 149–153, 1891 (in German).

[96] F. Uppenborn, "Power transmission Lauffen-Frankfurt a. M." *Elektrotechnische Zeitschrift*, pp. 379–382, 1892 (in German).

[97] R. Block, "3-dimensionale numerische feldberechnung und Simulation eines Klauenpolgenerators," Ph.D. dissertation, RWTH Aachen, 1993.

[98] U. Teichgräber, "A contribution to the theory of the claw-pole machine," Ph.D. dissertation, Technische Universität Hannover, 1973 (in German).

[99] M. Hecquet and P. Brochet, "Modeling of a claw-pole alternator using permeance network coupled with electric circuits," *IEEE Transactions on Magnetics*, vol. 31, no. 3, pp. 2131–2134, May 1995.

[100] G. Henneberger and S. Kuppers, "Field calculation and dynamic simulation of a claw-pole alternator," in *1995 Seventh International Conference on Electrical Machines and Drives (Conf. Publ. No. 412)*, Sep. 1995, pp. 286–290.

[101] G. Henneberger, S. Kuppers, and I. Ramesohl, "Numerical calculation, simulation and design optimisation of claw pole alternators for automotive application," in *IEE Colloquium on Machines for Automotive Applications (Digest No. 1996/166)*, Nov 1996, pp. 3/1–3/5.

[102] S. Kuppers and G. Henneberger, "Numerical procedures for the calculation and design of automotive alternators," *IEEE Transactions on Magnetics*, vol. 33, no. 2, pp. 2022–2025, Mar. 1997.

[103] S. Wu, S. Zuo, and Y. Zhang, "Optimization for electromagnetic noise reduction in claw pole alternator by rotor claw chamfering," *IEEE Transactions on Industrial Electronics*, vol. 65, no. 12, pp. 9325–9335, Dec. 2018.

[104] K. Yamazaki, R. Suzuki, M. Nuka, and M. Masegi, "Analysis and characteristics improvement of claw-pole alternators by reducing armature reaction," *IEEE Transactions on Industrial Electronics*, vol. 65, no. 11, pp. 8740–8748, Nov. 2018.

[105] A. Tan-Kim, N. Hagen, V. Lanfranchi, S. Clénet, T. Coorevits, J. Mipo, J. Legranger, and F. Palleschi, "Influence of the manufacturing process of a claw-pole alternator on its stator shape and acoustic noise," *IEEE Transactions on Industry Applications*, vol. 53, no. 5, pp. 4389–4395, Sep. 2017.

[106] S. Wu, S. Zuo, X. Wu, F. Lin, H. Zhong, and Y. Zhang, "Vibroacoustic prediction and mechanism analysis of claw pole alternators," *IEEE Transactions on Industrial Electronics*, vol. 64, no. 6, pp. 4463–4473, Jun. 2017.

[107] G. Dajaku, B. Lehner, X. Dajaku, A. Pretzer, and D. Gerling, "Hybrid excited claw pole rotor for high power density automotive alternators," in *2016 XXII International Conference on Electrical Machines (ICEM)*, Sep. 2016, pp. 2536–2543.

[108] A. Tan-Kim, V. Lanfranchi, S. Vivier, J. Legranger, and F. Palleschi, "Vibroacoustic simulation and optimization of a claw-pole alternator," *IEEE Transactions on Industry Applications*, vol. 52, no. 5, pp. 3878–3885, Sep. 2016.

[109] C. Min, W. Xiuhe, and Z. Changqing, "The basic research of novel hybrid excitation brushless claw pole alternator," in *2016 IEEE 11th Conference on Industrial Electronics and Applications (ICIEA)*, Jun. 2016, pp. 1479–1483.

[110] P. Upadhayay, A. Kedous-Lebouc, L. Garbuio, J. Mipo, and J. Dubus, "Design comparison of a conventional and permanent magnet based claw-pole

machine for automotive application," in *2017 15th International Conference on Electrical Machines, Drives and Power Systems (ELMA)*, June 2017, pp. 1–5.

[111] G. Starrermayr, "Modeling of a claw-pole motor," Master's thesis, Johannes Keppler University Linz, 1998 (in German).

[112] E. C. Prötsch, "Microprocessor control and simulation of a fan motor," Master's thesis, Johannes Keppler University Linz, 1997 (in German).

[113] H. D. Stölting and A. Beisse, *Small electric drives*. B. G. Teubner Stuttgart, 1987 (in German).

[114] C. Peham, "Modeling of a claw-pole stepper motor," Master's thesis, Johannes Keppler University Linz, 1998 (in German).

[115] W. H. Yeadon and A. W. Yeadon, *Handbook of small electric motors*. New York, NY, USA: McGraw-Hill, 2001.

[116] H. Hembach, D. Gerling, and S. Beyer, "Estimation of boundaries for the claw-pole geometry in electrical water pump applications," in *2006 International Conference on Electrical Machines (ICEM)*, Sep. 2006.

[117] H. Hembach, D. Gerling, and E. Nipp, "Analytical design of a claw-pole motor for electrical water pump applications," in *2007 International Conference on Power Engineering, Energy and Electrical Drives*, Apr. 2007, pp. 174–179.

[118] R. Felicetti and I. Ramesohl, "Design of a mass-production low-cost claw-pole motor for an automotive application," *COMPEL - The international journal for computation and mathematics in electrical and electronic engineering*, vol. 22, no. 4, pp. 937–952, Aug. 2003.

[119] Bühler Motor GmbH, "Kreiselpumpe," EP 1 850 010 A2, Oct. 2007.

[120] A. Reinap, "Design of powder core motors," Ph.D. dissertation, Lund University, 2005.

[121] S. K. T. Lundmark, "Application of 3-d computation of magnetic fields to the design of claw pole motors," Ph.D. dissertation, Chalmer University of Technology, 2005.

[122] E. Pinguey, "On the design and construction of modulated pole machines," Ph.D. dissertation, University of Newcastle Upon Tyne, 2010.

[123] Y. Shen, Z. Q. Zhu, J. T. Chen, R. P. Deodhar, and A. Pride, "Analytical modeling of claw-pole stator spm brushless machine having smc stator core," *IEEE Transactions on Magnetics*, vol. 49, no. 7, pp. 3830–3833, Jul. 2013.

[124] C. Liu, J. Zhu, Y. Wang, Y. Guo, and G. Lei, "Comparison of claw-pole machines with different rotor structures," *IEEE Transactions on Magnetics*, vol. 51, no. 11, pp. 1–4, Nov. 2015.

[125] X. Ba, Y. Guo, J. Zhu, and C. Zhang, "An equivalent circuit model for predicting the core loss in a claw-pole permanent magnet motor with soft magnetic composite core," *IEEE Transactions on Magnetics*, vol. 54, no. 11, pp. 1–6, Nov. 2018.

[126] F. Zhang, Y. Liu, and H. Bai, "Study and design of 3-d flux permanent magnet claw-pole motor with smc stator," in *2009 International Conference on Applied Superconductivity and Electromagnetic Devices*, Sep. 2009, pp. 316–319.

[127] J. Liang, A. Parsapour, E. Cosoroaba, M. Wu, I. Boldea, and B. Fahimi, "A high torque density outer rotor claw pole stator permanent magnet synchronous motor," in *2018 IEEE Transportation Electrification Conference and Expo (ITEC)*, Jun. 2018, pp. 389–393.

[128] Fengge Zhang, Hanyang Wei, Guangwei Liu, and Xueliang Bian, "Loss analysis of axial sectional claw pole high speed motor with permanent magnet outer rotor," in *2013 International Conference on Electrical Machines and Systems (ICEMS)*, Oct. 2013, pp. 1345–1350.

[129] C. Liu, J. Lu, Y. Wang, G. Lei, J. Zhu, and Y. Guo, "Techniques for reduction of the cogging torque in claw pole machines with smc cores," *Energies*, vol. 10, p. 1541, 10 2017.

[130] S. Leitner, H. Gruebler, and A. Muetze, "Innovative low-cost sub-fractional hp BLDC claw-pole machine design for fan applications," *IEEE Transactions on Industry Applications*, vol. 55, no. 3, pp. 2558–2568, May 2019.

[131] ——, "Cogging torque minimization and performance of the sub-fractional hp BLDC claw-pole motor," *IEEE Transactions on Industry Applications*, vol. 55, no. 5, pp. 4653–4664, Sep./Oct. 2019.

[132] ——, "Cogging torque minimization on a mass-produced sub-fractional horsepower brushless direct current claw-pole motor," in *2018 IEEE Energy Conversion Congress and Exposition (ECCE)*, Sep. 2018, pp. 6083–6089.

[133] F. Jeske, "Elektronisch kommutierter Aussenlaeufermotor," EP 0 766 370 A2, Apr. 1997.

[134] e. a. Wen-Shi Huang, "Miniature motor structure," US 2002 0117932 A1, August 2022.

[135] I. Boldea and L. N. Tutelea, *Electric Machines: Steady State, Transients, and Design with MATLAB*. CRC Press: Taylor & Francis Group, LLC, 2009.

[136] C. Chiu, Y. Chen, and W. Jhang, "Properties of cogging torque, starting torque, and electrical circuits for the single-phase brushless dc motor," *IEEE Transactions on Magnetics*, vol. 44, no. 10, pp. 2317–2323, Oct. 2008.

[137] C. Chiu, Y. Chen, Y. Liang, and R. Liang, "Optimal driving efficiency design for the single-phase brushless dc fan motor," *IEEE Transactions on Magnetics*, vol. 46, no. 4, pp. 1123–1130, Apr. 2010.

[138] H. Hembach, S. A. Evans, and D. Gerling, "Systematic comparison of bldc motors for small automotive water pump applications," in *2008 18th International Conference on Electrical Machines*, 2008, pp. 1–5.

[139] J. H. F. S.-L. B. J. Fleischer, *Handbook of coil winding*. Berlin: Springer Verlag, 2016 (in German).

[140] I. Boldea and L. N. Tutelea, *Reluctance Electric Machines*. CRC Press: Taylor & Francis Group, LLC, 2018.

[141] S. Leitner, H. Gruebler, and A. Muetze, "Effects of manufacturing imperfections and design parameters on radial magnetic forces in the BLDC claw-pole motor," in *2019 IEEE International Electric Machines Drives Conference (IEMDC)*, May 2019, pp. 2167–2173.

[142] S. Leitner, G. Krenn, H. Gruebler, and A. Muetze, "Rheometer-based cogging torque measurement for sub-fractional hp permanent magnet motors," in *2019 IEEE Transportation Electrification Conference and Expo (ITEC)*, Jun. 2019, pp. 1–7.

[143] S. Leitner, H. Gruebler, and A. Muetze, "Low-cost BLDC claw-pole motor design for fan applications with reduced cogging torque and balanced axial forces," in *2020 IEEE Applied Power Electronics Conference and Exposition (APEC)*, Mar. 2020, pp. 279–284.

[144] K. Vogt, *Calculation of electric machines*. Weinheim, Germany: VCH Verlagsgesellschaft, 1996 (in German).

[145] J. Bastos and N. Sadowski, *Magnetic materials and 3D finite element modeling*. CRC Press: Taylor & Francis Group, LLC, 2013.

[146] N. Bianchi, *Electrical Machine Analysis using Finite Elements*. CRC Press: Taylor & Francis Group, LLC, 2005.

[147] H. Goering, H.-G. Roos, and L. Tobiska, *The finite-element-method for beginners*. Wiley-VCH, 2010 (in German).

[148] K. Hameyer and R. Belmans, *Numerical Modelling and Design of Electrical Machines and Devices*. WIT Press, 1999.

[149] Voestalpine, "Electrical steel isovac 250-35A datasheet," Oct. 2018.

[150] T. G. Mezger, *The Rheology Handbook*. Hannover, Vincentz Network, 2011.

[151] G. Schramm, *Introduction to rheology and rheometry*. Karlsruhe, Thermo Electron, 2004 (in German).

[152] Anton Paar GmbH. (2018) Modular Compact Rheometer. [Nov., 21, 2018]. [Online]. Available: https://www.anton-paar.com/

[153] R. Worthoff, *Technical rheology*. Weinheim, WILEY-VCH,, 2013 (in German).

[154] Fengxiang Wang and Longya Xu, "Calculation and measurement of radial and axial forces for a bearingless pmdc motor," in *Conference Record of the 2000 IEEE Industry Applications Conference. Thirty-Fifth IAS Annual Meeting and World Conference on Industrial Applications of Electrical Energy (Cat. No.00CH37129)*, vol. 1, Oct. 2000, pp. 249–252.

[155] S. Leitner, T. Kulterer, H. Gruebler, and A. Muetze, "Characterization of the thermal performance of low-cost sub-fhp BLDC claw-pole motor designs," in *accepted for publication, 2020 IEEE Energy Conversion Congress and Exposition (ECCE)*, 2020.

[156] S. Leitner, G. Krenn, H. Gruebler, and A. Muetze, "Rheometer-based cogging and hysteresis torque and iron loss determination of sub-fhp motors," *IEEE Transactions on Industry Applications*, Apr. 2020.

[157] J. Lee, Y. Kim, S. Rhyu, I. Jung, S. Chai, and J. Hong, "Hysteresis torque analysis of permanent magnet motors using preisach model," *IEEE Transactions on Magnetics*, vol. 48, no. 2, pp. 935–938, Feb. 2012.

[158] Metrodata GmbH. (2019) GUM Workbench. [Oct., 31, 2019]. [Online]. Available: http://www.metrodata.de/\index_en.html

[159] M. Bali and A. Muetze, "Modeling the effect of cutting on the magnetic properties of electrical steel sheets," *IEEE Trans. Ind. Electron.*, vol. 64, no. 3, pp. 2547–2556, Mar. 2007.

[160] K. H. Decker, *Machine elements*. Muenchen, Germany: Carl Hanser Verlag, 2009 (in German).

[161] F. J. T. E. Ferreira, A. T. de Almeida, J. F. S. Carvalho, and M. V. Cistelecan, "Experiments to observe the impact of power quality and voltage-source inverters on the temperature of three-phase cage induction motors using an infra-red camera," in *2009 IEEE International Electric Machines and Drives Conference*, May 2009, pp. 1311–1318.

[162] L. Chang, A. R. Eastham, and G. E. Dawson, "Permanent magnet synchronous motor: finite element torque calculations," in *Conference Record of the IEEE Industry Applications Society Annual Meeting,*, vol. 1, Oct. 1989, pp. 69–73.

Part III

Appendices

Appendix A

Performance Specifications and System Parameters

The general performance specifications and system parameters of the studied single-phase BLDC claw-pole motors are presented below.

Table A.1 presents the general design specifications. For the analysis, the lower end of the voltage range is considered, because it is more critical with respect to the functionality of the motor, and room temperature is assumed as the measurements are also performed at this temperature. The remanent flux density B_{rem} of the magnet generally decreases with increasing temperature, as does the torque. Both the bearing friction and the friction of the working fluid typically increase with decreasing temperature.

Table A.1: Design Specifications.

Parameter	Value	Parameter	Value
U_{DC}	$8 - 16\,\mathrm{V}$	n	$5500\,\mathrm{rpm}$
$\overline{T}_{\mathrm{o}}$	$1\,\mathrm{mN}\cdot\mathrm{m}$	T_{A}	$-40 - 150^{\circ}\mathrm{C}$

Table A.2 presents the main system parameters used in the 3-D finite-element models and prototypes of the *Design 0–Design 3*. The claw-pole motor is designed based on the performance specifications presented in Table A.1 and a given PM rotor, which consists of a rotor yoke and a PM ring. The PM ring is made of a plastic bonded NdFeB material and shows a radial magnetization. In the finite-element analysis with JMAG® [91], the inter-pole region of the magnet is modeled as a linear

magnetization decay characterized by α. (The decay angle α has been varied such that the shape of the simulated back-EMF conforms with that of the measured one.) The current I_p is the rms phase current. The stator parts are milled from free-cutting steel 11SMnPb37. $l_{ax,r}$ and $l_{ax,s}$ are the axial lengths of the rotor and stator, where the axial stator length is $l_{ax,s} = 2w_{s,yoke}$, and w_{claw} is the axial length of the claws. As the axial lengths of the rotor, stator, and claws differ, the effective axial length l_{ax} is the average of $l_{ax,r}$ and w_{claw}.

Table A.2: System Parameters.

Parameter	Value	Parameter	Value
B_{rem}	0.40 T	μ_{rec}	1.29
α	24°	$2p$	4
$l_{ax,r}$	6 mm	l_{ax}	5.25 mm
r_2	3 mm	r_3	8 mm
$w_{s,yoke}$	2.9 mm	w_{claw}	4.5 mm
$\Delta\delta_{max}$	1.8 %	h_m	0.725 mm
δ	0.5 mm	φ_{cp}	72°
t_{steel}	1 mm	N_A, N_B	208
R_A, R_B	16.4 Ω	I_p	250 mA

The 3-D finite-element models and prototypes of *Design 4* and *Design 5* are realized with an increased axial length of the stator and the claws to obtain more design freedom with respect to the claw-poles implementing the proposed V-skew: $l_{ax,s}$ = 8 mm and w_{claw} = 7 mm. [The axial length of the stator has been increased to the same length as that of a comparable salient-pole motor of similar size (see e.g., [25]), taking the length of its end-winding into account.]

Appendix B

Analytic Determination of the Phase Current Waveform

In Subsection 1.2.1 the equivalent circuit of a single-phase BLDC motor is described, see Fig. 1.6. The inverter voltage u_{inv} is typically pulse-width-modulated or constant for a defined period; hence, it has a rectangular-like waveform. The back-EMF u_{EMF} typically has a trapezoidal-like waveform and can hence be sufficiently described by a dominant third order harmonic component in addition to the first order harmonic component. Due to the different waveforms of u_{inv} and u_{EMF}, the phase current i_{p} is highly non-sinusoidal. Because the waveforms of u_{inv}, u_{EMF}, and i_{p} are neither sinusoidal nor constant for defined intervals, the differential equation describing the equivalent circuit in Fig. 1.6 is derived and solved below. Inspired by [7], the effect of a bifilar winding on the phase current waveform is considered as well.

Differential Equation

Applying Kirchhoff's Law to the equivalent circuit in Fig. 1.6 yields

$$u_{\mathrm{inv}}(t) = i_{\mathrm{p}}(t)R + L\frac{di_{\mathrm{p}}(t)}{dt} + u_{\mathrm{EMF}}(t). \tag{B.1}$$

The trapezoidal back-EMF is described by a first and a third order harmonic component:

$$u_{\mathrm{EMF}}(t) = \hat{u}_{\mathrm{EMF},1}\sin(\omega_{\mathrm{el}}t + \varphi_1) + \hat{u}_{\mathrm{EMF},3}\sin(3\omega_{\mathrm{el}}t + \varphi_3). \tag{B.2}$$

For convenience, the time dependencies in (B.1) and (B.2) are replaced so that the quantities are presented as a function of the rotational angle θ

$$\theta = \omega_{\mathrm{el}}t. \tag{B.3}$$

The time derivative of (B.3) yields

$$\frac{d\theta}{dt} = \omega_{\mathrm{el}} = p\,\omega_{\mathrm{m}} = p2\pi\frac{n}{60}. \tag{B.4}$$

Performing said variable change for (B.1) yields

$$u_{\mathrm{inv}}(\theta) = i_{\mathrm{p}}(\theta)R + L\frac{di_{\mathrm{p}}(\theta)}{dt}\frac{d\theta}{d\theta} + u_{\mathrm{EMF}}(\theta). \tag{B.5}$$

Considering (B.2) yields

$$u_{\mathrm{inv}}(\theta) = i_{\mathrm{p}}(\theta)R + L\frac{di_{\mathrm{p}}(\theta)}{d\theta}\underbrace{\frac{d\theta}{dt}}_{\omega_{\mathrm{el}}} + \hat{u}_{\mathrm{EMF},1}\sin(\theta+\varphi_1) + \hat{u}_{\mathrm{EMF},3}\sin(3\theta+\varphi_3). \tag{B.6}$$

With (B.4), (B.6) yields

$$u_{\mathrm{inv}}(\theta) = i_{\mathrm{p}}(\theta)R + Lp\omega_{\mathrm{m}}\frac{di_{\mathrm{p}}(\theta)}{d\theta} + \hat{u}_{\mathrm{EMF},1}\sin(\theta+\varphi_1) + \hat{u}_{\mathrm{EMF},3}\sin(3\theta+\varphi_3). \tag{B.7}$$

Assuming constant inverter voltage for $0 < \theta < \pi$, i.e., $u_{\mathrm{inv}}(\theta) = U_{\mathrm{inv}}$, yields

$$U_{\mathrm{inv}} = i_{\mathrm{p}}(\theta)R + Lp\omega_{\mathrm{m}}\frac{di_{\mathrm{p}}(\theta)}{d\theta} + \hat{u}_{\mathrm{EMF},1}\sin(\theta+\varphi_1) + \hat{u}_{\mathrm{EMF},3}\sin(3\theta+\varphi_3). \tag{B.8}$$

Finally, for $0 < \theta < \pi$, the differential equation is as follows:

$$\underbrace{U_{\mathrm{inv}}}_{g_1(\theta)} - \underbrace{\hat{u}_{\mathrm{EMF},1}\sin(\theta+\varphi_1)}_{g_2(\theta)} - \underbrace{\hat{u}_{\mathrm{EMF},3}\sin(3\theta+\varphi_3)}_{g_3(\theta)} = i_{\mathrm{p}}(\theta)R + Lp\omega_{\mathrm{m}}\frac{di_{\mathrm{p}}(\theta)}{d\theta}, \tag{B.9}$$

where $g_1(\theta)$, $g_2(\theta)$, and $g_3(\theta)$ are the perturbation functions.

Homogeneous Solution

Setting $g_1(\theta)$, $g_2(\theta)$, and $g_3(\theta)$ to zero, the homogeneous equation is obtained

$$0 = i_{\mathrm{p}}(\theta)R + Lp\omega_{\mathrm{m}}\frac{di_{\mathrm{p}}(\theta)}{d\theta}. \tag{B.10}$$

To solve (B.10), the following Ansatz function is chosen:

$$i_{\mathrm{hom}}(\theta) = K_1 e^{\lambda\theta} \tag{B.11}$$

with its derivative

$$\frac{di_{\mathrm{hom}}(\theta)}{d\theta} = \lambda K_1 e^{\lambda\theta}. \tag{B.12}$$

Inserting the Ansatz functions into (B.10) yields

$$0 = K_1 e^{\lambda\theta} R + Lp\omega_\mathrm{m} \lambda K_1 e^{\lambda\theta}. \tag{B.13}$$

Solving for λ results in

$$\lambda = -\frac{R}{Lp\omega_\mathrm{m}}. \tag{B.14}$$

The homogeneous solution is then

$$i_\mathrm{hom}(\theta) = K_1 e^{-\frac{R\theta}{Lp\omega_\mathrm{m}}}. \tag{B.15}$$

Particular Solution 1

For the first part of the particular solution, $g_2(\theta)$ and $g_3(\theta)$ are set to zero:

$$U_\mathrm{inv} = i_\mathrm{p}(\theta) R + Lp\omega_\mathrm{m} \frac{di_\mathrm{p}(\theta)}{d\theta}. \tag{B.16}$$

Considering the constant function $g_1(\theta)$, a constant Ansatz function is chosen:

$$i_\mathrm{part1}(\theta) = K_2 \tag{B.17}$$

with its derivative

$$\frac{di_\mathrm{part1}(\theta)}{d\theta} = 0. \tag{B.18}$$

The differential equation then yields

$$U_\mathrm{inv} = K_2 R + Lp\omega_\mathrm{m} 0. \tag{B.19}$$

Solving for K_2, the following is obtained

$$K_2 = \frac{U_\mathrm{inv}}{R}. \tag{B.20}$$

Hence, the first part of the particular solution yields

$$i_\mathrm{part1}(\theta) = \frac{U_\mathrm{inv}}{R}. \tag{B.21}$$

Particular Solution 2

For the second part of the particular solution, $g_1(\theta)$ and $g_3(\theta)$ are set to zero:

$$-\hat{u}_{\mathrm{EMF},1}\sin(\theta+\varphi_1) = i_\mathrm{p}(\theta)R + Lp\omega_\mathrm{m}\frac{di_\mathrm{p}(\theta)}{d\theta}. \tag{B.22}$$

Therefore, the following Ansatz function is chosen:

$$i_{\mathrm{part2}}(\theta) = A_\mathrm{p}\sin(\theta+\varphi_1) + B_\mathrm{p}\cos(\theta+\varphi_1) \tag{B.23}$$

with its derivative

$$\frac{di_{\mathrm{part2}}(\theta)}{d\theta} = A_\mathrm{p}\cos(\theta+\varphi_1) - B_\mathrm{p}\sin(\theta+\varphi_1). \tag{B.24}$$

The differential equation then yields

$$\begin{aligned}-\hat{u}_{\mathrm{EMF},1}\sin(\theta+\varphi_1) =& R\left[A_\mathrm{p}\sin(\theta+\varphi_1) + B_\mathrm{p}\cos(\theta+\varphi_1)\right] \\ &+ Lp\omega_\mathrm{m}\left[A_\mathrm{p}\cos(\theta+\varphi_1) - B_\mathrm{p}\sin(\theta+\varphi_1)\right].\end{aligned} \tag{B.25}$$

Equating the coefficients of the left and right side of the equation yields:

$$-\hat{u}_{\mathrm{EMF}} = RA_\mathrm{p} - Lp\omega_\mathrm{m}B_\mathrm{p} \tag{B.26}$$

and

$$0 = RB_\mathrm{p} + Lp\omega_\mathrm{m}A_\mathrm{p}. \tag{B.27}$$

Solving (B.27) for A_p yields

$$A_\mathrm{p} = -\frac{RB_\mathrm{p}}{Lp\omega_\mathrm{m}}. \tag{B.28}$$

Inserting A_p into (B.26) yields

$$-\hat{u}_{\mathrm{EMF},1} = R\left(-\frac{RB_\mathrm{p}}{Lp\omega_\mathrm{m}}\right) - Lp\omega_\mathrm{m}B_\mathrm{p}. \tag{B.29}$$

Solving for B_p then yields

$$B_\mathrm{p} = \frac{\hat{u}_{\mathrm{EMF},1}Lp\omega_\mathrm{m}}{R^2 + (Lp\omega_\mathrm{m})^2}. \tag{B.30}$$

A_p is then obtained as

$$A_\mathrm{p} = -\frac{R}{Lp\omega_\mathrm{m}}\frac{\hat{u}_{\mathrm{EMF},1}Lp\omega_\mathrm{m}}{R^2 + (Lp\omega_\mathrm{m})^2} = -\frac{\hat{u}_{\mathrm{EMF},1}R}{R^2 + (Lp\omega_\mathrm{m})^2}. \tag{B.31}$$

The second part of the particular solution is

$$\begin{aligned}i_{\mathrm{part\,2}}(\theta) &= \left(-\frac{\hat{u}_{\mathrm{EMF},1}R}{R^2 + (Lp\omega_\mathrm{m})^2}\right)\sin(\theta+\varphi_1) + \left(\frac{\hat{u}_{\mathrm{EMF},1}Lp\omega_\mathrm{m}}{R^2 + (Lp\omega_\mathrm{m})^2}\right)\cos(\theta+\varphi_1) \\ &= -\frac{\hat{u}_{\mathrm{EMF},1}}{R^2 + (Lp\omega_\mathrm{m})^2}\Big(R\sin(\theta+\varphi_1) - Lp\omega_\mathrm{m}\cos(\theta+\varphi_1)\Big).\end{aligned} \tag{B.32}$$

Particular Solution 3

For the third part of the particular solution, $g_1(\theta)$ and $g_2(\theta)$ are set to zero:

$$-\hat{u}_{\mathrm{EMF},3}\sin(3\theta+\varphi_3) = i_\mathrm{p}(\theta)R + Lp\omega_\mathrm{m}\frac{di_\mathrm{p}(\theta)}{d\theta} \tag{B.33}$$

Following the procedure shown above for the second part of the particular solution, the third part of the particular solution is obtained as:

$$i_{\mathrm{part}\,3}(\theta) = -\frac{\hat{u}_{\mathrm{EMF},3}}{R^2+(L3p\omega_\mathrm{m})^2}\Big(R\sin(3\theta+\varphi_3) - L3p\omega_\mathrm{m}\cos(3\theta+\varphi_3)\Big). \tag{B.34}$$

General Solution of the Differential Equation

The solution of the differential equation of the phase current i_p is the sum of the homogeneous and all the particular solutions:

$$i_\mathrm{p}(\theta) = i_\mathrm{hom}(\theta) + i_{\mathrm{part}\,1}(\theta) + i_{\mathrm{part}\,2}(\theta) + i_{\mathrm{part}\,3}(\theta) \tag{B.35}$$

which yields, after insertion,

$$\begin{aligned} i_\mathrm{p}(\theta) = K_1 e^{-\frac{R\theta}{Lp\omega_\mathrm{m}}} + \frac{U_\mathrm{inv}}{R} &- \frac{\hat{u}_{\mathrm{EMF},1}}{R^2+(Lp\omega_\mathrm{m})^2}\Big(R\sin(\theta+\varphi_1) - Lp\omega_\mathrm{m}\cos(\theta+\varphi_1)\Big) \\ &- \frac{\hat{u}_{\mathrm{EMF},3}}{R^2+(L3p\omega_\mathrm{m})^2}\Big(R\sin(3\theta+\varphi_3) - L3p\omega_\mathrm{m}\cos(3\theta+\varphi_3)\Big). \end{aligned} \tag{B.36}$$

Initial Condition

During commutation, when one sub-phase is switched off, current continues to flow in the other sub-phase due to the coupling of the bifiliar winding. Assuming $\theta_\mathrm{on} = 0°$ and $\theta_\mathrm{off} = 180°$, see Fig. 2.4, the following holds true:

$$i_\mathrm{p}(\theta = 0) = -\zeta i_\mathrm{p}(\theta = \pi), \tag{B.37}$$

where ζ is the coupling factor of sub-phases A and B of the bifilar winding.

Using (B.36), the left side (LS) of (B.37) is obtained as

$$\begin{aligned} \mathrm{LS} = K_1 + \frac{U_\mathrm{inv}}{R} &- \frac{\hat{u}_{\mathrm{EMF},1}}{R^2+(Lp\omega_\mathrm{m})^2}\Big(R\sin(\varphi_1) - Lp\omega_\mathrm{m}\cos(\varphi_1)\Big) \\ &- \frac{\hat{u}_{\mathrm{EMF},3}}{R^2+(L3p\omega_\mathrm{m})^2}\Big(R\sin(\varphi_3) - L3p\omega_\mathrm{m}\cos(\varphi_3)\Big) \end{aligned} \tag{B.38}$$

Similarly, the right side (RS) of (B.37) is obtained as

$$\begin{aligned}\mathrm{RS} = -\zeta K_1 e^{-\frac{R\pi}{Lp\omega_\mathrm{m}}} - \frac{\zeta U_\mathrm{inv}}{R} &+ \frac{\zeta \hat{u}_{\mathrm{EMF},1}}{R^2 + (Lp\omega_\mathrm{m})^2}\Big(R\sin(\pi + \varphi_1) - Lp\omega_\mathrm{m}\cos(\pi + \varphi_1)\Big) \\ &+ \frac{\zeta \hat{u}_{\mathrm{EMF},3}}{R^2 + (L3p\omega_\mathrm{m})^2}\Big(R\sin(3\pi + \varphi_3) - L3p\omega_\mathrm{m}\cos(3\pi + \varphi_3)\Big)\end{aligned} \tag{B.39}$$

Combining LS and RS and solving for K_1 yields

$$\begin{aligned}K_1\left[1 + \zeta e^{-\frac{R\pi}{Lp\omega_\mathrm{m}}}\right] = &- \frac{\zeta U_\mathrm{inv}}{R} - \frac{U_\mathrm{inv}}{R} \\ &+ \frac{\hat{u}_{\mathrm{EMF},1}}{R^2 + (Lp\omega_\mathrm{m})^2}\Big(R\sin(\varphi_1) - Lp\omega_\mathrm{m}\cos(\varphi_1) + \zeta R\sin(\pi + \varphi_1) - \zeta Lp\omega_\mathrm{m}\cos(\pi + \varphi_1)\Big) \\ &+ \frac{\hat{u}_{\mathrm{EMF},3}}{R^2 + (L3p\omega_\mathrm{m})^2}\Big(R\sin(\varphi_3) - L3p\omega_\mathrm{m}\cos(\varphi_3) + \zeta R\sin(3\pi + \varphi_3) - \zeta L3p\omega_\mathrm{m}\cos(3\pi + \varphi_3)\Big)\end{aligned} \tag{B.40}$$

$$\begin{aligned}K_1 = \frac{-\frac{\zeta U_\mathrm{inv}}{R} - \frac{U_\mathrm{inv}}{R}}{1 + \zeta e^{-\frac{R\pi}{Lp\omega_\mathrm{m}}}} &+ \frac{\frac{\hat{u}_{\mathrm{EMF},1}}{R^2 + (Lp\omega_\mathrm{m})^2}\Big(R\sin(\varphi_1) - Lp\omega_\mathrm{m}\cos(\varphi_1) + \zeta R\sin(\pi + \varphi_1) - \zeta Lp\omega_\mathrm{m}\cos(\pi + \varphi_1)\Big)}{1 + \zeta e^{-\frac{R\pi}{Lp\omega_\mathrm{m}}}} \\ &+ \frac{\frac{\hat{u}_{\mathrm{EMF},3}}{R^2 + (L3p\omega_\mathrm{m})^2}\Big(R\sin(\varphi_3) - L3p\omega_\mathrm{m}\cos(\varphi_3) + \zeta R\sin(3\pi + \varphi_3) - \zeta L3p\omega_\mathrm{m}\cos(3\pi + \varphi_3)\Big)}{1 + \zeta e^{-\frac{R\pi}{L3p\omega_\mathrm{m}}}}\end{aligned} \tag{B.41}$$

Using $\sin(\pi + \varphi) = -\sin(\varphi)$ and $\cos(\pi + \varphi) = -\cos(\varphi)$, K_1 is obtained as

$$\begin{aligned}K_1 = i_0 = &\frac{-\frac{U_\mathrm{inv}}{R}(1 + \zeta) + \frac{\hat{u}_{\mathrm{EMF},1}}{R^2 + (Lp\omega_\mathrm{m})^2}\Big(R\sin(\varphi_1)[1 - \zeta] - Lp\omega_\mathrm{m}\cos(\varphi_1)[1 - \zeta]\Big)}{1 + \zeta e^{-\frac{R\pi}{Lp\omega_\mathrm{m}}}} \\ &+ \frac{\frac{\hat{u}_{\mathrm{EMF},3}}{R^2 + (L3p\omega_\mathrm{m})^2}\Big(R\sin(\varphi_3)[1 - \zeta] - L3p\omega_\mathrm{m}\cos(\varphi_3)[1 - \zeta]\Big)}{1 + \zeta e^{-\frac{R\pi}{Lp\omega_\mathrm{m}}}}.\end{aligned} \tag{B.42}$$

Final Solution of the Differential Equation

$$
\begin{aligned}
i_\mathrm{p}(\theta) = & \frac{-\frac{U_\mathrm{inv}}{R}(1+\zeta)}{1+\zeta e^{-\frac{R\pi}{Lp\omega_\mathrm{m}}}} e^{-\frac{R\theta}{Lp\omega_\mathrm{m}}} + \frac{\frac{\hat{u}_{\mathrm{EMF},1}[1-\zeta]}{R^2+(Lp\omega_\mathrm{m})^2}\Big(R\sin(\varphi_1) - Lp\omega_\mathrm{m}\cos(\varphi_1)\Big)}{1+\zeta e^{-\frac{R\pi}{Lp\omega_\mathrm{m}}}} e^{-\frac{R\theta}{Lp\omega_\mathrm{m}}} \\
& + \frac{\frac{\hat{u}_{\mathrm{EMF},3}[1-\zeta]}{R^2+(L3p\omega_\mathrm{m})^2}\Big(R\sin(\varphi_3) - L3p\omega_\mathrm{m}\cos(\varphi_3)\Big)}{1+\zeta e^{-\frac{R\pi}{Lp\omega_\mathrm{m}}}} e^{-\frac{R\theta}{Lp\omega_\mathrm{m}}} + \frac{U_\mathrm{inv}}{R} \\
& - \frac{\hat{u}_{\mathrm{EMF},1}}{R^2+(Lp\omega_\mathrm{m})^2}\Big(R\sin(\theta+\varphi_1) - Lp\omega_\mathrm{m}\cos(\theta+\varphi_1)\Big) \\
& - \frac{\hat{u}_{\mathrm{EMF},3}}{R^2+(L3p\omega_\mathrm{m})^2}\Big(R\sin(3\theta+\varphi_3) - L3p\omega_\mathrm{m}\cos(3\theta+\varphi_3)\Big).
\end{aligned}
\tag{B.43}
$$

As per (B.43), Fig. B.1 shows the calculated phase current waveform using the following parameter: $U_\mathrm{inv} = 8\,\mathrm{V}$, $\hat{u}_{\mathrm{EMF},1} = 4.3\,\mathrm{V}$, $\hat{u}_{\mathrm{EMF},3} = 0.3\,\mathrm{V}$, $\varphi_1 = 15°$, $\varphi_3 = 3\varphi_1$, $p = 2$, $R = 16.4\,\Omega$, $L = 6\,\mathrm{mH}$, $n = 5500\,\mathrm{rpm}$, and $\zeta = 1$.[1] (The calculated rms phase current is 226.3 mA.)

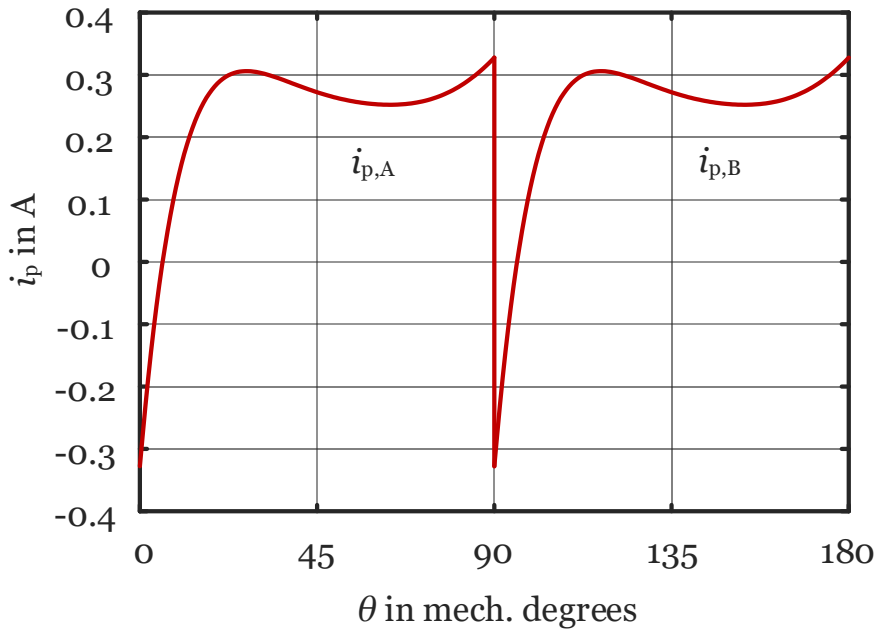

Fig. B.1: Calculated phase current waveform using (B.43).

[1] The parameters result from Tables A.1 and A.2, and Figs. 7.12 and S.1(a).

Appendix C

Excitation Effort and Flux Linkage: Claw-Pole versus Salient-Pole Motors

Claw-pole machines are well-known for their reduced excitation effort due to the global ring winding [140]. In fact, one coil can excite many poles, creating a hetero-polar magnetic field in the air-gap. Contrary to the BLDC salient-pole machine, the PM flux per pole $\Phi_{\mathrm{p,PM}}$ of the BLDC claw-pole motor links with all of the turns of the ring winding in the stator. From these perspectives, claw-pole motors are most effective when implemented with a high number of claw-poles.[1] The average linear current density over a pole pitch and the flux linkage of the BLDC claw-pole motor and the BLDC salient-pole motor are compared below.

Based on (1.12), the average linear current density over a pole pitch of the claw-pole motor, in which the number of conductors per slot $z_Q = N_{\mathrm{tot}}$, is

$$\overline{A}_{\tau_{\mathrm{p}},\mathrm{CP}} = \frac{2pN_{\mathrm{tot}}I_{\mathrm{p,av}}}{2\pi r_{\mathrm{s}}}, \tag{C.1}$$

where N_{tot} is the total number of turns in series per phase, r_{s} is the stator radius, and $I_{\mathrm{p,av}}$ is the average phase current.

Similarly, the average linear current density over a pole pitch of the salient-pole motor, in which the number of conductors per slot $z_Q = 2N_{\mathrm{pole}} = 2\frac{N_{\mathrm{tot}}}{2p}$, is

$$\overline{A}_{\tau_{\mathrm{p}},\mathrm{SP}} = \frac{2p2\frac{N_{\mathrm{tot}}}{2p}I_{\mathrm{p,av}}}{2\pi r_{\mathrm{s}}} = \frac{2N_{\mathrm{tot}}I_{\mathrm{p}}}{2\pi r_{\mathrm{s}}}, \tag{C.2}$$

where, in addition to the parameters described in the context of (C.1), N_{pole} is the number of turns per salient-pole.

[1] However, implementing a high pole number on a BLDC claw-pole motor for a given speed increases the electric and magnetic frequencies substantially and hence the switching and eddy current losses.

Comparing (C.1) and (C.2), it is evident that for the same average phase current $I_{\mathrm{p,av}}$ and total number of turns in series per phase N_{tot}, the average linear current density of the claw-pole motor is by the number of pole-pairs p larger than that of the salient-pole motor. Hence, the excitation effort linearly reduces with increasing number of pole-pairs p.

The flux linkage of the claw-pole motor and the salient-pole motor also differ, as do the resulting back-EMFs. As per Fig. 2.11(a), the back-EMF of the claw-pole motor is obtained from half the PM flux per pole $\frac{\Phi_{\mathrm{p,PM}}}{2}$ as follows:

$$u_{\mathrm{EMF,CP}} = 2p\, N_{\mathrm{tot}} \frac{d}{dt}\left(\frac{\Phi_{\mathrm{p,PM}}}{2}\right). \tag{C.3}$$

Similarly, following Fig. 2.11(b), the back-EMF of the salient-pole motor is obtained from half the flux per pole $\frac{\Phi_{\mathrm{p,PM}}}{2}$ as follows:

$$u_{\mathrm{EMF,SP}} = 2p \frac{N_{\mathrm{tot}}}{p} \frac{d}{dt}\left(\frac{\Phi_{\mathrm{p,PM}}}{2}\right) = 2\, N_{\mathrm{tot}} \frac{d}{dt}\left(\frac{\Phi_{\mathrm{p,PM}}}{2}\right). \tag{C.4}$$

As opposed to the claw-pole motor, $\frac{\Phi_{\mathrm{p,PM}}}{2}$ links only with the turns of two consecutive stator poles of the salient-pole motor, i.e., $\frac{N_{\mathrm{tot}}}{p}$. Comparing (C.3) and (C.4), the four-pole BLDC salient-pole motor needs double the number of turns than the four-pole BLDC claw-pole motor to obtain the same back-EMF provided that these motors share the same PM flux per pole $\Phi_{\mathrm{p,PM}}$. (Depending on the motor dimensions, the phase resistance might differ for the salient-pole and claw-pole motors which must be considered when choosing the number of turns.)

Appendix D

Magnetic Equivalent Circuit of the Claw-Pole Motor

Fig. D.1 shows the magnetic equivalent circuit (MEC) of the claw-pole motor, where the claw-pole motor is divided into a lumped reluctance network modeling its individual elements. The model of the main flux paths is shown in black, in which

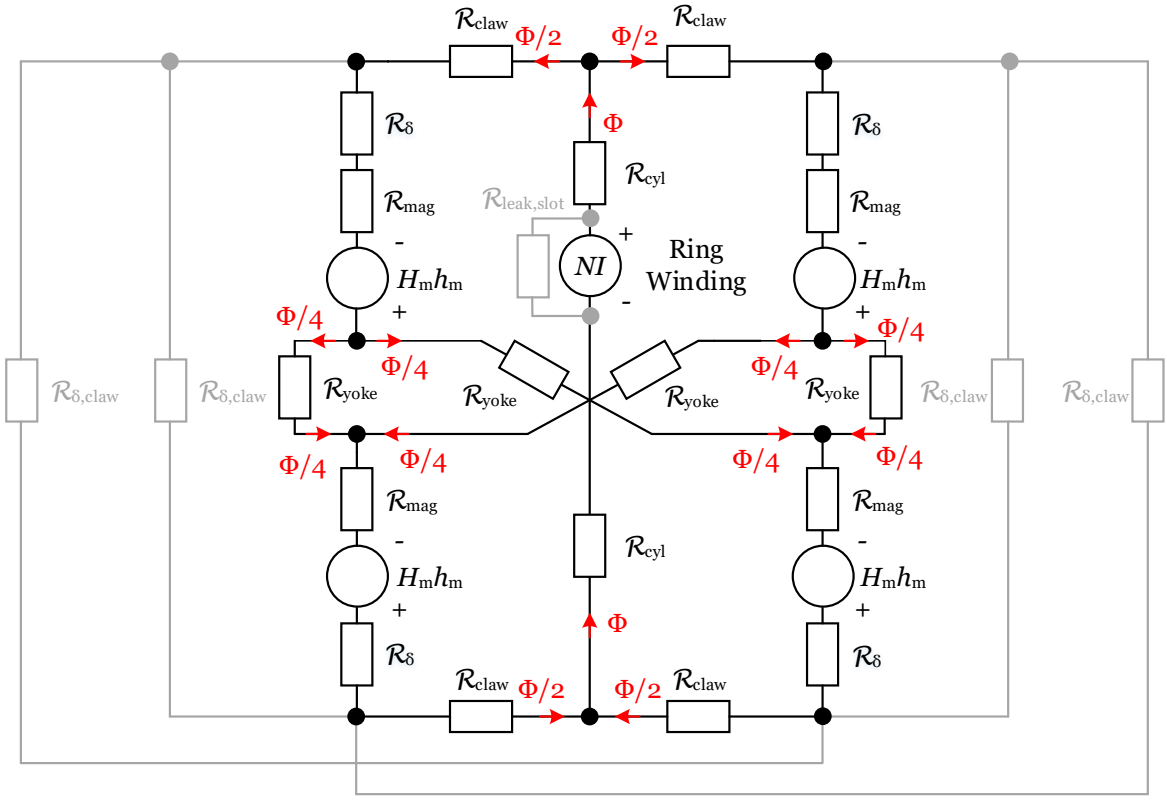

Fig. D.1: Magnetic equivalent circuit (MEC) of the four-pole four-slot claw-pole motor (main flux paths in black, leakage flux paths in gray).

leakage effects are neglected. Leaving the cylindrical portion of the stator part, the main flux Φ produced by the ring winding separates twice, once within the stator and once within the rotor, including cross-coupling in the rotor yoke section. (In addition, the leakage paths in the inter-claw region and the slot leakage are shown in gray.)

Assuming symmetric branches[1] and infinite permeability ($\mu_{\mathrm{fe}} \to \infty$) for the iron parts (modeled by $\mathcal{R}_{\mathrm{zyl}}$, $\mathcal{R}_{\mathrm{claw}}$, and $\mathcal{R}_{\mathrm{yoke}}$) yields, after rearrangement, the simplified MEC shown in Fig. D.2(a).

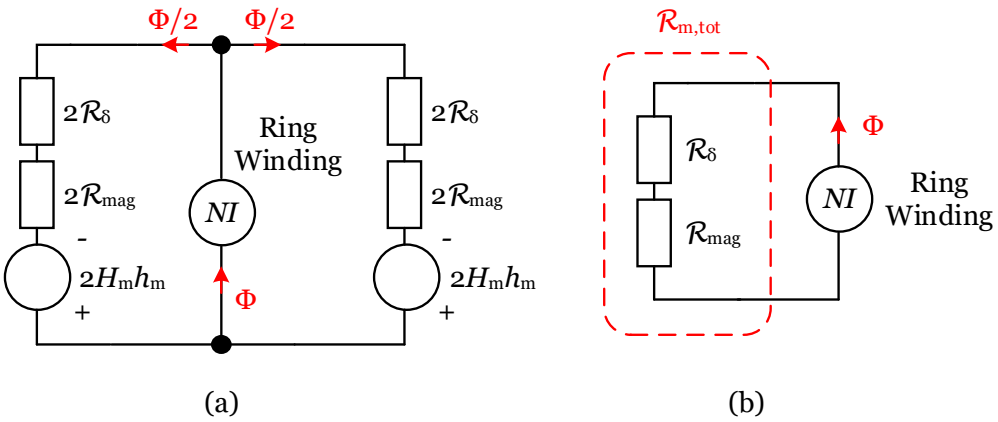

Fig. D.2: (a) simplified MEC and (b) simplified MEC with inactive PMs.

Since the magnet flux does not contribute to the self inductance of the ring winding, the magnet sources are short-circuited. Simplifying the parallel connection in Fig. D.2(a) then yields the circuit shown in Fig. D.2(b), in which the total reluctance consists of the addition of the air-gap and magnet reluctances, $\mathcal{R}_{\mathrm{m,tot}} = \mathcal{R}_\delta + \mathcal{R}_{\mathrm{mag}}$.

Following [38], the air-gap and magnet reluctances can be estimated as

$$\mathcal{R}_\delta \approx \frac{\ln\left(1+\frac{\delta}{r_3}\right)}{\mu_0 l_{\mathrm{ax}} \varphi_{\mathrm{cp}} \frac{2\pi}{360^\circ}} \tag{D.1}$$

and

$$\mathcal{R}_{\mathrm{mag}} \approx \frac{\ln\left(1+\frac{h_{\mathrm{m}}}{r_3+\delta}\right)}{\mu_0 \mu_{\mathrm{rec}} l_{\mathrm{ax}} \varphi_{\mathrm{cp}} \frac{2\pi}{360^\circ}}. \tag{D.2}$$

Then, the total reluctance can be calculated as:

$$\mathcal{R}_{\mathrm{m,tot}} = \frac{360^\circ}{2\pi\mu_0 l_{\mathrm{ax}} \varphi_{\mathrm{cp}}} \left[\frac{1}{\mu_{\mathrm{rec}}} \ln\left(1+\frac{h_{\mathrm{m}}}{r_3+\delta}\right) + \ln\left(1+\frac{\delta}{r_3}\right)\right]. \tag{D.3}$$

[1] When the motor is assumed to have pole-symmetry, the cross coupling can be omitted.

The flux Φ, caused by the excitation of the ring winding, can be determined as

$$\Phi = \frac{NI}{\mathcal{R}_{\mathrm{m,tot}}}. \tag{D.4}$$

Using $\Psi = N\Phi = L_{\mathrm{ph}}I$, the phase inductance can be estimated as:

$$L_{\mathrm{ph}} = \frac{N^2}{\mathcal{R}_{\mathrm{m,tot}}}. \tag{D.5}$$

Appendix E

Air-Gap Permeance Variation for Symmetric and Asymmetric Air-Gaps

Qualitatively, Fig. E.1 illustrates both the air-gap length $\delta(\varphi_m)$ and the resulting permeance $\mathcal{P}(\varphi_m) \propto \frac{1}{\delta(\varphi_m)}$ versus the circumferential angle φ_m for symmetric (*Baseline*) and asymmetric (*Design 0*) air-gaps. For symmetric air-gaps, the air-gap and permeance variations have rectangular-like shapes. (In the slots, i.e., for φ_{slot}, the air-gap length is assumed to have a certain value δ_{slot}.) In case of an asymmetric air-gap (see Fig. 4.1), the air-gap increases linearly from δ_{min} to δ_{max} over the claw-pole angle φ_{cp}. Correspondingly, the permeance variation shows the inverse behavior, leading to a hyperbolic decrease of $\mathcal{P}(\varphi_m)$ over φ_{cp}. The air-gap flux density caused by the PMs shows a hyperbolic behavior as well, which can be obtained inserting $\delta(\varphi_m)$ into (1.4).

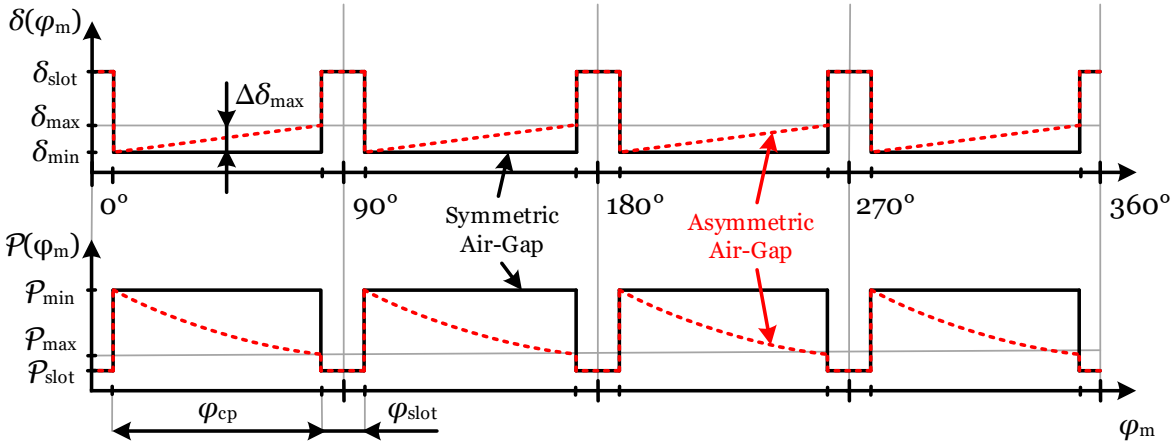

Fig. E.1: Air-gap and permeance variations for symmetric and asymmetric air-gaps.

Appendix F

Winding Model for Air-Gap Asymmetry

In general, the room for the winding reduces when air-gap asymmetry (*Design 0*) is implemented. In Figs. 5.1(a) and (b), for increasing $\Delta\delta_{\max}$, the radius r_3 reduces to r_3''. This in turn limits the winding window height h_w shown in Fig. F.1 (for a fixed radius r_2''), causing a linear decrease in the total winding window area A_{tot}:

$$r_3'' = r_3 - \Delta\delta_{\max}, \tag{F.1}$$

$$h_w = r_3'' - r_2'' - c_w, \tag{F.2}$$

$$A_{tot} = b_w h_w = b_w\,(r_3 - \Delta\delta_{\max} - r_2'' - c_w), \tag{F.3}$$

where b_w is the winding window width and c_w represents the clearance between the winding and the stator iron to prevent winding damage during motor assembly.

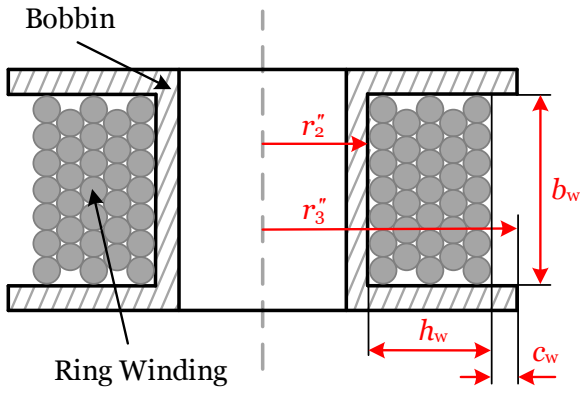

Fig. F.1: Section of the winding model.

For constant mechanical fill factor k_{mech} and number of turns N, the wire size d_{wire}

decreases with increasing $\Delta\delta_{\max}$ (unifilar: $k_w = 1$; bifilar: $k_w = 2$):

$$d_{\text{wire}} = \sqrt{\frac{4k_{\text{mech}}b_w(r_3 - \Delta\delta_{\max} - r_2'' - c_w)}{k_w N\pi}}. \tag{F.4}$$

For decreasing d_{wire}, the phase resistance R increases according to:

$$R \propto \frac{1}{(d_{\text{Cu}})^2}, \tag{F.5}$$

where d_{Cu} is the copper diameter excluding insulation material. This results, for constant rms phase current I_p, in a linear increase in copper losses P_{Cu}:

$$P_{\text{Cu}} = I_p^2 R. \tag{F.6}$$

The described increase in copper losses for increasing $\Delta\delta_{\max}$ is demonstrated in Fig. F.2 for *D0* using the relative air-gap asymmetry $\Delta\delta_{\text{rel}}$.[1] The arrows successively

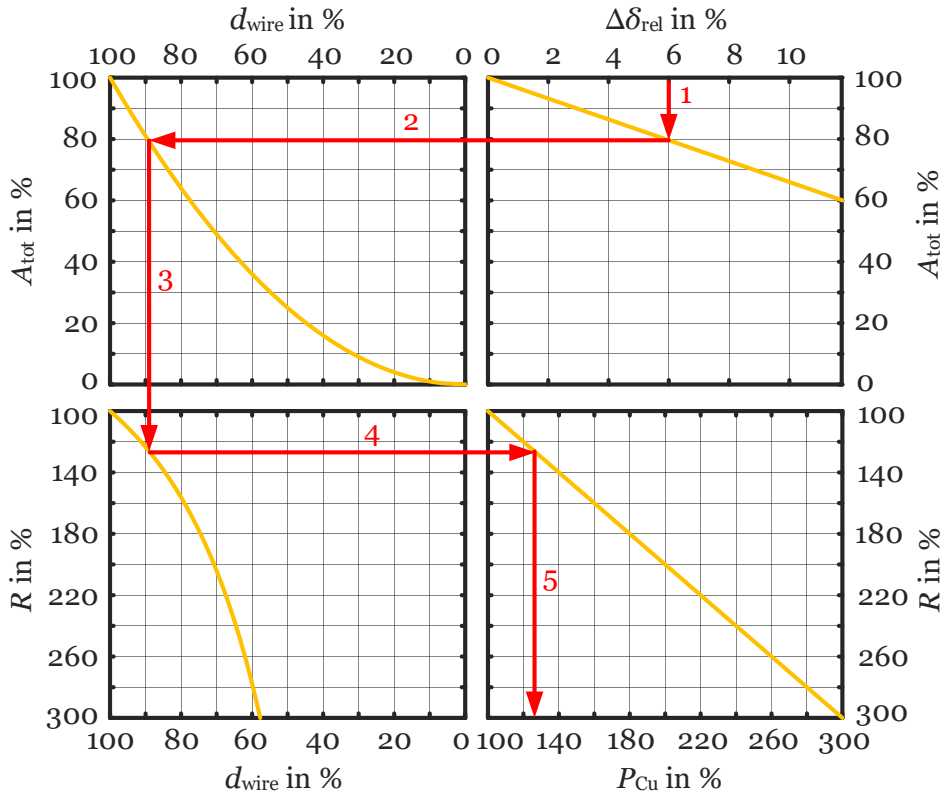

Fig. F.2: Relative increase in P_{Cu} of *D0* due to increasing $\Delta\delta_{\text{rel}}$.

[1] A copper-to-wire diameter ratio of $d_{\text{Cu}}/d_{\text{wire}} \approx 0.9$ is assumed, which is reasonable for grade 1 copper wires of diameters between 0.1 and 0.2 mm [115].

indicate (steps 1–5) that for an air-gap asymmetry $\Delta\delta_{rel} = 6\,\%$, the winding area is reduced by 20 %, requiring a reduction in wire diameter by about 10 % (for constant N), causing an increase in R and hence P_{Cu} by 33.3 % (from 100 % to 133.3 %).

Remark 1: Since increasing air-gap asymmetry $\Delta\delta_{max}$ reduces the room for the winding (see Fig. F.1), the smallest necessary $\Delta\delta_{max}$ should be designed for the following two reasons: Increasing $\Delta\delta_{max}$ 1) increases the effective air-gap δ_{eff}, which increases the air-gap reluctance and in turn decreases the PM flux per pole, and 2) reduces the room for the winding, requiring thinner wires which increases the phase resistances and copper losses.

Remark 2: In addition to the inertia of the mechanical system, the required starting torque and air-gap asymmetry also depend on the bearing friction and the operating temperature, because the viscous friction of the bearing increases with decreasing temperature. A small value of $\Delta\delta_{max}$ may suffice for ball bearings as they usually show lower friction during the start compared with sleeve bearings. (The Stribeck curve [160] should be considered.)

Appendix G

Analytic Derivation of the Air-Gap Asymmetry

The following shows the step-by-step derivation of the air-gap asymmetry, determining the parameter d_{asym} presented in (5.2) and illustrated in Figs. 5.1(a) and (b).

The air-gap asymmetry is defined by the maximum widening of the air-gap length

$$\Delta\delta_{\text{max}} = r_3 - r_3''. \tag{G.1}$$

Rearranging for r_3'' yields

$$r_3'' = r_3 - \Delta\delta_{\text{max}}. \tag{G.2}$$

In Fig. 5.1(b), the claw-pole baseplate is characterized by the following parameters:

$$h = r_3 \cos\left(\frac{\varphi_{\text{cp}}}{2}\right) \tag{G.3}$$

$$w_{\text{stat}} = 2\, r_3 \sin\left(\frac{\varphi_{\text{cp}}}{2}\right). \tag{G.4}$$

Considering h and w_{stat}, the x-axis displacement can be determined as

$$d_{\text{asym}} = \frac{w_{\text{stat}}}{2} - \sqrt{r_3'^2 - h^2}. \tag{G.5}$$

Applying the law of cosines

$$c^2 = a^2 + b^2 - 2\, a\, b \cos(\beta) \tag{G.6}$$

to the triangle in Fig. 5.1(b) with the sides r_3', r_3'', and d_{asym} yields

$$r_3'^2 = r_3''^2 + d_{\mathrm{asym}}^2 - 2\,r_3''\,d_{\mathrm{asym}}\cos\left(\frac{\varphi_{\mathrm{cp}}}{2} + 90^\circ\right). \tag{G.7}$$

Inserting (G.7) into (G.5) yields

$$d_{\mathrm{asym}} = \frac{w_{\mathrm{stat}}}{2} - \sqrt{r_3''^2 + d_{\mathrm{asym}}^2 - 2\,r_3''\,d_{\mathrm{asym}}\cos\left(\frac{\varphi_{\mathrm{cp}}}{2} + 90^\circ\right) - h^2} \tag{G.8}$$

and in turn

$$\sqrt{r_3''^2 + d_{\mathrm{asym}}^2 - 2\,r_3''\,d_{\mathrm{asym}}\cos\left(\frac{\varphi_{\mathrm{cp}}}{2} + 90^\circ\right) - h^2} = \frac{w_{\mathrm{stat}}}{2} - d_{\mathrm{asym}}. \tag{G.9}$$

Taking the square of (G.9) yields

$$r_3''^2 + d_{\mathrm{asym}}^2 - 2\,r_3''\,d_{\mathrm{asym}}\cos\left(\frac{\varphi_{\mathrm{cp}}}{2} + 90^\circ\right) - h^2 = \left(\frac{w_{\mathrm{stat}}}{2} - d_{\mathrm{asym}}\right)^2 \tag{G.10}$$

and, after expanding, in turn

$$r_3''^2 + d_{\mathrm{asym}}^2 - 2\,r_3''\,d_{\mathrm{asym}}\cos\left(\frac{\varphi_{\mathrm{cp}}}{2} + 90^\circ\right) - h^2 = \frac{w_{\mathrm{stat}}^2}{4} - w_{\mathrm{stat}}d_{\mathrm{asym}} + d_{\mathrm{asym}}^2. \tag{G.11}$$

Subtracting d_{asym}^2 from both sides of (G.11) and rearranging the same yields

$$r_3''^2 - h^2 - \frac{w_{\mathrm{stat}}^2}{4} = 2\,r_3''\,d_{\mathrm{asym}}\cos\left(\frac{\varphi_{\mathrm{cp}}}{2} + 90^\circ\right) - w_{\mathrm{stat}}d_{\mathrm{asym}} \tag{G.12}$$

and then

$$r_3''^2 - h^2 - \frac{w_{\mathrm{stat}}^2}{4} = d_{\mathrm{asym}}\left[2\,r_3''\cos\left(\frac{\varphi_{\mathrm{cp}}}{2} + 90^\circ\right) - w_{\mathrm{stat}}\right]. \tag{G.13}$$

Finally, separating d_{asym} yields (5.2) as follows:

$$d_{\mathrm{asym}} = \frac{r_3''^2 - h^2 - \frac{w_{\mathrm{stat}}^2}{4}}{2\,r_3''\cos\left(\frac{\varphi_{\mathrm{cp}}}{2} + 90^\circ\right) - w_{\mathrm{stat}}}. \tag{G.14}$$

Appendix H

Thermal Equivalent Circuit Model

Fig. H.1 depicts a simple thermal equivalent circuit model of the claw-pole stator, the parameters of which are determined from finite-element simulations and experiments. P_{Cu} is the loss source caused by current in the winding and the equivalent

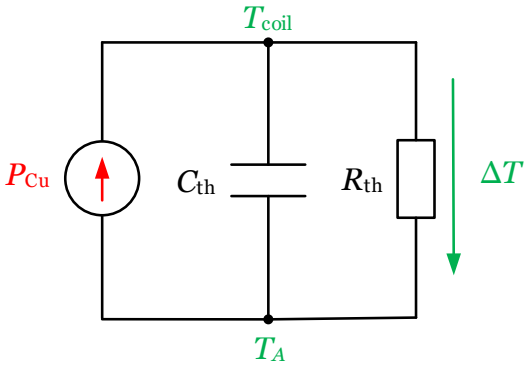

Fig. H.1: Thermal equivalent circuit of the claw-pole motor.

thermal resistance and capacitance R_{th} and C_{th} represent the heat transfer path from the winding (i.e., T_{coil}) to the ambience (i.e., T_{A}). While C_{th} characterizes the transient behavior, R_{th} determines the steady-state temperature.

According to [32,115,161], the overtemperature ΔT caused by the dissipated power P_{Cu} can be determined as

$$\Delta T = \frac{P_{\mathrm{Cu}}}{h_{\mathrm{th}} \cdot A_{\mathrm{th}}} = P_{\mathrm{Cu}} \cdot R_{\mathrm{th}}, \tag{H.1}$$

where h_{th} is the combined heat transfer coefficient (which is generally temperature-dependent but often assumed constant) and A_{th} is the equivalent heat transfer surface area. As per Fig. H.1, the total winding temperature T_{coil} is then

$$T_{\mathrm{coil}} = T_{\mathrm{A}} + \Delta T. \tag{H.2}$$

Equations (H.1) and (H.2) can be used to determine R_{th} from the finite-element simulations and experiments, or analytically.

The thermal time constant τ_{th}, which is defined as the time after which the rising temperature has reached 63.2 % of the thermal steady-state, is defined as

$$\tau_{\mathrm{th}} = C_{\mathrm{th}} R_{\mathrm{th}}. \tag{H.3}$$

It can be used to calculate the equivalent thermal heat capacitance C_{th} using the value for R_{th} from (H.1) [161]. The developed model can be used to study the thermal behavior of different claw-pole motor designs, given different input losses.

Appendix I

Radial Forces Caused by Eccentricity

Based on (P.1)[1] and using (1.4), the force in the air-gap over one pole, can be approximated (neglecting iron saturation and the MMF drop in the iron) as:

$$F_\delta = \frac{A_{\text{pole}}}{2\,\mu_0} B_{\delta,\text{PM}}^2 = \frac{A_{\text{pole}}}{2\,\mu_0} \left(\frac{B_{\text{rem}}}{1 + \mu_{\text{rec}} \frac{\delta}{h_{\text{m}}}} \right)^2 , \tag{I.1}$$

where A_{pole} is the pole area[2] over which a constant value of $B_{\delta,\text{PM}}$ is assumed. At diametrically opposed locations in the air-gap, these radial forces are equal for symmetric motors and hence cancel out, i.e., the net force is zero. However, with increasing eccentricity e_y, as shown in Fig. I.1, the air-gap length δ increases by e_y in

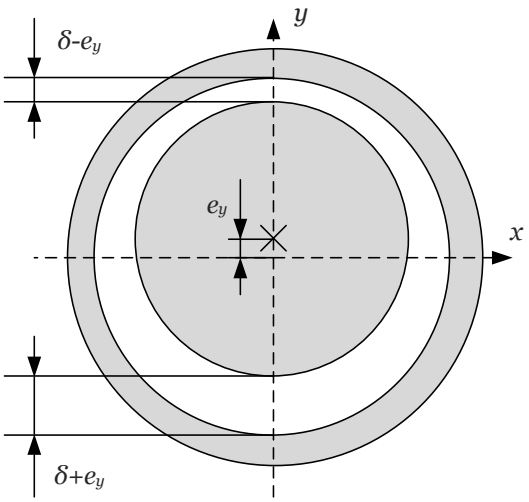

Fig. I.1: Simple eccentricity model.

one location and decreases by e_y in the other.

[1] B_{t} is typically much smaller than B_{r} and can hence be neglected because $B_{\text{t}}^2 << B_{\text{r}}^2$.
[2] The pole area can be calculated as $A_{\text{pole}} = r_{\text{s}} l_{\text{ax}} \varphi_{\text{cp}} \frac{2\pi}{360^\circ}$.

As a result, the net force (i.e., the difference of the opposing forces) caused by the eccentricity is non-zero and is given by

$$F_{\mathrm{y,mag}} = \frac{A_{\mathrm{pole}}}{2\,\mu_0}\left[\left(\frac{B_{\mathrm{rem}}}{1+\mu_{\mathrm{rec}}\frac{\delta-e_y}{h_{\mathrm{m}}}}\right)^2 - \left(\frac{B_{\mathrm{rem}}}{1+\mu_{\mathrm{rec}}\frac{\delta+e_y}{h_{\mathrm{m}}}}\right)^2\right]. \tag{I.2}$$

Taking the system parameters listed in Table A.2 into account, $F_{\mathrm{y,mag}}$ is shown in Fig. I.2 for $0 < e_y < 0.5\,\mathrm{mm}$, exhibiting a disproportional increase for increasing relative eccentricity ε.[3] However, when $\varepsilon < 0.4$, the increase in URMF is essentially

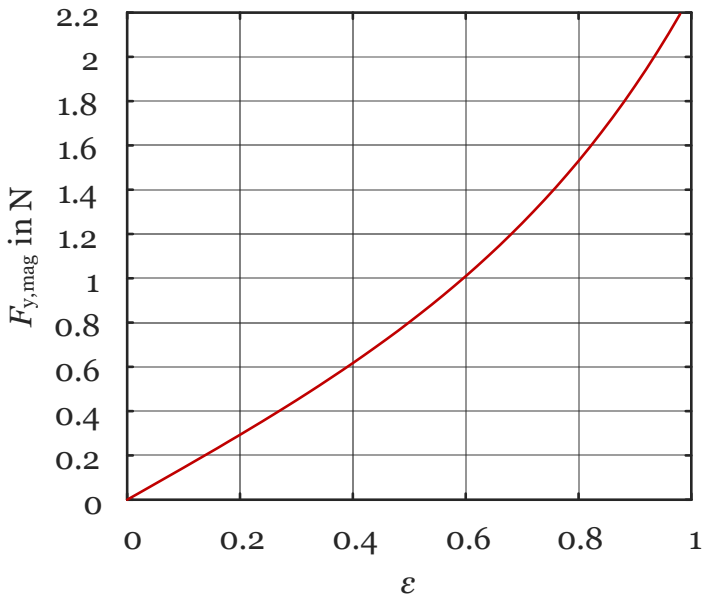

Fig. I.2: Theoretical URMF caused by eccentricity.

linear. Taking the non-linear behavior of the stator iron material into account, the URMF is likely to level off for large values of ε, suggesting a practically linear increase after all, as observed in the measured URMFs shown in Figs. 5.20 and 5.21.

[3] The relative eccentricity is defined in (P.8).

Appendix J

Radial Claw-Pole Deflection Analysis

As discussed in Section 5.7, the deep-drawn steel sheet claw-poles are generally subject to radial magnetic forces, as a result of the radial component of the air-gap flux density $B_{\delta,\mathrm{PM}}$ caused by the PM on the rotor, as illustrated in Fig. J.1. Depending

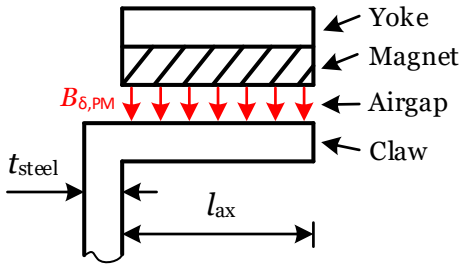

Fig. J.1: Axial cross-section of one claw-pole.

on the steel sheet thickness t_{steel}, the axial length l_{ax}, and the strength of the PM (and hence $B_{\delta,\mathrm{PM}}$), a deflection of the claw in the radial direction can occur. This can in turn lead to vibrations and disturbing noise.

In a first approximation, the claw can be modeled as a beam which is subject to a line load q causing a bending moment M as exhibited in Fig. J.2(a). The line load q can be defined for the claw-pole cross section shown in Fig. J.2(a) as

$$q = \frac{F_\delta}{l_{\mathrm{ax}}} = \frac{B_{\delta,\mathrm{PM}}^2 \, l_{\mathrm{ax}} \, r_3 \frac{\varphi_{\mathrm{cp}}}{2\pi}}{2\,\mu_0}, \tag{J.1}$$

where F_δ is the force caused by the radial component of the air-gap flux density, r_3 is the stator outer radius, and φ_{cp} is the claw-pole angle. The deflection curve

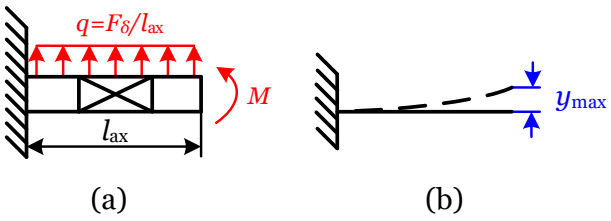

Fig. J.2: Beam approximation of one claw-pole: (a) line load and (b) maximum deflection.

indicated in Fig. J.2(b) can be calculated as follows:

$$y(z) = \frac{q\, l_{\mathrm{ax}}^4}{24\, E\, I_{\mathrm{area}}} \left[\left(\frac{z}{l_{\mathrm{ax}}}\right)^4 - 4\left(\frac{z}{l_{\mathrm{ax}}}\right)^3 + 6\left(\frac{z}{l_{\mathrm{ax}}}\right)^2 \right], \tag{J.2}$$

where E is the Young's Modulus and I_{area} is the area moment of inertia.

The maximum deflection y_{max} at the end of the claw illustrated in Fig. J.2(b) can be determined as

$$y_{\mathrm{max}} = \frac{F_\delta\, l_{\mathrm{ax}}}{8\, E\, I_{\mathrm{area}}}. \tag{J.3}$$

When approximated as a cantilever, the area moment of inertia of a flattened claw-pole can be estimated as

$$I_{\mathrm{area}} = \frac{r_3\, \varphi_{\mathrm{cp}}\, t_{\mathrm{steel}}^3}{2\,\pi\, 12}. \tag{J.4}$$

The exact area moment of inertia of one claw-pole I'_{area} can be calculated as

$$I'_{\mathrm{area}} = \frac{1}{8}\left(r_3^4 - (r_3 - t_{\mathrm{steel}})^4\right)(\varphi_{\mathrm{cp}} + \sin\varphi_{\mathrm{cp}}) - z_c^2\left(r_3^2 - (r_3 - t_{\mathrm{steel}})^2\right)\frac{\varphi_{\mathrm{cp}}}{2}, \tag{J.5}$$

where

$$z_c = \frac{2\left(r_3^3 - (r_3 - t_{\mathrm{steel}})^3\right)\sin\frac{\varphi_{\mathrm{cp}}}{2}}{3\left(r_3^2 - (r_3 - t_{\mathrm{steel}})^2\right)\frac{\varphi_{\mathrm{cp}}}{2}}. \tag{J.6}$$

Inserting (J.5) into (J.3), the maximum deflection can be described as a function of both the air-gap flux density $B_{\delta,\mathrm{PM}}$ and the steel sheet thickness t_{steel}

$$y_{\mathrm{max}} = \frac{3\, B_{\delta,\mathrm{PM}}^2 l_{\mathrm{ax}}^4}{4\mu_0 E t_{\mathrm{steel}}^3}. \tag{J.7}$$

As per (J.7), l_{ax} has the largest influence on the deflection, followed by t_{steel} and $B_{\delta,\mathrm{PM}}$. Fig. J.3 shows the maximum deviation y_{max}, determined by (J.7), as a function

of t_{steel} for different values of $B_{\delta,\text{PM}}$, assuming a Young's Modulus for free-cutting steel of $E = 210000\,\text{MPa}$ and an axial length of $l_{\text{ax}} = 6\,\text{mm}$. As expected, the maximum deviation increases with decreasing t_{steel} and increasing $B_{\delta,\text{PM}}$. Deflections even in the μm range can cause noise [18].

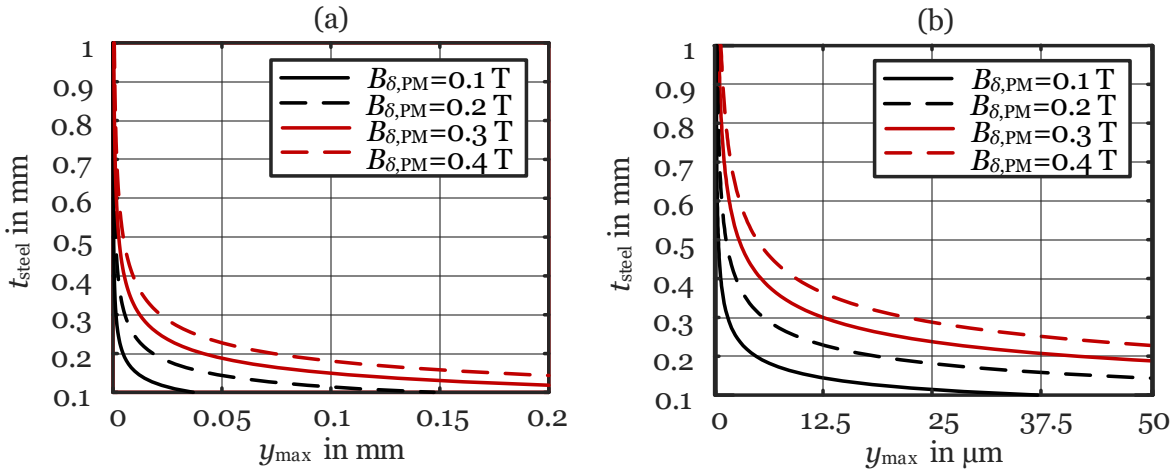

Fig. J.3: Maximum deflection as a function of steel sheet thickness and air-gap flux density (a) and inset (b).

Appendix K

Static Cogging Torque Measurement

The cogging torque of *D0* and *D01(30°)* is estimated in the following using a simple lever-based static cogging torque measurement. The utilized test setup is shown in Fig. K.1, where an additional mass m_{add} is attached to the rotor system at a distance r, tracking the angular displacement of the rotor θ. Starting from a stable equilibrium

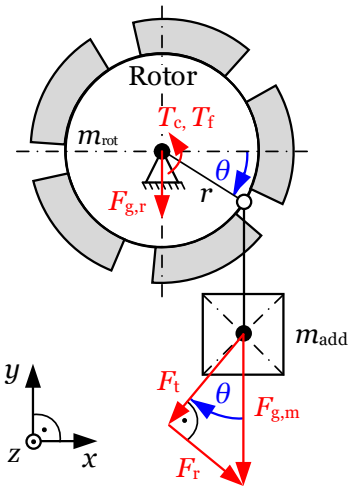

Fig. K.1: Experimental test setup for the static cogging torque measurement.

position, m_{add} is increased (and with it the gravitational force $F_{\text{g,m}} = m_{\text{add}}\, g$) such that the rotor leaves the stable equilibrium position, approaches the unstable equilibrium point, and exceeds it causing the rotor to break loose.

The rotor system, with the mass m_{rot}, consists of a rotor cup with a PM ring, a rotor yoke, plastic fan blades, and a shaft. The gravitational force of the rotor cup is $F_{\text{g,r}} = g\,(m_{\text{rot}}+m_{\text{add}})$, which can be separated into its tangential and radial components F_{t} and F_{r}, respectively. A slide bearing is axially placed inside the claw-pole stator

parts. The thread used to attach the mass can be considered massless, and the rotor cup can be assumed as a rigid body with no elastic displacement when attaching the mass.

The cogging torque T_c counteracts the enforced rotor displacement caused by the additional mass m_{add}. Increasing the mass m_{add}, the angular displacement θ is measured and the cogging torque T_c is calculated for each position according to

$$T_c = r\,F_t = r\,m_{add}\,g\cos(\theta). \tag{K.1}$$

Fig. K.2 shows the comparison of the simulated and measured cogging torque waveforms of *D0* and *D01(30°)* using the setup presented in Fig. K.1. Compared to *D0*, the effect of the single-sided skew in *D01(30°)* is evident. However, while in the same order, the simulated and measured cogging torques differ significantly.

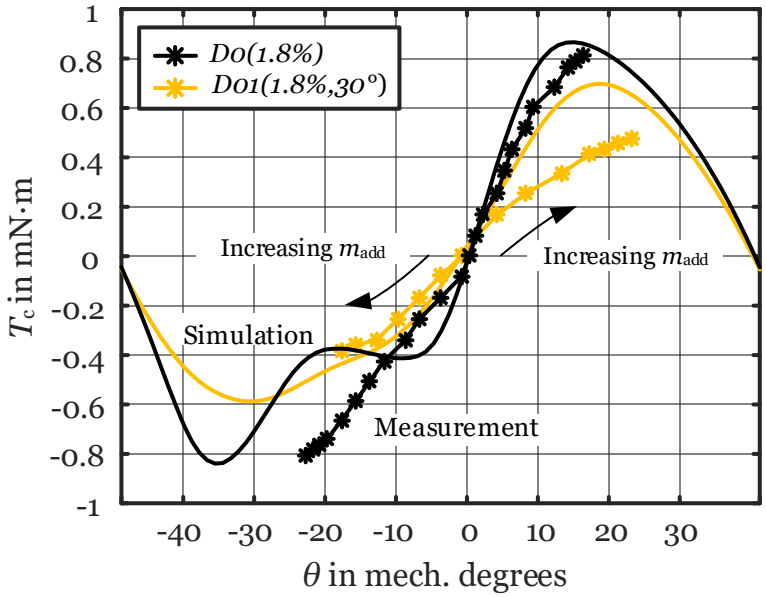

Fig. K.2: Measured cogging torque using the static torque measurement from Fig. K.1.

Remark 1: The used static torque measurement approach can determine the cogging torque waveform only partly in the region of a stable equilibrium position.

Remark 2: In addition to the cogging torque, the friction torque also counteracts the enforced rotation. The friction torque of the slide bearing is a function of the attached mass m: $T_f = \mu_s\,(m_{rot} + m_{add})\,g$, where μ_s is the coefficient of static friction. However, for the measurements, as neither a Stribeck curve nor a reliable coefficient

of static friction of the used bearing-shaft combination are available, the influence of the friction is neglected and partly overcome by forcing the rotor cup to reach the respective equilibrium position through a damped oscillation, caused by an impulse of force. Yet, a residual friction always remains, as does the influence of the hysteresis torque.

In summary, the static cogging torque measurement is unsuitable as it lacks accuracy as a result of the uncertainties with respect to the length of the lever, the influence of friction, and the weight of the attached mass. For accurate measurements, the rheometer-based cogging torque measurement, presented and discussed in Subsection 3.2.2, is highly recommended.

Appendix L

Rheometer: Speed Constancy, Torque Accuracy, and Run-Out Accuracy

The validity of the assumption of constant speed in (3.6) and (3.7), the accuracy of the torque measurement, and the run-out accuracy of the claw-pole motor and salient-pole motor test setups are discussed in the following:

The used rheometer-based measurement techniques rely on a constant rotational speed. The rotational speed versus rotor position during an exemplary measurement for $n = 1$ rpm is depicted in Fig. L.1. The speed can be considered constant because

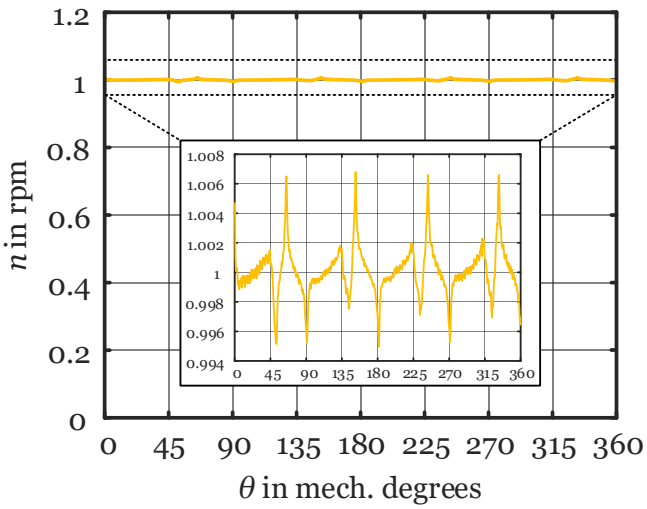

Fig. L.1: Rotational speed versus rotor position during an exemplary measurement for $n = 1$ rpm illustrating the speed constancy of the rheometer.

the inset in Fig. L.1 shows a maximum deviation below 0.7 % of the preset speed n. Similar results are obtained for elevated speeds. Hence, the assumption of zero

inertia related torque in (3.6) and (3.7), i.e., $J\frac{d\omega}{dt} = 0$, is valid.

As mentioned in Subsection 3.2.2, the measuring drive of the rheometer features a torque accuracy of ±0.5 % of the measured value (but maximum ±0.2 μN·m). Accordingly, the measurement uncertainty for a section of the measured torque waveform from Fig. 9.2 is indicated in Fig. L.2, illustrating in red the maximum positive and negative deviations, respectively. Notice that the measurement error is, in

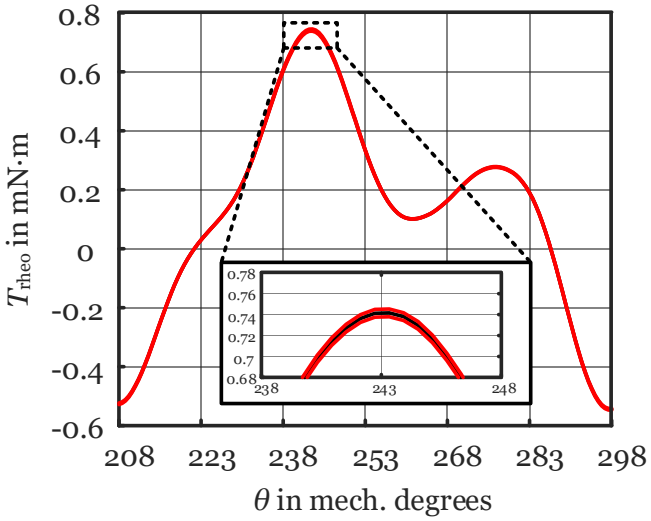

Fig. L.2: Illustration of the measurement uncertainty of the rheometer for an exemplary no-load torque waveform indicating the maximum deviation in red.

fact, extremely low. The inset shows the point of the highest torque measured, which is where the maximum measurement error is expected, illustrating the impressive accuracy of the used measuring device.

Measuring small quantities, the test setup alignment is of vital importance. The measured run-out accuracies of the test setup in Fig. 9.1(a) are ±25 μm for the stator outer perimeter and ±20 μm for the rotor inner perimeter, while those of the test setup in Fig. 9.1(b) are ±80 μm for the stator outer perimeter and ±65 μm for the rotor inner perimeter.

Appendix M

Estimation of the Windage Losses

The friction between the air in the air-gap and the rotor surface causes losses during operation, which increase with increasing speed. The windage losses P_{wind} (in W) of a small machine without a fan can be estimated for speeds below 6000 rpm as [22]:

$$P_{\text{wind}} \approx 2\, d_{\text{r}}^3\, l_{\text{ax}}\, n^3\, 10^{-6}, \tag{M.1}$$

where d_{r} is the rotor diameter (in m), l_{ax} is the axial length of the machine (in m), and n is the speed (in rpm).

By means of (M.1) and (9.1), the windage torque T_{wind} can be estimated. For the studied claw-pole motor ($d_{\text{r}} = 17\,\text{mm}$, $l_{\text{ax}} = 5.2\,\text{mm}$) operated at the maximum rheometer speed of 3000 rpm, the expected maximum windage torque is approximately $4.4\,\mu\text{N}\cdot\text{m}$. Compared to the offset torque of about $380\,\mu\text{N}\cdot\text{m}$ at 3000 rpm (extrapolating the results in Fig. 9.12), the maximum windage torque amounts to about 1.2 % of the maximum offset torque. Hence, the influence of the windage losses can be neglected. Similar results can be obtained for the salient-pole motor studied in Fig. 9.14, where the expected maximum windage torque at 3000 rpm amounts to about 6.1 % of the maximum offset torque. For lower speeds, the influence of windage is much smaller, because the rotational speed in (M.1) is cubed.

Appendix N

Cogging Torque and Hysteresis Torque Extractions

The derivations of (3.9) and (3.10), which are used to extract the cogging torque T_c and the hysteresis torque T_{hys}, is presented below. Based on (3.7), the measured torque T_{rheo} for the CW and CCW directions can be denoted as:[1]

$$T_{rheo,CW} = T_c + T_{hys}, \tag{N.1a}$$

$$T_{rheo,CCW} = T_c - T_{hys}. \tag{N.1b}$$

Adding (N.1a) and (N.1b), the hysteresis torque component T_{hys} vanishes, and the following equation is obtained:

$$T_{rheo,CW} + T_{rheo,CCW} = 2\,T_c. \tag{N.2}$$

Rearranging (N.2) for T_c yields (3.9):

$$T_c = \frac{T_{rheo,CW} + T_{rheo,CCW}}{2}. \tag{N.3}$$

Taking the difference between (N.1a) and (N.1b), the cogging torque T_c vanishes, and the following equation is obtained:

$$\pm T_{rheo,CW} \mp T_{rheo,CCW} = 2\,\left|T_{hys}\right|. \tag{N.4}$$

Rearranging for $\left|T_{hys}\right|$ yields (3.10):

$$\left|T_{hys}\right| = \frac{\pm T_{rheo,CW} \mp T_{rheo,CCW}}{2}. \tag{N.5}$$

[1] As illustrated in the context of Fig. 9.11, T_{hys} always counteracts the rotation; it is positive for the CW direction and negative for the CCW direction.

Appendix O

Additional URMF Calculations of the *Baseline*

Calculated URMF Caused by Eccentricity for Misaligned Stator Parts

As illustrated in Fig. P.1(b), the effects of misaligned claw-pole stator parts (i.e., non-zero φ_{off} causing unequal inter-claw distances) due to non-ideal assembly are studied for the *Baseline* in the following:

Fig. O.1 displays f_{r} and f_{t}, when $\theta = 0°$, $\varphi_{\text{off}} = 5°$, and $\varepsilon \in [0, 0.4]$. Compared

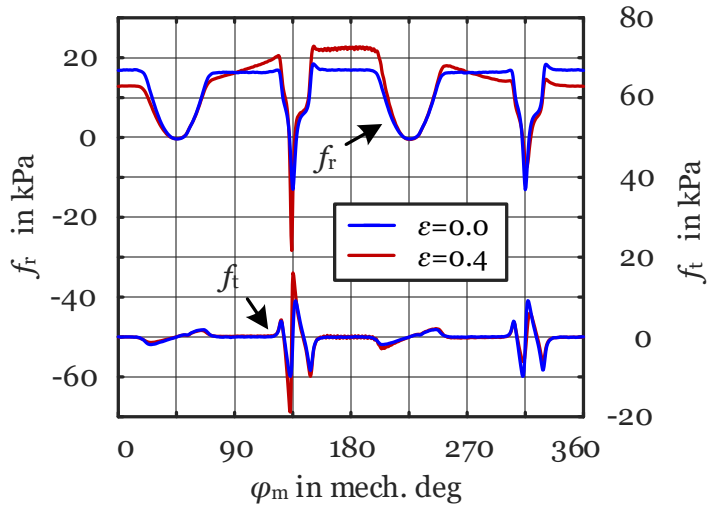

Fig. O.1: Analysis of eccentricity for misaligned stator parts of the *Baseline*: radial and tangential magnetic tractions when $\theta = 0°$, $\alpha = 24°$, and $\varphi_{\text{off}} = 5°$.

to Fig. 5.11, f_{r} decreases while f_{t} increases in Fig. O.1 in the regions of enlarged

inter-claw distance due to the stator part misalignment of $\varphi_{\text{off}} = 5°$, when $\varepsilon = 0$. When $\varphi_{\text{off}} = 5°$ and $\varepsilon = 0.4$, both f_{r} and f_{t} increase in the region of reduced air-gap due to the eccentricity. The change in f_{t} alters the cogging torque waveform.

Fig. O.2 depicts the corresponding loci of URMFs, showing that misaligned stator parts only cause URMFs in combination with eccentricity. (The force distribution is

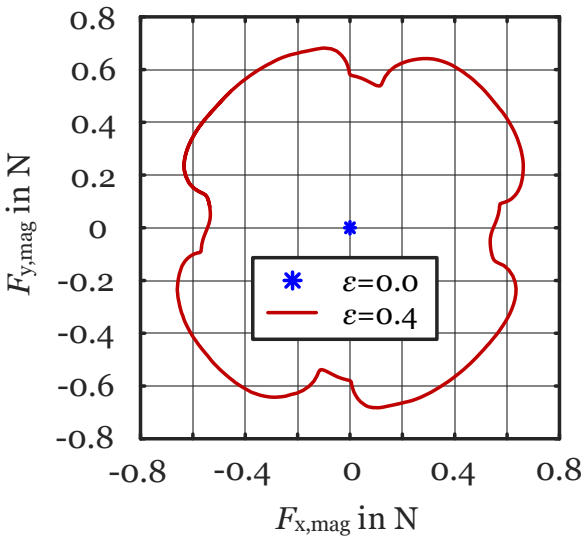

Fig. O.2: Analysis of eccentricity for misaligned stator parts of the *Baseline*: loci of URMFs, when $\alpha = 24°$ and $\varphi_{\text{off}} = 5°$.

asymmetric due to the misaligned stator parts.) Otherwise, when $\varepsilon = 0$, the radial forces cancel out for diametrically opposed positions in the air-gap.

Calculated URMF Caused by Eccentricity for Different Magnetization Patterns

The influence of radial and parallel magnetization patterns on the formation of URMFs as a result of static eccentricity is investigated for the *Baseline* hereafter. The decaying angle α in Fig. P.2 is also varied.

Figs. O.3 and O.4 show f_{r} and f_{t} for parallel and radial magnetization patterns, respectively, when $\varepsilon = 0.4$ and $\alpha \in [16, 20, 24]°$. As expected, f_{r} increases for both patterns in the region of reduced air-gap, while f_{t} changes insignificantly; the dashed

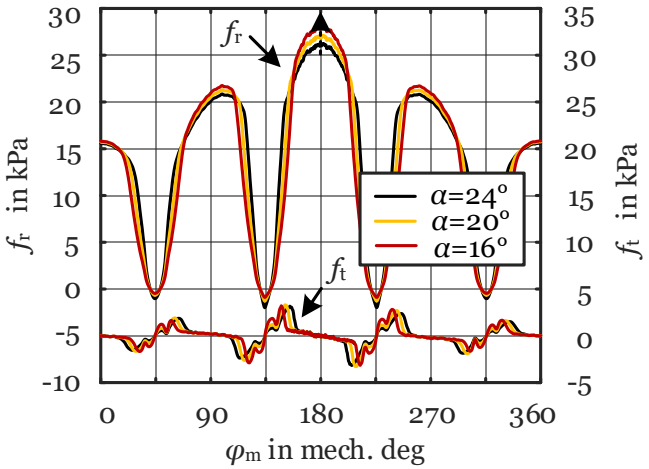

Fig. O.3: Analysis of eccentricity for a parallel magnetization pattern for the *Baseline*: radial and tangential magnetic tractions, when $\theta = 0°$ and $\varepsilon = 0.4$.

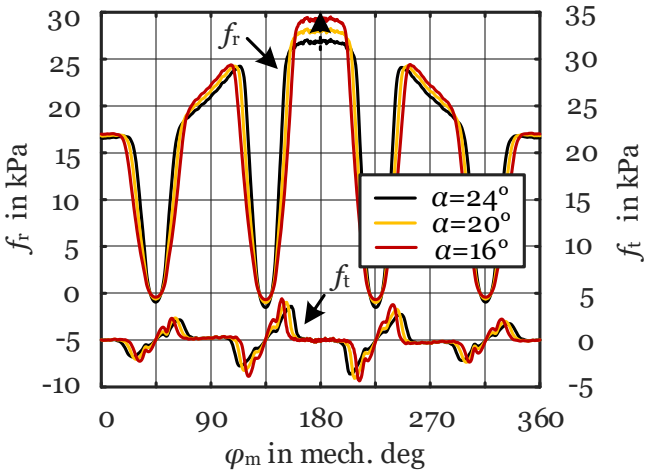

Fig. O.4: Analysis of eccentricity for a radial magnetization pattern for the *Baseline*: radial and tangential magnetic tractions, when $\theta = 0°$ and $\varepsilon = 0.4$.

arrows indicate decreasing α. Notice that a parallel magnetization pattern causes rounder f_r peaks than a radial one.

Fig. O.5 depicts the loci of URMFs for the studied magnetization patterns and eccentricity. For concentric rotor-stator arrangements (i.e., $\varepsilon = 0$), no URMFs occur for both magnetization patterns, independently of α. However, when $\varepsilon = 0.4$, the decaying angle α has a significant influence on the amplitude of higher order harmonics, indicated by the dashed arrows. The amplitudes increase with decreasing α for both magnetization because, thereby, the amplitude of the first order harmonic

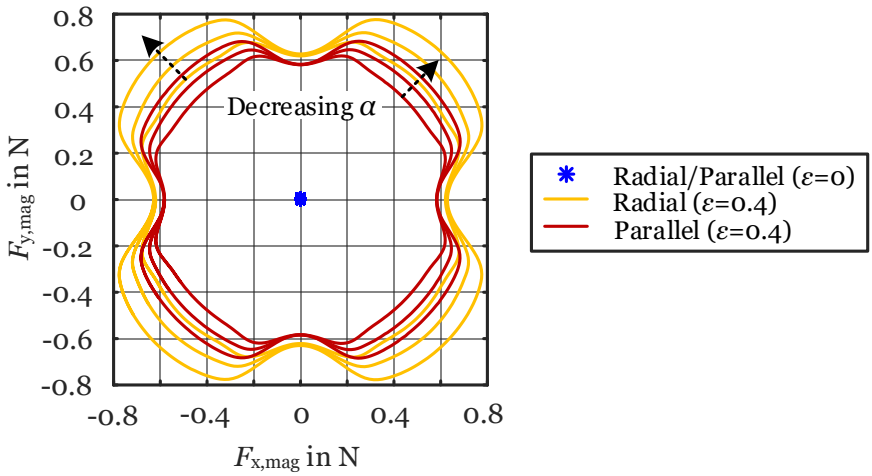

Fig. O.5: Analysis of eccentricity for different magnetization patterns for the *Baseline*: loci of the URMFs, when $\alpha \in [16, 20, 24]°$.

component of the air-gap flux density increases.[1]

The results shown in Fig. O.5 imply that a radial magnetization pattern induces larger UMFs than a parallel one.[2]

Calculated URMF Caused by Non-Uniform Magnetization

In the following, the formation of URMFs in the *Baseline* in consequence of a non-uniform magnetization of the PM ring illustrated in Fig. P.2 is studied. Since the magnetic pole pairs differ in strength, the air-gap flux density distributions deviate for said pole pairs [similar to the effect of eccentricity in Fig. 5.10], as do the radial forces acting on both the rotor and stator. Hence, URMFs can occur despite a concentric rotor-stator arrangement (i.e., $\varepsilon = 0$). For the analysis, the maximum radial magnetization M_{ro} shown in Fig. P.2 is increased by ΔM for one of the two pole pairs of the *Baseline*'s PM ring. The maximum value of ΔM considered in this analysis is 10 % of M_{ro}, represented by $m = \frac{\Delta M}{M_{ro}}$.

[1] The decaying angle α, characterizing the inter-pole region of the magnet, is not a design parameter because, ideally, it is zero. The magnetization of the inter-pole region is primarily determined by the magnetization process and fixture.

[2] However, a parallel magnetization causes a more sinusoidal back-EMF, like desirable in three-phase BLAC drives.

Fig. O.6 displays f_r and f_t when $m \in [0.05, 0.1]$, $\varepsilon = 0$, and $\alpha = 24°$.[3] The distri-

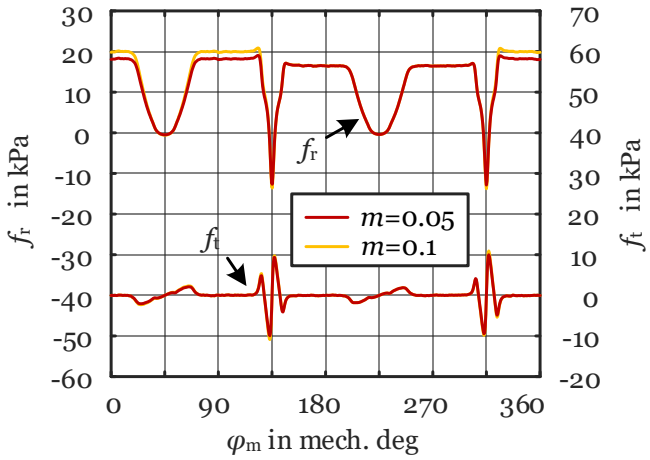

Fig. O.6: Analysis of non-uniform magnetization for the *Baseline*: radial and tangential magnetic tractions for $\theta = 0°$ for $\varepsilon = 0$ and $\alpha = 24°$.

butions of f_r and f_t of the studied non-uniform magnetizations are similar to those shown in Fig. O.1 in which $\varepsilon = 0$ and $\varphi_{off} = 5°$. In addition, f_r is larger in the regions where $m > 0$, while f_t does not change notably.

Fig. O.7 shows the corresponding loci of the URMFs for the studied non-uniform magnetizations. As expected, despite a concentric rotor-stator arrangement (i.e.,

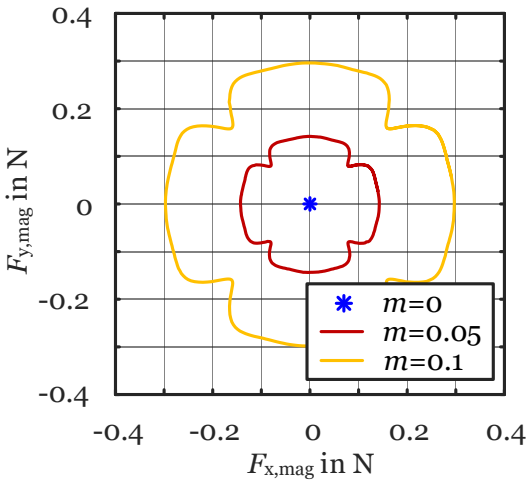

Fig. O.7: Analysis of non-uniform magnetization for the *Baseline*: URMF loci for $\varepsilon = 0$ and $\alpha = 24°$.

[3] Fig. 5.11 shows f_r and f_t for $m = 0$ and $\varepsilon = 0$.

$\varepsilon = 0$), a rotating URMF is identified. The pulsating character of the URMF is even more pronounced than that induced by eccentricity.

Again, resonances at four times the rotational frequency can be triggered, similar to the effects of the eccentricity studied in Figs. 5.14, 5.19, O.2, and O.5. As expected, the URMFs increase essentially linearly with increasing non-uniform magnetization m, as previously identified for the eccentricity ε.

Appendix P

Radial Magnetic Force Analysis

The radial magnetic forces are calculated analytically based on the air-gap flux density waveforms obtained from the no-load finite-element simulations. Thereby, the influence of eccentricity, stator part misalignment, and non-uniform magnetization can be studied. The used procedure is discussed in the following:

The local radial and tangential magnetic tractions,[1] f_r and f_t, can be determined for a certain rotor position θ from the corresponding air-gap flux density components, B_r and B_t, evaluated at the air-gap radius r_δ [162] for $0° \leq \varphi_\mathrm{m} \leq 360°$ [see Figs. P.1(a) and (b)] in the finite-element model, using the Maxwell stress tensor[2] [37, 40]:

$$f_\mathrm{r} = \frac{1}{2\mu_0}\left(B_\mathrm{r}^2 - B_\mathrm{t}^2\right) \tag{P.1}$$

$$f_\mathrm{t} = \frac{1}{\mu_0} B_\mathrm{r}\, B_\mathrm{t}, \tag{P.2}$$

where μ_0 is the permeability of free space. In Cartesian coordinates, this equals

$$f_\mathrm{x} = f_\mathrm{r}\cos(\varphi_\mathrm{m}) - f_\mathrm{t}\sin(\varphi_\mathrm{m}) \tag{P.3}$$

$$f_\mathrm{y} = f_\mathrm{r}\sin(\varphi_\mathrm{m}) + f_\mathrm{t}\cos(\varphi_\mathrm{m}). \tag{P.4}$$

To obtain the resultant radial force $F_\mathrm{r,mag}$ for the rotor position θ, the respective magnetic tractions into the x- and y-directions are integrated over the stator surface

$$F_\mathrm{x,mag} = l_\mathrm{ax}\, r_\delta \int_0^{2\pi} f_\mathrm{x}\, d\varphi_\mathrm{m} \tag{P.5}$$

$$F_\mathrm{y,mag} = l_\mathrm{ax}\, r_\delta \int_0^{2\pi} f_\mathrm{y}\, d\varphi_\mathrm{m}, \tag{P.6}$$

[1] They are also referred to as magnetic force densities.

[2] The assumptions made include $\mu_0 << \mu_\mathrm{fe}$ and constant flux density in the z-direction.

where l_{ax} is the axial length of the motor, to eventually determine $F_{r,mag}$ as

$$F_{r,mag} = \sqrt{(F_{x,mag})^2 + (F_{y,mag})^2}. \tag{P.7}$$

The above procedure can be used to study the radial magnetic force distributions caused by symmetric and asymmetric air-gaps [see Fig. P.1(a)], stator part misalignment [see φ_{off} in Fig. P.1(b)], and different magnetization patterns [e.g., radial versus parallel]. In addition, the unbalanced radial magnetic forces (URMFs) as a result of eccentricity [see e in Fig. P.1(a)] and non-uniform magnetization [see ΔM in Fig. P.2] can be calculated.

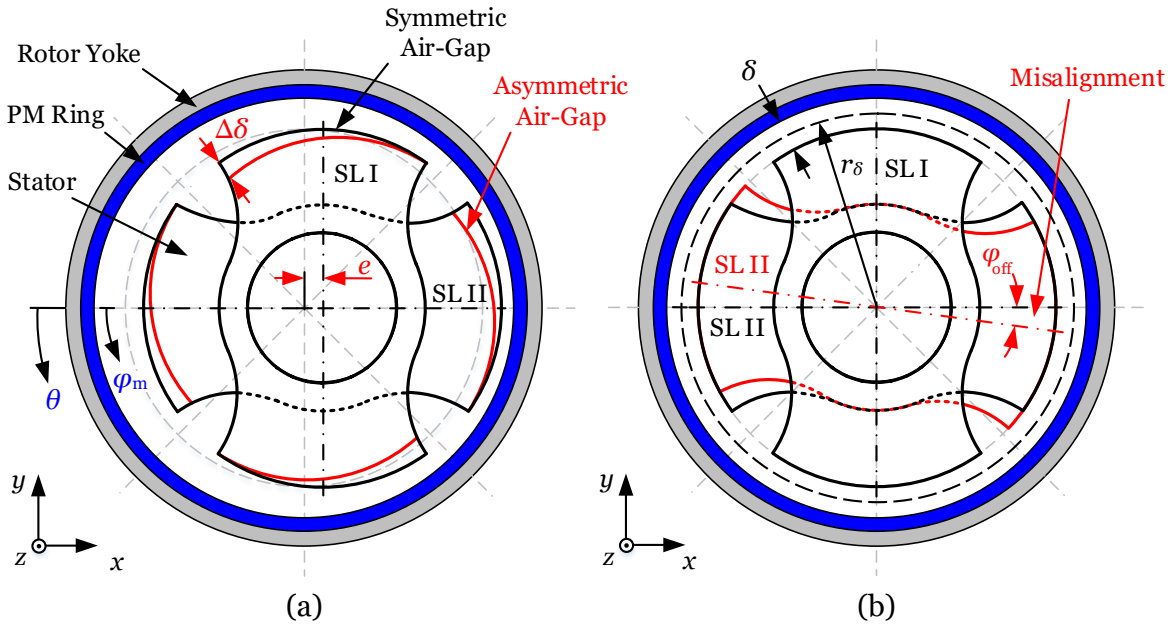

Fig. P.1: Illustrations of (a) static eccentricity and (b) misaligned stator parts.

For the analyses, the x- and y-components of the URMFs are determined evaluating (P.5)–(P.6) for a full rotation (i.e., $0° \leq \theta \leq 360°$) with an angular resolution of 0.5°, as are the URMF loci. Similarly, the URMFs as a function of θ can be determined using (P.7).

The used finite-element analysis program JMAG Designer® [91] offers a comfortable way to include eccentricity effects. Using the static eccentricity e and the air-gap length δ [see Figs. P.1(a) and (b)], the relative static eccentricity ε, which is used for the analyses, is defined as

$$\varepsilon = \frac{e}{\delta}, \quad \text{where} \quad 0 \leq \varepsilon \leq 1. \tag{P.8}$$

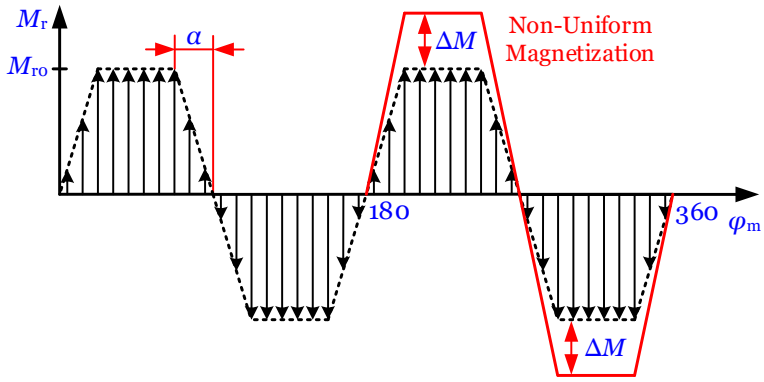

Fig. P.2: Non-uniform magnetization model of the PM ring in Fig. P.1.

JMAG Designer® [91] also offers a comfortable way to model the magnetization of the PM ring (see the radial magnetization M_r in Fig. P.2), where the transition zones can be specified by the decaying angle α. In addition, the magnetization pattern can be specified, e.g., radial or parallel.[3] By segmening the PM ring in the model, a non-uniform magnetization can also be applied for certain analyses, see ΔM in Fig. P.2.

[3]Polar anisotropic or custom patterns can be specified as well.

Appendix Q

Leakage Increase Caused by Skewing

Increasing the skewing angle ξ_{skew}, the leakage between two stator claws increases for a constant claw-pole angle φ_{cp}, because the effective inter-claw distance δ_{claw}, shown in Fig. Q.1(a), is reduced to δ^*_{claw}, as shown in Fig. Q.1(b). The following

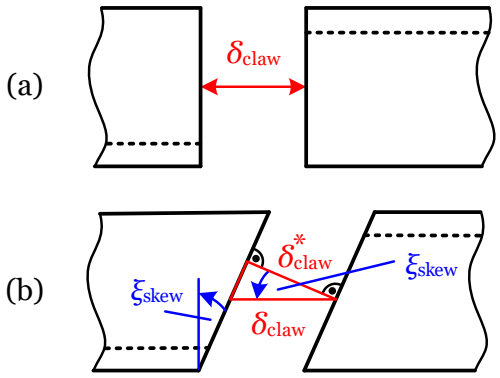

Fig. Q.1: Inter claw region: (a) no skew and (b) single-sided skew.

geometric relationship holds true:

$$\delta^*_{\text{claw}} = \delta_{\text{claw}} \cos(\xi_{\text{skew}}). \tag{Q.1}$$

The inter-claw region is modeled by the reluctance $\mathcal{R}_{\delta,\text{claw}}$ in Fig. D.1. The influence of skewing can hence be estimated as follows:

$$\mathcal{R}_{\delta,\text{claw}} \approx \frac{\delta^*_{\text{claw}}}{\mu_0\, t_{\text{steel}}\, \frac{l_{\text{ax}}}{\cos(\xi_{\text{skew}})}} = \frac{\delta_{\text{claw}} \cos^2(\xi_{\text{skew}})}{\mu_0\, t_{\text{steel}}\, l_{\text{ax}}}. \tag{Q.2}$$

Increasing the skewing angle ξ_{skew} reduces $\mathcal{R}_{\delta,\text{claw}}$, which in turn increases the leakage inductance of the motor.

Appendix R

Analysis of the Air-Gap Flux Density Distribution

The air-gap flux density distributions of the *Baseline*, *D2*, and *D3(45°)* are evaluated along a circular contour in the middle of the air-gap, i.e., at the air-gap radius r_δ, see Fig. P.1(b). The air-gap flux density's radial and tangential components, B_r and B_t, as well as its absolute value, $|B_{\delta,\mathrm{PM}}|$ are investigated.

Fig. R.1 shows B_r and B_t of the *Baseline*, *D2*, and *D3(45°)*, when the rotor and stator poles are centered, i.e., $\theta = 0°$. On the one hand, the auxiliary slots in *D2* cause

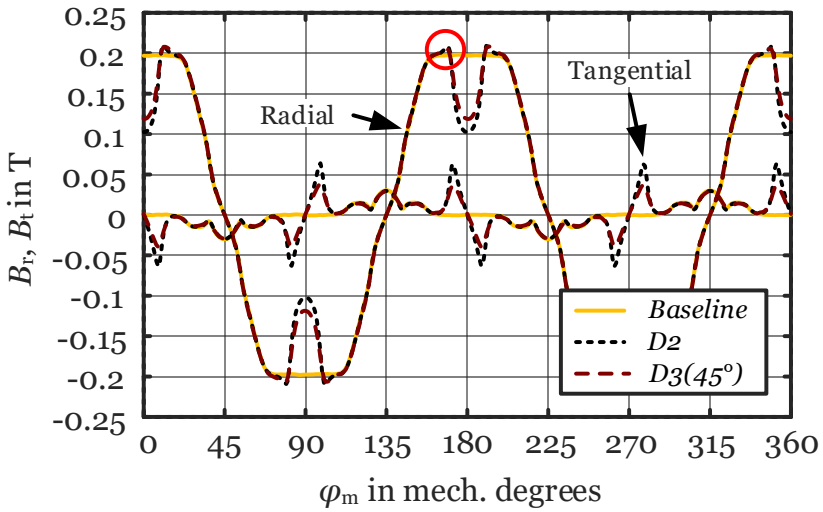

Fig. R.1: Calculated radial and tangential air-gap flux density distributions of the *Baseline*, *D2*, and *D3(45°)* for centered stator and rotor poles, i.e., $\theta = 0°$.

local drops in B_r in the middle of the auxiliary slots (i.e., at $\varphi_\mathrm{m} \in [0, 90, 180, 270]°$) and small local increases at the edges of the auxiliary slots (e.g., indicated by the

red circle) due to flux concentration. On the other hand, as iron is removed from the claw-pole center in *D2*, the magnet flux enters the stator iron to a significant portion in the tangential direction. This results in additional B_t components in the same locations as the local drops in B_r (i.e., at $\varphi_m \in [0, 90, 180, 270]°$), which are the reason for the additional cogging torque waveform (see $T_{c,aux}$ in Section 7.1). When a single-sided skew is applied in addition to auxiliary slots in *D3(45°)*, the described local drops in B_r in *D2* are mitigated due to the averaging effect of the skewing, and the significant tangential components at $\varphi_m \in [0, 90, 180, 270]°$ are reduced as well.

Fig. R.2 depicts the respective absolute air-gap flux density distributions $|B_{\delta,PM}|$ of the *Baseline*, *D2*, and *D3(45°)* determined from the radial and tangential components according to $|B_{\delta,PM}| = \sqrt{(B_r)^2 + (B_t)^2}$. (Comparing Figs. R.1 and R.2, it is evident that

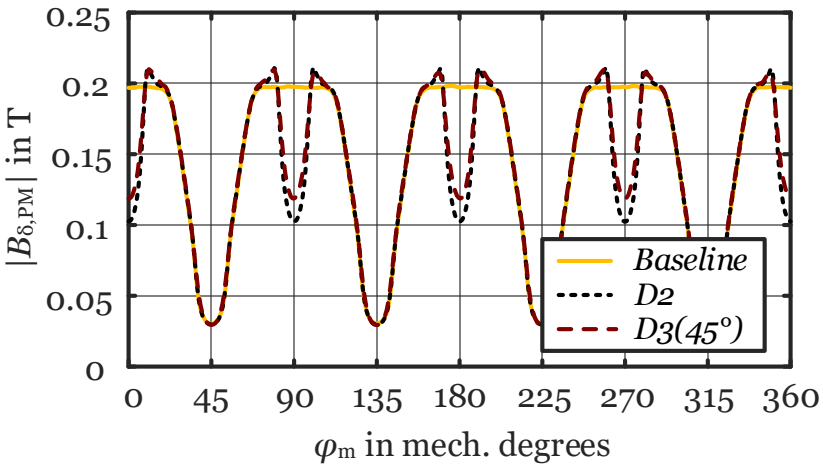

Fig. R.2: Calculated absolute air-gap flux density distributions of the *Baseline*, *D2*, and *D3(45°)* for centered stator and rotor poles, i.e., $\theta = 0°$.

$|B_\delta|$ is dominated by B_r.) The corresponding average values $|\overline{B}_{\delta,PM}|$ are 148 mT, 136 mT, and 140 mT in the *Baseline*, *D2*, and *D3(45°)*, respectively. Effectively, compared with the *Baseline*, the cogging torque reduction measures reduce $|\overline{B}_{\delta,PM}|$ by 8 % in *D2* but only by 5.5 % in *D3(45°)*. This reduction reduces the average output torque for the same phase current, see (1.13).

Remark: As per (1.4) and the system parameters listed in Table A.2, a maximum air-gap flux density of about 0.21 T is expected, which is in good agreement with the results shown in Figs. R.1 and R.2.

Appendix S

Analysis of the Phase Inductance and Leakage Flux Ratios

The phase inductance L_{ph} of the *Baseline*, *D2*, and *D3(45°)*, as well as the changes in the rotor and stator leakage flux ratios are studied below. To this aim, 3-D finite-element simulations are performed.

To identify the phase inductance, the magnetic system reluctance $\mathcal{R}_{\mathrm{m,sys}}$ is determined according to $\mathcal{R}_{\mathrm{m,sys}} = \frac{I_{\mathrm{DC}} N}{\phi_{\mathrm{s}}}$ (for constant phase currents I_{DC} between 0 A and 3 A in one sub-phase), where ϕ_{s} is the flux through the cylindrical portion of the two stator parts, i.e., the stator yoke. Therefore, the flux contribution of the magnet is set to zero (i.e., the material is set to μ_{rec} or even μ_0). The phase inductance is then calculated as $L_{\mathrm{ph}} = \frac{N^2}{\mathcal{R}_{\mathrm{m,sys}}}$ as a function of I_{DC}, see Fig. S.1(a). For the unsaturated case, L_{ph} is 6 mH, 5.7 mH, and 6.2 mH for the *Baseline*, *D2*, and *D3(45°)*, respectively. For currents larger than 1 A, L_{ph} decreases significantly down to approximately 3 mH.

For the stator leakage analysis, the already determined values of the stator yoke flux ϕ_{s} are compared with the cumulative flux in the rotor yoke sections ϕ_{r} to obtain the portion of the flux lost in the inter-claw region (i.e., leakage flux between adjacent claws). Hence, the stator leakage ratio λ_{s} is calculated from $\lambda_{\mathrm{s}} = \frac{\phi_{\mathrm{s}} - \phi_{\mathrm{r}}}{\phi_{\mathrm{s}}}$ and shown in Fig. S.1(b) as a function of I_{DC}. For the unsaturated case, the stator leakage ratios amount to 54.9 %, 55.9 %, and 62.7 % for the *Baseline*, *D2*, and *D3(45°)*, respectively. For currents larger than 1 A, λ_{s} increases by up to 7 %.

For the rotor leakage analysis, the flux contribution of the magnet is considered but the current I_{DC} is set to zero. Therefore, the rotor leakage ratio is determined from ϕ_{r} and ϕ_{s} as $\lambda_{\mathrm{r}} = \frac{\phi_{\mathrm{r}} - \phi_{\mathrm{s}}}{\phi_{\mathrm{r}}}$. This is the rotor flux that does not link with the stator coils for $\theta = 0$. As depicted in Fig. S.1(b), the calculated rotor leakage ratios are

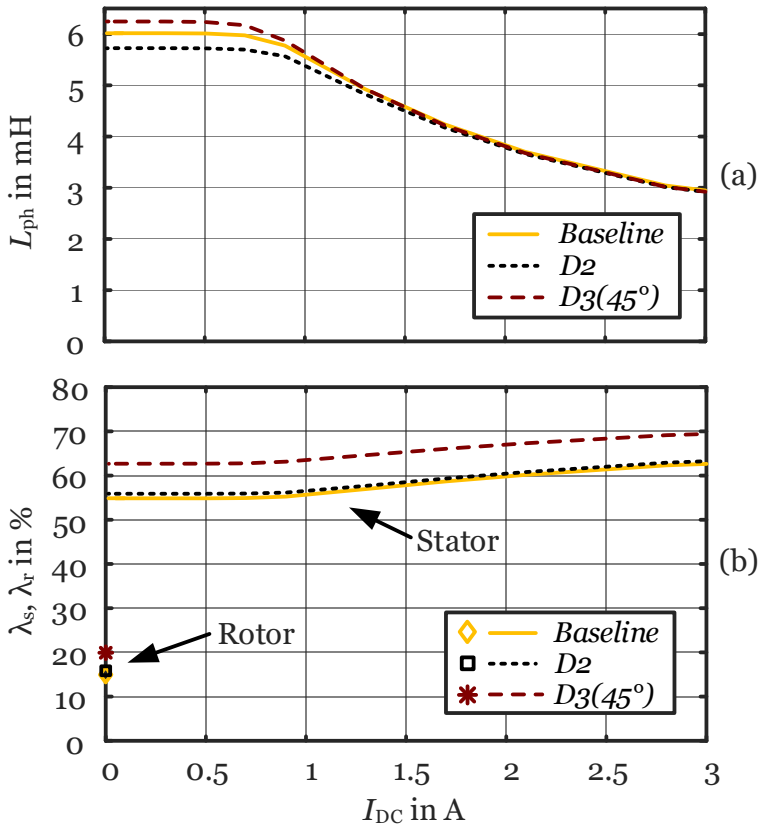

Fig. S.1: Calculated (a) phase inductance and (b) rotor and stator leakage ratios of the *Baseline*, *D2*, and *D3(45°)* as functions of the current, for $\theta = 0$.

14.6 %, 16.5 %, and 19.9 % for the *Baseline*, *D2*, and *D3(45°)*.

It can be concluded that, for a constant claw-pole angle φ_{cp}, the rotor and stator leakage ratios increase somewhat when the proposed cogging torque reduction measures are implemented.

Appendix T

Additional Thermal Analyses

Analysis of the Transient Temperature Drop of the *Baseline*

Fig. T.1 contrasts the measured with the calculated transient temperature drops of the *Baseline* for different input losses. Therefore, the DC source is turned off after the

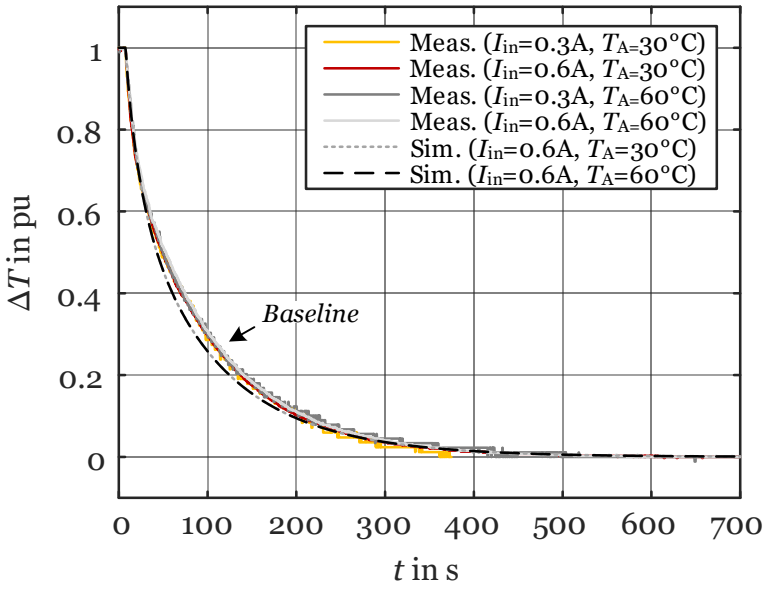

Fig. T.1: Calculated and measured transient temperature drop of the *Baseline* for different input losses.

thermal steady state temperature has been reached. For comparison, the temperature drop is displayed in per unit. As expected, Fig. T.1 shows essentially the inverse behavior of Fig. 7.20.

Analysis of the *Baseline* for Removed Claw-Poles

In this section, the thermal performance of the *Baseline* is studied when the claw-poles are taken off; this motor is denoted *Baseline*†. Figs. T.2(a) and (b) show the measurement setups for the thermal analysis of the *Baseline*†. The *Baseline*† is also

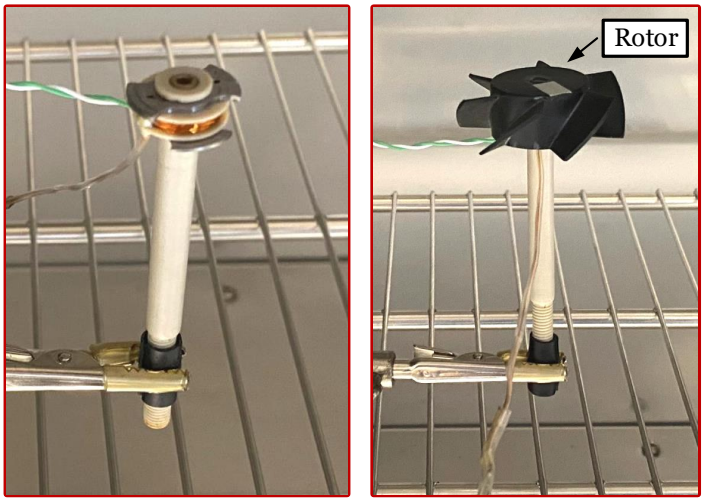

(a) (b)

Fig. T.2: Measurement setup of *Baseline*†: (a) without rotor and (b) with rotor.

investigated including the rotor, see Fig. T.2(b). For the shown arrangement, the rotor builds a heat trap from a natural convection point of view.

Fig. T.3 shows the measured steady-state temperatures of the *Baseline*† for T_A = 60°C for the arrangements without and with the rotor, as shown in Figs. T.2(a) and (b). The measured results are interpolated linearly. The thermal resistance of the *Baseline*† is determined to 43.2 K/W, similar to *D2* and *D3(45°)* at T_A = 60°C, see Table 7.2. When the rotor is placed on top of the stator, the thermal resistance increases by about 15 % to 50 K/W. Similar results are obtained for the *Baseline*, *D2*, and *D3(45°)*. Notice that the rotor notably reduces the cooling capability of the motor.

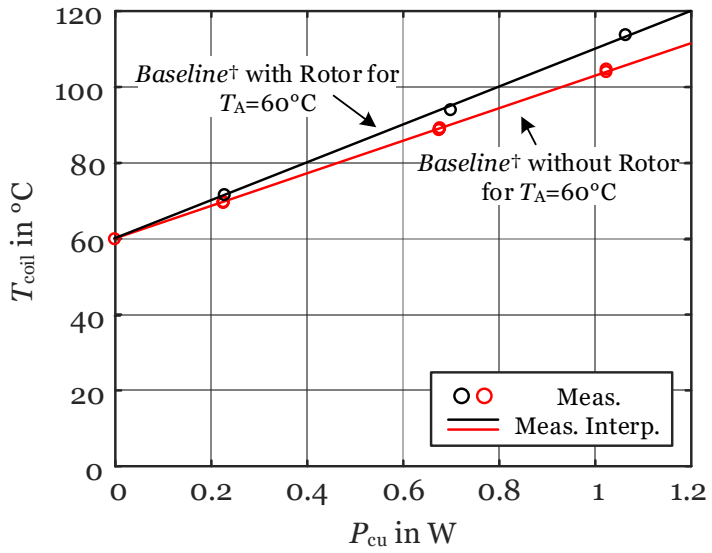

Fig. T.3: Measured steady-state temperatures of the *Baseline*†.

Thermal Characterization of the Winding Alone

In addition to the thermal investigations of the different claw-pole stator designs, the winding on the bobbin alone onto which no stator parts are mounted is studied hereafter. Therefore, the winding is placed both on and above a wooden plate.

Fig. T.4 shows the measured steady-state temperatures of the winding alone when placed on the plate. The thermal resistances are determined to 70.3 K/W and 58.5 K/W

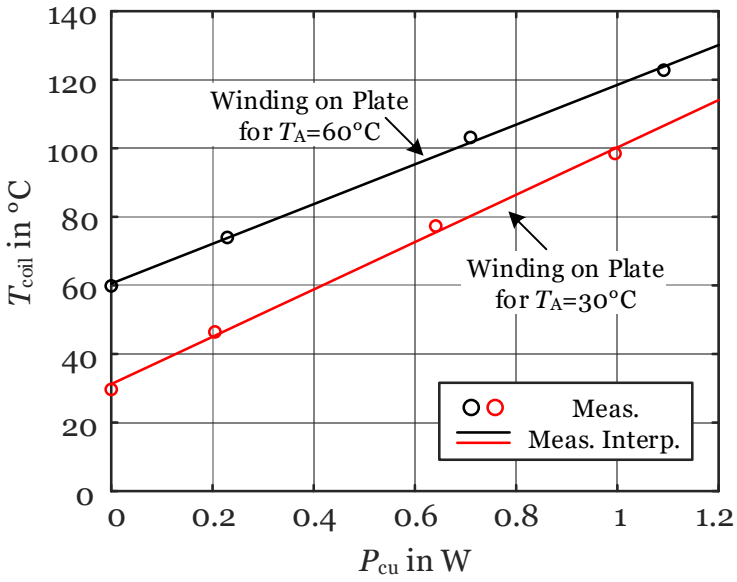

Fig. T.4: Measured steady-state temperatures of the winding placed on the plate.

for ambient temperatures of 30°C and 60°C, respectively. Again, the equivalent thermal resistance decreases with increasing ambient temperature (e.g., by 17 % for a ΔT_A of 30 K).

Fig. T.5 shows the measured steady-state temperatures of the winding alone when placed about 10 cm above the plate. The thermal resistances are determined to

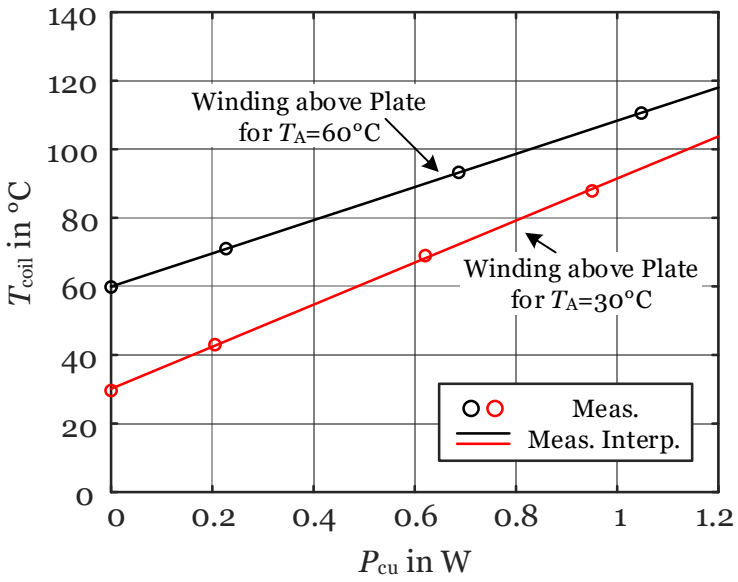

Fig. T.5: Measured steady-state temperatures of the winding placed above the plate.

61.7 K/W and 48.5 K/W for ambient temperatures of 30°C and 60°C, respectively. Again, the equivalent thermal resistance decreases with increasing ambient temperature (e.g., by 21 % for a ΔT_A of 30 K).

When the winding is placed above the plate, the measured thermal resistances are smaller compared to when placed on the plate. This is explained by the air that can pass through the inner hole of the winding, enhancing the natural convection of heat.

Appendix U

Axial Forces Caused by Skewing

The formation of axial forces caused by skewing is discussed below. Based on Ampere's law, the effect of a PM on the rotor can be described by an equivalent magnetization current $I_\mathrm{m} = H_\mathrm{m}\, h_\mathrm{m}$ on its edges, as illustrated in Figs. U.1(a) and (b). In combination with the radial magnetic field of the stator in the air-gap B_{δ,i_p}, a tangential Lorentz force F_t is created, see Fig. U.1(c).

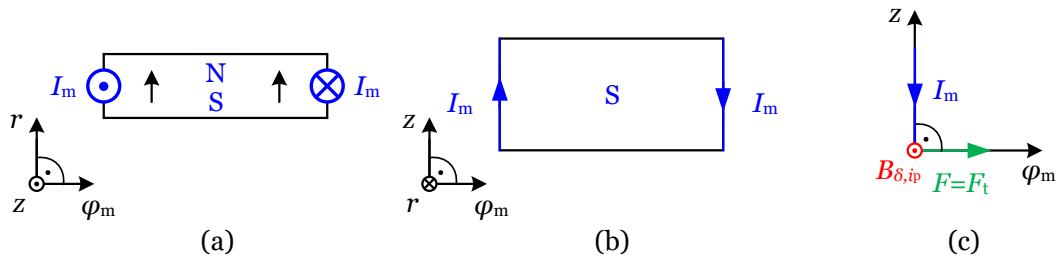

Fig. U.1: (a) equivalent magnetization current model front view, (b) equivalent magnetization current model bottom view, and (c) indication of Lorentz force.

When the stator lamination stack (or alternatively the PM) is skewed by the angle ξ_skew (*Design 1*), the resulting Lorentz force has both tangential and axial components as illustrated in Fig. U.2, see also the discussion in the context of (8.1).

One method to compensate the axial forces is to implement double skewing, i.e., a positive skewing angle for the leading and a negative skewing angle for the lagging edge of the stator or rotor pole, as depicted in Fig. U.3. A well-known example is the automotive claw-pole alternator, whose claw-poles are of the described trapezoidal shape.

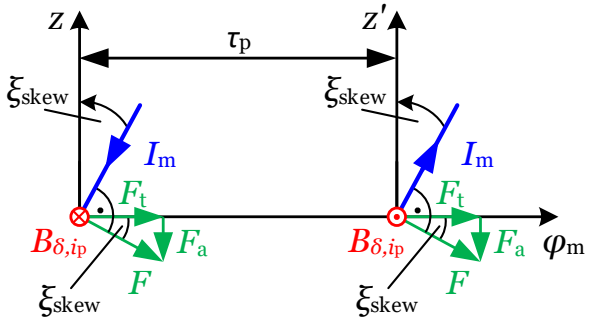

Fig. U.2: Formation of axial forces caused by a single-sided skew.

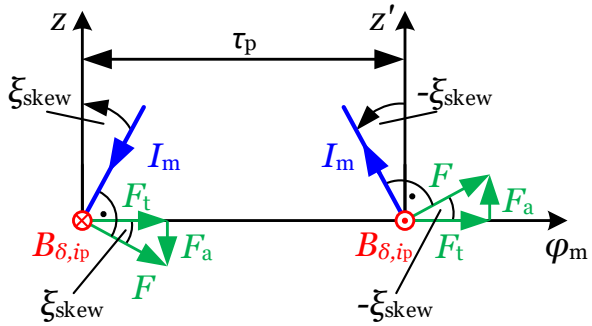

Fig. U.3: Implementation of double skewing to compensate axial forces.

Realizing a single-phase BLDC claw-pole motor with the presented double skewing is unsuitable when auxiliary slots are to be implemented (*Design 2* and *Design 3*), because then the auxiliary slot has a different shape than the actual slot, causing an ineffective modulation of the cogging torque. To provide a remedy, a V-skew is implemented for the proposed designs (*Design 4* and *Design 5*), see Fig. U.4, such that for *Design 5* the auxiliary slots and the actual slots are alike.

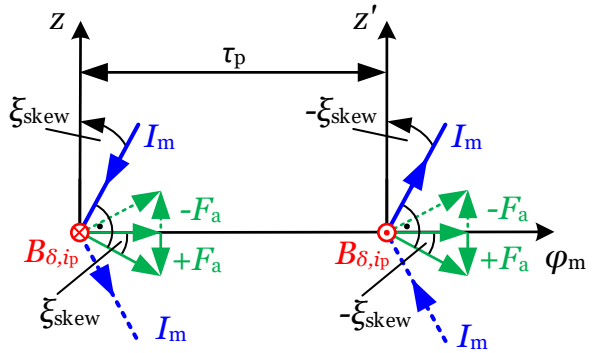

Fig. U.4: Implementation of a V-skew to compensate axial forces.